

Alma Mater Studiorum – Università di Bologna

DOTTORATO DI RICERCA IN

CHIMICA

Ciclo 34

**Settore Concorsuale:** 03/B1 - FONDAMENTI DELLE SCIENZE CHIMICHE E SISTEMI INORGANICI

**Settore Scientifico Disciplinare:** CHIM/03 - CHIMICA GENERALE E INORGANICA

DESIGN, REALIZATION, AND CHARACTERIZATION OF COMPLEX  
REACTION NETWORKS IN DYNAMIC MECHANICALLY  
INTERLOCKED MOLECULES

**Presentata da:** Federico Nicoli

**Coordinatore Dottorato**

Luca Prodi

**Supervisore**

Alberto Credi

**Co-supervisor**

Massimo Baroncini  
Marco Lucarini

**Esame finale anno 2022**



# Contents

---

|   |           |
|---|-----------|
| <b>Introduction</b>   | <b>1</b>  |
| <b>1. From supramolecular chemistry to mechanostereochemistry</b>                 | <b>2</b>  |
| <b>2. Synthesis of rotaxanes</b>  | <b>3</b>  |
| <b>3. MIMs as artificial molecular machines</b>                                   | <b>5</b>  |
| 3.1. Nature as muse   | 6         |
| 3.2. Switches and motors  | 9         |
| 3.3. Ratcheting in molecular machines   | 11        |
| <b>4. References</b>  | <b>14</b> |
| <b>Chapter 1: Toward a light operated molecular transporter</b>                   | <b>18</b> |
| <b>1.1. Introduction</b>  | <b>19</b> |
| 1.1.1. A light powered artificial molecular pump                                  | 19        |
| 1.1.2. Analysis of the cycle  | 21        |
| 1.1.3. Objective of the project   | 23        |
| <b>1.2. Design and synthetic aspects</b>  | <b>24</b> |
| <b>1.3. Synthesis of a dimeric model system</b>                                   | <b>25</b> |
| 1.3.1. Synthesis of the first pump-unit   | 26        |
| 1.3.2. Synthesis of the second pump-unit  | 27        |
| 1.3.3. Synthesis of the dimeric axle  | 28        |
| <b>1.4. A trifluoromethyl dibenzo-[24]-crown-8 derivative</b>                     | <b>29</b> |
| 1.4.1. Direct trifluoromethylation of DB24C8                                      | 29        |
| 1.4.2. Multistep synthesis of 3   | 30        |
| <b>1.5. <sup>1</sup>H-NMR characterization of EE-P1</b>                           | <b>32</b> |
| <b>1.6. Photoisomerization studies on the free axle P1</b>                        | <b>34</b> |
| <b>1.7. Complexation experiments</b>  | <b>37</b> |
| 1.7.1. Reaction network scheme  | 37        |
| 1.7.2. <sup>1</sup> H NMR spectrum of the complex                                 | 38        |
| 1.7.3. Association and rate constants of the equilibria involving pseudorotaxanes | 40        |
| <b>1.8. “Light-ON” experiment</b>   | <b>45</b> |
| <b>1.9. Conclusion and perspectives</b>   | <b>51</b> |
| <b>1.10. Experimental section</b>   | <b>52</b> |
| <b>1.11. Synthetic procedures</b>   | <b>54</b> |
| <b>1.12. NMR spectra</b>  | <b>72</b> |
| <b>1.13. References</b>   | <b>78</b> |

|   |            |
|---|------------|
| <b>Chapter 2: Synthesis and operation of a [2]rotaxane endowed with a novel photoactive recognition site.</b> | <b>81</b>  |
| <b>2.1. Introduction</b>  | <b>82</b>  |
| 2.1.1. Objective of the project   | 83         |
| 2.1.2. <i>E</i> -1H <sup>2+</sup> rotaxane  | 83         |
| <b>2.2. Synthesis of <i>E</i>-1H<sup>2+</sup></b>   | <b>85</b>  |
| 2.2.1. Synthesis of the recognition sites precursors  | 85         |
| 2.2.2. Synthesis of <i>E</i> -1H <sup>2+</sup> and model compound 2   | 86         |
| <b>2.3. <sup>1</sup>H NMR characterization of <i>E</i>-1H<sup>2+</sup></b>                                    | <b>87</b>  |
| <b>2.4. Study of the acid/base switching</b>  | <b>89</b>  |
| <b>2.5. Irradiation experiments</b>   | <b>90</b>  |
| 2.5.1. <sup>1</sup> H NMR photoisomerization study  | 90         |
| 2.5.2. UV-vis photoisomerization and thermal back <i>Z</i> → <i>E</i> isomerization                           | 92         |
| <b>2.6. [2]rotaxane reaction network</b>  | <b>95</b>  |
| 2.6.1. Acid/base properties of the ammonium recognition site  | 96         |
| 2.6.2. Light-on/light-off experiment  | 98         |
| 2.6.3. Out of equilibrium network operation   | 101        |
| <b>2.7. Conclusion</b>  | <b>104</b> |
| <b>2.8. Experimental Section</b>  | <b>105</b> |
| <b>2.9. Synthetic procedures</b>  | <b>108</b> |
| <b>2.10. NMR spectra</b>  | <b>122</b> |
| <b>2.11. References</b>   | <b>129</b> |
| <b>Chapter 3: Chemical induced mismatch of rings and stations in a [3]rotaxane</b>                            | <b>131</b> |
| <b>3.1. Introduction</b>  | <b>132</b> |
| 3.1.2. Objective of the project and RotH <sub>2</sub> <sup>3+</sup> structure                                 | 133        |
| <b>3.2. Synthesis of RotH<sub>2</sub><sup>3+</sup> and model compound 1</b>                                   | <b>135</b> |
| 3.2.1. Synthesis of RotH <sub>2</sub> <sup>3+</sup>   | 135        |
| 3.2.2. Synthesis of the free axle 1   | 136        |
| <b>3.3. <sup>1</sup>H NMR characterization of RotH<sub>2</sub><sup>3+</sup></b>                               | <b>137</b> |
| <b>3.4. Acid/base switching study</b>   | <b>138</b> |
| 3.4.1. Deactivation of one ammonium site ( <i>n<sub>S</sub></i> = <i>n<sub>R</sub></i> )                      | 138        |
| 3.4.2. Deactivation of two ammonium sites ( <i>n<sub>S</sub></i> < <i>n<sub>R</sub></i> )                     | 139        |
| 3.4.3. Functionalization of the deprotonated [3]rotaxane Rot <sup>+</sup>                                     | 140        |
| <b>3.5. Thermodynamic analysis of the deprotonation reaction</b>  | <b>141</b> |
| <b>3.6. Variable-Temperature NMR experiments</b>  | <b>144</b> |
| <b>3.7. Molecular Modelling</b>   | <b>146</b> |
| <b>3.8. Conclusion</b>  | <b>150</b> |
| <b>3.9. Experimental Section</b>  | <b>151</b> |
| <b>3.10. Synthetic procedures</b>   | <b>155</b> |
| <b>3.11. NMR spectra</b>  | <b>170</b> |
| <b>3.12. References</b>   | <b>176</b> |

|                               |            |
|-------------------------------|------------|
| <b><i>Conclusion</i></b>      | <b>179</b> |
| <b><i>Acknowledgement</i></b> | <b>182</b> |



# Abstract

---

The experimental projects discussed in this thesis are all related to the field of artificial molecular machines, specifically to systems composed of pseudorotaxane and rotaxane architectures. The characterization of the peculiar properties of these mechano-molecules is frequently associated with the analysis and elucidation of complex reaction networks; this latter aspect represents the main focus and central thread tying my thesis work. In each chapter, a specific project is described as summarized below:

**Chapter 1** presents the synthesis and characterization of a linear molecular motor designed to achieve the directional transport of a crown ether macrocycle along a linear molecular component using light as the sole energy source. This machine is composed by two photoactivated “pump-modules” derived from a supramolecular pump motif recently developed in our group. At the base of its operation is the  $E \rightleftharpoons Z$  photoisomerization of an azobenzene unit, which causes the directional threading and de-threading of a crown ether rings along a molecular axle. The presence of two pump modules in the synthesized linear molecular motor results in  $2^4 = 16$  possible states for the machine during its operation cycle ( $E$  or  $Z$  complexed/ $E$  or  $Z$  un-complexed/ one or two rings threaded). The study of such a complex operation scheme was made possible by using as a “cargo” molecule a trifluoromethyl substituted dibenzo-24-crown-8 (DB24C8) which enabled the use of  $^{19}\text{F}$ -NMR spectrometry. Equilibrated solutions of the linear motor and fluorinated DB24C8 were studied in the dark and under UV light irradiation by NMR to assess the operation mechanism of the nanomachine. In contrast with our expectations, in this system, the absorption of light induces the release of macrocycles into the solution. The mechanistic details of this process are still under investigation. However, present data suggest that an information ratchet mechanism is driving the observed behavior. A mostly fascinating result, if confirmed, due to the rarity of molecular machines operating according to such a mechanism.

**Chapter 2** reports on the synthesis and characterization of a [2]rotaxane endowed with an ammonium recognition site (*i.e.*, station), and a novel photoactive station for DB24C8. The [2]rotaxane was designed with the aim of altering the acid-base properties of an ammonium station with a light input by exploiting the peculiar characteristics present in rotaxane

architectures. Indeed, it was envisaged that a difference in the affinity of the macrocycle for the two isomeric forms (*E*, *Z*) of the photochromic station could be reflected in a change in the apparent  $pK_a$  of the ammonium site. This possibility was investigated by means of tailored UV-visible experiments. The obtained data suggest that this system can combine photoinduced isomerization and proton transfer in the same reaction network. This interplay between photochemical and acid-base reactions is amenable to conduct to out of equilibrium conditions, indeed the species involved in the network (protonated/deprotonated and *E*, *Z* isomers) are continuously interconverted when the system is kept under irradiation. In other words, in this system, light can sustain a dissipative state that results in a continuous movement of the ring between the stations of the axle component as long as light is furnished to the system.

**Chapter 3** describes the synthesis and characterization of a [3]rotaxane in which the relative number of rings and recognition sites can be changed on command. The [3]rotaxane is composed by a linear component containing two lateral ammonium recognition sites and one central triazolium station and two DB24C8 rings. Upon stepwise deactivation of the ammonium centers by deprotonation, the number of recognition sites can be made higher, equal, or smaller than the total number of interlocked macrocycles. Through a combination of NMR and UV-vis experiments, it was possible to measure some of the relevant thermodynamic parameters of the network of reactions interconverting these different species. Specifically, it was proved that the presence of a ring on the triazolium recognition site can affect the acidity of a nearby ammonium station. This is an example of how chemical information can be transferred between two remote sites in a rotaxane through the translational movement of an interlocked macrocycle. Furthermore, the combined NMR and computational investigation of the fully deprotonated species, in which two macrocycles are obliged to compete for a single “seat” represented by the triazolium station, enabled to elucidate some of the peculiar characteristics in this relatively rare and underexplored “frustrated” systems.

# Introduction

## 1. From supramolecular chemistry to mechanostereochemistry

The famous definition of supramolecular chemistry as “chemistry beyond the molecules”, given by the Nobel prize Jean Marie Lehn, clearly describes the field of interest of this branch of chemistry. This discipline focuses on the study of the different intermolecular interactions (such as donor-acceptor interactions, hydrogen bonding, metal coordination, hydrophobic interactions *etc.*) established between molecular entities along with the rational design of host-guest systems.<sup>1-2</sup> The same non-covalent forces are exploited for the synthesis of interlocked molecules (MIMs), in these compounds two or more distinct molecules are entangled in space in such a manner that the single components cannot be separated without breaking a covalent bond (Figure 1).<sup>3</sup> Rotaxanes (from Latin *rota*: wheel and *axis*: axle) and catenanes (from Latin *catena*: chain) are the two most common examples of MIMs. The former is minimally constituted by a linear axle surrounded by one macrocycle, whose dethreading is kinetically inhibited by bulky groups installed at the axle extremities, while catenanes are composed by two or more rings linked together in a chain like aspect.

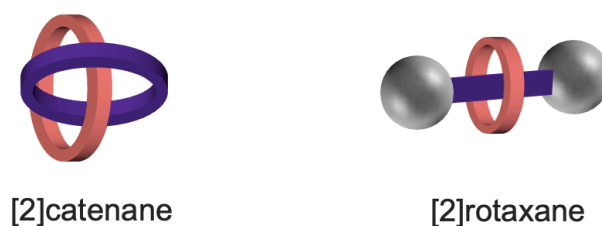


Figure 1. Graphical representation of a catenane and a rotaxane.

The naming convention for this class of molecular architectures clearly highlights their multi-component nature. Indeed, the total number of interlocked components is reported between squared parenthesis before the name molecule (*e.g.* a [2]rotaxane is composed by one ring and one axle, identically a [2]catenane is formed by two interconnected rings).<sup>4</sup> The introduction of the “mechanical bond” conducted to the birth of *mechanostereochemistry*, that in assonance with the definition of supramolecular chemistry, can be intended as the stereochemistry beyond the molecules and supermolecules.<sup>5,6</sup> The study of the structure, topology, dynamic covalent and non-covalent interactions of MIMs are the main aspects encompassed by this field.

In this thesis, the focus will be maintained on rotaxanes and pseudorotaxanes since the experimental projects discussed in the next chapters will concern the design, synthesis, and characterization of this class of molecules.

## 2. Synthesis of rotaxanes

The interest in mechanically interlocked molecules such as catenane and rotaxanes was initially addressed to their topology:<sup>7,8</sup> a branch of mathematics that studies the properties of geometrical objects that remain identical upon deformation, twisting or shape modification.<sup>9</sup> While a [2]catenane is a proper topological structure and represents an isomeric form of the two distinct rings, a [2]rotaxane is “*topologically trivial*”<sup>3</sup> because its components can be ideally disassembled either by stretching the macrocyclic component or by the contraction of the axle. The first rotaxane synthesized date back from 1967 by Harrison and Harrison,<sup>10</sup> curiously, the word “rotaxane” was never used in the original work. The term was firstly proposed<sup>11</sup> by Gottfried Schill that being the author of the pioneering monograph “*Catenanes, Rotaxanes, and Knots*”<sup>12</sup> published in 1971, is considered the “father” of mechanical bond by Fraser Stoddart.<sup>13</sup> Schill’s synthetic procedures are based on the “*directed synthesis*” approach,<sup>14</sup> in this method a macrocycle is built around an aromatic core in such a way that the breaking of a covalent bond leads to the formation of the interlocked structure. However, this strategy necessitates of numerous synthetic steps that, inevitably, leads to a poor final yield (Figure 2, *left*). An important contribution to the synthesis of MIMs, in terms of synthetic accessibility and applicability, was introduced by the template direct synthesis of catenanes<sup>15</sup> developed by Jean Pierre Sauvage. The groundbreaking intuition was to employ the supramolecular coordination of Cu (I) to drive the formation of a threaded structure (Figure 2, *right*), the latter was subsequently interlocked through nucleophilic substitution in reasonably high yields.

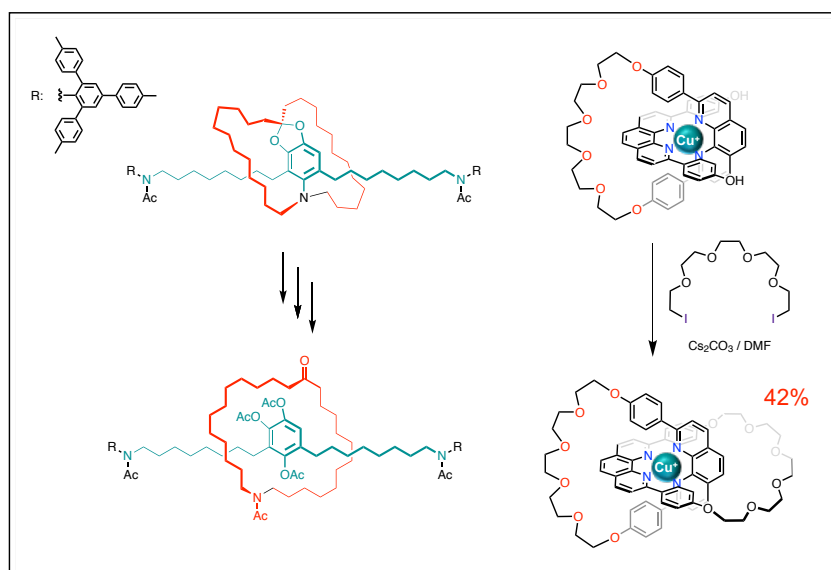


Figure 2. Left: “directed-synthesis” approach of a [2]rotaxane<sup>16</sup>, right: metal-template synthesis of a [2]catenane.

Modern approaches to rotaxanes synthesis are based on the self-assembly of rings and axle components driven by recognition sites installed in the linear part, termed “stations”. These sites are able to interact and bind to the macrocyclic unit *via* a range of different supramolecular interactions, such as hydrogen bond, hydrophobic and/or electrostatic interactions, halogen bonding, cation coordination... *etc*<sup>3,17</sup> to yield a *pseudorotaxane*. Figure 3 depicts the commonly used methods for rotaxane preparation.

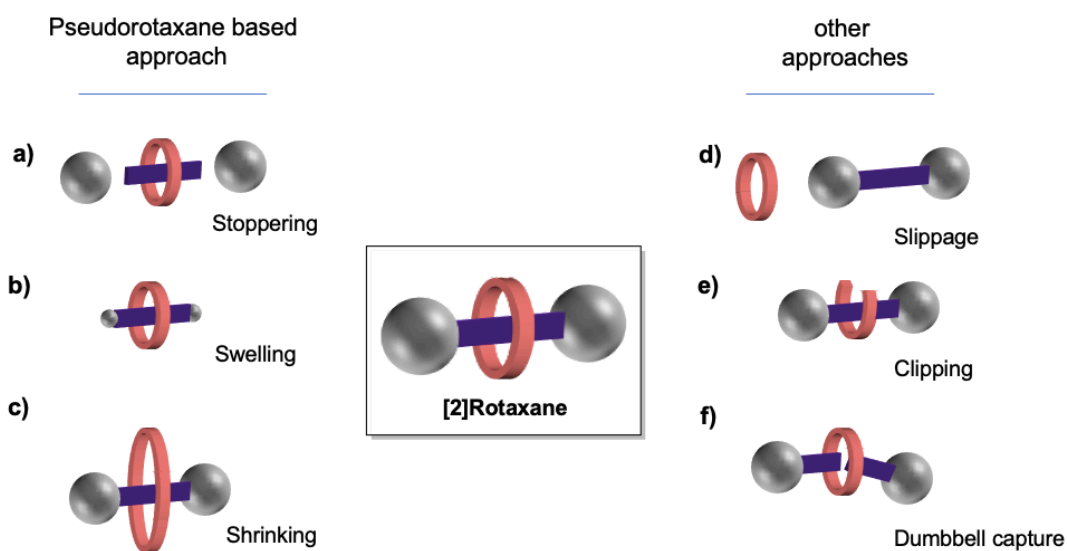


Figure 3. Modern synthetic approaches to the of rotaxanes. On the left the method based on the preliminary pseudorotaxane formation.

The most frequent synthesis of rotaxanes occurs by derivatization of self-assembled pseudorotaxane structures *via* the introduction of bulky end groups, a reaction aptly named *stoppering*<sup>3</sup> (a, Figure 3). The *swelling*<sup>18,19</sup> strategy (b, Figure 3) is conceptually similar to the stoppering one, however in this case the groups at the extremity of the axle are directly converted into bulky moieties acting as stoppers. Several alternatives can be exploited to synthesize rotaxanes that does not need the preliminary formation of a pseudorotaxane: the *slippage*<sup>20</sup> (d, Figure 3) of a ring onto the stoppers is an example, this technique require a certain amount of thermal energy to be furnished to the system in order to overcome the threading barrier of the stopper units. In other synthetic strategies the macrocycle has an active role in the mechanical bond realization: the macrocyclization of a linear molecule around the axle is known as *clipping* (e, Figure 3), while the *shrinking*<sup>21</sup> (c, Figure 3) approach exploits the reduction in the radius of the macrocycle to realize the interlocking of the components. Finally, a catalysis driven strategy has recently been developed, in which the cavity of a macrocycle actively *captures*<sup>22-24</sup> (f, Figure 3) two halves of a dumbbell shaped axle accelerating their covalent coupling.

### 3. MIMs as artificial molecular machines

The work in the field of artificial molecular machines (AMMs) was recognized with the Nobel prize in 2016 awarded to Jean Pierre Sauvage<sup>25</sup>, James Fraser Stoddart<sup>26</sup>, and Bernard Lucas Feringa.<sup>27</sup> It is not surprising that two of them (J. F. Stoddart and J. P. Sauvage) gave a huge contribution to development of MIMs, indeed the mechanical bond represents an attractive choice for chemists interested in AMMs.<sup>17</sup> A molecular machine is defined as an assembly of a discrete number of components able to perform a “*mechanical-like movement*” in response to an external stimulus.<sup>28</sup> The great advantage provided by MIMs in AMMs operation is that the supramolecular weak interactions, established between the components of rotaxanes and catenanes, can be modulated with external stimuli (pH variation, redox, light irradiation)<sup>29-31</sup> resulting in a fine control of the co-conformational arrangement of the interlocked parts. The linear translation of a macrocycle between axle’s specific recognition sites is named *shuttling*. This process was described for the first time by Stoddart and co-workers in 1991,<sup>32</sup> in this work the slow exchange between free and complexed hydroquinol recognition sites (in red, top Figure 4) of a cyclobis(paraquat-*p*-phenylene) macrocycle were observed in <sup>1</sup>H NMR spectroscopy at -50 °C.

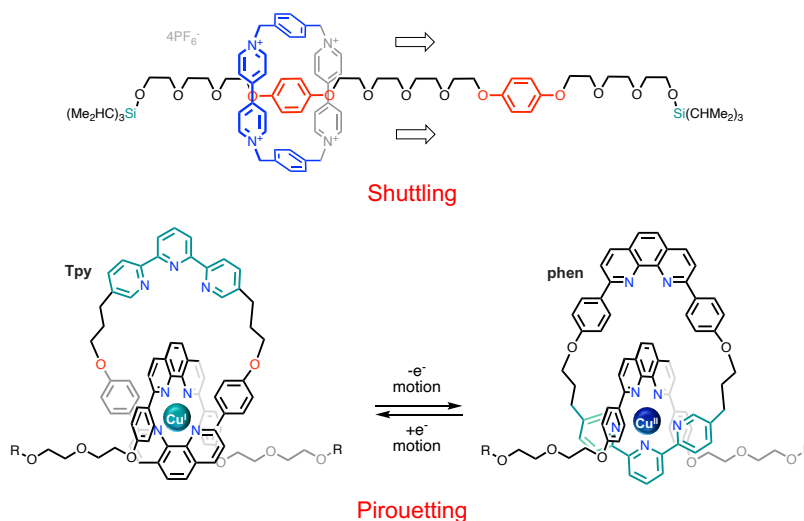


Figure 4. Top: shuttling in a [2]rotaxane, bottom: pirouetting motion, the macrocycle is endowed with a phenanthroline (phen) and terpyridine (Tpy) ligand.

Later, in 1999, Jean-Pierre Sauvage described the rotation of the macrocycle around the axle of a rotaxane, namely *pirouetting*.<sup>33</sup> In this case, the ring can be rotated on command by electrochemical reduction/oxidation of a copper ion by means of the subsequent rearrangement of the coordination sphere: at low oxidation state the two phenanthroline

ligands (one of the ring one of the axle) interact with the metal, at high oxidation state, copper II is coordinated by the terpyridine of the ring and the phenantroline of the axle (Figure 4, *bottom*).

However, despite the analogy of the mechanical movements operated, the comparison between macroscopic machines and their nanosized versions reveals fundamental differences in their operation.<sup>40</sup> Indeed, at the nanoscale thermal energy causes random motion of molecules (Brownian motion<sup>41,42</sup>), moreover, the momentum and gravity terms (that depends on the mass of the objects) are mostly irrelevant, while viscous forces are prevalent and responsible of convert in movement into heat. The Reynold number<sup>43</sup> as defined by the Equation 1 for a particle of dimension  $a$ , that is moving with velocity  $v$  in a medium with density  $\rho$  and viscosity  $\eta$ ,

$$\text{Eq.1} \quad R = \frac{a\rho v}{\eta}$$

is an dimensionless term which represents the ratio between inertial and viscous forces and is useful to discriminate systems in which the latter are dominant. Being directly proportional to the dimension of the particles, clearly at the molecular level is very low. To cite a suggestive sentence from R. Dean Astumian the operation of a molecular machines in terms of movements and direction control can be compared to “swim in a molasses and walk in a hurricane”.<sup>53</sup>

### 3.1. Nature as muse

Useful “guidelines” to design artificial molecular machines can be derived from the study of the physical and chemical mechanisms used by their natural counterpart to perform highly complex tasks.<sup>36, 39</sup>

Some types of bacteria (for example *E. coli*) exploit the rotary motion of a molecular motor to operate a linear shaped *flagellum* used to move across fluid medium by employing propulsion.<sup>40</sup> Even if living in a low Reynold number world (*E. coli* diameter: 0.6-0.7  $\mu\text{m}$ <sup>44</sup>), nature found a solution to the tendency of Brownian motion to randomize the trajectory and thus win viscous forces.<sup>40,43</sup> Zooming inside a cell, it is possible to find linear molecular motors like kinesine and myosine, these proteins are able to unidirectionally “walk” respectively along microtubule and actin filaments. In these motors, the binding and

hydrolysis of ATP causes a *conformational* change in specific domains that is amplified and transformed into motion thanks to accessory structural motifs.<sup>45,46</sup> Kinesin in particular can transport *cargos*, such as vesicles and organelles, in precise regions of the cell. The mechanism exploited to achieve directionality is still debated,<sup>47</sup> conversely, the unidirectional rotation of the ATP synthase motor is well documented.

ATP synthase and the previously cited flagellar motor belong to a class of natural machines able to perform unidirectional rotation.<sup>45</sup> This protein is actually composed by two distinct motors: F<sub>0</sub> (rotor) and F<sub>1</sub>, the first one is embedded in the membrane, and it is fueled by the protons flow due to a concentration gradient, while F<sub>1</sub> is an ATP-powered motor.

The rotation of F<sub>0</sub> induces three different conformational arrangements of F<sub>1</sub>  $\alpha$  and  $\beta$  subunits that correspond to three different events: (i) binding of ADP and inorganic phosphate, (ii) formation of a bond between them and, finally, (iii) the release of ATP (Figure 5, right).

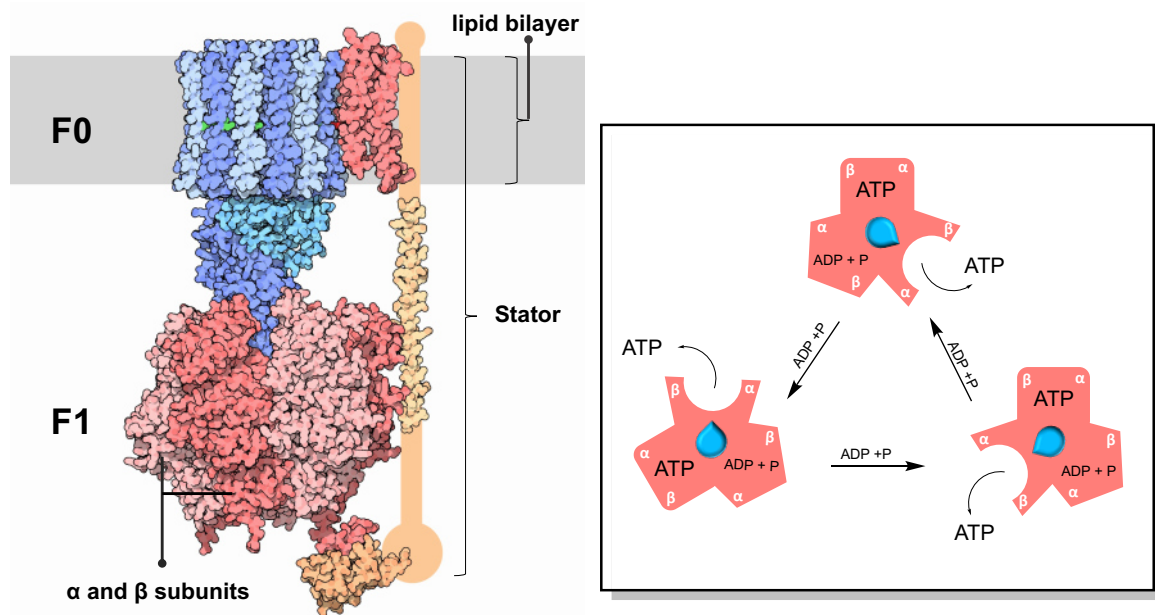


Figure 5. Left: structure of ATPase, the rotor F<sub>0</sub> is placed in the lipid bilayer, the stator connects F<sub>0</sub> with F<sub>1</sub> that is composed by  $\alpha$  and  $\beta$  sub-units. Adapted from reference 48. Right: the synthesis of ATP realized in F<sub>1</sub> subunits (pink structures), the F<sub>0</sub> central axle is represented in blue. The ATP synthesis cycle is accompanied by co-conformational modification in F<sub>1</sub> components.

F<sub>0</sub> is not simply an ion channel, indeed the transfer of a proton is associated to its unidirectional rotation. The mechanism exploited is similar to a *ratchet* gear and is obtained thanks to a stator subunit installed at its side (Figure 5, left). The rotor has a cylindrical shape in which negatively charged residues are present all around the structure, these charges are

stabilized by protons ( $H^+$ ) captured by means of a stator channel in communication with the side at higher  $H^+$  concentration. After a rotation cycle,  $F_0$  can release the proton into the compartment at lower  $H^+$  concentration through another stator channel. Importantly, the rotor  $F_0$  is subjected to random thermal motion, but the concentration gradient dissipation induces a preferential direction in its rotation (Figure 6).

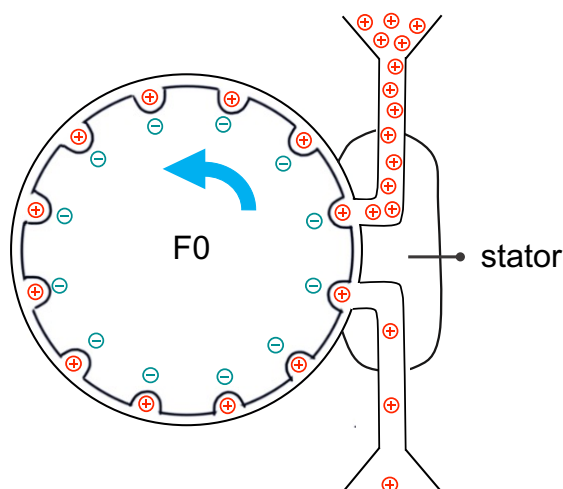


Figure 6. Representation of  $F_0$  rotor, the negatively charged residues are represented in blue, while the protons are depicted in red. The stator puts in communication the two compartments at different  $H^+$  concentration by mean of two different channels. The picture was inspired by an original illustration from reference 45.

From this example, nature provides us some important lessons: i) non-covalent interactions govern the operation of natural molecular machines ii) natural motors do not hamper the Brownian motions, on the contrary, they capture and exploit them to operate<sup>49</sup>, iii) biological machines are fueled by chemical energy (ATP and GTP hydrolysis) or gradient concentration,<sup>36,45</sup> iv) motion and performance of work, requires operation in *out of equilibrium*<sup>50,51</sup> condition that is often achieved thanks to compartmentalization (e.g. pH gradient across the membrane).

These aspects, here summarized in a list, underlie the most fascinating processes of life at the molecular level, and represent some fundamental “elements” for synthetic chemists interested in the design and operation of artificial molecular machines.<sup>36-40</sup> In the next paragraph, some of the concept here anticipated will be discussed.

### 3.2. Switches and motors

Artificial molecular machines are divided into two categories: switches and motors<sup>40</sup>, both of them require an energy source to operate, however, important differences can be underlined. Switches are multistate molecular devices that are not able to produce any net mechanical work, indeed, in a dual-state switch (0 - 1) the initial state (0) is restored travelling through the same pathway in the reverse direction; this means that the work produced in a switching cycle (0 → 1 → 0) is null (Figure 7, a).

Motors are more complex systems, in this case, the transition states to switch from 0 → 1 and from 1 → 0 are different and the work produced is given by the sum of the work of the single steps of the cycle<sup>38,40</sup> (Figure 7, b). Importantly, motors can use energy sources to sustain a cycle *away from equilibrium*, they are therefore capable to “break” the principle of *Detailed Balance*<sup>52,53</sup> that governs the relationship between rate constants in equilibrium systems. The principle states that in a system at equilibrium, the probabilities associated with the forward and backward reactions are identical and thus no work can be obtained.

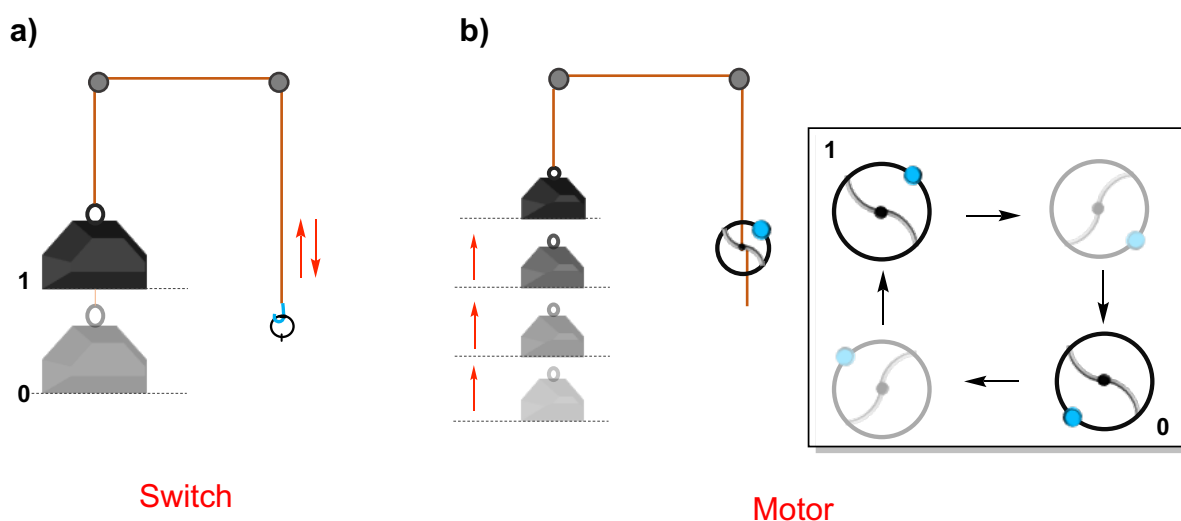


Figure 7. a) Representation of a switch operation, the application of a stimulus (the rope is pulled and fixed to a ring) cause the elevation of a weight, the inverse stimulus (the rope is unhooked) cancels the work done. b) representation of a motor, the complete cycle of a unidirectional crank handle produces the progressive elevation of the weight.

Motors are able to produce work such as mechanical work or directional motion.<sup>40</sup> The most important characteristic of a motor is the *directionality* of the operational cycle. At the molecular level thermal energy causes a ceaseless movement of the particles, i.e., Brownian motion, in molecular motors these random fluctuations are rectified through a *ratcheting*

mechanism<sup>54</sup> by exploiting an energy source. Two main types of ratchets can be identified: *information* and *energy* ratchets. In an *energy ratchet* (or *flashing ratchet*) the minima and the maxima of a potential energy surface are modified in response to an external source of energy.<sup>54,38,40</sup> A particle subjected to Brownian motion can be directionally moved between two successive minima, the process is realized because of the asymmetry of the kinetic barrier that results from the rising of wells and the lowering of adjacent maxima providing the more favorable movement of the particle in the forward path by thermal motion (Figure 8, *a*). The continuous application of an external stimulus results in the transport of the particle, importantly, the position of the latter is irrelevant for the process. Contrary to the previously described ratchet mechanism, in an *information ratchet*<sup>38,40,54</sup> the position of the particle is determinant, and the minima are unchanged along a working cycle. This process requires transfer of information from the particle to the energy profile, causing the selective lowering of the barrier in front of the particle, thus determining a direction in the motion (Figure 8, *b*).

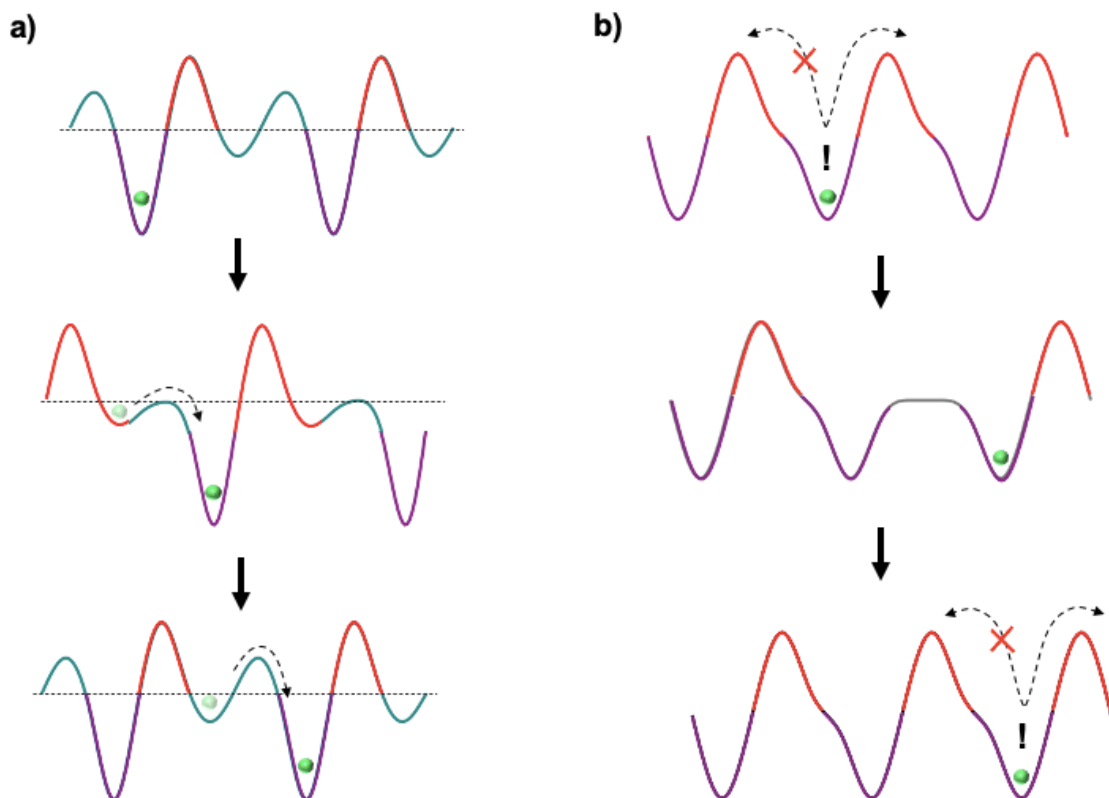


Figure 8. *a*) energy ratchet, the particle (green dot) starts in the first purple well, the modification of the energy profile causes the directional advance of the particle through the combined lowering of the barrier and rising of the well. *b*) in the information ratchet the particle signals its position (exclamation point) causing the lowering of the barrier to move to the next right-hand well.

### 3.3. Ratcheting in molecular machines

The information ratchet is reminiscent of the famous thought experiment of Maxwell's demon<sup>55,56</sup> in which the second law of thermodynamic seems to be violated. Maxwell imagined a machine composed by two closed compartments divided by a gate-endowed wall (Figure 9). In the initial stage the left compartment contains multiple Brownian particles with a statistical distribution of velocities, the demon is an intelligent creature able to open the gate and trap the particles with higher kinetic energy in one of the two compartments. The result is a difference in temperature in the two chambers and thus a decrease in entropy of the system, even without doing work (Figure 9).

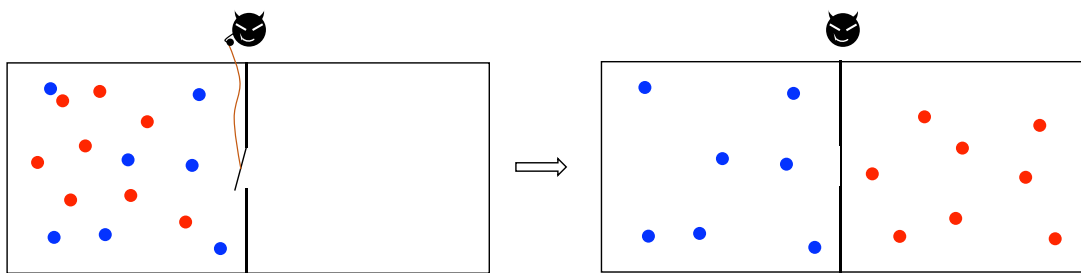


Figure 9. Representation of the Maxwell's famous thought experiment, the two compartments are divided by a gate that is controlled by a demon able to divide the particles with different kinetic energy.

The resolution to this paradox was given by Charles Henry Bennet: the memory of the demon (that was necessary to record information about the velocity and trajectory of the particles) need to be erased at the end of every stage of a particle selection, this operation is dissipative and the minimum amount of heat produced correspond to the limit of *Landauer* ( $W = K_B T \ln 2$  where  $K_B$  is the Boltzmann constant and T the temperature); in other words, for every *bit* cancelled the entropy of the system is increased.<sup>57</sup>

A similar though experiment is represented by the Marian Smoluchowski's trapdoor<sup>56,58</sup>, in the analogous Maxwellian two-compartment system the demon is replaced by a unidirectional door. The door can be selectively opened only from one side when a particle with sufficient kinetic energy hits the door (a unidirectional door hinge is installed). After some time, all the particles should be trapped in one of the two compartment and the entropy of the system would decrease. Smoluchowski proposed a solution for this paradox: following repeated impacts, the door would acquire a kinetic energy that is in the same order of magnitude of the thermal motion of the particles. The result is that the door itself would be subjected to random movements thus destroying any possibility to achieve directional gating.

The first example<sup>59</sup> of a molecular machine able to operate as an information ratchet was reported by Leigh and co-worker in 2007. In this work, a [2]rotaxane (*E,Z*-1) was described characterized by the presence of two ammonium stations (DBA and MBA) on its axle component and a benzophenone functionalized crown ether macrocycle as the ring (Figure 10).

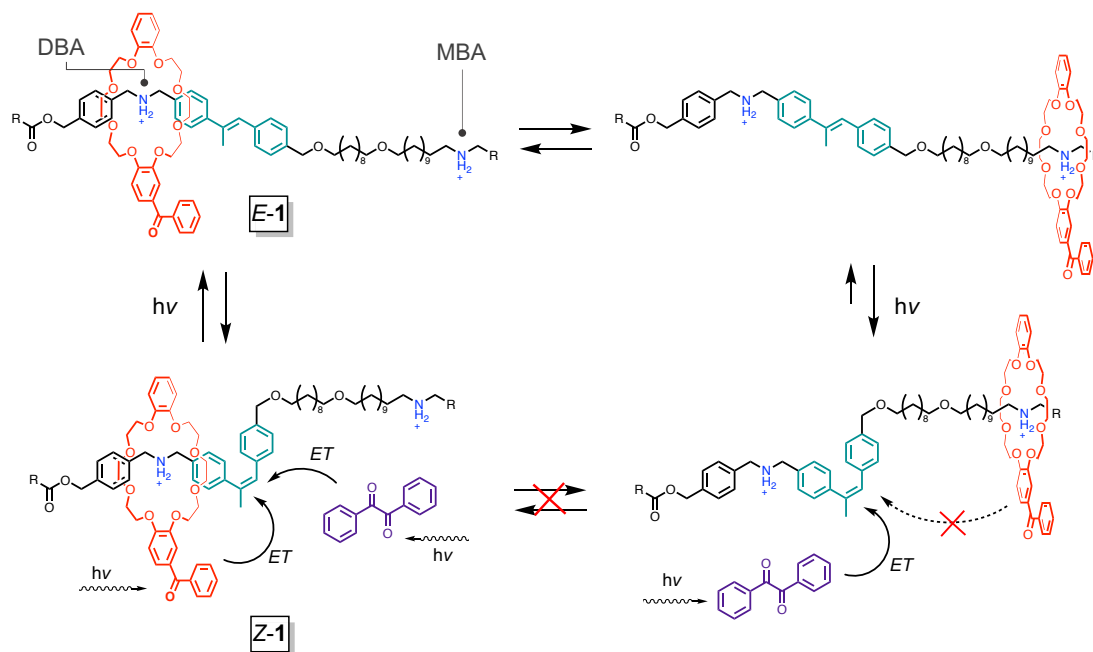


Figure 10. A chemical example of information ratchet realized by the photoisomerizable rotaxane 1 in presence of a benzyl sensitizer (in purple) under continuous irradiation. R = 3,5-di-tert-butyl phenyl.

The axle is endowed with a  $\alpha$ -methyl stilbene (cyan in Figure 10) unit that divides into two “compartments” the molecule; this photoactive moiety plays the role of a “gate” that can be closed on command in response to light stimulus. When the system is in the dark, the  $\alpha$ -methyl stilbene is in *E* configuration and the ring can shuttle between the two ammonium sites to reach an equilibrium distribution (DBA/MBA 65:35). The photoisomerization *E*  $\rightarrow$  *Z* of stilbene causes the rising of a non-traversable kinetic barrier for the ring. Importantly, the gate is asymmetrically installed on the axle being adjacent to only one (DBA) of the two ammonium sites.

The photostationary state (PSS) of the photochromic unit can be modulated by energy transfer in presence of a sensitizer: in this case an external benzyl (Purple in Figure 10) and the benzophenone on the ring. The situation observed for the case in which the ring occupies the DBA station and when the ring is on the MBA station is very different. In the first case, the PSS *Z/E* ratio is 41:59, due to the benzophenone-sensitized isomerization process; in the other case the intramolecular sensitization is less probable because of the distance of the ring

and the external benzyl sensitizer produces a higher *Z:E* PSS ratio (80:20). In other words, the macrocycle is capable to open the gate when it is located on the DBA station while the latter remains closed when the macrocycle is on the MBA station. The result is that, under light illumination, one third of the rings are moved from DBA station to MBA station against the thermal distribution (DBA/MBA 45:55).

This system satisfies the requisites necessary to operate an energy ratchet mechanism and therefore an out of equilibrium distribution of the ring between the two station is realized.

The second principle of thermodynamic is well preserved in the case of the [2]rotaxane **1**, simply because the transfer of information from the ring to the potential barrier requires an energetic cost to be paid.

In this brief introduction, some of the most important aspects dealing with the chemistry of MIMs have been summarized: from their discovery and synthesis methods to the importance that these molecules have reached in the field of AMMs, moreover the latter were classified, and the basic principles for their operation were discussed. These premises are important for the reader to easily go through the experimental projects that will be discussed in the next chapters.

The focus of the first chapter is the realization and characterization of a prototype model of a photoactivated molecular transporter based on a pseudorotaxane architecture. The prototype was investigated upon complexation and in the condition of light irradiation.

In the second chapter is reported the design, synthesis and characterization of a [2]rotaxane endowed with a dibenzylammonium station and a novel photochromic unit that acts as a recognition site for a DB24C8 crown ether macrocycle. This design allows the possibility to switch the [2]rotaxane by applying two different stimuli, light and pH variation.

In the third chapter is described the synthesis and characterization of a [3]rotaxane in which the relative number of rings ( $n_R$ ) and stations ( $n_S$ ) can be changed on command. The three possible states ( $n_R < n_S$ ,  $n_R = n_S$ ,  $n_R > n_S$ ) were separately studied, revealing important consequences on the chemical properties induced by the mismatch between rings and stations.

#### 4. References

1. J. M. Lehn, *Science*, **1993**, 260(5115), 1762-1764.
2. J. M. Lehn, *Supramolecular chemistry: concept and perspectives*, Wiley, **1995**.
3. C. J. Bruns and J. F. Stoddart, *The Nature of the Mechanical Bond*, Wiley, Hoboken, New Jersey, **2017**.
4. a) A. Yerin, E. S. Wilks, G. P. Moss & A. Harada, *Pur. App. Chem.*, **2008**, 80(9), 2041-2068. b) O. Safarowsky, B. Windisch, A. Mohry F. & Vögtle, *J. Prakt. Chem.*, **2000**, 342(5), 437-444.
5. M. A. Olson, Y. Y. Botros, & J. F. Stoddart, *Pure Appl. Chem.*, **2010**, 82(8), 1569-1574.
6. G. Barin, R. S. Forgan, J. F. & Stoddart, *Proc. Math. Phys. Eng. Sci.*, **2012**, 468(2146), 2849-2880.
7. E. Wasserman, *SciAm*, **1962**, 207(5), 94-106.
8. J. P. Sauvage & C. Dietrich-Buchecker, John Wiley & Sons, **2008**.
9. P. S. Alexandrov, *Elementary Concepts of Topology*. New York: Dover, **1961**.
10. I. T. Harrison, & S. Harrison, *J. Am. Chem. Soc.*, **1967**, 89(22), 5723-5724.
11. G. Schill & H. Zollenkopf, **1969**, *Justus Liebigs Ann. Chem.*, 721(1), 53-74.
12. G. Schill, *Catenanes, Rotaxanes, and Knots*, Academic Press, New York, **1971**.
13. J. F. Stoddart, *Angew. Chem. Int. Ed.*, **2014**, 53, 11102 – 11104.
14. G. Schill, A. Lüttringhaus, *Angew. Chem., Int. Ed. Engl.*, **1964**, 3, 546–547.
15. C. O. Dietrich-Buchecker, J. P. Sauvage & J. P. Kintzinger, *Tetrahedron lett.*, **1983**, 24(46), 5095-5098.
16. G. Schill, H. Zollenkopf, *Justus Liebigs Ann. Chem.* **1969**, 721, 53–74.
17. B. T. Shahraki, S. Maghsoudi, Y. Fatahi, N. Rabiee, S. Bahadorikhalili, R. Dinarvand, M. Bagherzadeh & F. Verpoort, *Coord. Chem. Rev.*, **2020**, 423, 213484.
18. C. W. Chiu, C. C. Lai & S. H. Chiu, *J. Am. Chem. Soc.*, **2007**, 129(12), 3500-3501.
19. J. L. Ko, S. H. Ueng, C. W. Chiu, C. C. Lai, Y. H. Liu, S. M. Peng & S. H. Chiu, *Chem. Eur. J.*, **2010**, 16(23), 6950-6960.
20. I. T. Harrison, *J. Chem. Soc., Chem. Comm.*, **1972**, (4), 231-232.
21. I. Yoon, M. Narita, T. Shimizu & M. Asakawa, *J. Am. Chem. Soc.*, **2004**, 126(51), 16740-16741.

22. W. L. Mock, T. A. Irra, J. P. Wepsiec & M. Adhya, *J. Org. Chem.*, **1989**, *54*(22), 5302-5308.
23. J. D. Crowley, S. M. Goldup, A.-L. Lee, D. A. Leigh, R. T. McBurney, *Chem. Soc. Rev.* **2009**, *38*, 1530–1541.
24. C. Tian, S. D. Fielden, G. F. Whitehead, I. J. Vitorica-Yrezabal & D. A. Leigh, *Nat. Commun.*, **2020**, *11*(1), 1-10.
25. J.-P. Sauvage, From Chemical Topology to Molecular Machines (Nobel Lecture). *Angew. Chem. Int. Ed.* **2017**, *56*, 11080–11093.
26. J. F. Stoddart, Mechanically Interlocked Molecules (MIMs) - Molecular Shuttles, Switches, and Machines (Nobel Lecture). *Angew. Chem. Int. Ed.* **2017**, *56*, 11094–11125.
27. B. L. Feringa, The Art of Building Small: From Molecular Switches to Motors (Nobel Lecture). *Angew. Chem. Int. Ed.* **2017**, *56*, 11060–11078.
28. a) V. Balzani, M. Gómez-López & J. F. Stoddart, *Acc. Chem. Res.*, **1998**, *31*(7), 405-414. b) Sauvage, J.-P. *Acc. Chem. Res.* **1998**, *31*, 611-619. c) V. Balzani, A. Credi, M. Venturi, Molecular- Level Devices. In *Supramolecular Science: Where It Is and Where It Is Going*; Ungaro, R., Dalcanale, E., Eds.; Kluwer: Dordrecht, 1999; pp 1-22.
29. A. W. Heard & S. M. Goldup, *ACS Centr. Sci.*, **2020**, *6*(2), 117-128.
30. H. Y. Zhou, Y. Han & C. F. Chen, *Mat. Chem. Front.*, **2020**, *4*(1), 12-28.
31. A. Credi, S. Silvi & M. Venturi, *Top. Curr. Chem.*, **2014**, *354*.
32. P. L. Anelli, N. Spencer, & J. F. Stoddart, *J. Am. Chem. Soc.*, **1991**, *113*(13), 5131-5133.
33. L. Raehm, J. M. Kern & J. P. Sauvage, *Chem. Eur. J.*, **1999**, *5*(11), 3310-3317.
34. V. Balzani, A. Credi, F. M. Raymo & J. F. Stoddart, *Angew. Chem. Int. Ed.*, **2000**, *39*(19), 3348-3391.
35. Y. Feng, M. O valle, J. S. Seale, C. K. Lee, D. J. Kim, R. D. Astumian & J. F. Stoddart, *J. Am. Chem. Soc.*, **2021**, *143*(15), 5569-5591.
36. E. R. Kay, D. A. Leigh & F. Zerbetto, *Angew. Chem. Int. Ed.*, **2007**, *46*(1-2), 72-191.
37. W. R. Browne & B. L. Feringa, 2010, *Nanoscience and Technology: A Collection of Reviews from Nature Journals*, 79-89.

38. S. Erbas-Cakmak, A.D. Leigh, C. T. McTernan & A. L. Nussbaumer. *Chem. Rev.*, **2015**, *115*(18), 10081-10206.
39. L. Zhang, V. Marcos & D. A. Leigh, *PNAS*, **2018**, *115*(38), 9397-9404.
40. M. Baroncini, S. Silvi & A. Credi, *Chem. Rev.*, **2019**, *120*(1), 200-268.
41. R. D. Astumian, *Phys. Chem. Chem. Phys.*, **2007**, *9*, 37, 5067–5083
42. G. Parisi, *Nature*, **2005**, *433*(7023), 221-221.
43. E. M. Purcell, *Am. J. Phys.*, **1977**, *45*(1), 3-11.
44. Rogers, Kara and Kadner, Robert J. "bacteria". *Encyclopedia Britannica*, 4 Dec. 2020, <https://www.britannica.com/science/bacteria>.
45. D. S. Goodsell, *Bionanotechnology: lessons from nature*. **2004**, John Wiley & Sons.
46. M. Schliwa & G. Woehlke, *Nature*, **2003**, *422*(6933), 759-765.
47. a) R. D. Astumian & I. Derényi, *Biophys. J.*, **1999**, *77*(2), 993-1002. b) R. F. Fox & M. H. Choi, *Phys. Rev. E*, **2001**, *63*(5), 051901.
48. PDB ATP Synthase web page: <https://pdb101.rcsb.org/motm/72>
49. P. M. Hoffmann, *Life's ratchet: how molecular machines extract order from chaos*. **2012**, Basic Books.
50. A. I. Brown, & D. A. Sivak, *Chem. Rev.*, **2019**, *120*(1), 434-459.
51. J. H. Van Esch, R. Klajn & S. Otto, *Chem. Soc. Rev.*, **2017**, *46*(18), 5474-5475.
52. R. D. Astumian, *Nat. Nanotechnol.*, **2012**, vol. 7 684–688.
53. R. D. Astumian, *Phys. Chem. Chem. Phys.*, **2007**, *9*(37), 5067-5083.
54. P. Reimann, *Phys. Rep.* **2002**, *361*, 57–265.
55. J. C. Maxwell, *Letter to P. G. Tait, 11 December 1867*. Quoted in C. G. Knott, *Life and Scientific Work of Peter Guthrie Tait*; Cambridge University Press: London, 1911; pp 213-214. (b) J. C. Maxwell, *Theory of Heat*; Longmans, Green and Co.: London, 1871; Chapter 12.
56. M. N. Chatterjee, E. R. Kay, & D. A. Leigh, *J. Am. Chem. Soc.*, **2006**, *128*(12), 4058-4073.
57. C. H. Bennett, *Int. J. Theor. Phys.*, **1982**, *21*(12), 905-940.
58. a) von M. Smoluchowski. *Phys. Z.* **1912**, *13*, 1069-1080. (b) von M. Smoluchowski, *Vortgage u'ber die Kinetische Theorie der Materie und der Elektrizitat*; Planck, M., Ed.; Teubner und Leipzig: Berlin, **1914**; pp 89-121.
59. V. Serreli, C. F. Lee, E. R. Kay, & D. A. Leigh, *Nature*, **2007**, *445*(7127), 523-527.



**Chapter 1:** *Toward a light operated  
molecular transporter*

## 1.1. Introduction

### 1.1.1. A light powered artificial molecular pump

A molecular pump<sup>1,2</sup> is a machine able to unidirectionally transport a molecular entity consuming a source of energy. The construction<sup>3-7</sup> and operation<sup>8,9</sup> of this kind of devices is a challenge for synthetic chemists. Only few examples of artificial molecular pumps are reported in the literature, and they can be classified based on the energy source exploited for their operation: electrochemical,<sup>10,11</sup> light<sup>12-17</sup> and chemical.<sup>19,20</sup>

In 2015, our group described the first autonomous artificial molecular pump able to exploit light energy to unidirectionally transport a macrocycle.<sup>17</sup> The system is composed by a di-naphtho-24-crown-8 (DN24C8) based pseudorotaxane whose axle is endowed with an ammonium recognition site (R), a photoresponsive azobenzene unit (A) and a cyclopentyl pseudo-stopper (S) (Figure 1).

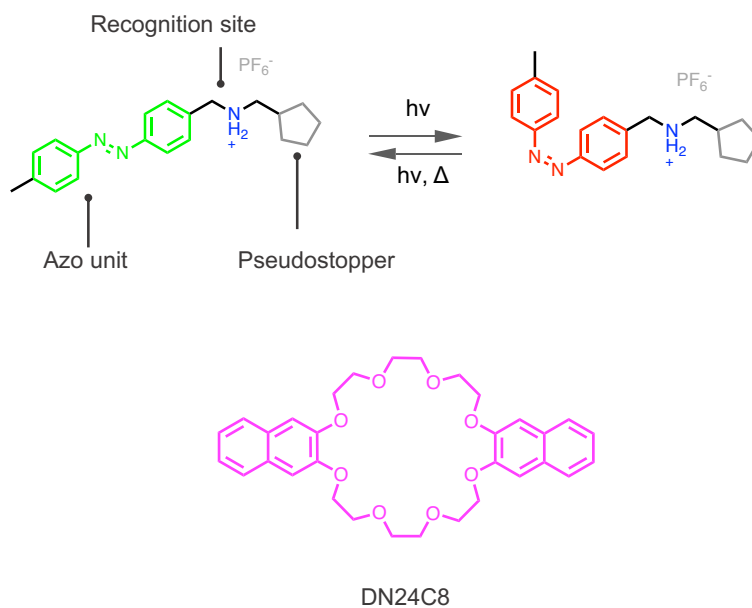


Figure 1. Molecular structure of the photoactive molecular pump in the E (green) and Z (red) configuration and of the di-naphtho-24-crown-8 ether (DN24C8).

Every component of the axle was accurately selected. The ammonium recognition site establishes hydrogen bonds with the crown ether resulting in the self-assembly of the system. The E-A unit can be photoisomerized to the Z-A isomer; this structural modification has a consequence on the (de-)threading process,<sup>21</sup> which is faster for the E configuration. Finally, the pseudo-stopper<sup>22</sup> was selected in reason of its hindrance, which is in between that of the E-A and E-A units toward the transit of the ring component over the axle moiety.

The assembly of the pseudorotaxane occurs preferentially from the *E*-A moiety (Figure 2, *a*), because, compared to the S unit, its threading kinetic constant ( $k$ ) is higher ( $k_{E-A} = 54 \text{ M}^{-1} \text{ s}^{-1}$ ,  $k_S = 0.81 \text{ M}^{-1} \text{ s}^{-1}$ ). The irradiation of the system results in two simultaneous effects: the destabilization of the ring-ammonium complex (the association constant of *E*-A is four times higher than that of the *Z*-A,  $K_E = 6.3 \cdot 10^5 \text{ M}^{-1}$ ,  $K_Z = 1.7 \cdot 10^5 \text{ M}^{-1}$ ), and the increase of the energy barrier that the ring has to overcome to transit over the *Z*-A unit (Figure 2, *c* and *d*).

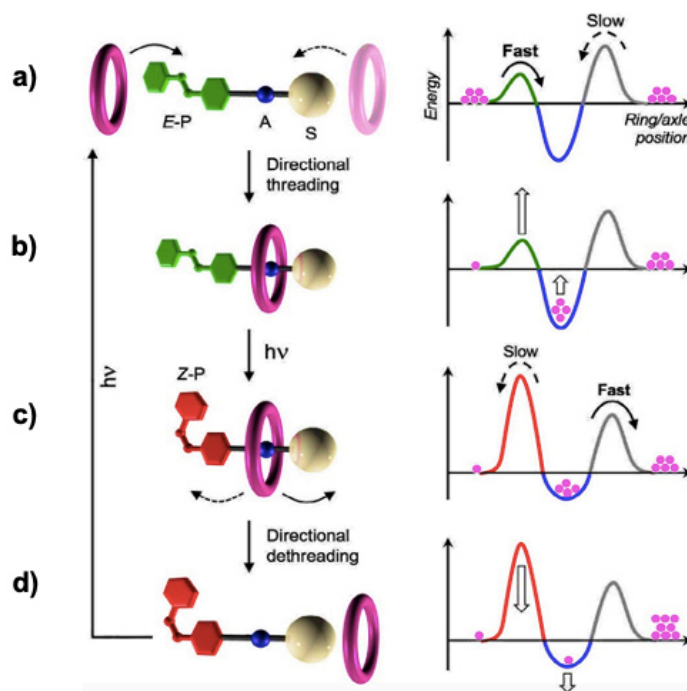
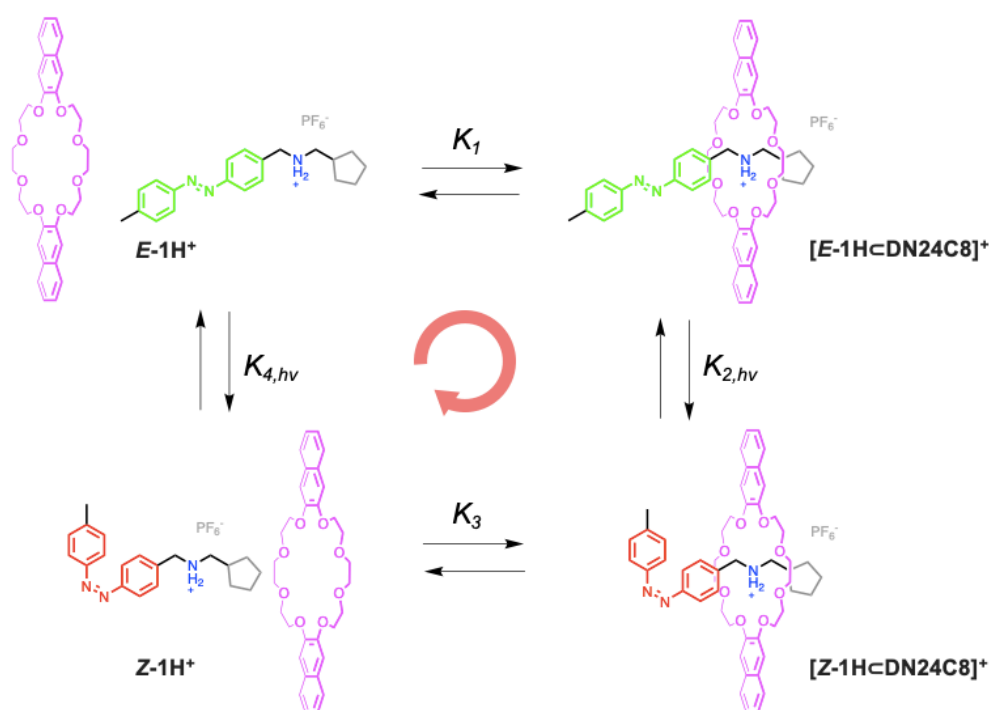


Figure 2. Photoinduced translation of DN24C8 along a non-symmetrical axle and simplified potential energy profiles. The unidirectional transit of the ring is guaranteed from the periodic modulation of the maxima and minima induced by light. Adapted with permission from reference 51.

The reduced stability of the complex causes the ring de-threading, this process takes place faster from the S unit ( $k_{Z-A} = 3.9 \cdot 10^{-2} \text{ M}^{-1} \text{ s}^{-1}$ ), Figure 2, *c*. In this way, the unidirectionality of the process is guaranteed. The system continuously cycles as long as light is provided, because the absorption spectra of the *E* and *Z* isomers are partially superimposed, thus photons of the same wavelength can induce both the *E*-*Z* and the *Z*-*E* photoisomerization processes.

### 1.1.2. Analysis of the cycle

The cycle described doesn't respect the principle of microscopic reversibility according to which in a closed path of reactions, the cycle probability is identical in both directions.<sup>23</sup> However, this situation is not surprising since the principle is valid only for systems at equilibrium, while the photoactive supramolecular pump described operates far from equilibrium. The reason for this behavior can be retraced in the peculiar interconnection of photochemical and thermal reactions depicted in the Scheme 1.



*Scheme 1. Self-assembling of the molecular pump (horizontal) and photochemical reactions (vertical). The chemical and photochemical constants refer to the reaction from left to right and from top to bottom.*

The two constants  $K_{2,hv}$  and  $K_{4,hv}$  are not thermodynamic constants, they are defined by the ratio of the concentrations of the  $Z$  and  $E$  isomers of the complexed and un-complexed axle at the photostationary state (PSS). The Equation 1 is valid in a system at thermal equilibrium, the out of equilibrium operation of the system can be proved following the consideration raised from the experimental evidence:

$$\text{Eq 1} \quad K_1 * K_{2,hv} = K_3 * K_{4,hv}$$

When the system is irradiated at  $\lambda > 400$  nm  $K_{2,h\nu} = K_{4,h\nu}$  because the PSS of the axle in the presence of absence of the macrocycle is identical, hence being  $K_1 > K_3$  (see paragraph 1.1) Eq 1 is not valid. The result is that the Z complex ( $[Z-1H\text{C}DN24C8]^+$ ) is accumulated and the “excess” of ring is expelled from the R unit. In this regime a mechanism of *energy ratchet* (the maxima and the wells of the energy minima are different in the Z and E complex, Figure 2) determines a clockwise preferential travel of the cycle (*red arrow*, Scheme 1).

Interestingly, the system can operate by means of an *information ratchet* mechanism simply by irradiating at 298 nm. In this case, an energy transfer process from the naphthalene moiety of the ring to the A-unit occurs preferentially in the assembled pseudorotaxane thus generating a Z/E PSS ratio higher for the complex, resulting in  $K_{2,h\nu} > K_{4,h\nu}$ . Again, also in this case, the clockwise operation is provided from both the photochemical reactions and the thermodynamic equilibria directions.

The same result, but with a different mechanism, is achieved by irradiating at 365 nm. In this case the molar absorbance coefficient of the axle is lower compared to the one of the complex therefore determining that  $K_{2,h\nu} > K_{4,h\nu}$ .

In analogy with the natural molecular pumps, this system is able to rectify the Brownian motion by exploiting either an energy (irradiating with  $\lambda > 400$  nm) or information (irradiating at 365 nm or 287 nm) ratchet mechanism. Furthermore, thanks to the simplicity of the design, a lot of different architectures can be envisaged based on the fundamental structure of this pump. In this chapter is reported the design, synthesis, and interpretation of the experimental data of a dimeric pump system developed with the aim of building a molecular linear transporter.

### 1.1.3. Objective of the project

The realization of an artificial molecular transporter is a challenge in nanoscience and could have a disruptive impact on many technological fields.<sup>24-28</sup> In this framework, a photo-responsive linear molecule was designed to realize the directional transport of a crown ether macrocycle along a linear axle by exploiting light energy. The designed system is based on the repetition of photoisomerizable “pump-modules”, based on the supramolecular pump described in the previous paragraph.<sup>16,18</sup> (Figure 3).

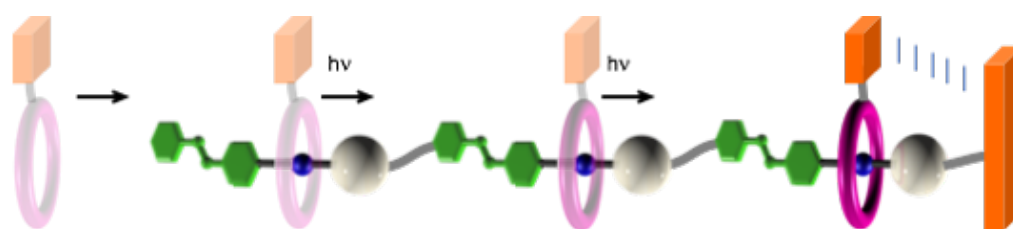


*Figure 3. Graphical representation of an oligomeric thread composed by multiple photoactive pumps. The orange box stands for a cargo that can be eventually appended to the macrocycle, in this way, a nanosized molecular transporter would be realized.*

We envisaged that the irradiation with light would produce the continued modification of the linked pumps energy profiles generating a net transport of a macrocycle exploiting an energy ratchet mechanism.<sup>16-18</sup> Moreover, the ring can be functionalized with a cleavable *cargo*, in this manner the macrocycle would act as a carrier for the transport of compounds over a nanosized track. The operation of this artificial molecular machine would be similar to the directionally “walk” of *kinesin* proteins on microtubules (fueled by ATP hydrolysis) that transports vesicles in cells.<sup>30,31</sup>

## 1.2. Design and synthetic aspects

An artificial molecular transporter can be designed as the composition of three fundamental parts: a “head” pump unit, a repetitive “core” pump module and a bulky stopper molecule at the end, all connected through suitable functional groups (Z) (Figure 4).

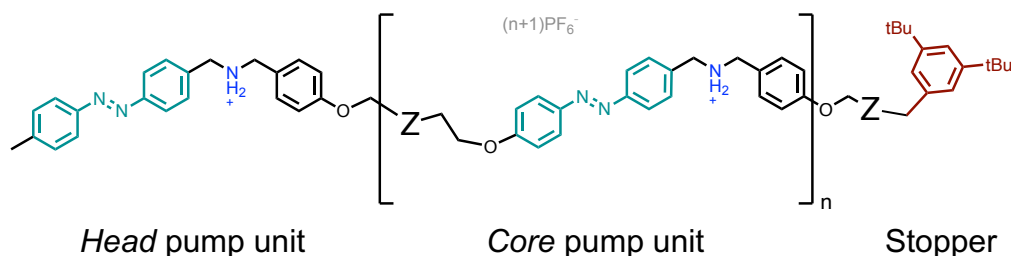


Figure 4: Design of a photoactivated molecular transporter

The modular design of the oligomeric transporter requires a synthetic approach able to control the repetitive units, growth and their axial directionality. Nonetheless, these aspects represent one of the most demanding challenges in polymer and oligomer synthesis. Whiting and co-workers reported in 1982 one of the most reliable strategies to obtain oligomers and polymers with a definite structure and degree of polymerization ( $PD_n$ ), based on an iterative convergent/divergent (IDC) synthesis.<sup>32</sup> In this method (Figure 5), a monomer is functionalized at its extremities with protective groups, the orthogonal deprotection of the groups (reaction  $x$ ) and the subsequent coupling with a second monomer (reaction  $y$ ) leads to the elongation of the thread.<sup>33</sup>

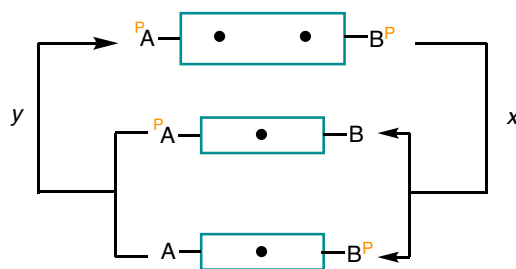


Figure 5. Iterative divergent-convergent scheme (IDC) used in the controlled elongation of polymers and oligomers; after the completion of a cycle (reactions  $x+y$ ) the chain results in the double (the two black dots represent the monomeric unit) of the original length.

The iterative convergent strategy is a straightforward approach that can be applied to the synthesis of the transporter oligomer. Hence, every “core” pump module (*left*, Figure 6) is functionalized at the extremities with an azide group and a protected alkyne group. After the initial coupling reaction between the alkyne terminated “head” and the first “core” monomer,

followed by the deprotection of the alkyne group, elongation of the molecule is made possible by the iteration of the Copper catalyzed Azido Alkyne Coupling (CuAAC) reaction; the terminal stopper group is introduced last. Similarly, to the IDC approach, the convergent iterative strategy chosen for the oligomer pump has the advantage to ensure a controlled elongation of the molecule.

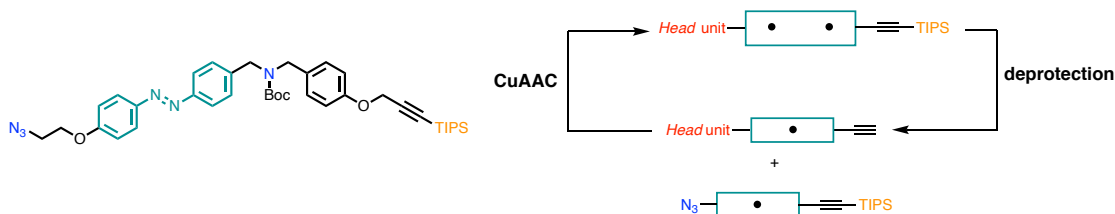


Figure 6. Left, pump core module precursor for the iterative synthesis of the oligomeric axle. Right, iterative elongation of the photoactivated oligomer, one core module is added to the oligomer “Head” after a cycle of deprotection and CuAAC click reaction.

### 1.3. Synthesis of a dimeric model system

In order to investigate the behavior of covalently linked photoactive molecular pumps, the simple dimeric prototype was synthesized, the detailed description of the synthetic steps and the relative procedures are reported in the experimental section (Paragraph 1.10.). The prototype P1 (Figure 7) is composed by two pump units (**I** and **II**) whose structure resembles the original photoactivated supramolecular pump described in Paragraph 1.1.

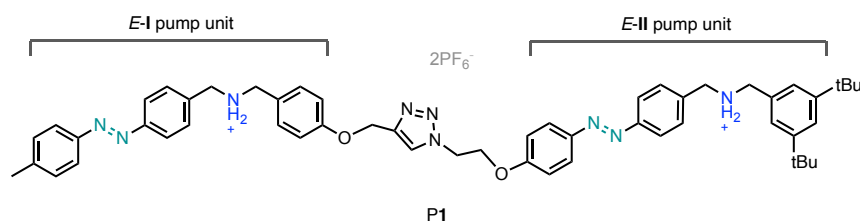


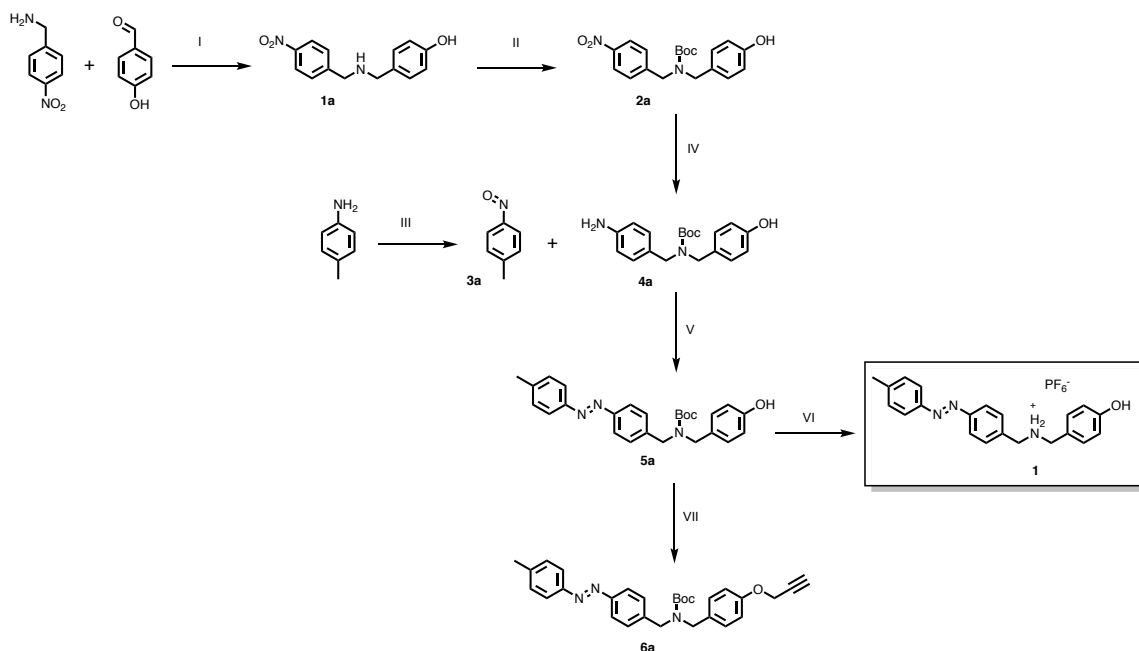
Figure 7. Molecular structure of the dimeric prototype P1 of an oligomeric molecular transporter

P1 was designed to respond to different needs: it had to be similar to the final oligomer transporter, but at the same time, its investigation had to be easier and prelude to understand the more complex oligomeric system. While the first pump module (**I-E**) is identical to the one designed for the head of the oligomer (Figure 4), in the second unit (**II-E**) the “stopper” is part of the module. This choice was done to differentiate the two pump modules in the NMR spectrum, which is fundamental to characterize the operation of the dimer.

The two modules of the dimer were separately prepared and then covalently linked, hence the realization of the dimeric prototype was articulated in two phases: the preparation of an

alkyne derivative of the first pump unit and the synthesis of an azide substituted second pump unit. In the final convergent step, the dimeric compound was obtained by means of the CuAAC reaction. The detailed procedures are reported in the experimental section, while the description of the steps is reported below.

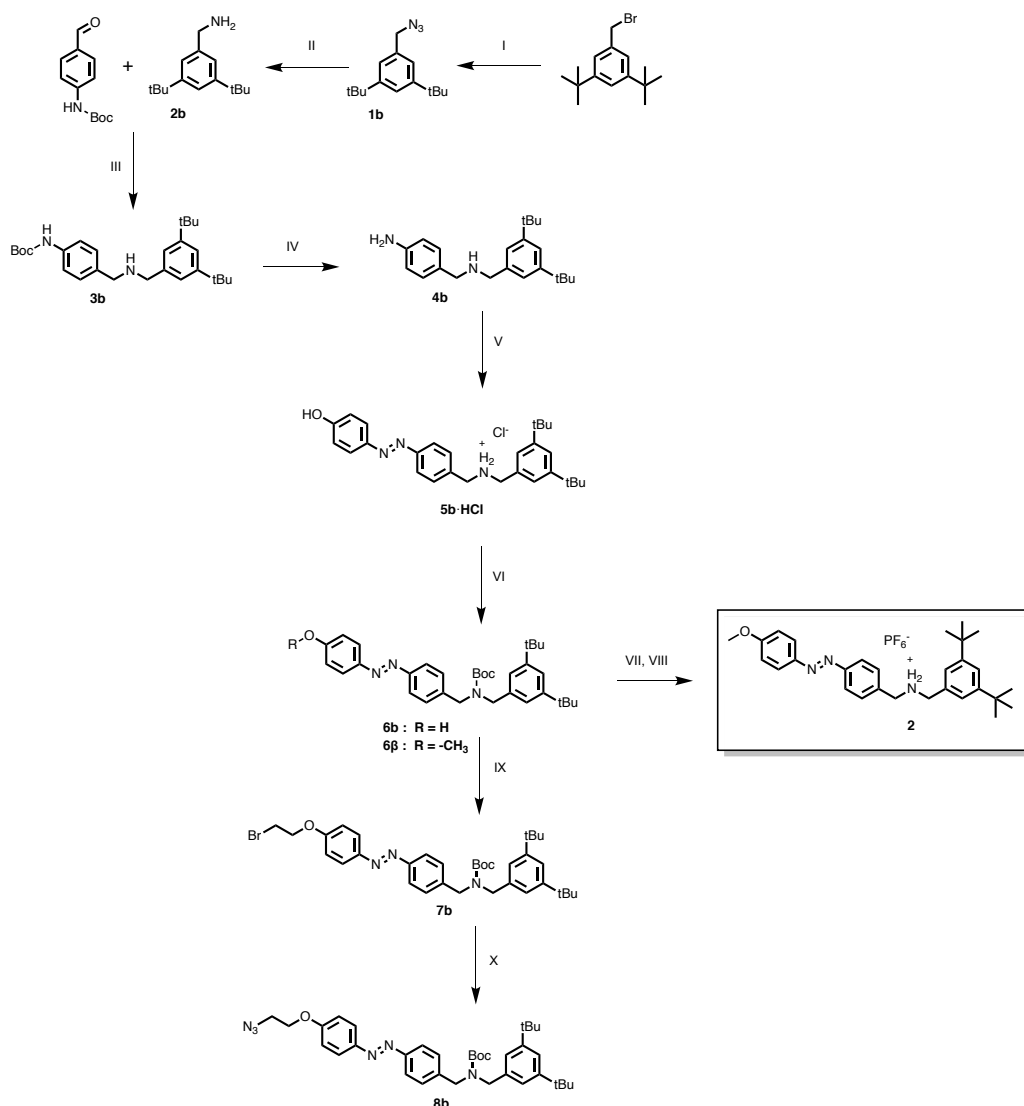
### 1.3.1. Synthesis of the first pump-unit



*Scheme 2. Synthetic route to the compounds 6a and 1. I) a. Toluene, b. NaBH<sub>4</sub>, MeOH. 93% II) Boc<sub>2</sub>O, THF r.t. 94% III) Oxone, DCM/H<sub>2</sub>O, 0 °C 30 min. 20% IV) Flow reactor, H<sub>2</sub> Pd/C 10%, MeOH. Quant. V) CH<sub>3</sub>CO<sub>2</sub>H r.t. 75% VI) ACN, HPF<sub>6</sub> VII) Propargyl bromide, K<sub>2</sub>CO<sub>3</sub> CH<sub>3</sub>CN (dry). 70%.*

For the synthesis of the first pump unit (Scheme 2) compound **2a** was obtained through reductive amination followed by the protection with di-*tert*-butyl dicarbonate (Boc<sub>2</sub>O), the introduction of the protective group was necessary to selectively drive the last nucleophilic substitution (VII) on the hydroxyl group. Catalytic hydrogenation was performed with a continuous flow reactor<sup>34</sup> equipped with a 10% Pd/C catalyst cartridge, the conversion to the aniline derivative **4a** was quantitative and clean. The introduction of the azobenzene functionality was realized through a Mills coupling reaction<sup>35</sup> of **4a** with nitroso-toluidine in acidic media; the latter was prepared from the partial oxidation of toluidine with Oxone (III). Compound **5a** was finally reacted with propargyl bromide in refluxing acetonitrile (ACN) in presence of K<sub>2</sub>CO<sub>3</sub> to afford the alkyne-derivative molecular pump precursor **6a**. The deprotection reaction of **5a** in a solution of hexafluorophosphoric acid provided the model compound **1** that was used as a reference for the characterization studies.

### 1.3.2. Synthesis of the second pump-unit



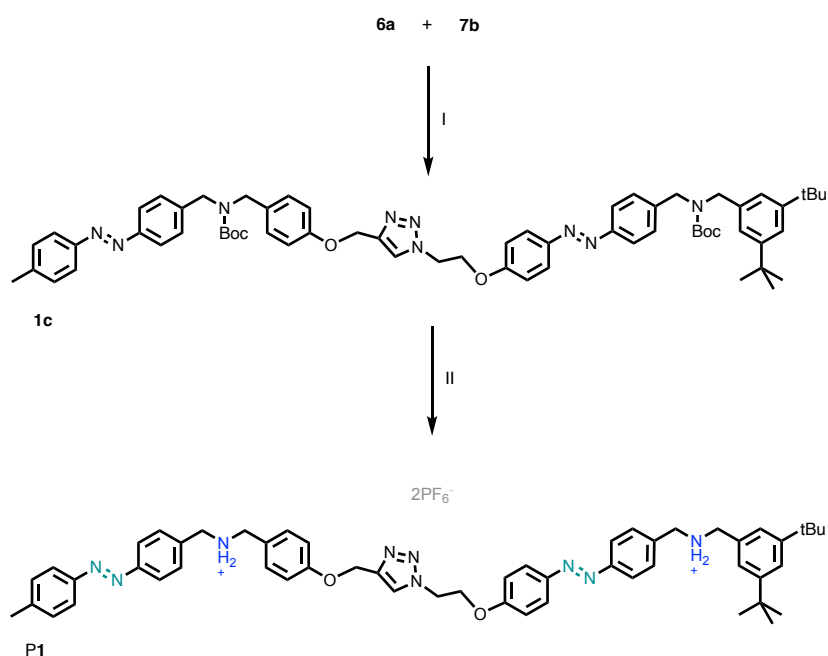
*Scheme 3. Synthetic route to the compounds 7b and 2 I) NaN<sub>3</sub>, DMF 70 °C 3h. Quant. II) Flow reactor H<sub>2</sub> Pd/C 10%, MeOH. Quant. III) a. Toluene, b. NaBH<sub>4</sub>, MeOH. 92% IV) HCl, EtOH, reflux. 94% V) a. HCl, NaNO<sub>2</sub>, EtOH 0°C 2h b. phenol, NaOH, EtOH 2h r.t., c. HCl 45% VI) a. NaHCO<sub>3</sub>, b. Boc<sub>2</sub>O, THF. 83% VII) K<sub>2</sub>CO<sub>3</sub>, CH<sub>3</sub>I, CH<sub>3</sub>CN reflux. 57% VIII) a. TFA, DCM, b. NaHCO<sub>3</sub>, c. HCl, NH<sub>4</sub>PF<sub>6</sub>. 41% IX) K<sub>2</sub>CO<sub>3</sub>, Br(CH<sub>2</sub>)<sub>2</sub>Br, CH<sub>3</sub>CN reflux. 75 % X) NaN<sub>3</sub>, DMF 70°C. quant.*

For the synthesis of the *tail* module (Scheme 3), precursor **2b** was prepared by means of two preliminary steps: a nucleophilic substitution with sodium azide (NaN<sub>3</sub>) on 3,5-di-*tert*-butylbenzyl bromide to afford **1b** in quantitative yield, followed by catalytic hydrogenation of **1b** in a continuous flow reactor employing a 10% Pd/C catalyst. Dibenzylamine **3b** was obtained by reductive amination starting from 4-(Boc-amino)benzaldehyde, in this way, the subsequent deprotection reaction in refluxing EtOH with an excess of HCl provided (after basic treatment) the anilino precursor **4b** ready for the subsequent diazo coupling

reaction. The diazonium salt intermediate **5b** was prepared in EtOH in presence of HCl and sodium nitrite, cannulation of the diazonium solution into a solution of sodium phenolate provided the azobenzene compound in 45% yield.

Compound **2**, used as a model compound for the tail module of the dimer, was prepared from *tert*-butyloxycarbonyl (Boc) protected product **6b** employing iodomethane as methylating agent in a refluxing mixture of ACN and K<sub>2</sub>CO<sub>3</sub> (VII). Lastly, the hexafluorophosphate salt was obtained upon deprotection with trifluoroacetic acid and anion exchange with NH<sub>4</sub>PF<sub>6</sub> (VIII). Compound **6b** was obtained by nucleophilic substitution with dibromoethane, in the final step, the substitution of **6b** with NaN<sub>3</sub> afforded the second-unit pump precursor **7b**.

### 1.3.3. Synthesis of the dimeric axle



Scheme 4. Synthesis of P1. [Cu(CH<sub>3</sub>CN)<sub>4</sub>]PF<sub>6</sub> CH<sub>2</sub>Cl<sub>2</sub>, 7 days. 63%. II) a. TFA, DCM, b. NaHCO<sub>3</sub> c. HCl, NH<sub>4</sub>PF<sub>6</sub> 47%.

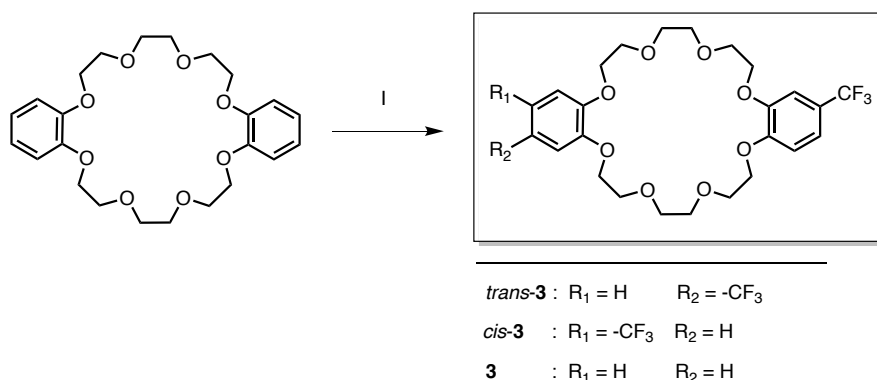
The dimeric track was obtained by coupling the two precursors **6a** and **7b** through a CuAAC reaction (Scheme 4), followed by Boc deprotection in acidic media. The dicationic hexafluorophosphate salt derivative of the dimer was provided by anion exchange using a saturated solution of NH<sub>4</sub>PF<sub>6</sub>, the overall yield of the process was 47%. The anion exchange step required the optimization of a synthetic procedure, since the compound present a scarce solubility in the commonly used solvents for the exchange, for the detail see the experimental section (Paragraph 1.10.).

## 1.4. A trifluoromethyl dibenzo-[24]-crown-8 derivative

Considering the *modularity* of the dimeric track, it was envisaged that the study of the compound by  $^1\text{H-NMR}$  could be overly complex due to an excessively crowded proton spectrum.

For this reason, we decided to employ  $^{19}\text{F-NMR}$  spectroscopy to have an additional tool to investigate the system. A trifluoromethyl derivative of a dibenzo crown ether was synthesized to achieve this purpose. The routes employed were based on two different approaches: in a first attempt, the direct functionalization of DB24C8 was performed using the Langlois reagent<sup>36</sup> (a reagent used in trifluoromethylation reactions) in a second approach a classical macrocyclization reaction was performed.

### 1.4.1. Direct trifluoromethylation of DB24C8

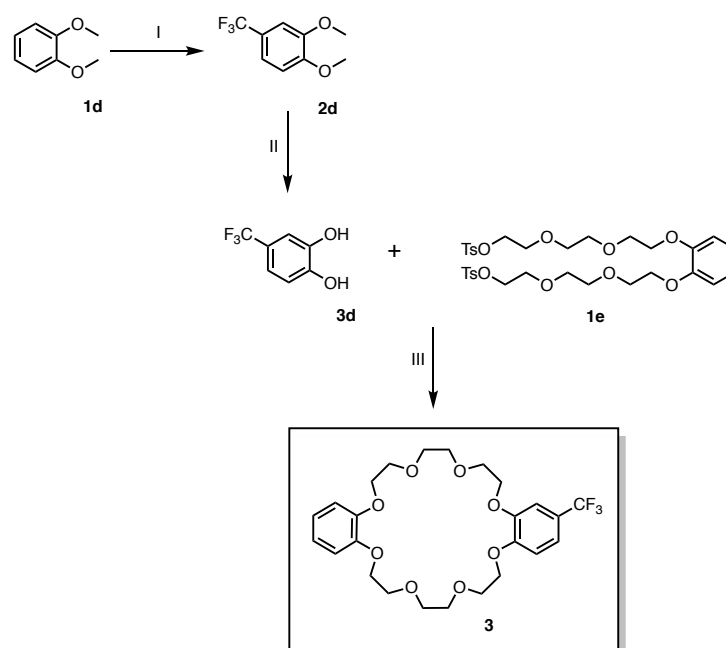


Scheme 5. Direct synthesis of **3**.  $\text{CF}_3\text{SO}_2\text{Na}$ , *t*BuOOH, DMSO:CH<sub>3</sub>CN r.t. 24 h.

The direct functionalization of crown ether presents numerous advantages in terms of time and resources economy,<sup>37</sup> moreover the trifluoromethylation of a DB24C8 has never been reported in the literature. Sodium trifluoromethanesulfinate ( $\text{CF}_3\text{SO}_2\text{Na}$ ), namely Langlois reagent, together with di-*tert*-butyl peroxide (DTBP) can provide the trifluoromethylation of electron-rich aromatic rings.<sup>38</sup> During the reaction, the DTBP act as a radical initiator and leads to the decomposition of the sulfinate to yield the  $\cdot\text{CF}_3$  electrophilic radical<sup>39</sup> that attacks the aromatic ring of the DB24C8 (Scheme 5). The reaction was optimized to find the best conditions, in particular a mixture of ACN and dimethyl sulfoxide (DMSO) was found

to be the best medium. Moreover, the yield was improved by employing a syringe pump for the continuous and slow addition of DTBP. Unfortunately, together with the product, the unwanted di-substituted products (*E*, *Z*-**3**, Scheme 5) were obtained since an excess of  $\text{CF}_3\text{SO}_2\text{Na}$  is needed in the operative conditions. A lower amount of Langlois reagent causes a poor conversion of the reagent into the desired product and subsequently a difficult isolation by means of classical purification procedures (column chromatography). For these reasons, the route was abandoned, and the desired compound **3** was obtained through the classical procedure of templated macrocyclization. However, the direct functionalization of DB24C8 with perfluoroalkyl chains was recently reported in good yields employing the dyad Rose Bengal and vitamin B<sub>12</sub> as photocatalyst and co-catalyst.<sup>40</sup>

#### 1.4.2. Multistep synthesis of **3**



Scheme 6. Synthesis route to **3** I)  $\text{CF}_3\text{SO}_2\text{Na}$  *t*BuOOH,  $\text{CH}_3\text{CN}$  r.t. 12 h. 38% II)  $\text{BBr}_3$ ,  $\text{DCM}$ ,  $-15^\circ\text{C}$ , 60% III)  $\text{Cs}_2\text{CO}_3$ , THF,  $70^\circ\text{C}$ , 48 h. 72%.

The synthesis of the macrocycle **3** (Scheme 6) started from the trifluoromethylation reaction of veratrole by means of the previously described procedure using the Langlois reagent to afford 38% conversion to the product **2d**. Subsequently boron tribromide ( $\text{BBr}_3$ ) in dry solvent was employed to cleave the methyl groups resulting in 60% yield. The tosyl-triethylene glycol di-substituted catechol **1e** was just available in the laboratory since its use is common for our routinary synthetic procedures. The crown ether macrocyclization reaction must be carried in a large multi-neck round bottom flask, endowed with a dropping

funnel and a refrigerator. The reactant **3d** and **1e** are slowly added to a refluxing mixture of tetrahydrofuran and cesium carbonate ( $\text{Cs}_2\text{CO}_3$ ). Once the first nucleophilic substitution of one hydroxyl group occurred, the intramolecular reaction with the second hydroxy group is favored for two reasons: the high dilution, and the template-directed coordination of the oxygen atoms of the glycol chains with the cesium cation. The isolated yield of this step was 72%.

### 1.5. $^1\text{H-NMR}$ characterization of *EE-P1*

The resonances of the proton and carbon nuclei of compound **P1** were assigned through the combination of 1D and 2D NMR experiments ( $^{13}\text{C-NMR}$ , HSQC, HMBC are reported in the experimental section Paragraph 1.12). The  $^1\text{H-NMR}$  spectrum recorded in  $\text{CD}_3\text{CN}$  at 298 K is reported in Figure 8.

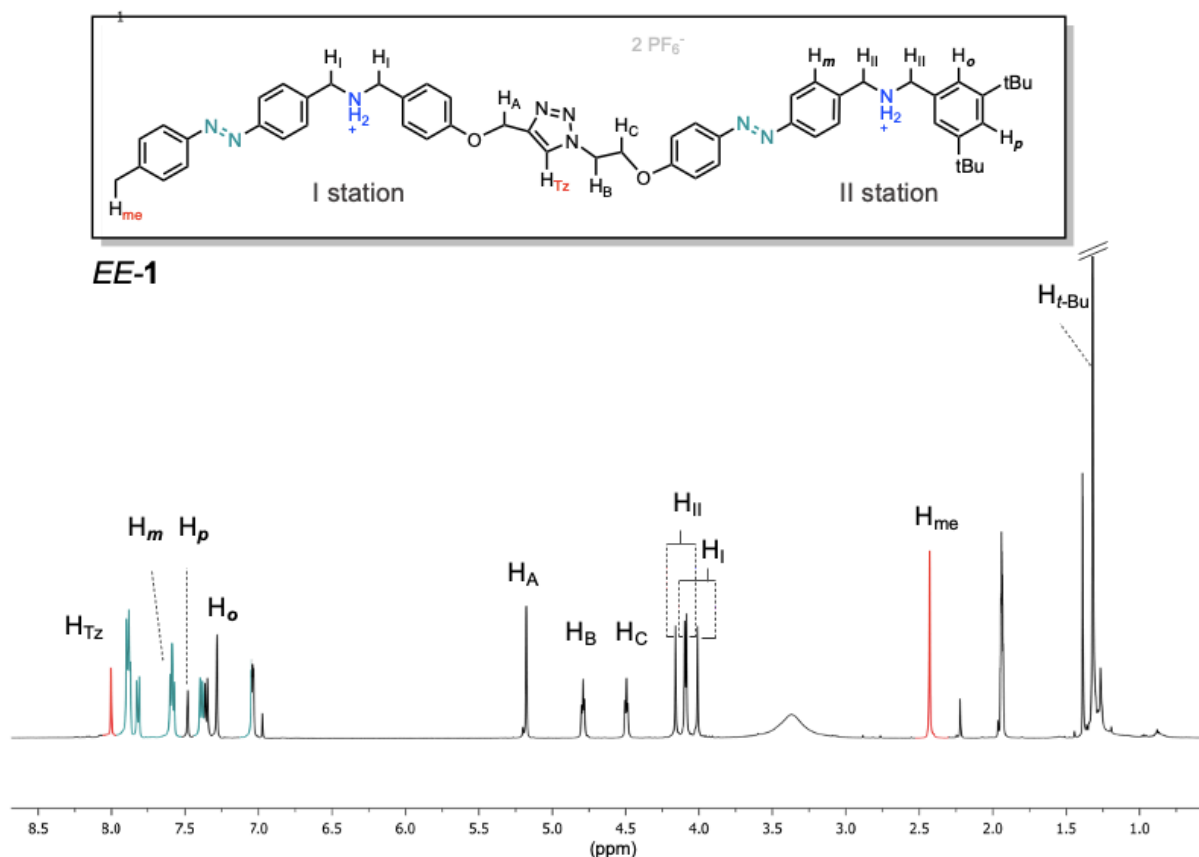


Figure 8.  $EE-[P1] = 5.0 \text{ mM}$ ,  $^1\text{H-NMR}$   $\text{CD}_3\text{CN}$  298 K, 500 MHz.

The peaks in *cyan* belong to the azobenzene units of the **I** and **II** stations, the signal labeled as  $H_o$  at (7.29 ppm) and  $H_p$  (7.48 ppm) are respectively assigned to the proton in *para* and *ortho* position in respect of the benzylammonium moiety of the **II** station (Figure 8). The triazole peak (8.00 ppm) and the methyl peak (2.43 ppm) are marked in red. The signal labeled as  $H_m$  (7.59 ppm) is in *meta* position respect to the second azo unit and is overlapped with a second aromatic proton, however it is evidenced because it is useful for the assignment of the methylene ( $-\text{CH}_2-$ ) benzylic protons  $H_I$  (4.10 ppm, 4.01 ppm) and  $H_{II}$  (4.16 ppm, 4.09 ppm) discussed in the next paragraph.

The benzylic signals of ammonium stations are commonly employed to study the complexation with crown-ether macrocycles since their chemical shift and multiplicity is

strongly affected by this process.<sup>41</sup> The assignation of these peaks was important to dispose of target signals for **I** and **II** station. The similarity in the chemical shift of the proton and carbon NMR resulted in difficulties in the interpretation of the bidimensional spectra. To unambiguously assign the benzylic resonances relative to the **I** and **II** station a mono dimensional NOESY (Nuclear Overhauser Enhancement Spectroscopy) experiment was performed. The NOE (Nuclear Overhauser Effect) may be defined as the change in intensity of a frequency observed upon the perturbation of the spin transition of another frequency,<sup>42</sup> this technique is routinely employed to investigate the spatial proximity between protons. A positive NOE is observed for small molecules in low-viscosity solvents, meaning that an increase of the intensity of a peak would be observed as a result of the frequency saturation of a nucleus near in space. The approach of “difference spectroscopy” is employed to observe the variation in the peak intensities, the method is based on the subtraction of a control spectrum to the NOE spectrum; with this method, a negative intensity will result for the irradiated peak while all the other signals will be cancelled except for the ones in which a variation in intensity occurred. In Figure 9 are reported the 1D NOESY experiments performed on the P1 dimer.

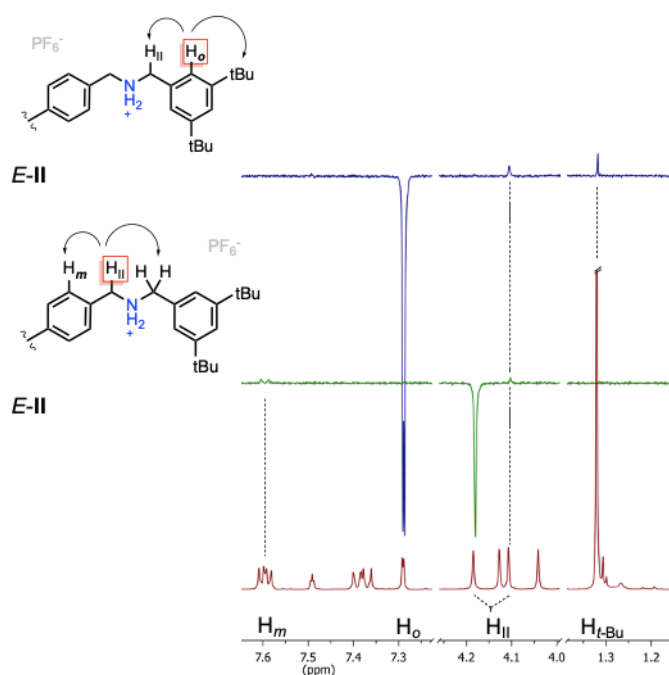


Figure 9. Stacked spectra: red, <sup>1</sup>H NMR reference spectrum of EE-P1; blue, 1D NOESY experiment on EE-P1, saturated frequency 7.29 ppm; green, 1D NOESY experiment on EE-P1, saturated frequency 4.16 ppm. EE-[P1] = 5.3 mM, <sup>1</sup>H-NMR CD<sub>3</sub>CN 298 K, 500 MHz. Structures on the left, the red squared protons are the saturated nuclei, the circle arrow indicates the nuclei whose peaks increase in intensity.

In the *blue* spectrum (Figure 9) the resonance of the nucleus Ho (7.29 ppm) was saturated (negative intensity in the NOE spectrum) and the peaks at 4.08 ppm and 1.32 ppm increased

in intensity. This result indicates that the signal at 4.08 ppm is the **II** station benzylic peak near to  $H_o$ , obviously the increase in intensity of  $H_{tBu}$  is also observed. In a second experiment (*green* spectrum, Figure 9), the resonance of the benzylic peak at 4.16 ppm was saturated and two signals increased their intensity: the previously found (4.08 ppm) belonging to the second station benzylic peak ( $H_{II}$ ), and the aromatic proton  $H_m$  confirming that the saturated resonance belong to the other benzylic peak of **II**. To conclude, the information provided these two NOE experiments was useful to assign the benzylic protons of **II** station and, by exclusion, the other two benzylic signals of **I** station.

### 1.6. Photoisomerization studies on the free axle P1

As previously mentioned, axle **P1** can be photoisomerized upon irradiation with UV light. The isomerization process leads to strong variation in  $^1\text{H}$  NMR chemical shift as evidenced by the comparison of the spectra of *EE-P1* (*cyan* spectrum in Figure 10) and the mixture at photostationary state (PSS) of *Z* isomers (*EZ-P1*, *ZE-P1*) in which the most abundant is *ZZ-P1* (*purple* spectrum, Figure 10).

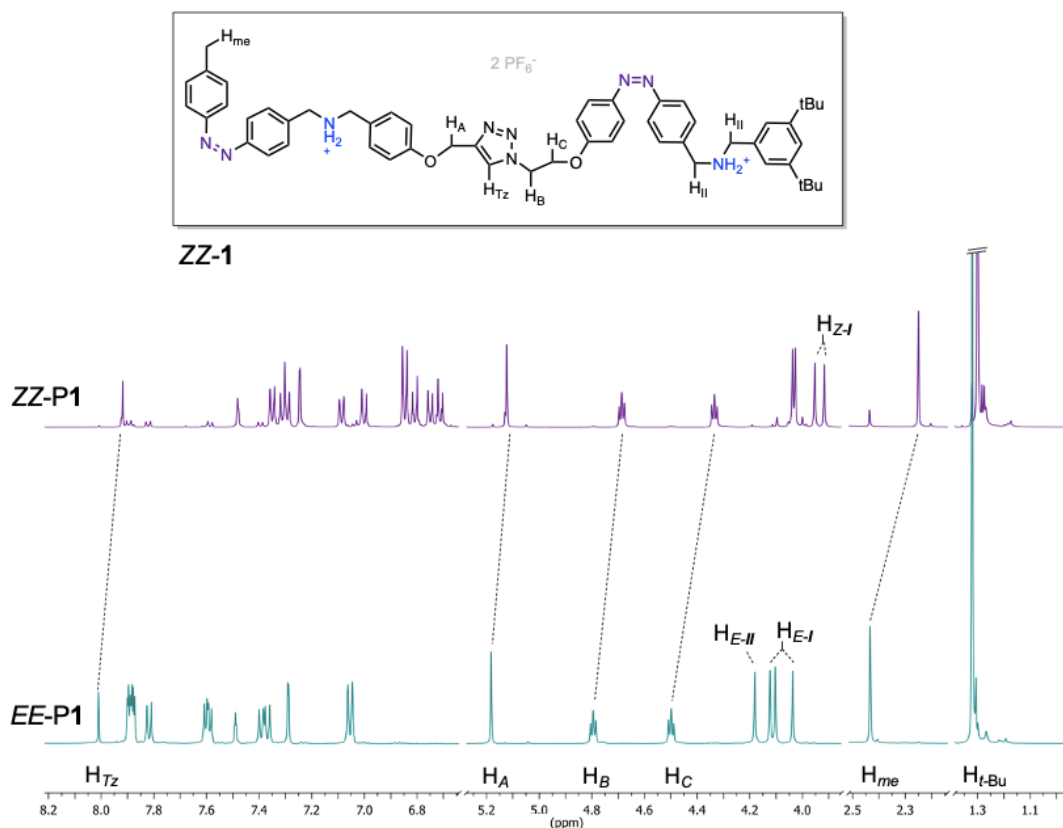


Figure 10. Stacked spectra: purple  $^1\text{H}$  NMR spectrum of *EZ*, *ZE*, *ZZ-P1* mixture at PSS, irradiation wavelength  $369 \pm 10$  nm; cyan  $^1\text{H}$  NMR spectrum of *EE-P1*.  $EE-[P1]_0 = 4.3$  mM,  $\text{CD}_3\text{CN}$  298 K, 500 MHz.

The resonances of the *Z* (*purple*, Figure 10) isomer of the dimeric axle are shielded in respect of the *E* one (*cyan*, Figure 10). The methyl peak  $H_{me}$  was particularly useful to follow the photoisomerization process of station **I**, the same is valid for  $H_{E-I}$  (4.10 ppm, 4.01 ppm) and  $H_{Z-I}$  (3.95 ppm, 3.92 ppm) that are nicely separated in the spectra. The *tert*-butyl signals provided information about the isomerization of the **II** station together with  $H_{E-II}$  (4.16 ppm). The chemical shift of methylene peaks  $H_A$ ,  $H_B$ ,  $H_C$  and  $H_{TZ}$ , relative to the *bridge* connecting the two pump modules, are influenced by the isomerization processes of both **I** and **II** station and thus they are not diagnostic of the state, complex or uncomplexed of the stations.

The irradiation experiments were conducted adopting an experimental setup described by Gschwind and coworker,<sup>43</sup> the UV light ( $\lambda_{irr} = 369 \pm 10$  nm) from a LED source was delivered inside the NMR spectrometer probehead using a quartz optical fiber directly inserted in the NMR tube. A solution of **P1** in air equilibrated  $CD_3CN$  (concentration of the sample 4.3 mM, volume 600  $\mu$ L, 298 K) was irradiated until the composition became constant (photostationary state, PSS). In figure 11 are reported the integrals variation of target nuclei signals for **I** and **II** that occur during irradiation, the time dependent profiles of the curves are differently colored to distinguish the *Z* isomer formation (*purple* curves) and the *E* isomer disappearance (*cyan* curves).

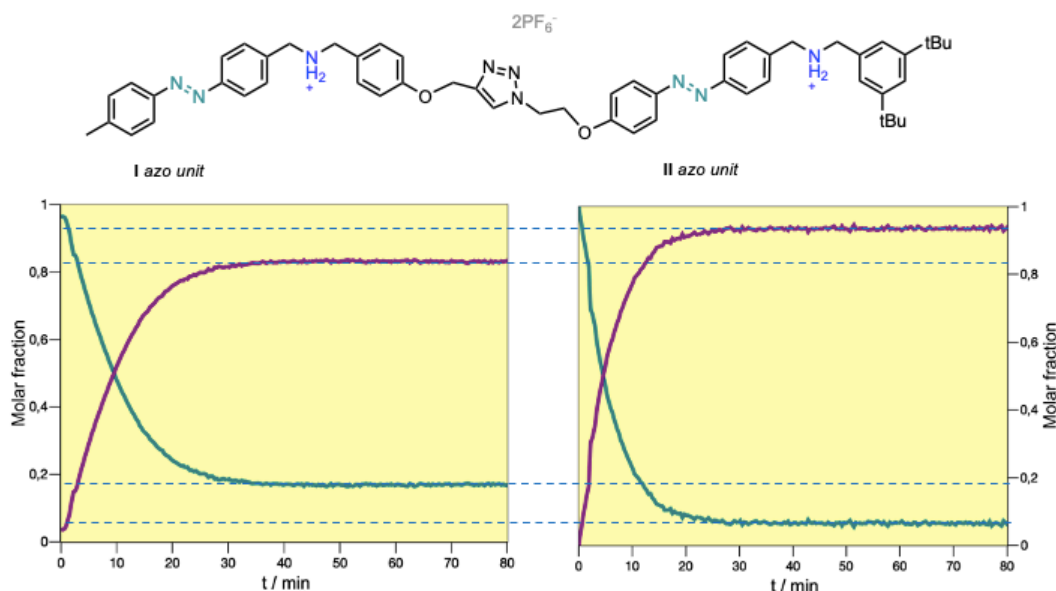


Figure 11. Top: structure of the axle **P1**. Down: *E*  $\rightarrow$  *Z* photoisomerization of the dimeric axle **P1**, the signals of the nuclei of the two stations can be separately followed in the  $^1H$ -NMR spectrum. Left: photoisomerization curves profile of **I** azo unit. Right: photoisomerization curves profile of **II** azo unit. In both graphs, traces: purple *Z* isomer; cyan *E* isomer.  $[P1]_0 = 4.3$  mM, irradiation wavelength  $369 \pm 10$  nm, data from  $^1H$ -NMR  $CD_3CN$  298 K, 500 MHz.

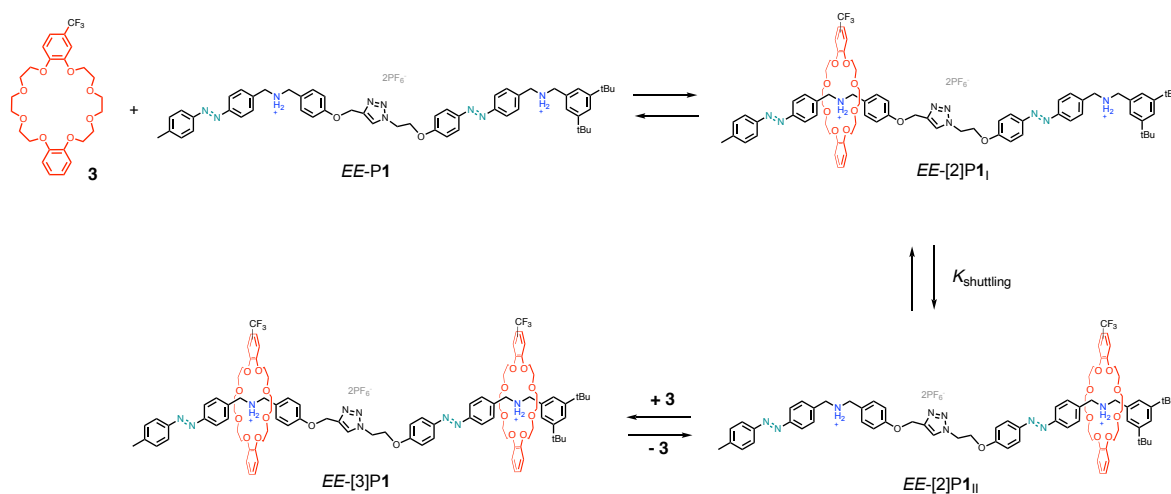
Interestingly, the rate of the  $E \rightarrow Z$  photoisomerization process is different between the two azobenzene moieties. The PSS composition for the **I** station is about 80:20 as reported in structurally analogous systems,<sup>16-18,44</sup> while a 95:5 ratio is observed for the **II** station. This results from the fact that the photochemical properties of a substituted azobenzene are affected by the presence of substituents on the aromatic rings,<sup>45</sup> as an example, the presence of an alkoxy substituent such as in the azo unit of **II** station, cause the shift of the  $\pi\pi^*$  absorption band to longer wavelength. The PSS is reached in about 35 minutes and distribution of the different isomers of **P1** is the following: *EE-P1*: 1%; *ZE-P1*: 19%; *EZ-P1*: 4%; *ZZ-P1*: 76%.

## 1.7. Complexation experiments

### 1.7.1. Reaction network scheme

Upon addition of a solution of crown ether to **P1** in  $\text{CD}_3\text{CN}$ , three different species are formed ( $EE$ -[2]**P1**<sub>I</sub>,  $EE$ -[2]**P1**<sub>II</sub>,  $EE$ -[3]**P1**, Scheme 7). The pseudorotaxanes  $EE$ -[2]**P1**<sub>I</sub> and  $EE$ -[2]**P1**<sub>II</sub> are co-conformers and interconverted through the shuttling of the ring between the  $E$ -I and the  $E$ -II ammonium stations, while the doubly complexed  $EE$ -[3]**P1** is obtained upon complexation with a second macrocycle. Given the complexity of the equilibria network presented in Scheme 7, the investigation of the evolution of the system upon light irradiation would have been an arduous venture by  $^1\text{H}$ -NMR spectroscopy.

A trifluoromethyl substituted dibenzo-24-crown-8 (DB24C8) was synthesized (**3**) and used in complexation experiments. In this way, the network could also be studied from the “point of view” of the macrocycle by  $^{19}\text{F}$ -NMR spectroscopy. In fact, the difference in the structure of the two pump modules is reflected in a different chemical shift of the trifluoromethyl substituent on the crown ether for the complexes on the **I** and the **II** stations.



Scheme 7. Network of equilibria that interconnect the dimeric axle **P1** in *E* configuration with the trifluoromethyl substituted DB24C8 **3**.

### 1.7.2. $^1\text{H}$ NMR spectrum of the complex

The  $^1\text{H}$  NMR stacked spectra reported below (Figure 12) correspond to the macrocycle **3** (*top*, red), the axle *EE-1* (*down*, black) and the spectrum of an equilibrated mixture of *EE-P1* ( $[\text{EE-P1}]_0 = 3.4 \text{ mM}$ ) with one equivalent of the macrocycle **3** in  $\text{CD}_3\text{CN}$  at 298 K (*middle*, cyan). In Figure 13 is reported an enlargement of the stacked spectra.

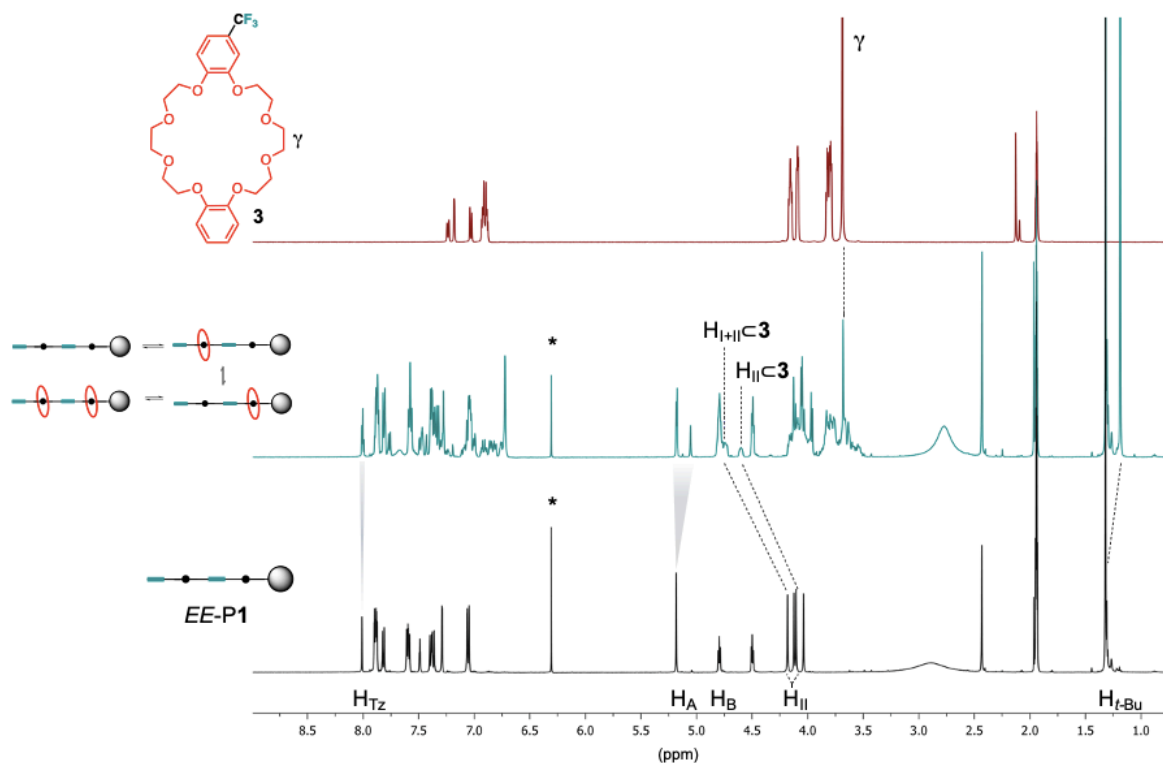


Figure 12.  $^1\text{H}$  NMR stacked spectra: *top*, trifluoromethyl-substituted DB24C8 (**3**); *bottom*,  $[\text{EE-P1}]_0 = 5.02 \text{ mM}$ ; *middle*: equilibrated mixture of *EE-P1* and **3**.  $\text{CD}_3\text{CN}$ , 298 K, 500 MHz.

The equilibria of complexation are slow on the NMR timescale, for this reason the entire set of species (*EE-P1*, *EE-[2]P1<sub>I</sub>*, *EE-[2]P1<sub>II</sub>*, *EE-[3]P1* and **3**) can be observed. The pseudorotaxanes formation is confirmed by the appearance of a new set of signals relative to the benzylic methylene ( $-\text{CH}_2-$ ) groups (Figures 12 and 13, labeled as  $\text{H}_{\text{I}<\mathbf{3}}$  and  $\text{H}_{\text{II}<\mathbf{3}}$ ) with a typical multiplicity<sup>41</sup> indicating the complexation of the ammonium site. These signals are deshielded respect to the free benzylic peaks ( $\text{H}_{\text{I}}$  and  $\text{H}_{\text{II}}$ ) because of the presence of the macrocycle on the adjacent ammonium station. In particular, the benzylic peak of the **II** station complex (labeled as  $\text{H}_{\text{II}<\mathbf{3}}$ ) is the only isolated (4.60 ppm, Figure 13), the other peaks are overlapped with a multiplet corresponding to  $\text{H}_{\text{B}}$  (4.79 ppm, Figure 13). The signals of the free and complexed **3** are mostly overlapped with other resonances; however, the  $\gamma$

protons of the ring can be observed at 3.68 ppm (Figure 12). Lastly, the resonances of the *tert*-butyl protons ( $H_{t-Bu}$ ) of the free and complexed axle are clearly observed (Figure 13, respectively 1.32 ppm and 1.19 ppm), the study of these peaks can be used to determine the amount of total complexed **II** station.

From Figure 13 is possible to notice that the signal of the triazole proton  $H_{Tz}$  (around 8 ppm) is split in three peaks analogously to methylene proton  $H_A$  (around 5.2 ppm). In both cases, one of the peaks correspond to the free axle *EE*-P1 while the other two belong to the [2]pseudorotaxanes (*EE*-[2]P1<sub>I</sub>, *EE*-[2]P1<sub>II</sub>) that are interconverted by shuttling of the ring. The fact that the signals for the [3]pseudorotaxane (*EE*-[3]P1) are not directly observed can be explained either by its negligible yield of formation, or the overlap of its resonances with those of the [2]pseudorotaxanes.

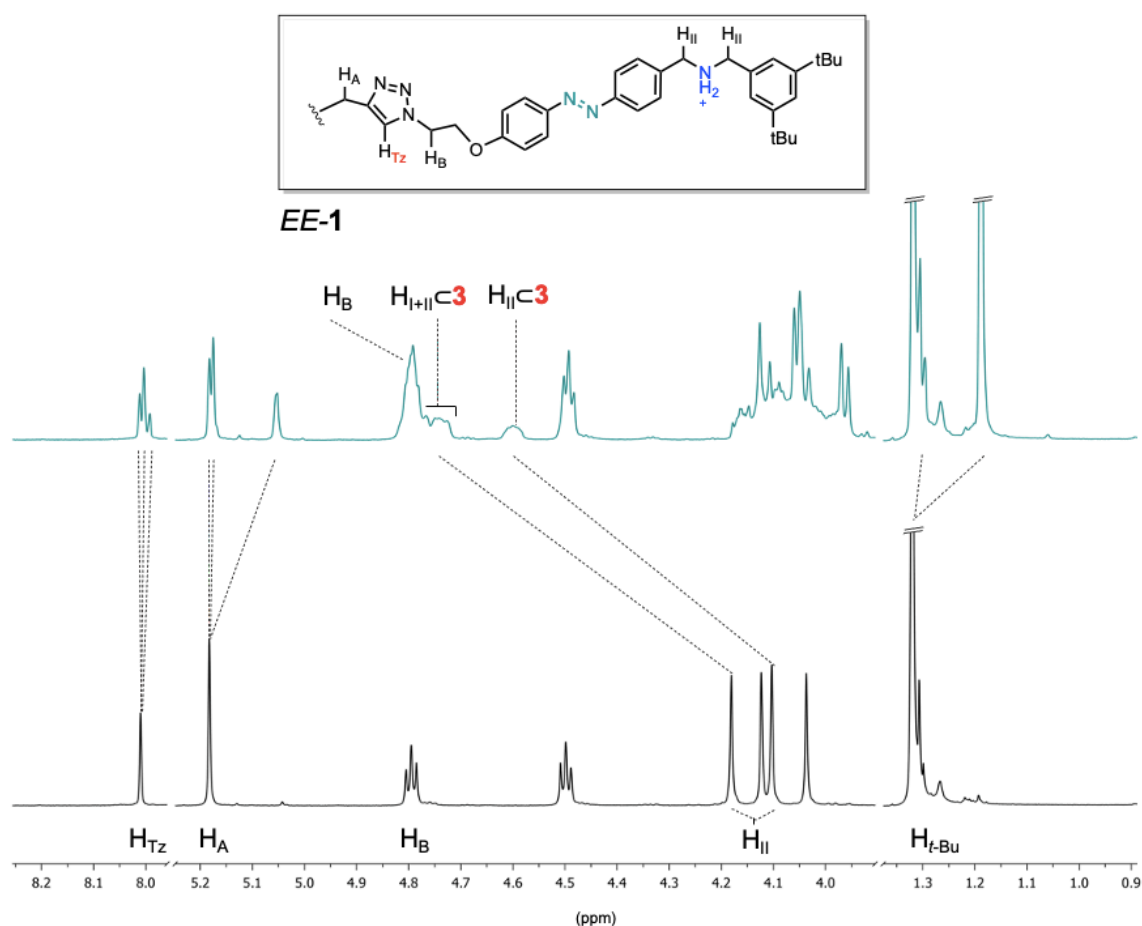


Figure 13. Magnification of  $^1H$  NMR stacked spectra: **top**,  $[EE-P1]_0 = 5.02$  mM; **bottom**: equilibrated mixture of *EE*-P1 and **3**.  $CD_3CN$ , 298 K, 500 MHz.

### 1.7.3. Association and rate constants of the equilibria involving pseudorotaxanes

Unfortunately, it was not possible to determine the concentration of the complexed species (*EE*-[2]P1<sub>I</sub>, *EE*-[2]P1<sub>II</sub>, *EE*-[3]P1) from the <sup>1</sup>H-NMR spectrum due to the overlap of the signals. For this reason, model stations **1** and **2** (Figure 14) were investigated to estimate the association constants (*K<sub>a</sub>*) of stations **I** and **II** of the dimeric axle. The *K<sub>a</sub>* for *E*-**1** and *Z*-**1** were determined in CD<sub>3</sub>CN through single point measurements:<sup>46</sup> the concentration of the free and complexed species in an equilibrated equimolar mixture of *E*, *Z* - **1** and the ring **3** were obtained from the integrals of diagnostic peaks in the <sup>1</sup>H-NMR spectrum and used (see Experimental Section paragraph 1.10.3.) to provide the value of the association constant. An identical strategy was employed for the determination of the association constant of *E*-**2** with the macrocycle **3**.

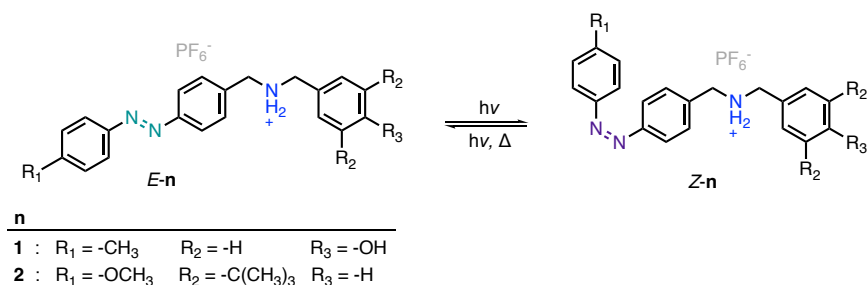


Figure 14. Chemical structures of compounds **1** and **2** designed as models for station **I** and **II** of the dimeric axle P1.

In *Z*-**2** the *tert*-butyl substituents on the phenyl ring are too bulky to be overcome by the macrocycle, threading over the *Z* azobenzene unit is the only available path for the interlocking of the components. The kinetic of this process resulted to be very slow for similar reported systems,<sup>21</sup> pointing to an insurmountable obstacle to the determination of the kinetics of threading because the equilibration would compete with the thermal *Z* → *E* back isomerization reaction.

For this reason, we used a different approach based on the fitting of the equilibration kinetic of *Z*-**2** with **3** to determine the thermodynamic and kinetic parameters.

The threading of the macrocycle is a bimolecular process that occurs faster by increasing the concentration of the reagents. In order to have a fast equilibration (in respect of the thermal *Z* → *E* isomerization) 6 equivalents of the macrocycle **3** were mixed with a PSS solution of **2** (*Z*/*E* 97:3). The equilibration kinetic was recorded with an array of <sup>1</sup>H-NMR spectra (Figure 15, left), the experimental points in purple correspond to the concentration of *Z*-**2** formed while the red ones describe the decreasing of the free *Z*-**2** axle, the equilibration is

almost complete in 12 hours. The fitting was performed according to a mixed order kinetic model and the association constant was determined from the ratio between the threading and de-threading rate constants. These constants ( $k_{in}$  and  $k_{out}$ ) are in line with those previously determined for related systems.<sup>17</sup> The thermal back isomerization of the compound **Z-2** is reported in Figure 15 (*right*), importantly the process was negligible in the timescale of the experiment.

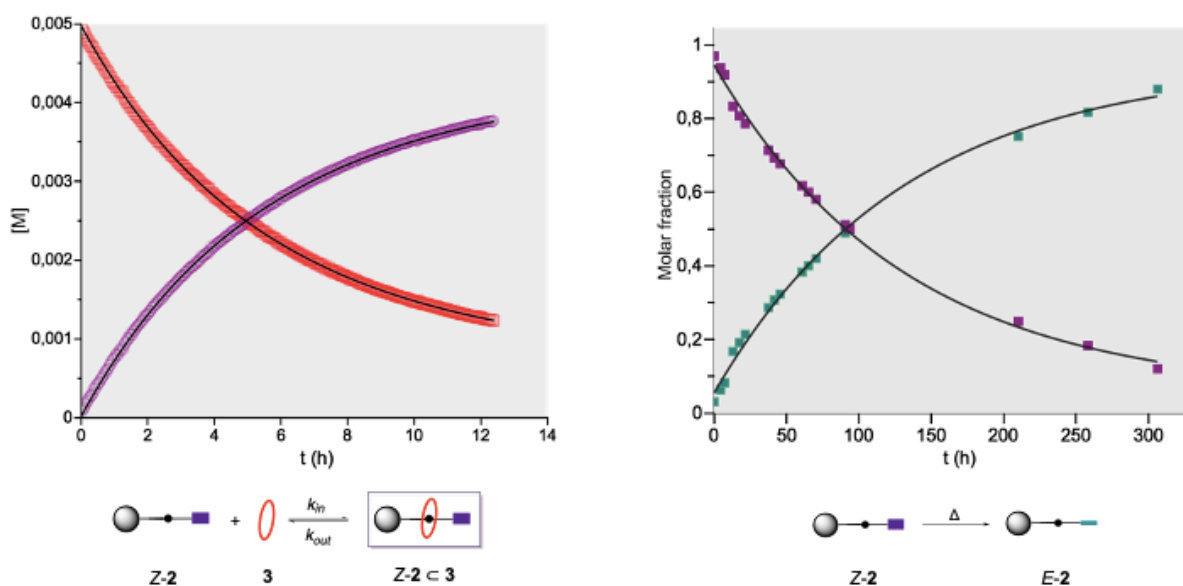


Figure 15. Left, equilibration kinetic profile of complexation between the model **2** and the macrocycle **3**, experimental points: **Z-2** $\subset$ **3** purple; **Z-2** red (fitting black lines);  $[Z-2]_0 = 5.02$  mM, data from  $^1\text{H-NMR}$   $\text{CD}_3\text{CN}$ , 298 K. Right, Thermal **Z E** back-isomerization of **Z-2**, experimental points: **Z-2** purple; **E-2** cyan;  $[Z-2]_0 = 7.3$  mM, data from  $^1\text{H-NMR}$   $\text{CD}_3\text{CN}$ , 298 K.

The entire set of  $K_a$  found for model compounds **1** and **2** in *E* and *Z* configuration is summarized in Table 1. **E-2** has a higher affinity for **3** compared to **E-1** ( $K_{E-1} < K_{E-2}$ ), most likely due to the  $\pi$ -stacking interaction between the aromatic rings of **3** and azobenzene unit which is electron rich due to the electron donor properties of the methoxy substituent. While no relevant differences were observed between the association constants of **E-1** $\subset$ **3** and **Z-1** $\subset$ **3**. A significant variation in the association constant was observed going from **E-2** $\subset$ **3** to **Z-2** $\subset$ **3**; indeed  $K_{E-2}$  resulted 2.5 times higher than  $K_{Z-2}$ , this destabilization effect can be explained by an increased steric hindrance of the *Z* isomer that is enhanced (compared to **Z-1**) by the presence of tert-butyl groups.

| Complex                 | $K_a$ [M <sup>-1</sup> ] | $k_{in}$ [M <sup>-1</sup> s <sup>-1</sup> ] | $k_{out}$ [s <sup>-1</sup> ]      |
|-------------------------|--------------------------|---|-----------------------------------|
| <i>E</i> -1 $\subset$ 3 | 440 <sup>a</sup>         | - <sup>c</sup>                              | - <sup>c</sup>                    |
| <i>E</i> -2 $\subset$ 3 | 580 <sup>a</sup>         | - <sup>c</sup>                              | - <sup>c</sup>                    |
| <i>Z</i> -1 $\subset$ 3 | 450 <sup>a</sup>         | - <sup>c</sup>                              | - <sup>c</sup>                    |
| <i>Z</i> -2 $\subset$ 3 | 230 <sup>b</sup>         | $1.46 \cdot 10^{-3}$ <sup>d</sup>           | $6.37 \cdot 10^{-6}$ <sup>d</sup> |

Table 1. The experimental data was obtained from <sup>1</sup>H-NMR recorded at 298 K. <sup>a</sup> determined by single point measurement, error <10%. <sup>b</sup> $K_{2-Z}$  was calculated with the expression  $K = k_{in}/k_{out}$ . <sup>c</sup>Not determined because the rate of threading is too high for NMR experiments. <sup>d</sup>  $k_{in}$  and  $k_{out}$  were obtained from fitting.

We then proceeded with the study of the equilibria involving molecule *EE*-P1 and macrocycle **3**. As detailed above, upon complexation an abundance of peaks was observed in the <sup>1</sup>H-NMR spectra, consistently with the presence of up to four distinct photoactive species: *EE*-[2]P1<sub>I</sub>, *EE*-[2]P1<sub>II</sub>, *EE*-[3]P1. In order to simplify the picture, we decided to use <sup>19</sup>F NMR spectrum where just three signals were present for the species involved in the reaction network under study. Once complexation occurs, the structural differences between the first pump unit (**I** station) and the second pump unit (**II** station), allow for the differentiation of the trifluoromethyl group <sup>19</sup>F NMR signals when **3** is occupying either the ammonium station in **I** or in **II**.

The chemical shift in fluorine NMR is highly sensitive to several physical factors such as solvent, concentration, and intermolecular interactions occurring in mixtures.<sup>47</sup> The titration of P1 with 3 proved a dependence of its chemical shift on the concentration (dashed line, Figure 16). At higher concentration of 3 two over three peaks were partially overlapped. Conversely, at 0.25 equivalents of ring added (first spectrum, Figure 16) all the frequencies were separately observed. Hence, at equilibrium, two peaks at -61.91 ppm and -62.01 ppm are present alongside the signal for the free crown at -61.94 ppm.

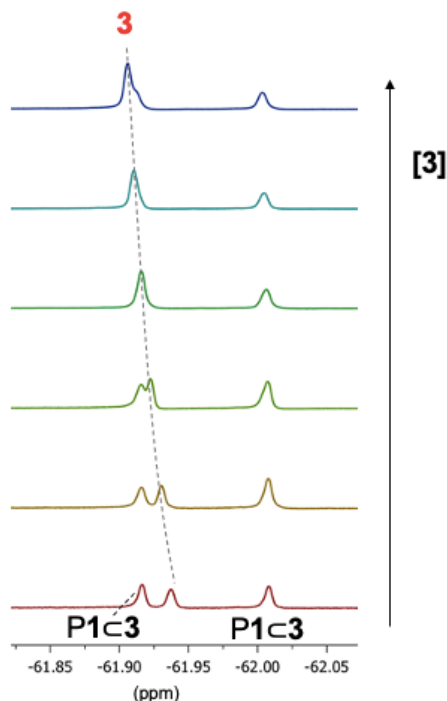


Figure 16. Titration of EE-P1 with the macrocycle 3.  $[EE-P1]_0 = 6,1 \text{ mM}$ , red spectrum  $[3]/[EE-P1]_0 = 0,25$ .  $^{19}\text{F-NMR}$   $\text{CD}_3\text{CN}$ , 298 K, 470 MHz.<sup>1</sup>

The correct assignment of the resonances was performed via an equilibration experiment. The geometry of the dimeric axle imposes that the complexation of the II station by a macrocycle must occur only after threading over the first pump module (I) (Scheme 7). According to this constraint, the equilibration of the I and II station upon complexation should occur on different timescales. In order to assign which signals belong to each station, the time dependency of the three signals was, thus, monitored using  $^{19}\text{F}$  NMR spectroscopy. Upon the addition of 0.25 equivalents of 3 a sharp resonance at -61.91 ppm formed after few seconds which was assigned to fast-forming station I complex (cyan experimental points, Figure 17). While less pronounced changes were observed for the resonances at -61.91 ppm and -61.94 ppm, the peak at -62.01 ppm (purple, Figure 17) increases over time reaching a

<sup>1</sup> I am particularly grateful to Dr. Marina Tranfić Bakić that performed the following  $^1\text{H}$  and  $^{19}\text{F}$  NMR experiments.

plateau after about 5 minutes. Having the slowest equilibration, this peak was assigned to the ring complexed with the **II** station.

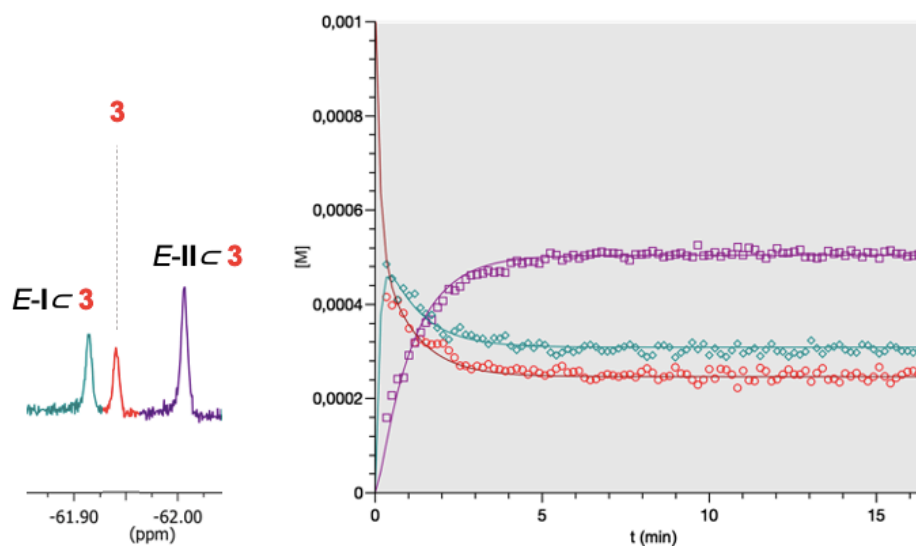
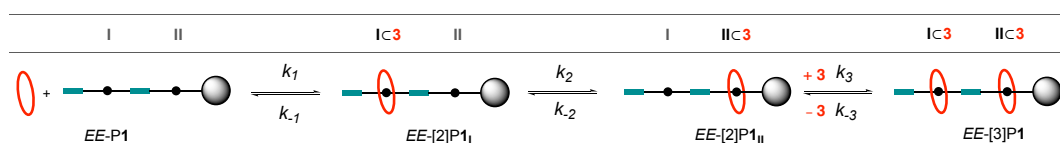


Figure 17. Left,  $^{19}\text{F}$ -NMR spectrum of the equilibrated solution of  $[\text{P1}]_0 = 5.2 \text{ mM}$  and  $[\text{3}]_0 = 1.1 \text{ mM}$  in  $\text{CD}_3\text{CN}$ , 298 K. Right, equilibration kinetic profile of the experimental points: **3** Red circles; **E-Ic3** cyan diamonds; **E-IIc3** purple squares (fitting solid lines).

The association constants of the model compounds **1** and **2** (Table 1) were used as starting values for the fitting of the concentration profiles of the dimer to a kinetic model including all the equilibria reported in Scheme 8. In particular the model describes well the experimental data assuming that the threading and de-threading processes to afford the pseudorotaxanes  $EE\text{-}[2]\text{P1}_I$  and  $EE\text{-}[3]\text{P1}$  occurred with the same kinetic parameters ( $k_I = k_3$  and  $k_{-I} = k_{-3}$ ).



Scheme 8. Equilibria of complexation between **P1** and **3** to provide the pseudorotaxanes  $EE\text{-}[2]\text{P1}_I$ ,  $EE\text{-}[2]\text{P1}_{II}$  and  $EE\text{-}[3]\text{P1}$  and relative kinetic constants.

The entire set of thermodynamic and kinetic constants determined is reported in Table 2. The estimated association constants for the first and second station (respectively  $K_{I-E}$  and  $K_{II-E}$ ) resulted  $257 \text{ M}^{-1}$  and  $439 \text{ M}^{-1}$ . As a result, the shuttling equilibrium is 1.7 folds shifted toward the **II** station. These values and the relative “strength” of the two stations are coherent with those determined for models **1** and **2** (Table 1).

| $K_{I-E} [\text{M}^{-1}]$ | $K_{II-E} [\text{M}^{-1}]$ | $k_I [\text{M}^{-1}\text{s}^{-1}]^a$ | $k_{-I} [\text{s}^{-1}]^a$ | $k_2 [\text{s}^{-1}]$ | $k_{-2} [\text{s}^{-1}]$ | $k_3 [\text{M}^{-1}\text{s}^{-1}]^a$ | $k_{-3} [\text{s}^{-1}]^a$ |
|---------------------------|----------------------------|--------------------------------------|----------------------------|-----------------------|--------------------------|--------------------------------------|----------------------------|
| 257                       | 439                        | 17                                   | $6.60 \cdot 10^{-2}$       | $1.51 \cdot 10^{-2}$  | $8.88 \cdot 10^{-3}$     | 17                                   | $6.60 \cdot 10^{-2}$       |

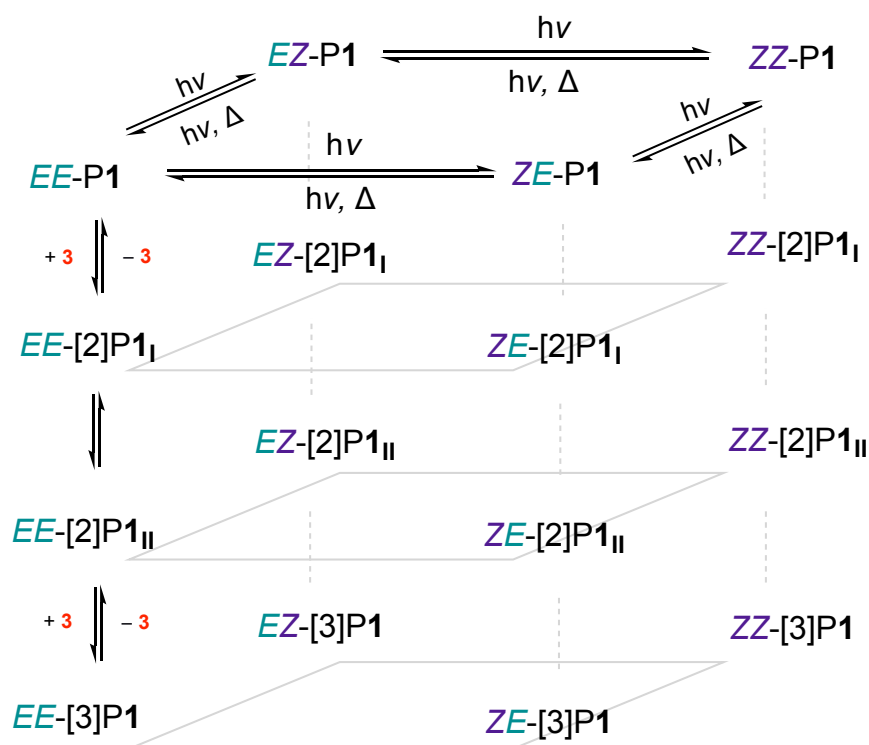
Table 2. The thermodynamic and kinetic constants were determined from the fitting of the experimental data obtained from  $^{19}\text{F}$ -NMR recorded at 298 K in  $\text{CD}_3\text{CN}$ .

## 1.8. “Light-ON” experiment

The supramolecular pump described in the introduction Paragraph (1.1) is able to unidirectionally transfer macrocycles; in particular, the rings are charged from the azo unit and expelled from the pseudo stopper in condition of light irradiation.<sup>17</sup> The dimeric axle is endowed with two modules structurally analogous to the previous pump. For this reason, a unidirectional transport of the macrocycle from the azo unit to the stoppered **II** station was expected by irradiating the system.

Surprisingly, the irradiation experiments on the dimeric axle revealed a more complex behavior, that will be described in this paragraph.

A dramatic increase in complexity is achieved when the complexed dimeric system is irradiated, the  $E \rightarrow Z$  photoisomerization of the azobenzene units results in the generation of a mixture containing 16 species that are interconverted by photoisomerization reactions (parallel planes of the tridimensional Scheme 9) and thermally activated complexation equilibria (sides of the parallelepiped, scheme 9).



Scheme 9. Complete scheme of reactions including the E-Z photoisomerization of the dimeric axle P1 and the pseudorotaxanes  $EE-[2]P1_I$ ,  $EE-[2]P1_{II}$ ,  $EE-[3]P1$ ; the arrows of reaction were replaced by dashed lines (vertical sides) and opaque planes (horizontal reactions) to enhance the readability.

Also in this case the irradiation was performed directly inside the NMR spectrometer using a quartz optical fiber to channel the light ( $\lambda_{\text{irr}} = 369 \pm 10 \text{ nm}$ ) from the source to the sample. This setup allowed to monitor the photoisomerization process over time upon recording  $^{19}\text{F}$ -NMR spectra. Fluorine NMR was chosen in these experiments as it remarkably simplifies the spectral patterns.

Upon reaching the PSS, irradiation was continued for 14 hours and the system composition monitored over time. After reaching the PSS, the concentration of Z-II complex decreases until a new photostationary state is reached after 7 hours (Figure 18, *purple trace*). This is accompanied by an increase of free crown in solution (Figure 18, *red trace*). Conversely, a small difference can be noted in the concentration of the Z-I complex. (Figure 18, *grey trace*). Overall, our experimental data shows that, under light irradiation, macrocycles are pumped out from II station to the I station and finally to the solution.

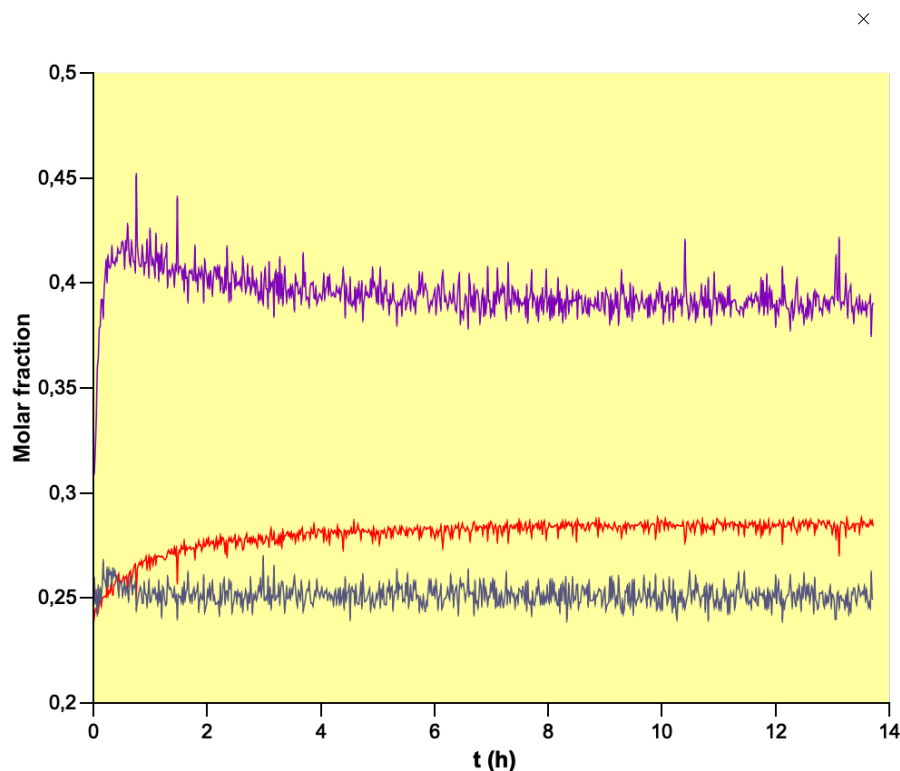


Figure 18. Experimental data from  $^{19}\text{F}$ -NMR spectra of an equilibrated solution of  $[P1]_0 = 8.73 \text{ mM}$  and  $[3]_0 = 8.62 \text{ mM}$  in condition of continuous irradiation at  $369 \pm 10 \text{ nm}$  in  $\text{CD}_3\text{CN}$  at  $298 \text{ K}$ . Traces: red, **3**; purple, **II-ZC3**; grey, **I-ZC3**.

Taking into consideration the model stations **1** and **2**, the association constant of the **I** station can be assumed to be identical between the two isomers of the pump ( $K_{1-E} \sim K_{1-Z}$ , Table 1). In light of this, the **I** module pump cannot operate as the supramolecular pump described in the introduction because the condition for the energy ratchet are not satisfied.

On the contrary, the depth of the potential energy minimum of the **II** station can be modulated *via* the  $E \rightarrow Z$  photoisomerization process ( $K_{2-E} > K_{2-Z}$ , Table 1). In this case, the ring cannot de-thread and it would be “trapped” in the complex because of the presence of the *tert*-butyl stoppers and the *Z* azo moiety. This behavior was effectively observed in the light-on experiment of the model compound **2** (Figure 19, black trace). In this experiment, the concentration of the complex in *Z* configuration remains constant after 12 hours of irradiation. This is due to the realization of a kinetically trapped state (Figure 19, *right*) caused by the fact that de-threading constant observed for **2-Z** ( $k_{out\ B-Z} = 6.36 \cdot 10^{-6} \text{ s}^{-1}$ , Table 1) is ten thousand folds lower compared to the de-threading constant from an azobenzene unit in *E* configuration ( $k_{-1\ P1-EE} = 0.07 \text{ s}^{-1}$ , Table 2).

However, as shown in Figures 18 and 19, in the dimeric axle the experimental results are consistent with a depopulation of the **II** station complex. The thermodynamic destabilization of the latter is not sufficient to explain the rings escaping; indeed, the destabilization of the energy minimum occurs simultaneously with the rising of the kinetic barrier.<sup>16-18</sup>

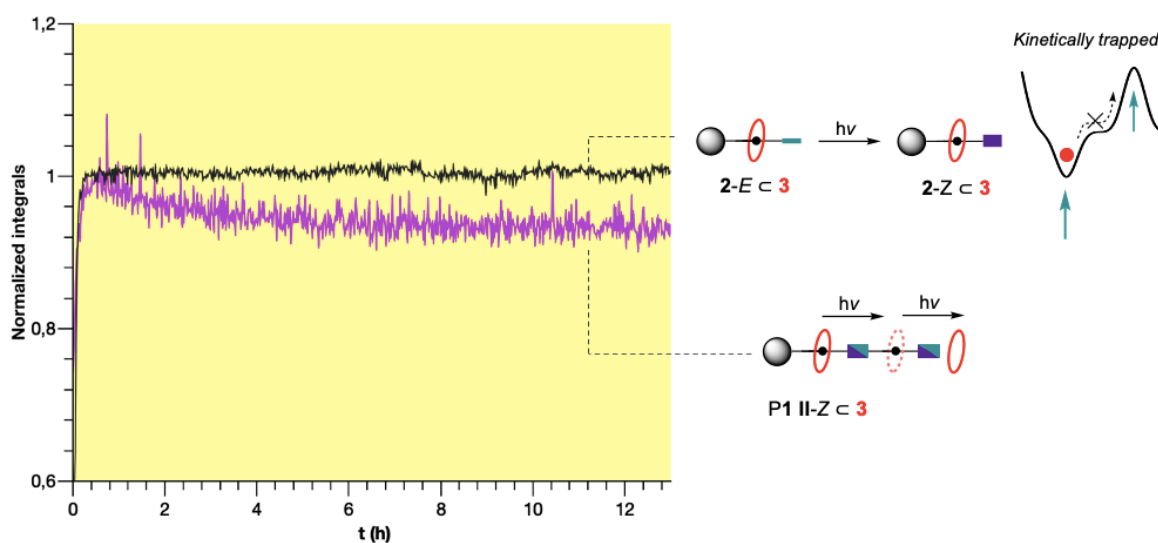


Figure 19. Experimental data from  $^{19}\text{F}$ -NMR spectra in  $\text{CD}_3\text{CN}$  at 298 K. Comparison between two different experiments: black trace (corresponding to **Z-2** $\subset$ **3**) light-ON experiment of an equilibrated mixture of  $[\mathbf{2}]_0 = 5.22 \text{ mM}$  and  $[\mathbf{3}]_0 = 5.91 \text{ mM}$ ; purple trace (corresponding to **Z-II** $\subset$ **3**) light-ON experiment described in Figure 18. On the right, graphical representation of the kinetically trapped state triggered by  $E \rightarrow Z$  photoisomerization in **2**, and de-threading process observed in **P1 II** station upon light irradiation.

The situation realized in condition of light irradiation can be also represented by the schematization of the energy profiles corresponding to the complexation reaction of the dimeric axle. In the dark ( $EE$ , Figure 20) the macrocycles **3** (red dots) are distributed between the two energy potential minima corresponding to the **I** and **II** recognition sites, when the light is switched-on the  $E \rightarrow Z$  photoisomerization of the azobenzene units creates a kinetic

barrier between the two linked pump modules and between station **I** and the medium (*ZZ*, *EZ* and *ZE*, Figure 20).

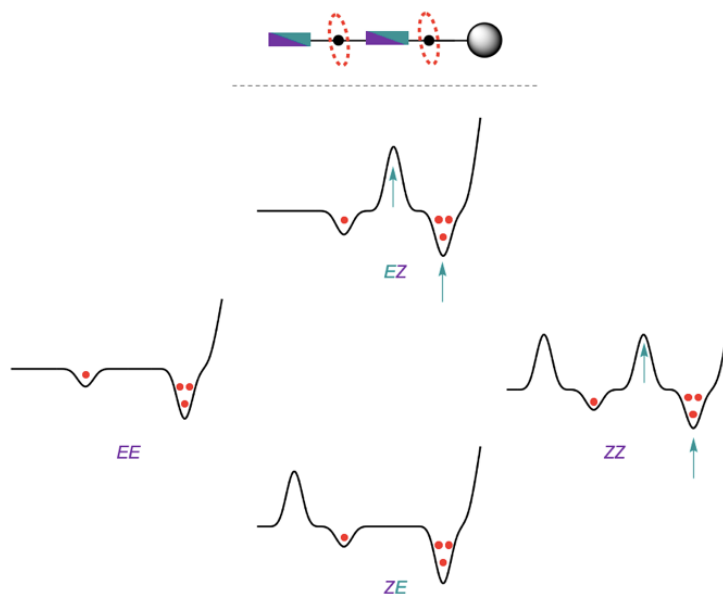


Figure 20. Energy profiles describing the dimeric system **P1** in the four possible isomeric forms (*EE*, *EZ*, *ZE*, *ZZ*) achieved upon light irradiation.

Considering the kinetically trapped state observed in the model **2** (Figure 19), the light induced de-population of **II** station should occur through the ring translation over the *E* photochromic unit. This situation would imply that a possible component of information ratchet could be present in the system, indeed the  $Z \rightarrow E$  photoisomerization of the **II** complexed station would be more favorable in respect of the un-complexed one. This hypothesis is represented in Figure 21, the macrocycle **3** would be able to favor the  $Z \rightarrow E$  photoisomerization of the **II** azobenzene unit (*a*, Figure 21), subsequently a proportion of the rings would be trapped by the **I** station (*c*, Figure 21) if the  $E \rightarrow Z$  photoisomerization of the un-occupied **II** station occur more efficiently (*b*, Figure 21). At the PSS the proportion of *E*-**I** is about 20% in respect of *Z*-**I** (Figure 11), considering that the PSS of **II** station is composed by 96% of *Z*-**II**, this means that *EZ* (Figure 20) represent the 20% of the total distribution. The equilibria of complexation of **3** with *E*-**I** are fast (see  $k_I$  and  $k_{-I}$ , Table 2), for this reason the excess of ring accumulated on the **I** station, as a consequence of information ratchet, could be easily “drained” from **I** to the solution (*c*, Figure 21).

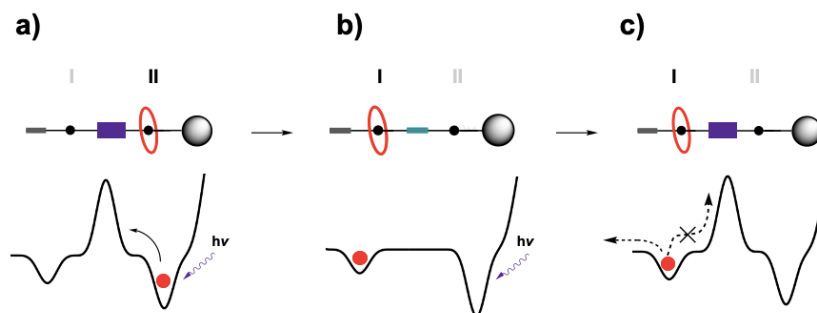


Figure 21. Graphical representation of the light sustained information ratchet mechanism occurring in the P1 dimer pseudorotaxanes and relative energy profiles.

The situation described would prove an interplay between the distribution of the rings between station I and II and the photoisomerization process. The photoisomerization sustained by continuative irradiation, would be responsible for an out of equilibrium re-distribution of the complexed and free species in the Scheme 9.

Effectively, such an explanation of the experimental results is conceptually equivalent to a Smoluchowski's Trapdoor<sup>48</sup> (or identically a Maxwell's demon could be invoked),<sup>49,50</sup> for which compound P1 would represent a molecular realization. The two stations I and II are depicted as closed compartments ( $\alpha$  and  $\beta$  respectively in Figure 22) comprised in the medium ( $\Omega$  in Figure 22).

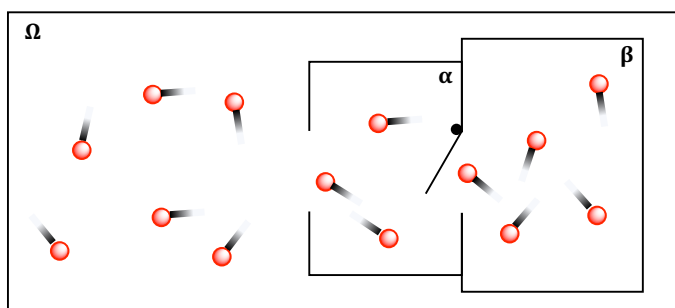


Figure 22. Alternative representation of the dimeric axle P1 (enclosed compartments alpha and beta) and the macrocycles 3 (red spheres) resembling the model of a Smoluchowski's Trapdoor.

In our system, the function of trapdoor is fulfilled by the azobenzene moiety, while the ratcheted Brownian particles (red dots in figure 22) are the macrocycles. Importantly, the door can be opened upon the collision with a red dot from one side (from right to left) but remains closed if the same event occurs from the opposite direction.

At first, it would seem that the particles with higher kinetic energy are trapped in the  $\alpha$  compartment. This situation is impossible, indeed an out of equilibrium distribution of the particles between  $\alpha$  and  $\beta$ , and thus a decrease of entropy of the system, would never be

realized by only exploiting the random collisions. The door itself would acquire the same kinetic energy of the particles and its unidirectional gating function would be lost.<sup>48</sup>

As in the information ratchet described by Leigh and co-worker,<sup>15</sup> also in this case, the out of equilibrium distribution requires an energetic cost to be paid. The latter is represented by the energy dissipation due to the transfer of information in agreement with the second law of the thermodynamic. This means that the relative localization of the spheres in respect of the door would produce a different effect. This “positional” information fate would be realized in the dimeric system through the difference in the photoisomerization pathway of the free and un-complexed recognition site.

We hypothesize that the information on the position depends on a variation of the quantum yield of photoisomerization between the complex and the free station, specifically a PSS richer in *E* must be obtained when station **II** is occupied, which allows rings to re-equilibrate with station **I**, escaping from the thermodynamic minimum of the system.

## 1.9. Conclusion and perspectives

In this chapter was reported the design, synthesis, and characterization of a dimeric prototype of a photoactivated molecular transporter. In the preparation of the track, it was chosen to employ a proven synthetic strategy with the ultimate goal to limit the number of steps. Moreover, the synthesis of a new un-reported trifluoromethyl substituted DB24C8 (**3**) was accomplished. The preparation of the latter was based on two approaches: the classical template directed synthesis and, more interestingly, through the optimization of a direct route for the DB24C8 trifluoromethylation reaction.

The dimeric axle was fully characterized and its behavior upon complexation with macrocycle **3** was studied in the dark and under illumination. Fluorine NMR spectroscopy was efficaciously applied for the study of the complex network of interconnected species arising from the interplay between complexation and photoisomerization processes. Contrary to what was observed for analogous monomeric pumps,<sup>16-18</sup> the unidirectional transport of the macrocycles occurs in an opposite direction; this phenomenon can be attributed to the unexpected realization of an information ratchet mechanism. This fascinating interpretation of the experimental data will be further investigated in future studying and comparing the photophysical parameters (quantum yields, thermal back-isomerization constants) of the  $E \rightleftharpoons Z$  photoisomerization process of specifically designed model compounds: as an example, the macrocycle **3** could be interlocked in a rotaxane architecture with an axle structurally analogous to the **II** station.

The information provided from the investigation of the dimer **P1** is precious for the design of new prototypes of molecular transporters. The difference in the stability of the complex between  $E$  or  $Z$  configuration of the **I** station could be enhanced in a future design with appropriate structural modifications, alternatively the orientation of the dimeric pump in respect of the stopper could be reversed to exploit the information ratchet in an advantageous manner.

## 1.10. Experimental section

|   |           |
|---|-----------|
| <b>Experimental Details</b>   | <b>53</b> |
| <b>1.11. Synthetic procedures</b>   | <b>54</b> |
| 1.11.1 synthesis of the first pump unit <b>6a</b>   | <b>54</b> |
| Synthesis of <b>1a</b>  | 55        |
| Synthesis of <b>2a</b>  | 55        |
| Synthesis of <b>3a</b>  | 56        |
| Synthesis of <b>4a</b>  | 56        |
| Synthesis of <b>5a</b>  | 56        |
| Synthesis of <b>6a</b>  | 57        |
| 1.11.2. Synthesis of the second pump unit <b>8b</b> and model compound <b>2</b>                       | <b>58</b> |
| Synthesis of <b>1b</b>  | 59        |
| Synthesis of <b>2b</b>  | 59        |
| Synthesis of <b>3b</b>  | 59        |
| Synthesis of <b>4b</b>  | 60        |
| Synthesis of <b>5b</b> ·HCl   | 61        |
| Synthesis of <b>6b</b>  | 61        |
| Synthesis of <b>7b</b>  | 62        |
| Synthesis of <b>8b</b>  | 62        |
| Synthesis of <b>6β</b>  | 63        |
| Synthesis of <b>2</b>   | 63        |
| 1.11.3. Synthesis of the dimeric thread P1  | <b>65</b> |
| Synthesis of <b>1c</b>  | 66        |
| Synthesis of P1   | 67        |
| 1.11.4. Synthesis of the macrocycle <b>3</b>  | <b>68</b> |
| Synthesis of <b>3</b> though direct functionalization of DB24C8                                       | 69        |
| Template-direct synthesis of <b>3</b>   | 69        |
| Synthesis of <b>1d</b>  | 69        |
| Synthesis of <b>3d</b>  | 70        |
| Synthesis of <b>3</b>   | 70        |
| <b>1.12. NMR Spectra</b>  | <b>72</b> |
| <sup>1</sup> H NMR spectrum of <b>1</b>   | 72        |
| <sup>1</sup> H and <sup>13</sup> C NMR spectra of <b>2</b>  | 73        |
| <sup>1</sup> H and <sup>13</sup> C NMR spectra of P1  | 74        |
| HSQC and HMBC spectra of P1   | 75        |
| <sup>1</sup> H and <sup>13</sup> C NMR spectra of <b>3</b>  | 76        |
| <sup>1</sup> H NMR spectra of <i>E,Z</i> - <b>1</b> and <i>E,Z</i> - <b>2</b> complexes with <b>3</b> | 76        |

### 1.10.1. Experimental details

Solvents and reagents were all used as supplied by Fluorochem, Sigma-Aldrich or VWR. Flash column chromatography was performed using Sigma Aldrich Silica 40 (230-400 mesh size or 40-63  $\mu\text{m}$ ) as the stationary phase. Thin layer chromatography was performed on TLC Silica gel 60 F254 coated aluminium plates from Merck without further purification.

### 1.10.2. NMR measurements and photochemistry:

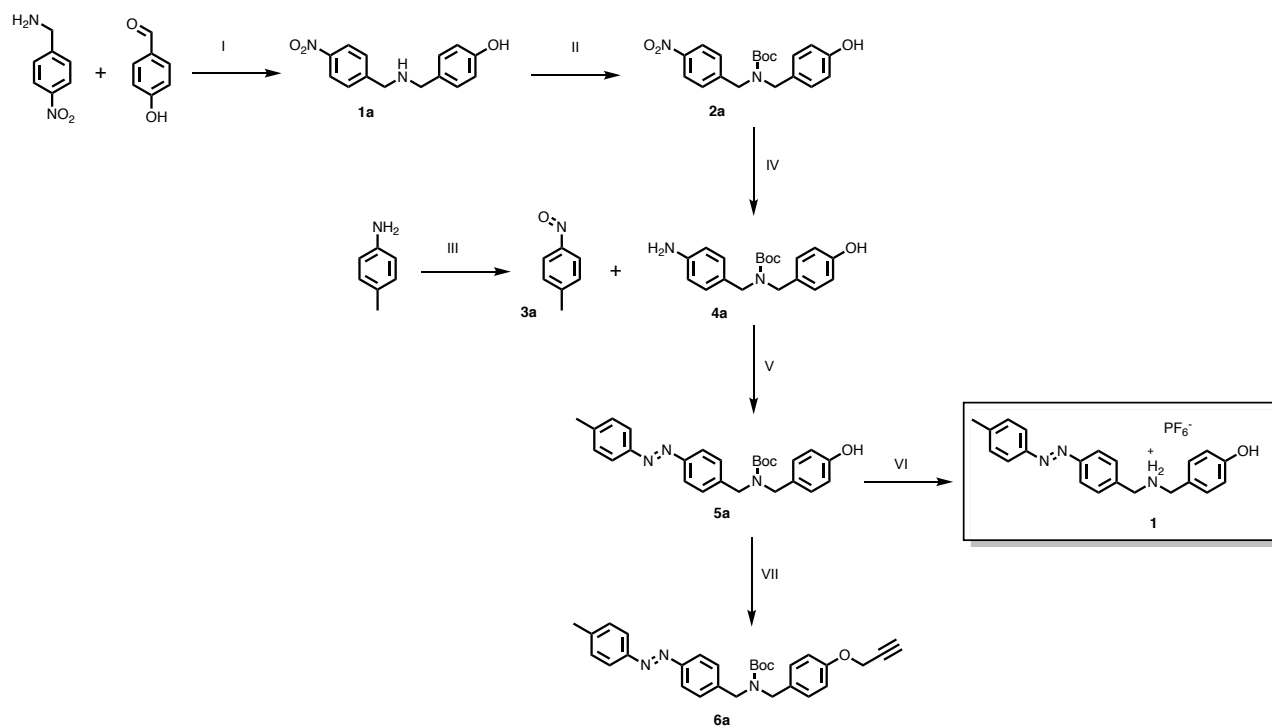
$^1\text{H}$  NMR spectra were recorded on an Agilent DD2 spectrometer operating at 500 MHz or a Varian Mercury spectrometer operating at 400 MHz;  $^{13}\text{C}$  NMR spectra were recorded on an Agilent DD2 spectrometer operating at 126 MHz or a Varian Mercury spectrometer operating at 101 MHz;  $^{19}\text{F}$  NMR spectra were recorded on an Agilent DD2 spectrometer operating at 470 MHz. Chemical shifts are quoted in ppm relative to tetramethylsilane ( $\text{SiMe}_4$ ,  $\delta = 0$  ppm), using the residual solvent peak as a reference standard; all coupling constants ( $J$ ) are expressed in Hertz (Hz). Photochemical reactions were performed in air-equilibrated  $\text{CD}_3\text{CN}$  solutions at 298 K into the spectrometer probehead, using a Prizmatix UHP-T-365-SR LED Illuminator (1.5 W,  $\lambda_{\text{max}}=369$  nm, FWHM=15.56 nm) equipped with an FCA-SMA adaptor for optical fiber directly inserted in the NMR tube. The protective coating of a quartz optical fiber was removed (about 6 cm) and the exposed fiber was sanded to enable the diffusion of light from the fiber core into the solution (550  $\mu\text{L}$  of 5 mM solution of the pseudorotaxane/free axle).

### 1.10.3. Determination of stability and rate constants:

The stability constants ( $K_{I-E}$ ,  $K_{II-E}$  and  $K_{I-Z}$ ) were obtained from the  $^1\text{H}$  NMR spectra of equimolar solutions (ca.  $10^{-3}$  M) of the ring (**3**) and the axle at 298 K using the single-point method.<sup>46</sup> The concentration of all the species at equilibrium was determined using the initial concentrations and the integration of the resonances of the complexed and uncomplexed species. The stability constant was calculated as  $K=[\text{complex}]/[\text{ring}][\text{axle}]$ . The threading rate constants ( $k_{\text{in}}$ ) were obtained from the fitting of the time-dependent concentration profiles recorded by  $^1\text{H}$  NMR upon mixing the ring **3** and the axle in acetonitrile at 298 K. In all cases the experimental data were fitted using a mixed order kinetic model (second order for threading, first order for dethreading) using SPECFIT or Berkeley Madonna 10 software. The dethreading rate constant was obtained from the fitting by imposing  $k_{\text{in}}/k_{\text{out}}=K$ .

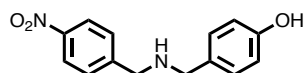
## 1.11. Synthetic procedures

### 1.11.1. synthesis of the first pump unit **6a**



*Scheme 10. I) a. Toluene, rotavapor b. NaBH<sub>4</sub>, MeOH. 93% II) Boc<sub>2</sub>O, THF r.t. 94% III) Oxone, DCM/H<sub>2</sub>O, 0 °C 30 min. 20% IV) Flow reactor, H<sub>2</sub> Pd/C 10%, MeOH. Quant. V) CH<sub>3</sub>CO<sub>2</sub>H r.t. 75% VI) ACN, HPF<sub>6</sub> procedure not reported VII) Propargyl bromide, K<sub>2</sub>CO<sub>3</sub> CH<sub>3</sub>CN (dry) 80°C. 70%.*

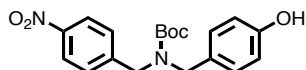
## Synthesis of **1a**



10 g (81.2 mmol) of 4-hydroxy benzylamine and 12.3 g of 4-nitro benzaldehyde were dissolved in 40 mL of toluene. The mixture was stirred for 30 minutes, and the solvent was removed under reduced pressure, then 40 mL of toluene were added and distilled for other 2 times to remove the H<sub>2</sub>O formed upon condensation of the reagents through azeotropic distillation. The imine intermediate appears as a yellow solid that was dissolved in 200 mL of MeOH. Portionwise addition of 12.3 g (0.3 mol) of NaBH<sub>4</sub> in the stirred solution provided the complete reduction of the imine, the completion of the reaction was monitored by TLC. At the end of the reaction the solvent was removed under reduced pressure and H<sub>2</sub>O was added, the aqueous phases were extracted with AcOEt (30 mL X 4), the organic phases were washed with brine and dried on Na<sub>2</sub>SO<sub>4</sub>. No further purification needed. Pale-yellow solid Yield 93%.

<sup>1</sup>H NMR (500 MHz, CDCl<sub>3</sub>, 298 K) δ 8.18 (d, *J* = 8.6 Hz, 2H), 7.52 (d, *J* = 8.1 Hz, 2H), 7.18 (d, *J* = 8.3 Hz, 2H), 6.78 (d, *J* = 8.4 Hz, 2H), 3.90 (br, 1H), 3.74 (br, 1H). <sup>13</sup>C NMR (126 MHz, CDCl<sub>3</sub>) δ 155.04, 148.07, 147.23, 131.85, 129.71, 128.88, 123.79, 115.55, 52.81, 52.38.

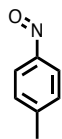
## Synthesis of **2a**



0,64 g (2.5 mmol) of **1a** and 0.59 g (2.7 mmol) of di-*tert*-butyl decarbonate (Boc<sub>2</sub>O) were dissolved in 50 mL of THF and stirred at room temperature. The reaction was monitored by TLC. At the end of the reaction the solvent was removed under reduced pressure and H<sub>2</sub>O was added, the aqueous phases were extracted with AcOEt (30 mL X 4), the organic phases were washed with brine and dried on Na<sub>2</sub>SO<sub>4</sub>. No further purification needed. Pale-yellow solid Yield 94%.

<sup>1</sup>H NMR (500 MHz, CDCl<sub>3</sub>, 298 K) δ 8.17 (d, *J* = 8.5 Hz, 2H), 7.32 (m, 2H), 7.08 (m, 2H), 6.78 (d, *J* = 8.3 Hz, 2H), 4.94 (s, 1H), 4.39 (m, 4H), 1.65 – 1.37 (m, 9H). <sup>13</sup>C NMR (126 MHz, CDCl<sub>3</sub>, 298K) δ 156.28, 155.78, 147.25, 145.85, 129.28, 128,85, 128.10, 123.87, 115.69, 81.24, 49.82, 49.04, 28.53.

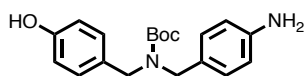
## Synthesis of **3a**



10 g (93 mmol) of toluidine were dissolved in 250 mL of DCM, the solution was cooled to 0°C and maintained under vigorous stirring. Subsequently a solution of 28.7 g (93 mmol) of Oxone in 300 mL in H<sub>2</sub>O was added, followed by about 30 g of ice water. The formation of the product was monitored every 10 minutes with TLC (AcOEt:*n*-hex, 1:4). After 30 minutes the reaction was stopped, the organic phases were collected and firstly washed with 50 mL HCl 1M, then with H<sub>2</sub>O until neutralization of the aqueous phases and finally with brine. The organic phases were dried under Na<sub>2</sub>SO<sub>4</sub> and the solvent was removed under reduced pressure. The product appears as yellow brownish solid. Yield 20%.

<sup>1</sup>H NMR (400 MHz, CDCl<sub>3</sub>, 298 K) δ 7.81 (d, *J* = 8.0 Hz, 2H), 7.39 (d, *J* = 8.5 Hz, 2H), 2.45 (s, 3H).

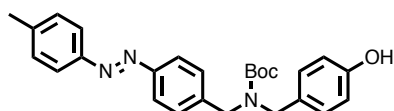
## Synthesis of **4a**



A 50 mM solution of **2a** (0.85 g, 2.36 mmol) in MeOH was prepared. The reduction reaction was performed using H-Cube hydrogenation system: 10% Pd/C CatCart, 1 mL/min flow rate, 10 bar at 25 °C. No purification needed, quantitative Yield.

<sup>1</sup>H NMR (400 MHz, CDCl<sub>3</sub>, 298 K) δ 7.04 (m, 4H), 6.77 (d, *J* = 8.6 Hz, 2H), 6.64 (d, *J* = 8.5 Hz, 2H), 4.96 (br, 1H), 4.24 (m, 4H), 3.64 (br., 2H), 1.49 (s, 9H). <sup>13</sup>C NMR (126 MHz, CDCl<sub>3</sub>, 298 K) δ 156.34, 155.37, 145.50, 129.54, 128.99, 128.02, 115.58, 115.55, 115.44, 114.69, 80.30, 48.31, 28.67.

## Synthesis of **5a**

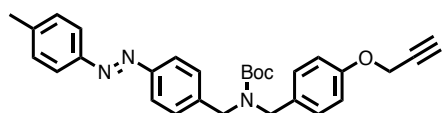


0,4 g (1.22 mmol) of **4a** and 0.22 (1.84 mmol) of 1-methyl-4-nitrosobenzene were dissolved in 10 mL of CH<sub>3</sub>CO<sub>2</sub>H. The solution was stirred for 18 h at room temperature. The solvent was removed under reduced pressure and the crude mixture was dissolved in AcOEt. The organic phases were washed with

NaHCO<sub>3</sub> (sat) and then with H<sub>2</sub>O until the neutralization of aqueous phases, finally the organic phases were washed with brine and dried on Na<sub>2</sub>SO<sub>4</sub>. The product was purified with column chromatography (2:1, *n*-hex:AcOEt). Orange solid, Yield 75%.

<sup>1</sup>H NMR (500 MHz, CDCl<sub>3</sub>, 298 K) δ 7.86 (d, *J* = 8.3 Hz, 2H), 7.83 (d, *J* = 8.2 Hz, 2H), 7.32 (m, 4H), 7.10 (m, 2H), 6.79 (d, *J* = 8.5 Hz, 2H), 4.87 (s, 1H, br), 4.38 (m, 4H), 2.44 (s, 3H), 1.58 – 1.47 (m, 9H). <sup>13</sup>C NMR (126 MHz, CDCl<sub>3</sub>, 298 K) δ 156.23, 155.30, 152.14, 150.91, 141.71, 129.89, 129.76, 129.17, 128.73, 128.01, 125.89, 123.05, 122.98, 115.60, 80.60, 49.05, 28.63, 21.65.

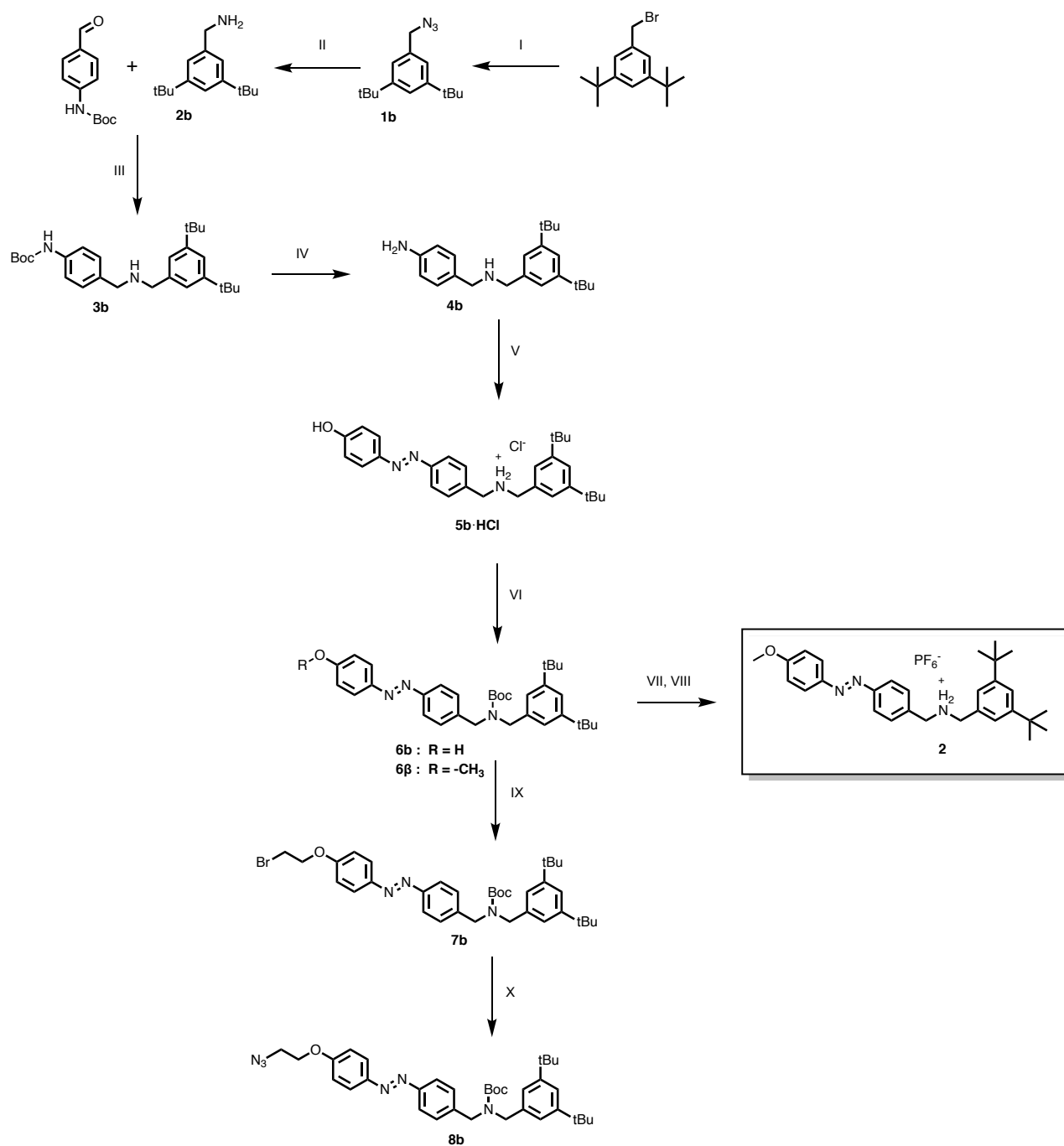
### Synthesis of **6a**



0.38 g (0.88 mmol) of **5a**, 0.32 g (2.28 mmol) of anhydrous K<sub>2</sub>CO<sub>3</sub> were introduced in a round bottom flask and suspended with 5 mL of anhydrous CH<sub>3</sub>CN. Subsequently, 0.5 mL (4.4 mmol) of 80% propargyl bromide in toluene solution was added to the mixture maintained under stirring. The reaction mixture was refluxed for 2 hours. At the end of the reaction the solvent was removed under reduced pressure and H<sub>2</sub>O was added, the mixture was extracted with AcOEt. The organic phases were washed with brine and finally dried on Na<sub>2</sub>SO<sub>4</sub>. The mixture was purified by column chromatography (1:4, AcOEt : *n*-hex). The product appears as a red-brownish solid, yield 70%.

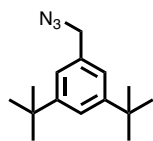
<sup>1</sup>H NMR (500 MHz, CDCl<sub>3</sub>, 298 K) δ 7.88 (d, *J* = 8.4 Hz, 2H), 7.84 (d, *J* = 8.3 Hz, 2H), 7.34 (m, 4H), 7.19 (m, 2H), 6.96 (d, *J* = 8.6 Hz, 2H), 4.71 (d, *J* = 2.4 Hz, 2H), 4.41 (m, 4H), 2.55 (t, *J* = 2.3 Hz, 1H), 2.46 (s, 3H), 1.52 (m, 9H). <sup>13</sup>C NMR (126 MHz, CDCl<sub>3</sub>, 298 K) δ 157.00, 156.02, 152.09, 150.87, 141.63, 130.96, 129.85, 129.50, 128.94, 128.69, 128.02, 123.01, 122.94, 115.09, 80.35, 78.67, 75.68, 55.96, 48.97, 28.57, 21.61.

### 1.11.2. Synthesis of the second pump unit **8b** and model compound **2**



*Scheme 11. I) NaN<sub>3</sub>, DMF 70 °C 3h. Quant. II) Flow reactor H<sub>2</sub> Pd/C 10%, MeOH. Quant. III) a. Toluene, rotavapor b. NaBH<sub>4</sub>, MeOH. 87% IV) HCl, EtOH, reflux 94%. V) a. HCl, NaNO<sub>2</sub>, EtOH 0°C 2h b. phenol, NaOH, EtOH 2h r.t. 45% VI) a. NaHCO<sub>3</sub> b. Boc<sub>2</sub>O, THF, 83% VII) K<sub>2</sub>CO<sub>3</sub>, CH<sub>3</sub>I, CH<sub>3</sub>CN reflux 57% VIII) a. TFA, DCM, b. NaHCO<sub>3</sub>, c. HCl, NH<sub>4</sub>PF<sub>6</sub>, 41% IX) K<sub>2</sub>CO<sub>3</sub>, Br(CH<sub>2</sub>)<sub>2</sub>Br, CH<sub>3</sub>CN reflux, 75 % X) NaN<sub>3</sub>, DMF 70°C quant.*

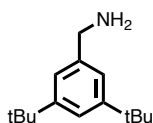
## Synthesis of **1b**



10.32 g (36.5 mmol) of 1-(bromomethyl)-3,5-di-*tert*-butylbenzene and 2.37g (36.5 mmol) NaN<sub>3</sub> were suspended in 200 mL dry DMF. The reaction mixture was heated to 70°C and stirred for 3 hours. At the end of the reaction the mixture was cooled to room temperature and 200 mL of H<sub>2</sub>O were added. Subsequently the aqueous phases were extracted with Et<sub>2</sub>O, washed with brine and dried over Na<sub>2</sub>SO<sub>4</sub>. The product was isolated as a pale-yellow oil in quantitative yield and purification was not necessary.

<sup>1</sup>H NMR (500MHz, CDCl<sub>3</sub>, 298 K) δ 7.47 (t, *J* = 1.9 Hz, 1H), 7.20 (d, *J* = 1.9 Hz, 2H), 4.39 (s, 2H), 1.40 (s, 18H). <sup>13</sup>C NMR (126 MHz, CDCl<sub>3</sub>, 298 K) δ 151.51, 134.68, 122.51, 122.42, 55.62, 34.96, 31.55.

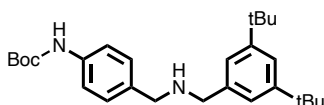
## Synthesis of **2b**



The H-Cube hydrogenation system was used to perform the reduction reaction of a 50 mM solution of **1b** in MeOH. The catalyst used was: 10% Pd/C CatCart, with a flow rate of 1 mL/min at 10 bar pressure at 25 °C. No purification needed, the product appear as a colorless viscous oil. Quantitative Yield.

<sup>1</sup>H NMR (500 MHz, CDCl<sub>3</sub>, 298 K) δ 7.34 (t, *J*=1.9Hz,1H), 7.17 (d, *J*=1.9Hz, 2H), 3.88 (s, 2H), 1.35 (s, 18H) <sup>13</sup>C NMR (126 MHz, CDCl<sub>3</sub>, 298 K) δ 150.99, 142.53, 121.29, 120.90, 47.18, 34.86, 31.51.

## Synthesis of **3b**

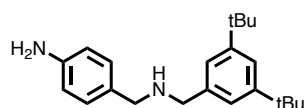


1.83 g (8.25 mmol) of compound **2b** and 1.81 g (8.25 mmol) of *tert*-butyl (4-formylphenyl)carbamate were dissolved in 30 mL of toluene. The mixture was stirred for 30

minutes, and the solvent was removed under reduced pressure to remove the water formed upon the condensation reaction through azeotropic distillation. The imine intermediate was isolated as a crystalline solid that was dissolved in 150 mL of MeOH. Portionwise addition of 1.25 g (33 mmol) of NaBH<sub>4</sub> in the stirred solution provided the complete reduction of the imine. At the end of the reaction the solvent was removed, and 100 mL of H<sub>2</sub>O were added. The aqueous phases were extracted with AcOEt (30 mL x 2). The organic phase was washed with brine and finally dried on Na<sub>2</sub>SO<sub>4</sub>. The product was purified by column chromatography (3% MeOH, DCM). White solid, Yield 87 %.

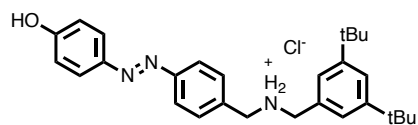
<sup>1</sup>H NMR (400 MHz, CDCl<sub>3</sub>, 298 K) δ 7.33 (dd, *J* = 4.7, 2.8 Hz, 3H), 7.30 – 7.26 (m, 2H), 7.17 (d, *J* = 1.9 Hz, 2H), 3.78 (s, 4H), 1.53 – 1.51 (m, 9H), 1.35 – 1.31 (m, 18H). <sup>13</sup>C NMR (126 MHz, CDCl<sub>3</sub>, 298 K) δ 152.98, 150.88, 139.22, 137.38, 134.92, 128.97, 122.47, 121.11, 118.69, 80.43, 53.63, 52.75, 34.91, 31.62, 28.50.

#### Synthesis of **4b**



3.49 g (8.25 mmol) of compound **3b** were dissolved in 250 mL of EtOH, subsequently 16.5 mL (0.2 mol) of HCl 37% was gently added to the solution. The mixture was stirred and refluxed for 12 hours. At the end of the reaction the solvent was removed under reduced pressure, the white crystalline chloride salt obtained was dissolved in AcOEt, neutralized with a solution of NaHCO<sub>3</sub> and washed with brine. The organic phases were dried over Na<sub>2</sub>SO<sub>4</sub>. The reagent was quantitatively deprotected and no further purification were needed. White powder, yield 94% <sup>1</sup>H NMR (500 MHz, CDCl<sub>3</sub>, 298 K) δ 7.36 (s, 1H), 7.21 (s, 2H), 7.16 (d, *J* = 7.5 Hz, 2H), 6.66 (d, *J* = 7.2 Hz, 2H), 3.82 (s, 2H), 3.75 (s, 2H), 1.37 (s, 18H). <sup>13</sup>C NMR (126 MHz, CDCl<sub>3</sub>, 298 K) δ 150.74, 145.39, 139.35, 130.24, 129.41, 122.42, 120.93, 115.11, 53.59, 52.84, 34.86, 31.59.

## Synthesis of **5b**·HCl

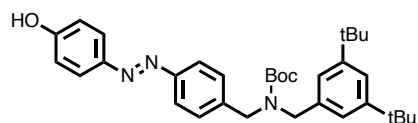


2.5 g (7.7 mmol) of compound **4b** were dissolved in 180 mL of EtOH and the solution was stirred at room temperature (Flask A). After cooling to 0°C, 2.55 mL (15.4 mmol) of 60% HPF<sub>6</sub> solution in water was added. Subsequently 7.15 g (69.3 mmol) of *tert*-butyl nitrite were added dropwise. The mixture was stirred for 2 hours and left to return to room temperature.

In another round bottom flask (B), 1.8 g (19.25 mmol) of phenol and 1.5 g (38.25 mmol) of NaOH were dissolved in 150 mL of EtOH. The content of the first two-neck round bottom flask A was transferred in the second one B, the solution immediately turned to a deep red color. The reaction was stirred for 2 hours.

At the end of the reaction the solvent was removed under reduced pressure and 70 mL H<sub>2</sub>O were added. The mixture was extracted with AcOEt (40 mL x 2), finally the organic phases were dried on Na<sub>2</sub>SO<sub>4</sub>. The product was dissolved in the minimum amount of MeOH and 2 mL of HCl 37% were added, the solvent was removed under reduced pressure and the bright red chloride salt was washed with Et<sub>2</sub>O. The compound that appears as an orange solid, was directly used in the next step.

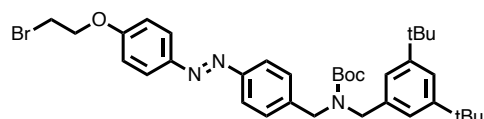
## Synthesis of **6b**



1.42 g (3.3 mmol) of neutralized compound **6b** and 0.72 g (3.3 mmol) of di-*tert*-butyl dicarbonate were dissolved in 50 mL of THF and stirred at room temperature. The reaction completion was monitored with TLC. At the end of the reaction the solvent was removed under reduced pressure and H<sub>2</sub>O was added, the aqueous phases were extracted with AcOEt (30 mL X 4), the organic phases were washed with brine and dried on Na<sub>2</sub>SO<sub>4</sub>. The product appears as a orange solid and was purified through column chromatography (eluent 1:1, Et<sub>2</sub>O : cyclohexane). Yield 83%

$^1\text{H}$  NMR (500 MHz,  $\text{CD}_3\text{CN}$ , 298 K)  $\delta$  7.85 (d,  $J = 8.9$  Hz, 2H), 7.80 (d,  $J = 8.4$  Hz, 2H), 7.37 (m, 3H), 7.12 (m, 2H), 7.00 (d,  $J = 8.9$  Hz, 2H), 4.48 (m, 4H), 1.47 (s, 9H), 1.30 (s, 18H).  $^{13}\text{C}$  NMR (126 MHz,  $\text{CDCl}_3$ , 298 K)  $\delta$  159.36, 156.50, 152.17, 151.21, 146.84, 140.11, 136.87, 128.96, 128.31, 125.01, 122.86, 121.54, 115.99, 80.88, 50.89, 49.36, 34.94, 31.61, 28.67.

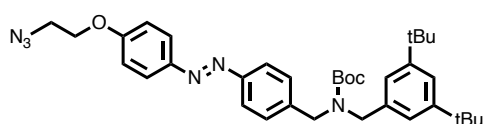
### Synthesis of **7b**



0.3 g (0.57 mmol) of compound **6b**, 2.7 g (14.3 mmol) of 1, 2 dibromoethane, 0.21 g (1.23 mL, 1.5 mmol) of  $\text{K}_2\text{CO}_3$  and 75 mg of 18-Crown-6 were suspended in 60 mL of  $\text{CH}_3\text{CN}$ . The mixture was refluxed and 12 hours. After this period the solvent was removed under reduced pressure and water was added to the mixture, the aqueous phases were extracted with AcOEt (30 mL x 3). The collected organic phases were washed with brine and dried on  $\text{Na}_2\text{SO}_4$ . The column chromatography (eluent n-hex:AcOEt 3:1) provided the pure product as an orange solid providing 75% yield.

$^1\text{H}$  NMR (500 MHz,  $\text{CDCl}_3$ , 298 K)  $\delta$  7.94 (d,  $J = 7.9$  Hz, 2H), 7.86 (d,  $J = 7.7$  Hz, 2H), 7.35 (t,  $J = 14.6$  Hz, 3H), 7.06 (m, 4H), 4.56 – 4.32 (m, 6H), 3.68 (m, 2H), 1.55 (s, 9H), 1.34 (s, 18H).  $^{13}\text{C}$  NMR (126 MHz,  $\text{CDCl}_3$ , 298 K)  $\delta$  160.54, 156.14, 151.10, 147.60, 141.07, 137.09, 128.80, 128.13, 124.89, 122.91, 122.49, 122.07, 121.40, 115.05, 80.21, 68.17, 50.41, 34.93, 31.62, 28.89, 28.65.

### Synthesis of **8b**

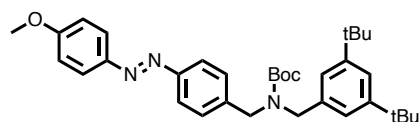


0.25 g (0.39 mmol) of **7b** and 28 mg (0.43 mmol) of  $\text{NaN}_3$  were suspended in 6 mL dry DMF. The reaction mixture was heated at  $70^\circ\text{C}$  and stirred for 3 hours. At the end of the reaction the mixture was cooled to room temperature and 20 mL of  $\text{H}_2\text{O}$  were added, the mixture was

extracted with Et<sub>2</sub>O. The organic phase was washed with brine and dried on Na<sub>2</sub>SO<sub>4</sub>. The reagent was quantitatively converted in the orange solid product **7b**, there was no need for further purification.

<sup>1</sup>H NMR (500 MHz, CDCl<sub>3</sub>, 298 K) δ 7.92 (d, *J* = 8.8 Hz, 2H), 7.84 (d, *J* = 7.8 Hz, 2H), 7.33 (m, 3H), 7.05 (m, 4H), 4.42 (m, 4H), 4.24 (t, *J* = 4.4 Hz, 2H), 3.65 (t, *J* = 4.5 Hz, 2H), 1.52 (s, 9H), 1.32 (s, 18H). <sup>13</sup>C NMR (126 MHz, CDCl<sub>3</sub>, 298 K) δ 160.54, 156.14, 152.11, 151.10, 147.60, 141.10, 136.92, 128.80, 124.89, 122.88, 122.30, 121.40, 115.05, 80.21, 68.17, 50.20, 49.00, 34.93, 31.62, 28.89, 28.65.

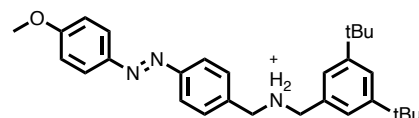
### Synthesis of **6β**



0.55 g (0.99 mmol) of compound **6b**, 0.71 g (5 mmol) of CH<sub>3</sub>I and 0.34 g (2.5 mmol) of K<sub>2</sub>CO<sub>3</sub> were suspended in 50 mL of CH<sub>3</sub>CN. The mixture was refluxed and 12 hours. After this period the solvent was removed under reduced pressure and water was added to the mixture, the aqueous phases were extracted with AcOEt (30 mL x 3). The collected organic phases were washed with brine and dried on Na<sub>2</sub>SO<sub>4</sub>. The column chromatography (eluent DCM) provided pure product as an orange viscous oil, 57% yield.

<sup>1</sup>H NMR (400 MHz, CDCl<sub>3</sub>, 298 K) δ 7.98 (d, *J* = 8.9 Hz, 2H), 7.91 (d, *J* = 7.8 Hz, 2H), 7.47 – 7.31 (m, 3H), 7.14 (d, *J* = 20.7 Hz, 2H), 7.05 (d, *J* = 9.0 Hz, 2H), 4.50 (dd, *J* = 46.4, 12.8 Hz, 4H), 3.89 (s, 3H), 1.60 (s, 9H), 1.38 (s, 18H). <sup>13</sup>C NMR (101 MHz, CDCl<sub>3</sub>) δ 162.05, 156.03, 152.06, 150.97, 147.02, 140.84, 136.94, 128.65, 127.96, 124.76, 122.71, 122.34, 121.27, 114.21, 80.07, 55.53, 50.15, 34.83, 31.55, 28.56.

### Synthesis of **2**

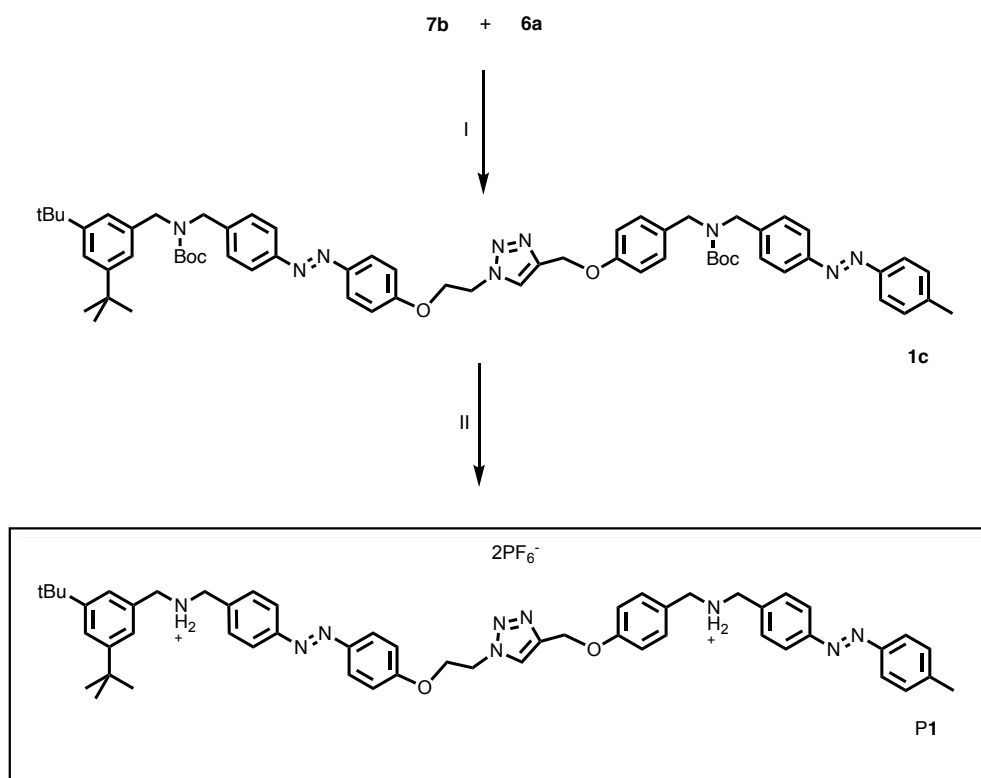


A solution of 0.31 g (0.55 mmol) of **6β** and 0.87 mL of TFA (11.1 mmol) in DCM was stirred for 6 hours. The deprotection reaction was monitored with TLC. At the end of the reaction the solvent was removed then the trifluoroacetate salt was dissolved in DCM and deprotonated with

NaHCO<sub>3</sub>. The crude was purified with column chromatography (eluent 5:1, *n*-hexane:AcOEt). The purified compound was dissolved in the minimum amount of MeOH, subsequently about 1 mL of HCl 37% was added and the solvent was removed under reduced pressure. The bright-red solid obtained was dissolved in MeOH. The dropwise addition of a saturated solution of NH<sub>4</sub>PF<sub>6</sub> in water caused the precipitation of an orange-yellow salt that was collected by filtration and washed with H<sub>2</sub>O. The solid product was dissolved in DCM and dried over Na<sub>2</sub>SO<sub>4</sub>. Orange solid, yield 41%.

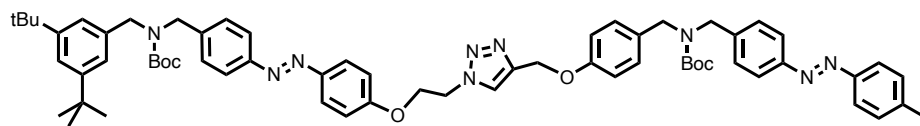
<sup>1</sup>H NMR (500 MHz, CD<sub>3</sub>CN, 298 K) δ 7.94 – 7.89 (m, 4H), 7.64 (d, *J* = 8.4 Hz, 2H), 7.54 (t, *J* = 1.8 Hz, 1H), 7.32 (d, *J* = 1.8 Hz, 2H), 7.14 (br. NH<sub>2</sub>, 2H), 7.11 (d, *J* = 9.0 Hz, 2H), 4.31 (m, 2H), 4.25 – 4.20 (m, 2H), 3.90 (s, 3H), 1.33 (s, 18H). <sup>13</sup>C NMR (126 MHz, CD<sub>3</sub>CN) δ 163.75, 154.17, 152.78, 147.66, 133.32, 132.36, 130.57, 125.77, 125.34, 124.67, 123.64, 115.48, 56.45, 52.96, 51.95, 35.59, 31.48. <sup>19</sup>F NMR (470 MHz, CD<sub>3</sub>CN) δ -72.94 (d, *J* = 706.4 Hz).

### 1.11.3. Synthesis of the dimeric thread P1



Scheme 12. I)  $[\text{Cu}(\text{CH}_3\text{CN})_4]\text{PF}_6$   $\text{CH}_2\text{Cl}_2$ , 1 week. 63%. II) a. TFA, DCM, b.  $\text{NaHCO}_3$  c. HCl,  $\text{NH}_4\text{PF}_6$  47%.

## Synthesis of **1c**

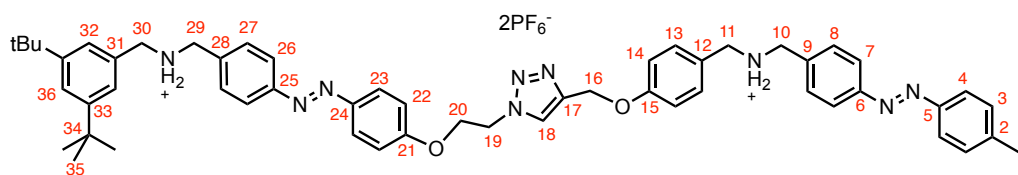


80 mg (0.17 mmol) of compound **6a**, 100 mg (0.17 mmol) of **8b** and 200 mg (0.54 mmol) of [Cu(CH<sub>3</sub>CN)<sub>4</sub>]PF<sub>6</sub> were dissolved in 80 mL of degassed CH<sub>2</sub>Cl<sub>2</sub> in a round bottom flask under N<sub>2</sub> flux. The mixture was stirred for 1 week at room temperature, the reaction completion was monitored with TLC (DCM, MeOH 2%). At the end of the reaction water and CH<sub>2</sub>Cl<sub>2</sub> were added. The organic phases were washed with water to remove the copper salts. The product was purified through column chromatography (eluent CHCl<sub>3</sub>, MeOH 3%). Orange solid, yield 63%.

<sup>1</sup>H NMR (500 MHz, CD<sub>3</sub>CN, 298 K) δ 7.96 (s, 1H), 7.86 – 7.72 (m, 8H), 7.54 – 7.46 (m, 4H), 7.36 (m, 3H), 7.25 (d, *J* = 8.5 Hz, 2H), 7.20 (d, *J* = 1.6 Hz, 2H), 7.00 (d, *J* = 8.9 Hz, 2H), 6.95 (d, *J* = 8.6 Hz, 2H), 5.15 (s, 2H), 4.77 (t, *J* = 5.0 Hz, 2H), 4.46 (t, *J* = 5.0 Hz, 2H), 3.82 (s, 2H), 3.79 (s, 2H), 3.75 (s, 2H), 3.69 (s, 2H), 2.41 (s, 3H), 2.28 (s, 18H), 1.28 (d, *J* = 18.7 Hz, 18H).  
<sup>13</sup>C NMR (126 MHz, CD<sub>3</sub>CN, 298 K) δ 161.60, 161.54, 158.26, 152.53, 152.51, 151.88, 151.68, 151.65, 148.19, 145.27, 144.92, 144.57, 142.89, 140.60, 134.14, 130.86, 130.39, 129.95, 129.87, 129.38, 125.62, 125.45, 124.27, 123.54, 123.45, 123.42, 123.32, 121.80, 121.36, 120.98, 116.06, 115.62, 67.77, 62.39, 54.09, 53.19, 53.10, 53.00, 50.41, 35.46, 31.75, 21.50.

## Synthesis of P1

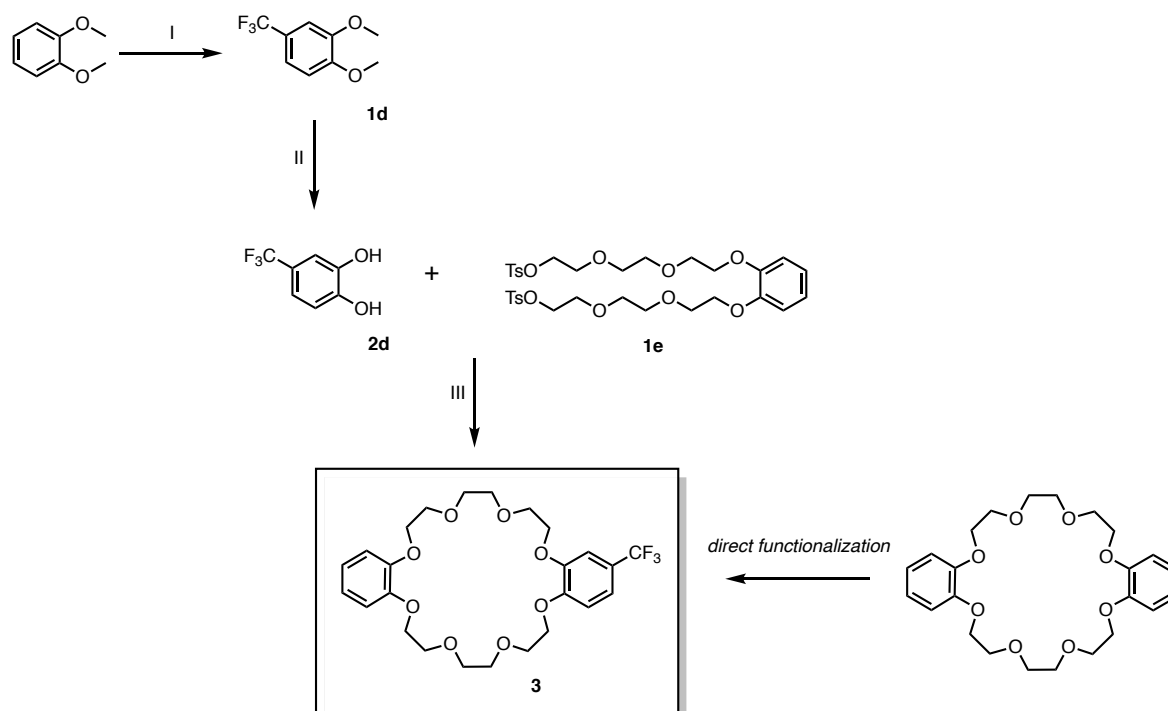
0.3 g (0.28 mmol) of **1c** were dissolved in 50 mL of CH<sub>2</sub>Cl<sub>2</sub> and 2 mL of trifluoroacetic acid (26 mmol). The solution was stirred at room temperature for 5 hours and the progress of the reaction was monitored with TLC. At the end of the reaction the solvent was removed under reduced pressure, the resulting trifluoroacetate salt was dissolved in 30 mL of AcOEt, washed with NaHCO<sub>3</sub> and finally with H<sub>2</sub>O. The organic phases were dried over Na<sub>2</sub>SO<sub>4</sub>. The crude was filtered on silica (eluent CH<sub>2</sub>Cl<sub>2</sub>, MeOH 5%). For the synthesis of the hexafluorophosphate salt the molecule was dissolved in the minimum amount of acetone and few drops of 37% HCl were added, immediately a bright-red solid has precipitated. The solvent was removed and the solid was suspended in about 1 mL of CH<sub>2</sub>Cl<sub>2</sub>, few drops of MeOH was added until the product was completely solubilized. A saturated solution of NH<sub>4</sub>PF<sub>6</sub> in water was added dropwise resulting in the separation of two phases, at this stage CH<sub>2</sub>Cl<sub>2</sub> was added. The organic phases were washed with water and dried over Na<sub>2</sub>SO<sub>4</sub>. Orange solid, yield 47%.



<sup>1</sup>H NMR (500 MHz, CD<sub>3</sub>CN, 298 K) δ 8.00 (s, 1H, **18**), 7.92 – 7.85 (m, 6H, **7**, **23**, **26**), 7.81 (d, *J* = 8.0 Hz, 2H, **4**), 7.58 (m, 4H, **8**, **27**), 7.48 (s, 1H, **36**), 7.37 (m, 4H, **3**, **13**), 7.28 (s, 2H, **32**), 7.05 (m, 4H, **14**, **22**), 5.18 (s, 2H, **16**), 4.79 (t, *J* = 4.8 Hz, 2H, **19**), 4.49 (t, *J* = 4.9 Hz, 2H, **20**), 4.16 (s, 2H, **30**), 4.09 (d, 4H, **11**, **29**), 4.04 (s, 2H, **10**), 2.43 (s, 3H, **1**), 1.32 (s, 9H, **35**).

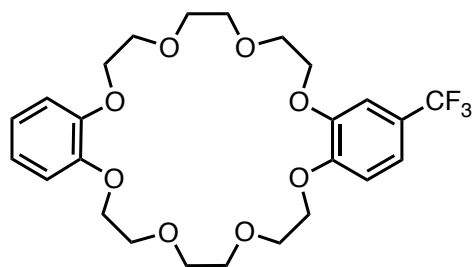
<sup>13</sup>C NMR (126 MHz, CD<sub>3</sub>CN, 298 K) δ 161.93 (**21**), 159.63 (**15**), 153.67 (**33**), 153.52 (**6**), 152.51 (**2**), 151.60 (**25**), 148.13 (**24**), 144.28 (**17**), 143.45 (**5**), 138.16 (**9**), 136.93 (**28**), 133.57 (**31**), 131.96 (**13**), 131.68 (**27**), 131.38 (**7**), 130.94 (**3**), 127.58 (**12**), 125.75 (**26**), 125.72 (**18**), 124.80 (**32**), 123.88 (**8**), 123.71 (**36**), 123.69 (**4**), 123.62 (**23**), 116.12 (**22**), 115.97 (**14**), 67.79 (**20**), 62.42 (**16**), 53.34 (**30**), 52.44 (**11**), 52.33 (**10**), 52.24 (**29**), 50.44 (**19**), 35.59 (**34**), 31.60 (**35**), 21.52 (**1**).

### 1.11.4. Synthesis of the macrocycle **3**



Scheme 13. I)  $\text{CF}_3\text{SO}_2\text{Na}$  *t*BuOOH,  $\text{CH}_3\text{CN}$  r.t. 12 h, 38% II)  $\text{BBr}_3$ , DCM,  $-15^\circ\text{C}$ , 60% III)  $\text{Cs}_2\text{CO}_3$ , THF,  $70^\circ\text{C}$ , 48 h, 72%. Direct functionalization:  $\text{CF}_3\text{SO}_2\text{Na}$  *t*BuOOH, DMSO: $\text{CH}_3\text{CN}$  r.t. 24 h.

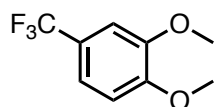
## Synthesis of **3** through direct functionalization of DB24C8



0.2 g of DB24C8 (0.45 mmol) and 0,1 mg of CF<sub>3</sub>SO<sub>2</sub>Na (0.68 mmol) were dissolved in a mixture of acetonitrile (1 mL) and dimethyl sulfoxide and stirred in a Schlenk flask at 0 °C under nitrogen flux. Subsequently 0.2 mL (1.46 mmol) of a 70% solution of *tert*-butyl hydroperoxide (DTBP) in H<sub>2</sub>O were added to the flask, the flux (0.1 mL/hour) was controlled by mean of a syringe pump. The reaction was left to return at room temperature and stirred for 12 hours. After this time, the mixture was quenched with water and extracted with Et<sub>2</sub>O, the organic phases were washed with water and brine and finally dried over Na<sub>2</sub>SO<sub>4</sub>. The conversion to the product was estimated by <sup>1</sup>H NMR around the 40% however several attempts of purification on silica didn't result in an efficient separation of the product from the byproducts and the starting material.

## Template-direct synthesis of **3**

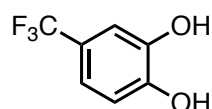
### Synthesis of **1d**



2 g of Veratrole (14.3 mmol) and 3,4 g of sodium triflate (NaCF<sub>3</sub>SO<sub>2</sub>) (21.8 mmol) were dissolved in acetonitrile (60 mL) and stirred in a Schlenk flask at 0 °C under nitrogen flux. Subsequently 6,4 mL of a 70% solution of *tert*-butyl hydroperoxide in H<sub>2</sub>O were added to the flask, the flux (3mL/hour) was controlled by mean of a syringe pump. The reaction was left to return at room temperature and stirred for 12 hours. After this time, the mixture was quenched with water and extracted with Et<sub>2</sub>O (80 mL for 3 times), the organic phases were washed with water and brine and finally dried over Na<sub>2</sub>SO<sub>4</sub>. The product was purified through column chromatography (eluent dichloromethane / cyclohexane 1:1). Yield 38%.

$^1\text{H}$  NMR (500 MHz,  $\text{CDCl}_3$ , 298 K)  $\delta$  7.18 (d,  $J = 8.3$  Hz, 1H), 7.05 (s, 1H), 6.87 (d,  $J = 10.2$  Hz, 1H), 3.88 (s, 6H).  $^{13}\text{C}$  NMR (126 MHz,  $\text{CDCl}_3$ , 298 K)  $\delta$  151.68, 149.13, 124.40 (q,  $J = 271.2$  Hz), 122.95 (q,  $J = 32.7$  Hz), 118.37 (q,  $J = 4.2$  Hz), 110.65, 108.07 (q,  $J = 3.5$  Hz), 56.01, 55.98.  $^{19}\text{F}$  NMR (470 MHz,  $\text{CDCl}_3$ )  $\delta$  -61.65 (s, 3F).

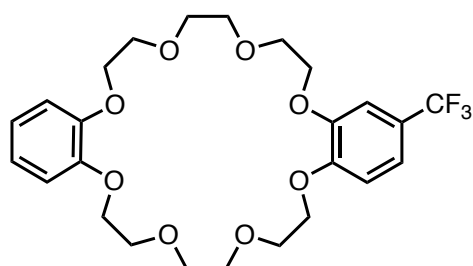
### Synthesis of **3d**



1.14 g **1d** (5.54 mmol) was dissolved in anhydrous dichloromethane (100 mL). Boron tribromide (3.9 mL, 39 mmol) was slowly added to the solution maintained at  $-15$  °C with a frigorific mixture bath (20% w/w  $\text{NH}_4\text{Cl}$  in ice and  $\text{H}_2\text{O}$ ). The reaction mixture was left to return at room temperature and stirred overnight. At the end of the reaction the mixture was quenched with water and extracted with ethyl acetate (50 mL for three times). The organic phase was washed with brine and dried over  $\text{Na}_2\text{SO}_4$ . The product was purified with chromatography on silica (eluent dichloromethane). Pale green oil, yield 60%.

$^1\text{H}$  NMR (500 MHz,  $\text{CDCl}_3$ , 298 K)  $\delta$  7.12 (s, 1H), 7.09 (d,  $J = 8.4$  Hz, 1H), 6.92 (d,  $J = 8.3$  Hz, 1H), 6.35 (br. 2H).  $^{19}\text{F}$  NMR (470 MHz,  $\text{CDCl}_3$ , 298 K)  $\delta$  -61.67 (s, 3F).

### Synthesis of **3**



In a three-neck round bottom flask a mixture of 3.1 g (9.5 mmol) of  $\text{Cs}_2\text{CO}_3$  in 60 mL tetrahydrofuran was stirred at reflux. A solution of 1,3 g (1.5 mmol) of **1e** and 0,34 g of **3d** in 50 mL was slowly added by mean of a dropping funnel. The reaction was stirred at reflux for 48 h, at the end of this time the solvent was removed under reduced pressure and the mixture was suspended in 100 mL of toluene. The organic phases were washed with water (100 mL X 3) and finally dried over  $\text{Na}_2\text{SO}_4$ . The product was purified with column chromatography on

silica (eluent 3% MeOH in DCM) and subsequently recrystallized from boiling cyclohexane. White solid, yield 72%.

$^1\text{H}$  NMR (500 MHz,  $\text{CD}_3\text{CN}$ )  $\delta$  7.23 (d,  $J = 8.4$  Hz, 1H), 7.18 (d,  $J = 2.0$  Hz, 1H), 7.03 (d,  $J = 8.4$  Hz, 1H), 6.95 – 6.86 (m, 4H), 4.18 – 4.13 (m, 4H), 4.11 – 4.07 (m, 4H), 3.84 – 3.77 (m, 8H), 3.69 (d,  $J = 1.8$  Hz, 8H).  $^{13}\text{C}$  NMR (126 MHz,  $\text{CD}_3\text{CN}$ , 298 K)  $\delta$  152.64, 149.79, 149.77, 149.72, 125.59 (q,  $J = 270.4$  Hz), 123.04 (q,  $J = 32.5$  Hz), 122.20, 122.18, 119.45 (q,  $J = 4.3$  Hz), 114.84, 114.81, 113.73, 111.12 (q,  $J = 3.6$  Hz), 71.77, 71.73, 71.67, 70.57, 70.55, 70.32, 70.22, 70.10, 69.86, 69.72, 69.70.  $^{19}\text{F}$  NMR (470 MHz,  $\text{CD}_3\text{CN}$ )  $\delta$  -61.93.

## 1.12. NMR spectra

### $^1\text{H}$ NMR spectrum of **1**

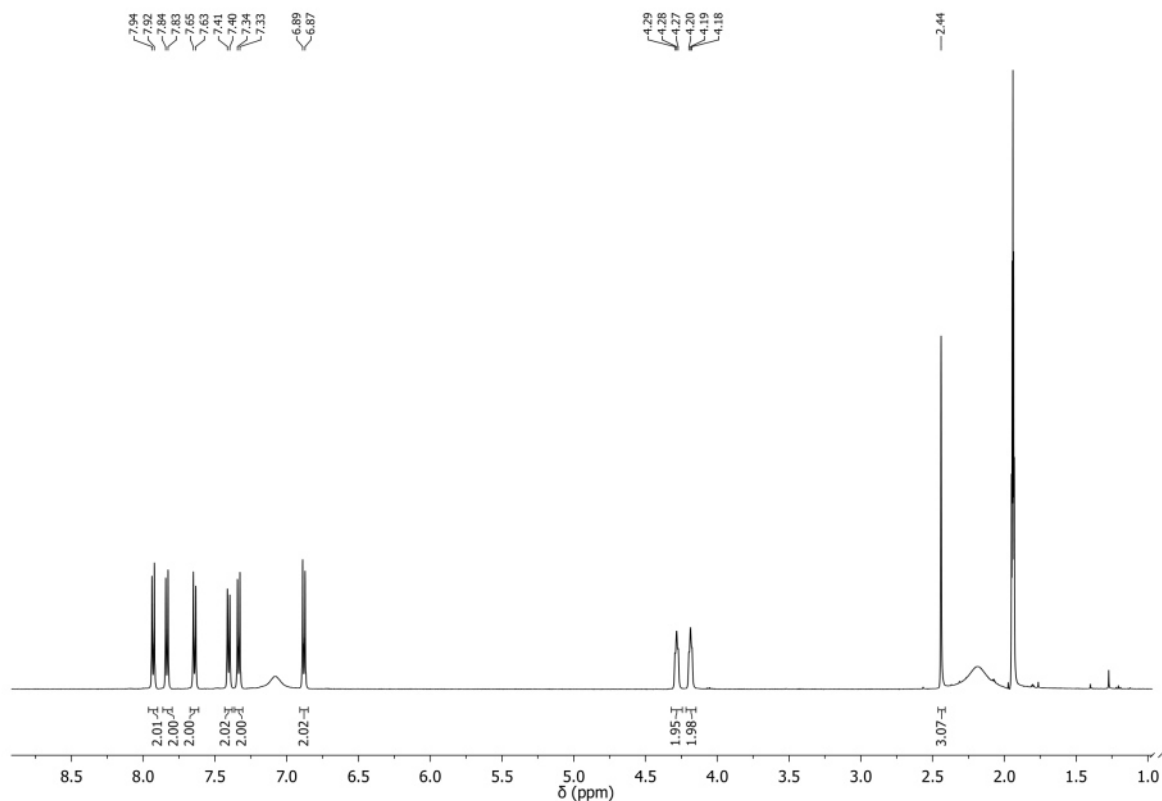


Figure 23.  $^1\text{H}$  NMR spectrum of the model compound **1** ( $\text{CD}_3\text{CN}$ , 298 K, 500 MHz).

### $^1\text{H}$ NMR and $^{19}\text{F}$ NMR resonances of the model compound **1**:

$^1\text{H}$  NMR (500 MHz,  $\text{CD}_3\text{CN}$ , 298 K)  $\delta$  7.93 (d,  $J = 8.4$  Hz, 2H), 7.83 (d,  $J = 8.3$  Hz, 2H), 7.64 (d,  $J = 8.4$  Hz, 2H), 7.40 (d,  $J = 8.2$  Hz, 2H), 7.33 (d,  $J = 8.6$  Hz, 2H), 6.88 (d,  $J = 8.6$  Hz, 2H), 4.31 – 4.26 (m, 2H), 4.19 (m, 2H), 2.44 (s, 3H).  $^{19}\text{F}$  NMR (470 MHz,  $\text{CD}_3\text{CN}$ )  $\delta$  -72.86 (d,  $J = 706.4$  Hz).

---

I am grateful to Dr. Jessica Groppi that provided the compound **1**.

# $^1\text{H}$ and $^{13}\text{C}$ NMR spectra of **2**

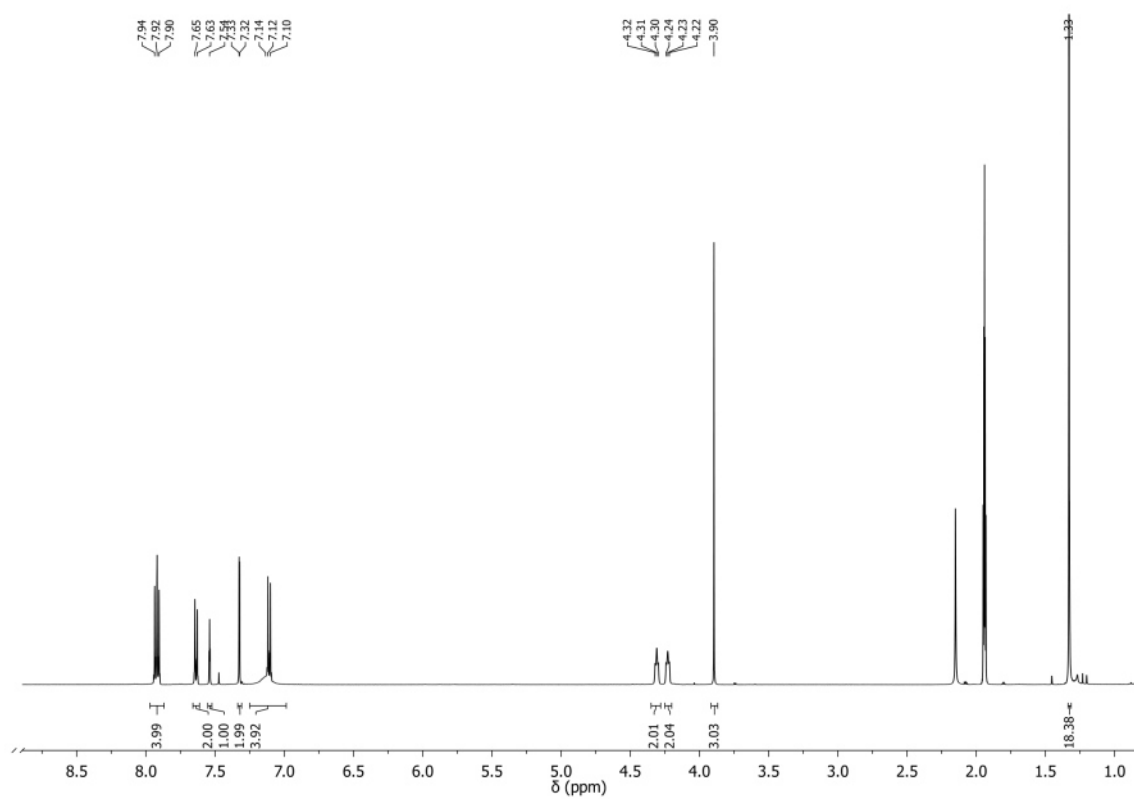


Figure 24.  $^1\text{H}$  NMR spectrum of the model compound **2** ( $\text{CD}_3\text{CN}$ , 298 K, 500 MHz).

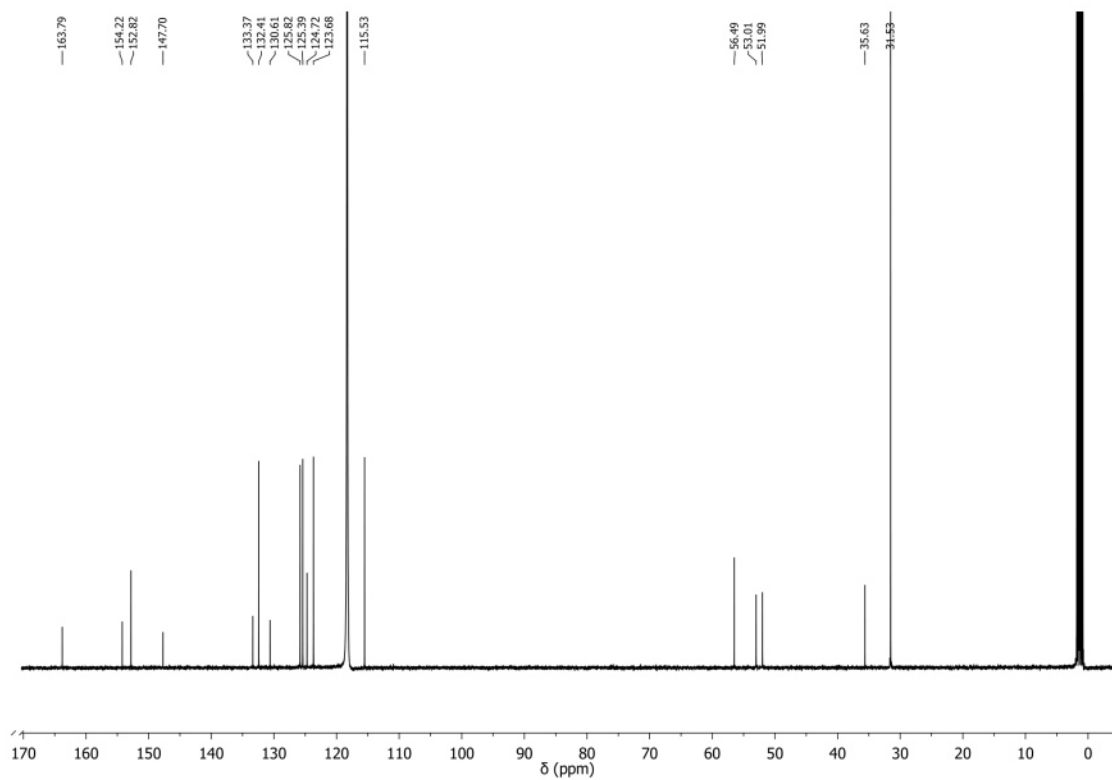


Figure 25.  $^{13}\text{C}$  NMR spectrum of the model compound **2** ( $\text{CD}_3\text{CN}$ , 298 K, 126 MHz).

# $^1\text{H}$ and $^{13}\text{C}$ NMR spectra of P1

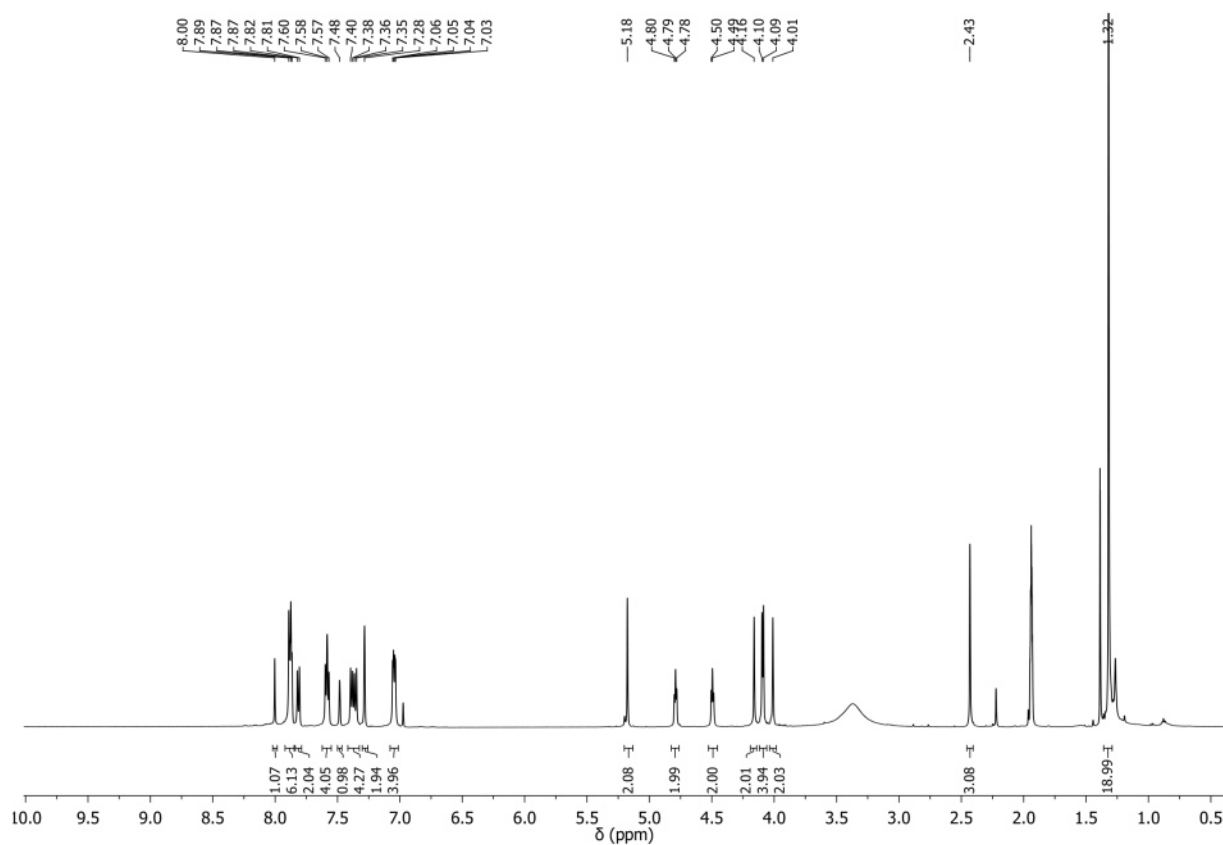


Figure 26.  $^1\text{H}$  NMR spectrum of the dimeric axle P1 ( $\text{CD}_3\text{CN}$ , 298 K, 500 MHz).

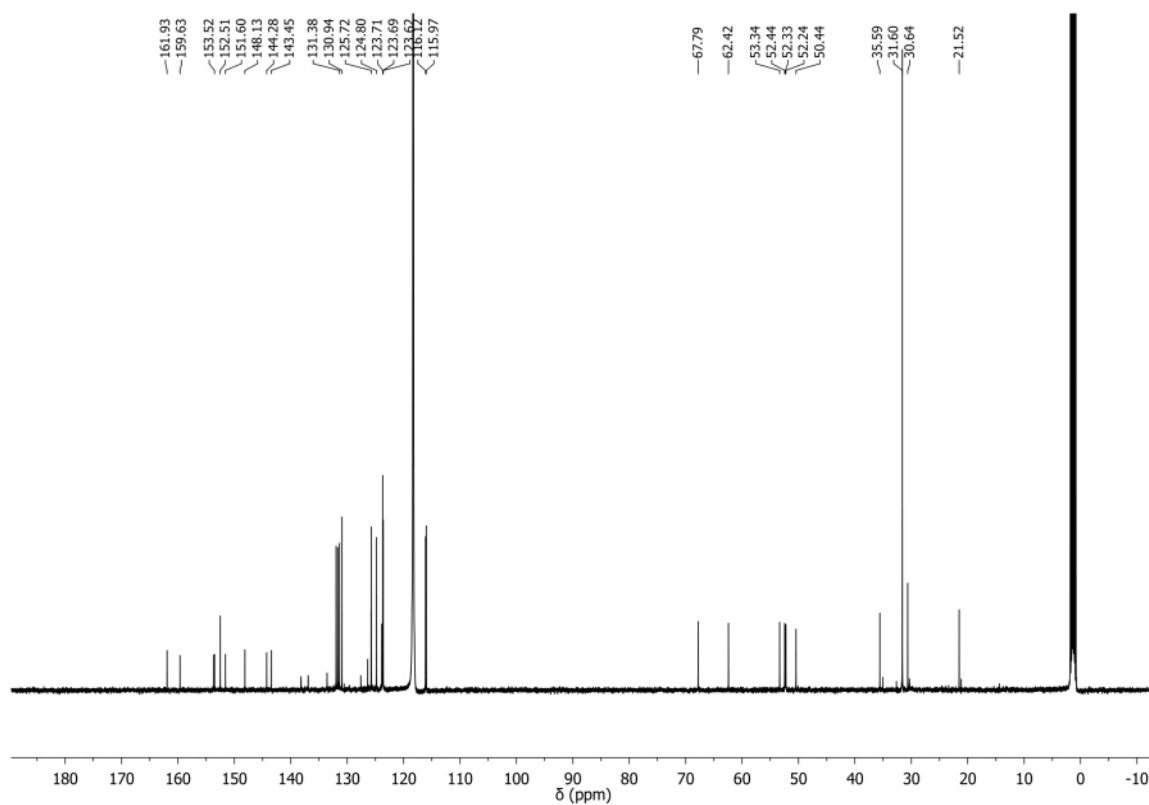


Figure 27.  $^{13}\text{C}$  NMR spectrum of the dimeric axle P1 ( $\text{CD}_3\text{CN}$ , 298 K, 126 MHz).

## HSQC and HMBC spectra of P1

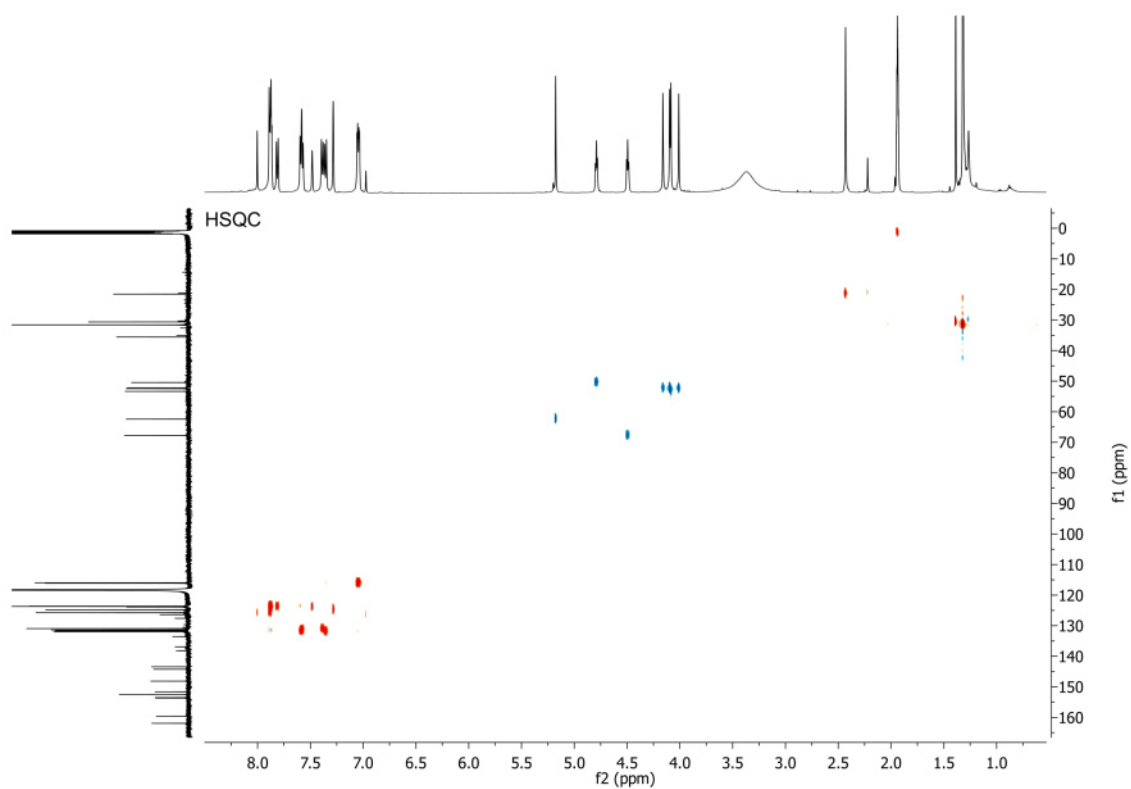


Figure 28. Heteronuclear Single Quantum coherence Spectroscopy (HSQC). P1, f1:  $^{13}\text{C}$  NMR, f2:  $^1\text{H}$  NMR, ( $\text{CD}_3\text{CN}$ , 298 K, 126 MHz, 500 MHz).

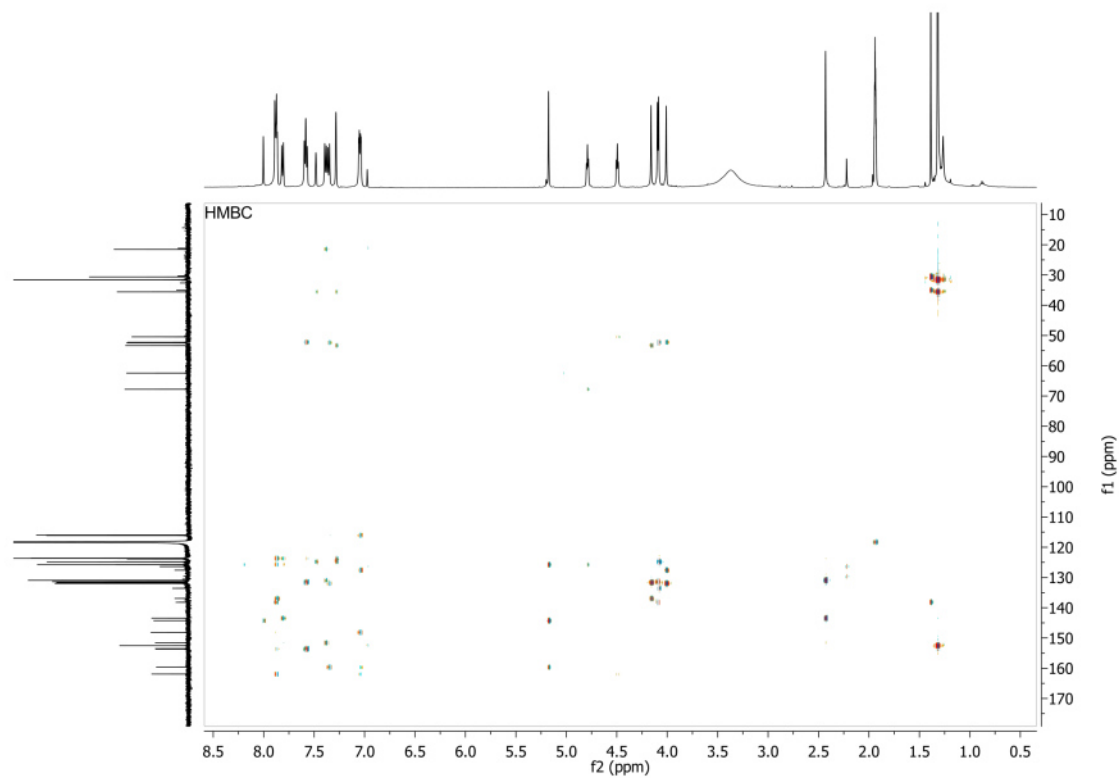


Figure 29. Heteronuclear Multiple Bond Correlation (HMBC). P1, f1:  $^{13}\text{C}$  NMR, f2:  $^1\text{H}$  NMR P1, ( $\text{CD}_3\text{CN}$ , 298 K, 126 MHz, 500 MHz).

# $^1\text{H}$ and $^{13}\text{C}$ NMR spectra of **3**

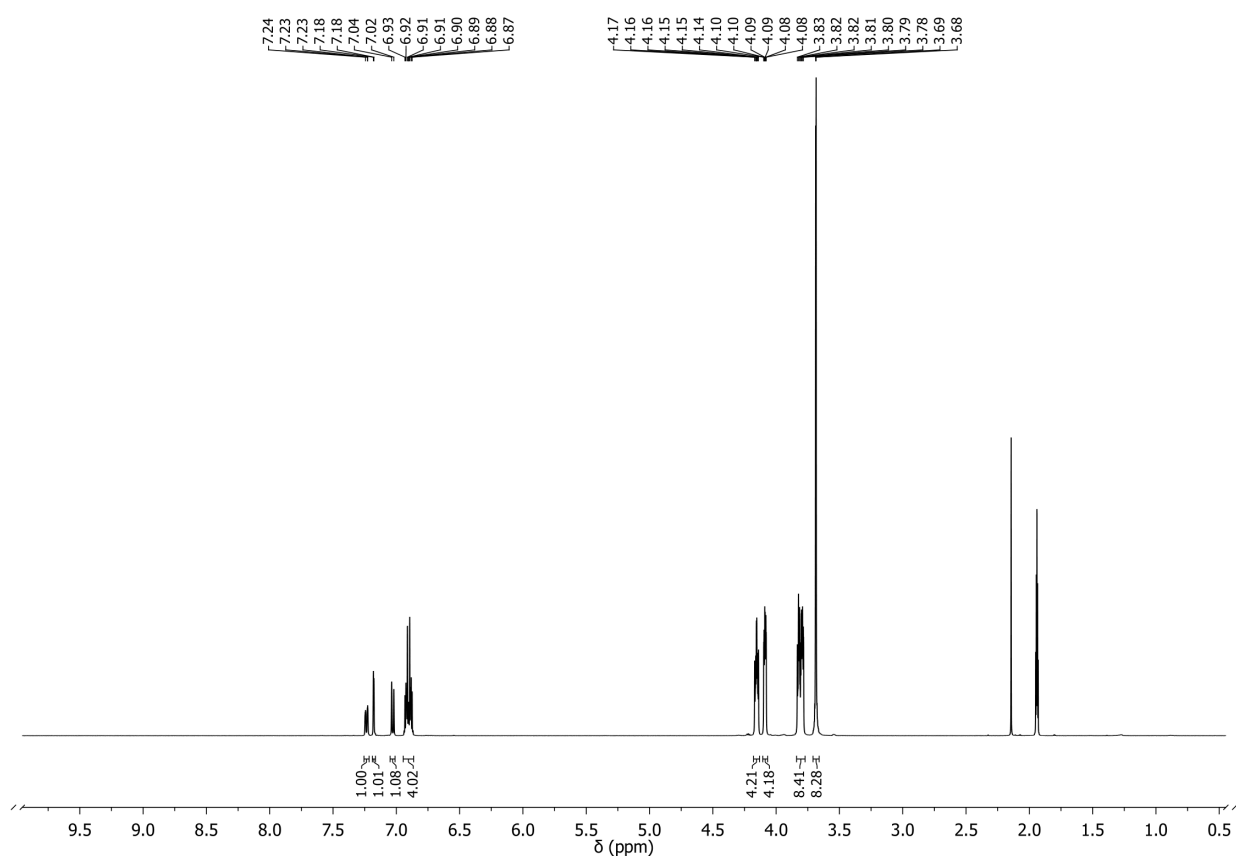


Figure 30.  $^1\text{H}$  NMR spectrum of the compound **3** ( $\text{CD}_3\text{CN}$ , 298 K, 500 MHz).

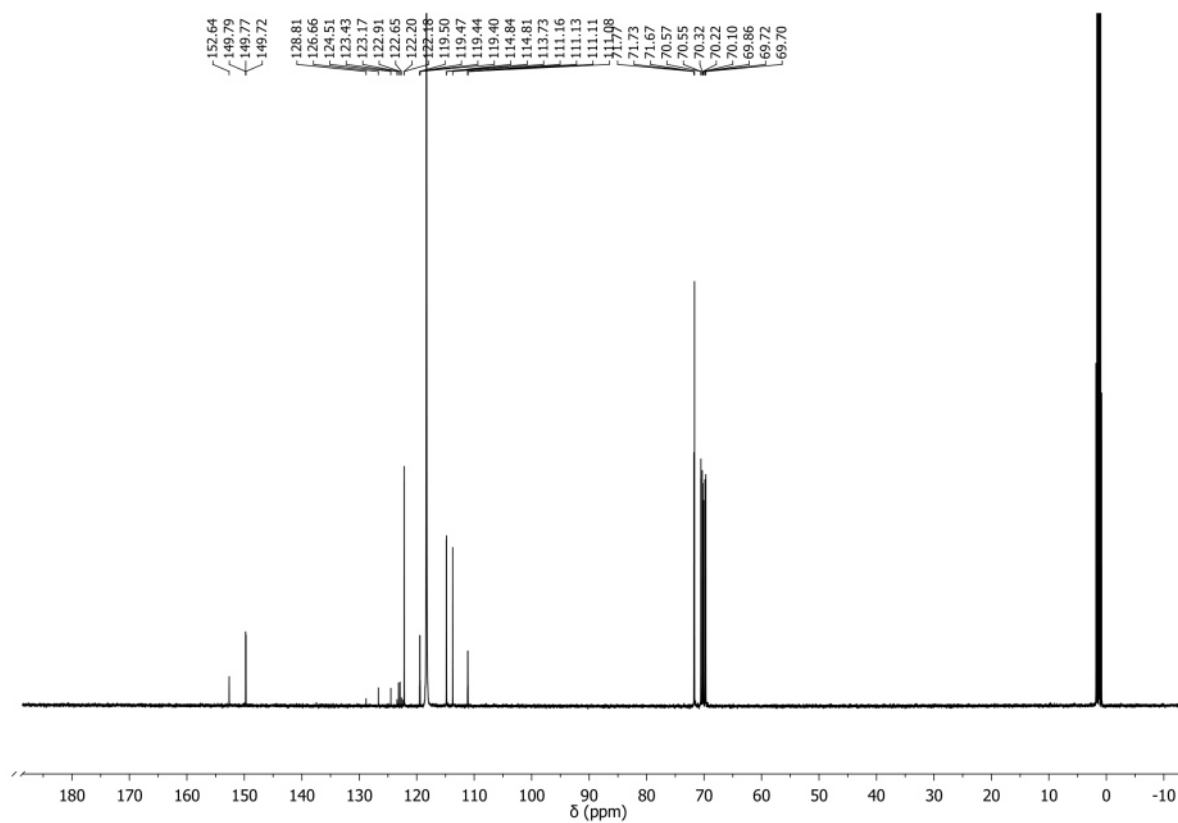


Figure 31.  $^{13}\text{C}$  NMR spectrum of the compound **3** ( $\text{CD}_3\text{CN}$ , 298 K, 500 MHz).

### $^1\text{H}$ NMR spectra of *E,Z*-1 and *E,Z*-2 complexes with 3

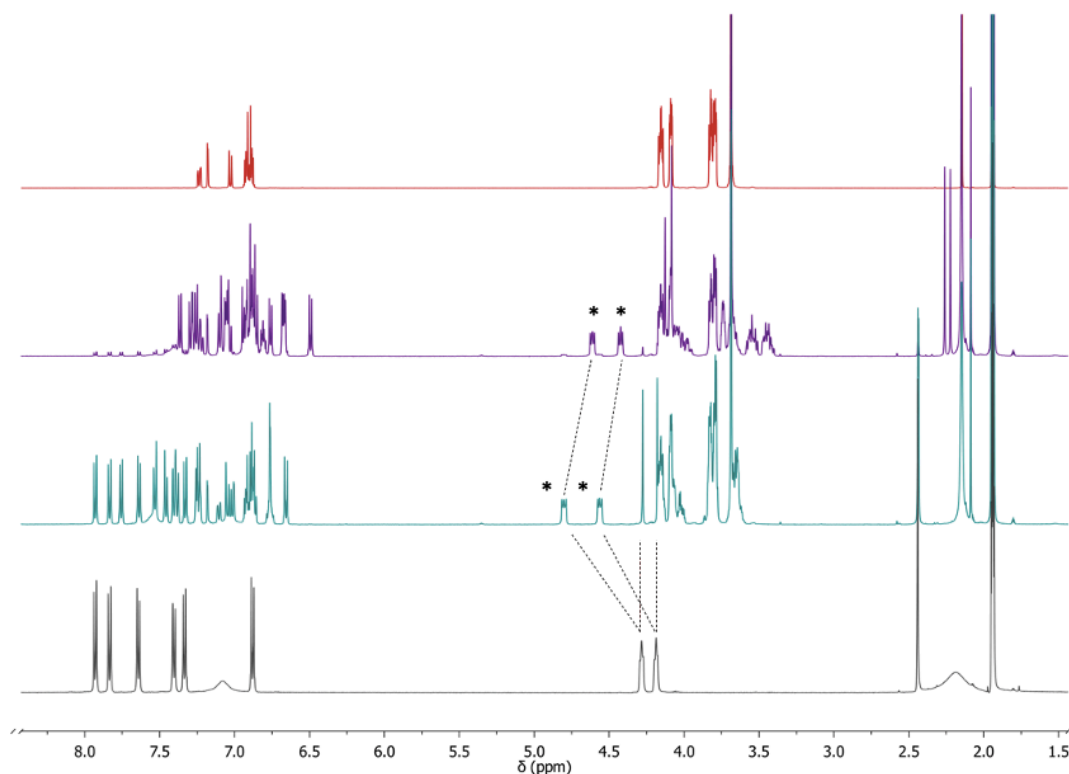


Figure 32.  $^1\text{H}$  NMR stacked spectra. Bottom: spectrum of **1**,  $[\mathbf{1}] = 5.53 \text{ mM}$ ; cyan: 1:1 mixture of *E*-**1** and **3**, the benzylic peaks univocally associated with the complex are labeled with an asterisk,  $[\mathbf{E}\text{-}\mathbf{1}]_0 = 5.3 \text{ mM}$ ; purple, the same 1:1 mixture after exhaustive irradiation ( $\lambda_{\text{irr}} = 369 \pm 10 \text{ nm}$ ) and equilibration for 30 minutes in the dark; red, spectrum of **3**. ( $\text{CD}_3\text{CN}$ , 298 K, 500 MHz).

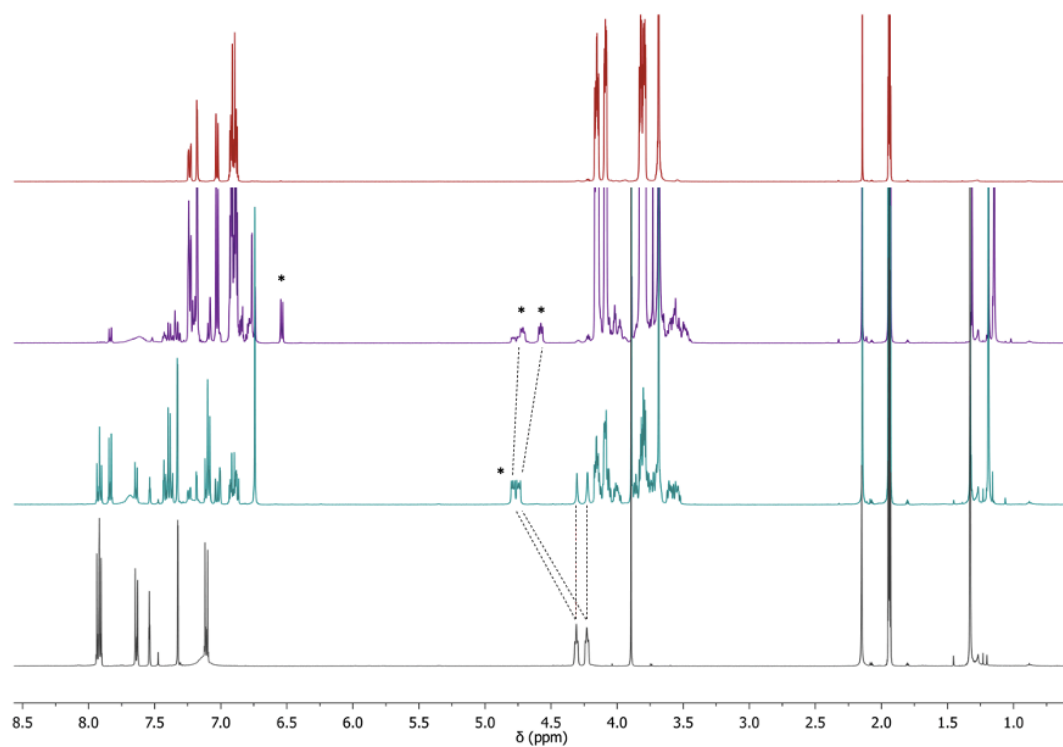


Figure 33.  $^1\text{H}$  NMR stacked spectra. Bottom: spectrum of **2**,  $[\mathbf{2}] = 5.23 \text{ mM}$ ; cyan: 1:1 mixture of *E*-**2** and **3**, the peaks univocally associated with the complex are labeled with an asterisk,  $[\mathbf{E}\text{-}\mathbf{2}]_0 = 5.23 \text{ mM}$ ; purple, mixture of *Z*-**2** obtained upon exhaustive irradiation ( $\lambda_{\text{irr}} = 365 \pm 10 \text{ nm}$ ) and **3** after 12 hours of equilibration in the dark,  $[\mathbf{E}\text{-}\mathbf{2}]_0 = 5.02 \text{ mM}$ ,  $[\mathbf{3}]_0 = 30 \text{ mM}$ ; red, spectrum of **3**. ( $\text{CD}_3\text{CN}$ , 298 K, 500 MHz).

### 1.13. References

1. Y. Qiu, Y. Feng, G. H. Guo, R. D. Astumian & J. F. Stoddart, *Chem*, **6**(8), **2020**, 1952-1977.
2. Y. Feng, M. Ovalle, J. S. Seale, C. K. Lee, D. J. Kim, R. D. Astumian & J. F. Stoddart, *J. Am. Chem. Soc.*, **2021**, *143*(15), 5569-5591.
3. E. R. Kay, D. A. Leigh & F. Zerbetto, *Angew. Chem. Int. Ed.*, **2007**, *46*(1-2), 72-191.
4. C. Cheng, P. R. McGonigal, J. F. Stoddart & R. D. Astumian, *ACS nano*, **2015**, *9*(9), 8672-8688.
5. S. Erbas-Cakmak, D. A. Leigh, C. T. McTernan & A. L. Nussbaumer, *Chem. Rev.*, **2015**, *115*(18), 10081-10206.
6. L. Zhang, V. Marcos & D. A. Leigh, *PNAS*, **2018**, *115*(38), 9397-9404.
7. M. Baroncini, S. Silvi & A. Credi, *Chem. Rev.*, **2019**, *120*(1), 200-268.
8. R. D. Astumian, C. Pezzato, Y. Feng, Y. Qiu, P. R. McGonigal, C. Cheng & J. F. Stoddart, *Mater. Chem.*, **2020**, *4*(5), 1304-1314.
9. A. I. Brown, & D. A. Sivak, *Chem. Rev.*, **2019**, *120*(1), 434-459.
10. C. Cheng et al. *Nat. Nanotechnol.*, **2015**, *10*, 547-553. 12.
11. C. Pezzato et al. *Angew. Chem. Int. Ed.*, **2018**, *57*, 9325-9329.
12. G. Steinberg-Yfrach et al. *Nature*, **1997**, *385*, 239-241.
13. I. M. Bennett, et al. *Nature*, **2002**, *420*, 398-401.
14. S. Bhosale et al., *Science*, **2006**, *313*, 84-86 (2006).
15. V. Serreli, C.-F. Lee, E. R. Kay & D. A. Leigh, *Nature*, **2007**, *445*, 523-527.
16. M. Baroncini, S. Silvi, M. Venturi & A. Credi, *Angew. Chem. Int. Ed.*, **2012**, *51*, 4223-4226.
17. G. Ragazzon, M. Baroncini, S. Silvi, M. Venturi & A. Credi, *Nat. Nanotechnol.*, **2015**, *10*, 70-75.
18. M. Canton, J. Groppi, L. Casimiro, S. Corrà, M. Baroncini, S. Silvi & A. Credi, *J. Am. Chem. Soc.*, **2012**, *143*(29), 10890-10894.
19. S. Erbas-Cakmak et al., *Science*, **2017**, *358*, 340-343.
20. S. Amano, S. D. Fielden & D. A. Leigh, *Nature*, **2021**, *594*(7864), 529-534.
21. M. Baroncini, S. Silvi, M. Venturi & A. Credi, *Chem. Eur. J.*, **2010**, *16*(38), 11580-11587.

22. P. R. Ashton, I. Baxter, M. C. Fyfe, F. M. Raymo, N. Spencer, J. F. Stoddart, J. P. White & D. J. Williams, *J. Am. Chem. Soc.*, **1998**, *120*(10), 2297-2307.
23. R. D. Astumian, *Nature Nanotechnol.*, **2012**, *7*, 684–688.
24. C. Schäfer, G. Ragazzon, B. Colasson, M. La Rosa, S. Silvi & A. Credi, *ChemistryOpen*, **2016**, *5*(2), 120.
25. J. S. Shin & N. A. Pierce, *J. Am. Chem. Soc.*, **2004**, *126*(35), 10834-10835.
26. M. von Delius & D. A. Leigh, *Chem. Soc. Rev.*, **2011**, *40*(7), 3656-3676.
27. J. Wang & B. L. Feringa, *Science*, **2011**, *331*(6023), 1429-1432.
28. B. Lewandowski, G. De Bo, J. W. Ward, M. Pappmeyer, S. Kuschel, M. J. Aldegunde, P. M. E. Gramlich, D. Heckmann, S. M. Goldup & Leigh, D. A. (2013), *Science*, **2013**, *339*(6116), 189-193.
29. G. Li, G. Fuks, E. Moulin, M. Maaloum, M. Rawiso, I. Kulic, J. T. Foy & N. Giuseppone, *Nat. Nanotechnol.*, **2015**, *10*(2), 161-165.
30. D. S. Goodsell, *Bionanotechnology: lessons from nature*. 2004, John Wiley & Sons.
31. M. Schliwa & G. Woehlke, *Nature*, **2003**, *422*(6933), 759-765.
32. O. I. Paynter, D. J. Simmonds & M. C. Whiting, *J. Chem. Soc. Chem. Comm.*, **1982**, *20*, 1165-1166.
33. S. Binauld, D. Damiron, L. A. Connal, C. J. Hawker & E. Drockenmuller, *Macromol. Rap. Commun.*, **2011**, *32*(2), 147-168.
34. Company web site: <https://thalesnano.com/products-and-services/h-cube-pro/>
35. E. Merino, *Chem. Soc. Rev.*, **2011**, *40*(7), 3835-3853.
36. B. R. Langlois, E. Laurent & N. Roidot, *Tetrahedron Lett.*, **1991**, *32*(51), 7525-7528.
37. F. Nicoli, M. Baroncini, S. Silvi, J. Groppi & A. Credi, *Org. Chem. Front.*, **2021**, *8*(19), 5531-5549.
38. a) B. R. Langlois, Once Upon a Time Was the Langlois' Reagent: A “Sleeping Beauty”. In *Modern Synthesis Processes and Reactivity of Fluorinated Compounds* (pp. 125-140). **2017**, Elsevier. b) A. Studer, *Angew. Chem. Int. Ed.*, **2012**, *51*(36), 8950-8958.
39. Y. Ji, T. Brueckl, R. D. Baxter, Y. Fujiwara, I. B. Seiple, S. Su, D. G. Blackmond & P. S. Baran, *PNAS*, **2011**, *108*(35), 14411-14415.
40. D. E. Yerien, A. Postigo, M. Baroncini, & S. Barata-Vallejo, *Curr. Green Chem.*, **2021**, *23*(20), 8147-8153.
41. M. Curcio, F. Nicoli, E. Paltrinieri, E. Fois, G. Tabacchi, L. Cavallo, S. Silvi, M. Baroncini & A. Credi, *J. Am. Chem. Soc.*, **2021**, *143*(21), 8046-8055.

42. T. D. Claridge, *High-resolution NMR techniques in organic chemistry* (Vol. 27), 2016, Elsevier.
43. a) C. Feldmeier, H. Bartling, E. Riedle, R. M. Gschwind, *J. Magn. Reson.* **2013**, *232*, 39-44; b) P. Nitschke, N. Lokesh, R. M. Gschwind, *Prog. Nucl. Magn. Reson. Spectrosc.* **2019**, *114*, 86-134.
44. S. Corrà, L. Casimiro, M. Baroncini, J. Groppi, M. La Rosa, M. T. Bakić, S. Silvi & A. Credi, *Chemistry*, **2021**, *27*(43), 11076.
45. H. Rau, *Photochromism: Molecules and Systems*, Elsevier, Amsterdam, revised edn, 2003.
46. a) J. C. Andrew, C. S. Wilcox *J. Am. Chem. Soc.* **1991**, *113*, 678-680; b) K. Connors, *Binding Constants: The Measurement of Molecular Complex Stability*, Wiley-Interscience, New York, **1987**, Ch. 5, pp. 189-212.
47. C. P. Rosenau, B. J. Jelier, A. D. Gossert & A. Togni, *Angew. Chem. Int. Ed.*, **2018**, *57*(30), 9528-9533.
48. a) von M. Smoluchowski, *M. Phys. Z.* **1912**, *13*, 1069-1080. (b) von M. Smoluchowski; Planck, M., Ed.; Teubner und Leipzig: Berlin, 1914; pp 89-121
49. a) J. C. Maxwell, *Letter to P. G. Tait, 11 December 1867*. Quoted in Knott, C. G. *Life and Scientific Work of Peter Guthrie Tait*; Cambridge University Press: London, 1911; pp 213-214. b) J. C. Maxwell, *Theory of Heat*; Longmans, Green and Co.: London, 1871; Chapter 12.
50. M. N. Chatterjee, E. R. Kay & D. A. Leigh, *J. Am. Chem. Soc.*, **2006**, *128*(12), 4058-4073.
51. M. Baroncini, L. Casimiro, C. De Vet, J. Groppi, S. Silvi & A. Credi, *ChemistryOpen*, **2018**, *7*(2), 169.

**Chapter 2:** *Synthesis and operation of a [2]rotaxane endowed with a novel photoactive recognition site.*

## 2.1. Introduction

From the pioneering work of Stoddart and coworkers on bistable rotaxane based on pH switchable recognition sites and bi-pyridinium secondary stations,<sup>1</sup> a myriad of pH controlled rotaxanes were reported<sup>2</sup> thanks to the simplicity of their synthesis and operation.<sup>3</sup> The area of application of these compounds is wide and ranges from catalysis<sup>4-5</sup> to the construction of artificial muscles.<sup>6-7</sup>

In rotaxanes composed by dibenzo-24-crown-8 (DB24C8) macrocycle and endowed with an ammonium recognition site, the latter is commonly defined as a “stronger” station compared to a secondary ammonium site such as N-methyl triazolium,<sup>8</sup> bi-pyridinium,<sup>9</sup> or imidazolium;<sup>10</sup> hence, it is generally assumed that the ring translation on the second recognition site occurs only upon deactivation (employing a base) of the ammonium site.

However, this simplification is often misleading, since most of the time, the macrocycle actually shuttles between the different stations, populating each one of them in reason of their relative binding strength. Indeed, it is more accurate to define a thermodynamically stable co-conformation (SCC) and a metastable co-conformation (MCC)<sup>11</sup> as the translational isomers in which, respectively, the ring encircles either the stronger or weaker binding station. The statistical distribution of the SCC and MCC populations depends on the shuttling between the two stations, therefore on the relative affinity of the macrocycles for them. The existence of an equilibrium between the SCC and MCC is the reason for the apparent acidity measured in rotaxanes<sup>12</sup> and catenanes.<sup>13</sup> In other words, in a MIM the  $pK_a$  of an ammonium site strongly depends on the affinity of the ring for an eventual secondary station, indeed the apparent acidity of the ammonium site would be drastically lowered in absence of the latter.<sup>14</sup> A practical example is represented by a recent work<sup>15</sup> in which the  $pK_a$  of a [2]rotaxane ammonium site was modulated by modifying the affinity of the ring component for a secondary station (bi-pyridinium unit). In this example, upon reduction of the bi-pyridinium unit the interaction with the crown ether is weakened and the  $pK_a$  of the primary ammonium station of the rotaxane is increased by seven units.

### 2.1.1. Objective of the project

In this chapter is described the synthesis and investigation of a [2]rotaxane designed with the aim of modifying the acid/base properties of an ammonium station installed in its linear component using light energy. For this purpose it was devised a simple [2]rotaxane composed by a pH sensitive ammonium station and a weaker photoactive station based on an azo chromophore. It was envisaged that a difference in the affinity of the macrocycle for the two isomeric forms (*E*, *Z*) of the secondary station could be reflected in the apparent  $pK_a$  of the ammonium site. This rotaxane is interesting for the construction of molecular machines able to respond to light stimuli.<sup>16,17</sup> This energy source has the advantage<sup>18,19</sup> that no waste products are accumulated in the medium. Moreover, the energy of the irradiation provided can be finely controlled. These characteristics are attractive for several applications in technology and medicine<sup>20-23</sup> as well as in the field of energy conversion.<sup>24</sup>

### 2.1.2. *E*-1H<sup>2+</sup> rotaxane

[2]rotaxane *E*-1H<sup>2+</sup> (Figure 1) is composed by a DB24C8 ring and is endowed with two stations: a dibenzyl ammonium recognition site, and a novel photoactive 2-phenyl azoimidazolium station (*cyan* in Figure 1). Even though the imidazolium cation has already been explored as a constituent in rotaxanes,<sup>10</sup> 2-phenylazoimidazolium has only been investigated in fields such as photoresponsive drugs<sup>25</sup> and light-effected ionic liquids.<sup>26,27</sup> The introduction of this new photochromic station in MIMs opens the possibility for new and more complex interlocked architectures whose photoresponsivity can be controlled on command.

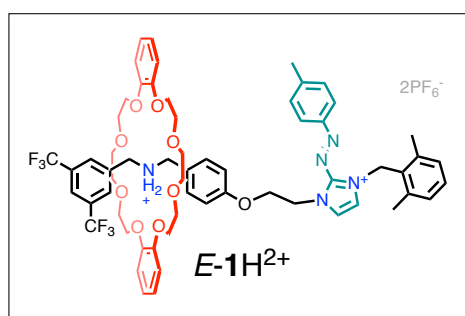


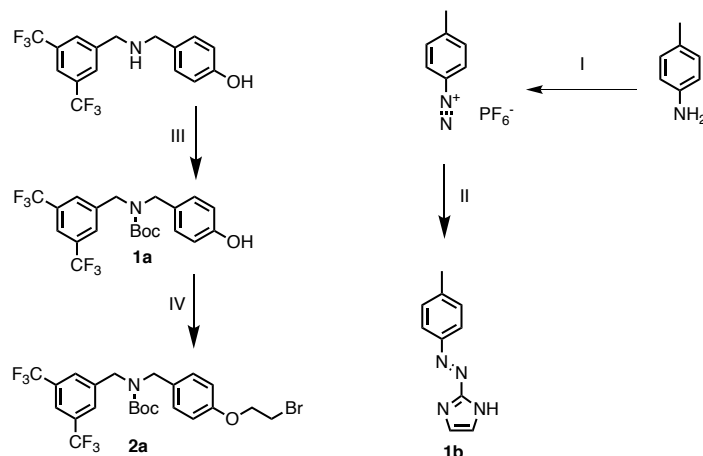
Figure 1. Chemical structure of the synthesized [2]rotaxane.

Rotaxane *E*-1H<sup>2+</sup> responds to different stimuli: the ammonium site can be deactivated through the addition of a base, while the azoimidazolium moiety can be cleanly photo-isomerized from *E* → *Z* by employing UV light.

This work is the fruit of the collaboration between different members of the research group in which I work and my main contribution was relative to the design and ideation of this new [2]rotaxane. In particular, my efforts were addressed to the synthesis, characterization, and NMR irradiation experiments that were performed together with Erica Paltrinieri and Dr. Massimiliano Curcio. The UV visible experiments described in the last part of the chapter were performed by Dr. Marina Tranfić Bakić. I am particularly grateful to all of them.

## 2.2. Synthesis of $E-1H^{2+}$

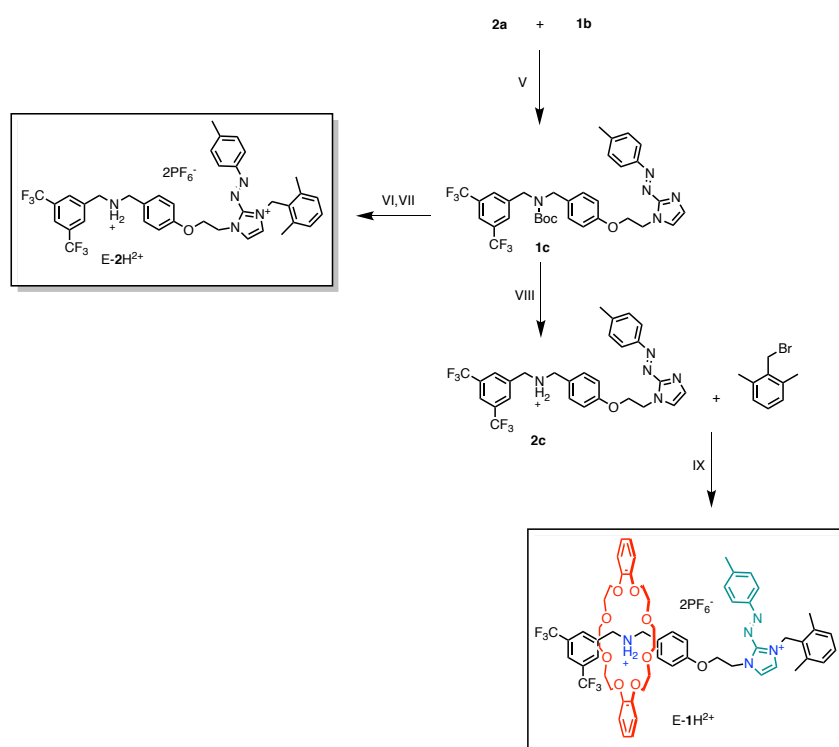
### 2.2.1. Synthesis of the recognition sites precursors



Scheme 1. Synthetic route to the compounds **2a** and **1b**. I)  $HPF_6$ ,  $NaNO_2$ ,  $H_2O$ , 0-20 °C II) Imidazole,  $K_2CO_3$ ,  $H_2O$ , 0-20 °C. 23% III)  $Boc_2O$ , THF. 87% IV)  $BrCH_2CH_2Br$ ,  $K_2CO_3$ , MeCN. 45%

In Scheme 1 are reported the synthetic steps to afford **2a** and **1b**, which are respectively the precursors of the  $E-1H^{2+}$  ammonium and the azoimidazolium stations. The preparation of the 2-phenyl azoimidazole **1b** was adapted from a reported procedure,<sup>28</sup> the diazotization of imidazole is achieved through the reaction with 4-methylbenzene diazonium hexafluorophosphate in basic aqueous medium (II). The poor yield of the isolated compound (23%) was due to the workup and purification procedures (see experimental section for details). This problem was compensated by the availability of the starting materials (imidazole and toluidine). Compound **1a** was afforded in two steps: a reductive amination reaction followed by protection of the dibenzylamine moiety with *tert*-butoxycarbonyl group (Boc) resulting in a 67% total yield of isolated compound. Nucleophilic substitution of the phenyl hydroxy moiety of **1a** with dibromoethane (IV) afforded compound **2a**.

## 2.2.2. Synthesis of $E\text{-1H}^{2+}$ and model compound **2**



Scheme 2. V)  $\text{K}_2\text{CO}_3$ ,  $\text{CH}_3\text{CN}$ , reflux. 63% VI)  $o\text{-Me}_2\text{-BnBr}$ ,  $\text{CH}_3\text{CN}$ , reflux. 93% VII)  $\text{HPF}_6$ ,  $\text{THF}$ . 41% VIII)  $\text{HPF}_6$ ,  $\text{THF}$ . 52% IX)  $\text{DB24C8}$ ,  $o\text{-Me}_2\text{-BnBr}$ , microwave reactor,  $\text{CH}_3\text{CN}$ ,  $80^\circ\text{C}$ . 65%.

A convergent synthetic strategy was employed for the synthesis of  $E\text{-1H}^+$  and of the “free” axle  $E\text{-2H}^{2+}$  (Scheme 2). Phenylazoimidazole **1b** was reacted in refluxing  $\text{CH}_3\text{CN}$  with compound **2a** in the presence of potassium carbonate ( $\text{K}_2\text{CO}_3$ ) to afford product **1c** in 63% yield. Intermediate **1c** was used for the synthesis of model axle  $E\text{-2H}^{2+}$ . This compound was prepared through the substitution of azoimidazole with 2,6-dimethylbenzyl bromide followed by deprotection with a solution of hexafluorophosphoric acid to yield the corresponding dibenzylammonium salt. Compound **2c** was prepared in a similar fashion by deprotection and subsequent salification reaction. For the synthesis of the rotaxane, the hexafluorophosphate salt of **2c** was complexed with DB24C8 in  $\text{CH}_3\text{CN}$  and reacted with bulky 2,6 dimethylbenzyl bromide in a microwave reactor to obtain a relatively high yield (60%). The *stopping* reaction was achieved by exploiting the pyridine-like<sup>29</sup> behavior of the azoimidazolium moiety, conveniently, together with *stopping* the cationic azoimidazolium recognition site was formed.

### 2.3. $^1\text{H}$ NMR characterization of $E\text{-}1\text{H}^{2+}$

The resonances of the proton and carbon nuclei of compound  $E\text{-}1\text{H}^{2+}$  were assigned through a combination of 1D and 2D NMR experiments ( $^{13}\text{C}$ -NMR, HSQC, HMBC can be found in the experimental section paragraph 2.11). The  $^1\text{H}$ -NMR spectrum in  $\text{CD}_3\text{CN}$  at 298 K is reported in Figure 2.

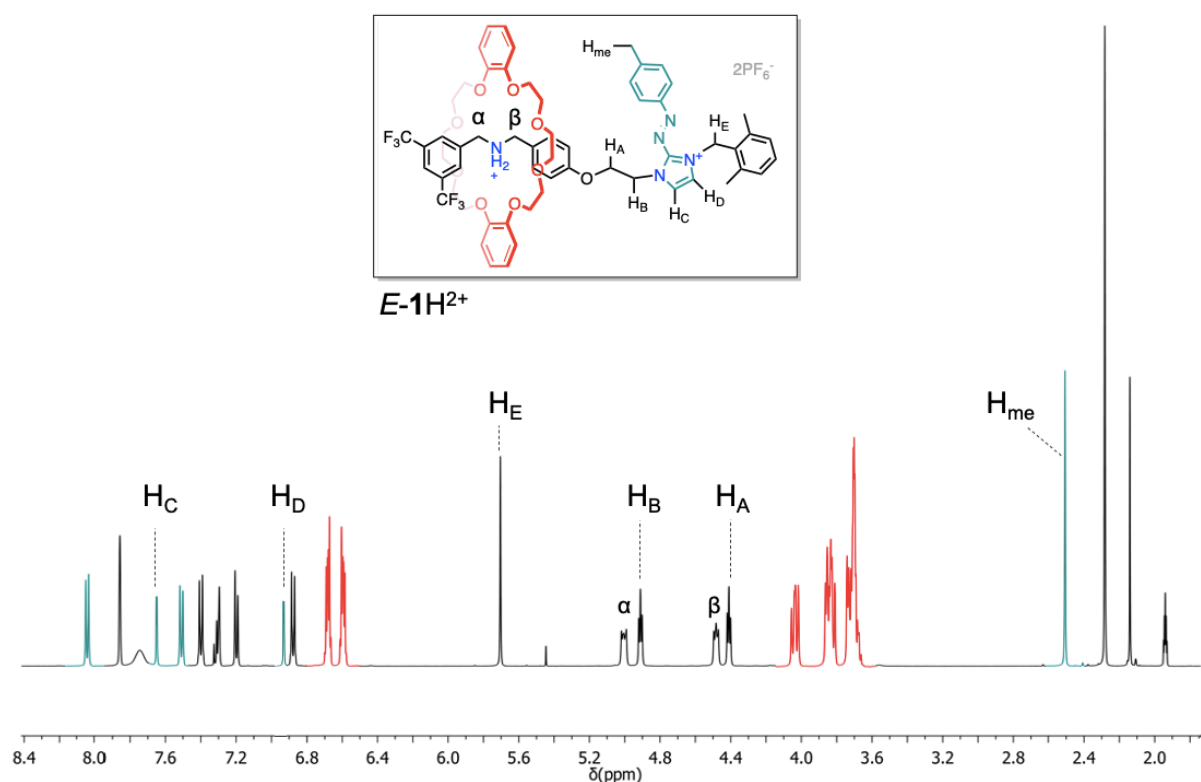


Figure 2.  $^1\text{H}$ -NMR of the compound  $E\text{-}1\text{H}^{2+}$  in  $\text{CD}_3\text{CN}$ , 298 K, 500 MHz.

The peaks colored in red belong to the interlocked DB24C8 macrocycle. In more detail the resonances around 6.63 ppm are attributed to the aromatic moieties while the three series of multiplets from 4 to 3.6 ppm are assigned to the resonances of the glycolic chains. The peaks in cyan belong to the phenylazoimidazolium unit, in particular, the heterocycle resonances are labeled as  $\text{H}_\text{C}$  (7.65 ppm) and  $\text{H}_\text{D}$  (6.93 ppm). For the study of the photochromic unit isomerization, it was fundamental to have clear diagnostic signals in the spectrum, the methyl peak  $\text{H}_\text{me}$  (2.51 ppm) in *para* position with respect to the azo group is particularly useful in this purpose.

The ammonium station interacts through strong hydrogen bonds with the crown ether, this interaction causes the benzylic proton alpha (5.01 ppm) and beta (4.48 ppm) to assume a peculiar multiplicity.<sup>12,30</sup> Moreover, the resonances of these peaks result to be deshielded by

the presence of the ring on the adjacent ammonium site. The triplets  $H_A$  (4.41 ppm) and  $H_B$  (4.91 ppm) belong to the ethylene “bridge” that connects the two recognition sites. These signals were useful to study the localization of the ring in the acid/base switching studies. To conclude, the peak labeled as  $H_E$  (5.70 ppm) belongs to the methylene benzylic protons of the stopper placed on the azoimidazolium side.

## 2.4. Study of the acid/base switching

Due to the presence of an acid/base switchable ammonium recognition site, the rotaxane  $E-1H^{2+}$  can be treated with a base to afford the deprotonated form  $E-1^+$ . The changes induced by deprotonation were investigated by  $^1H$ -NMR spectrometry (Figure 3).

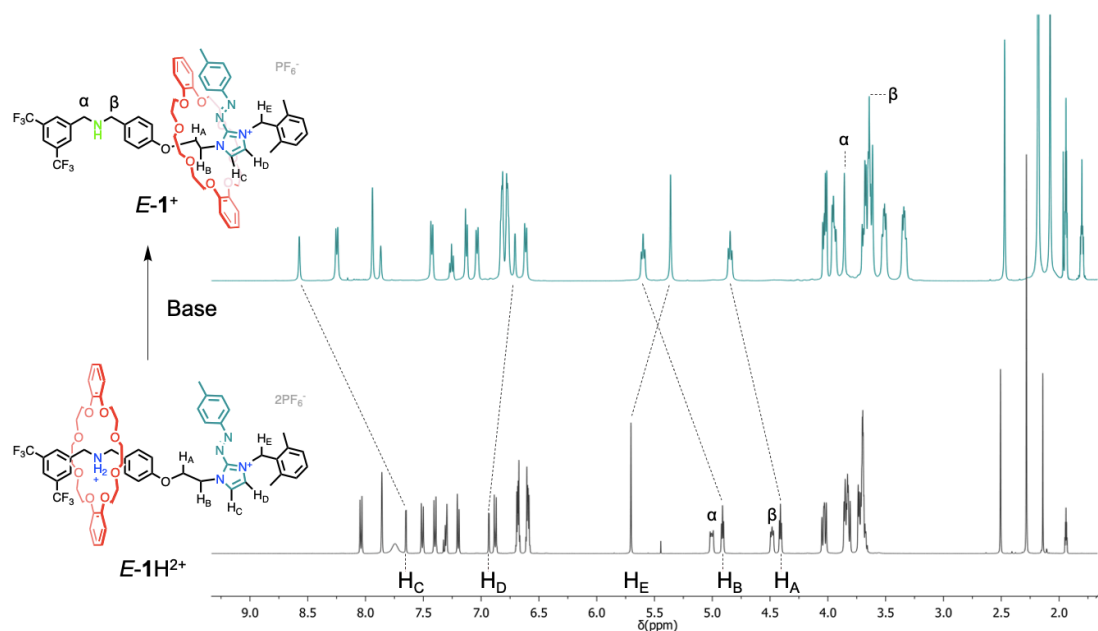


Figure 3.  $^1H$  NMR stacked spectra: bottom,  $E-1H^{2+}$ ; top,  $E-1^+$  obtained upon deprotonation.  $CD_3CN$ , 298 K, 500 MHz.

To achieve the deprotonation of  $E-1H^{2+}$ , a sample was dissolved in  $CD_3CN$  and an heterogeneous base, composed by a polymer bound 1,8-diazabicyclo[5.4.0]undec-7-ene, was directly added to the NMR tube. The deprotonation process was followed by NMR and the supported base was filtered off when the rotaxane resulted to be completely deprotonated. The spectrum of  $E-1^+$  results to be markedly different from the one of the starting dicationic rotaxane. The resonances of the ethylene bridge nuclei next to the azoimidazolium station are clearly deshielded ( $H_A$ ,  $H_B$  Figure 3). An analogous lower field shift is observed for the imidazolium peak  $H_C$  while the benzylic signal of the stopper  $H_E$  and the imidazolium resonance  $H_D$  are shielded. These changes can be interpreted as the translation of the DB24C8 from the dibenzylamine site to the azoimidazolium station. This latter co-conformation is predominant since the hydrogen bonding interactions of the crown ether with the benzylamine site in  $E-1^+$  is much weaker than the ones present in  $E-1H^{2+}$ . This is also the reason that determines a shielding of the  $\alpha$  and  $\beta$  benzylic signals in the deprotonated rotaxane, in which the two resonances are partially overlapped to the signals of the glycol chains of the crown ether ring.

## 2.5. Irradiation experiments

### 2.5.1. $^1\text{H}$ NMR photoisomerization study

In Figure 4 are reported the spectra of  $E\text{-}1\text{H}^{2+}$  recorded in the dark and after irradiation with UV light to yield  $Z\text{-}1\text{H}^{2+}$ . In rotaxane  $Z\text{-}1\text{H}^{2+}$  the resonances of the photochromic unit are shielded compared to those recorded for the  $E$  isomer. This effect can be noted for the imidazole nuclei  $\text{H}_\text{C}$ ,  $\text{H}_\text{D}$  and for the methyl group  $\text{H}_\text{me}$ . A remarkable high-field shift is observed for the signals of the protons adjacent to the photochromic unit such as  $\text{H}_\text{B}$  and  $\text{H}_\text{E}$  (Figure 4), most likely because the chemical shift of these nuclei is influenced by the ring current of the azoimidazolium phenyl moiety.

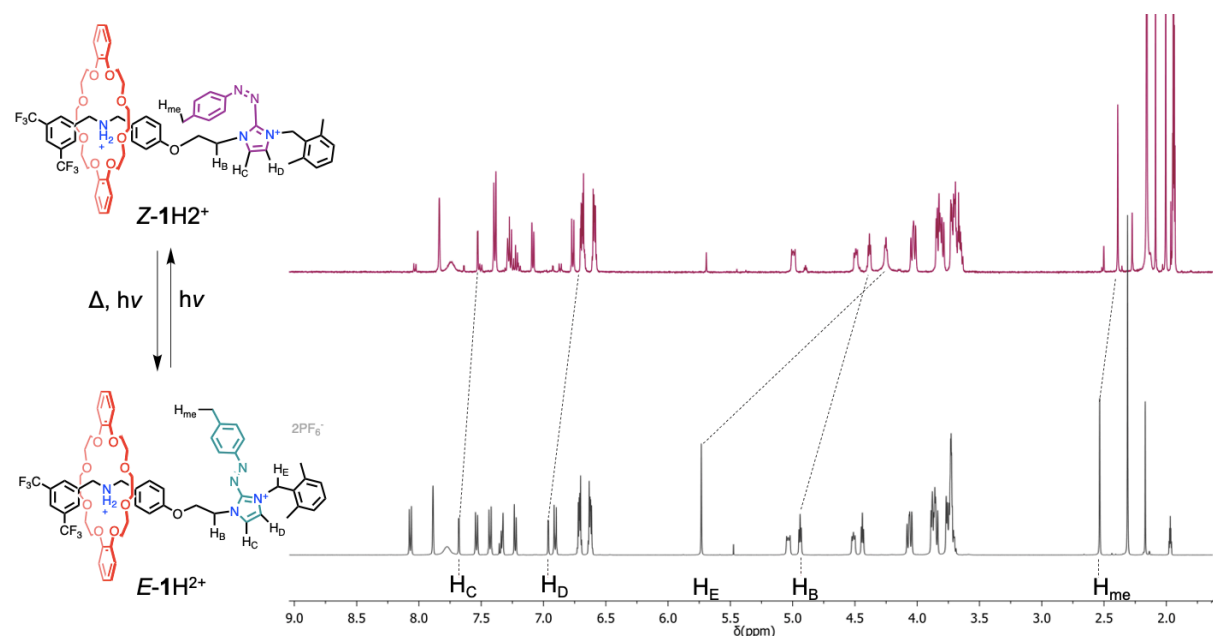


Figure 4. Bottom:  $^1\text{H}$  NMR spectrum of  $E\text{-}1\text{H}^{2+}$ ; Top: the same compound after irradiation ( $\lambda_{\text{irr}}=369 \pm 10 \text{ nm}$ ) at the PSS ( $E\text{-}1\text{H}^{2+}/Z\text{-}1\text{H}^{2+}$  91:9).  $\text{CD}_3\text{CN}$ , 298 K, 500 MHz.

The methyl signal was particularly useful to quantitatively follow the photoisomerization process. The irradiation experiments were performed by  $^1\text{H}$ -NMR adopting an experimental setup described by Gschwind and coworker.<sup>31</sup> The light of a LED source ( $\lambda_{\text{irr}} = 369 \pm 10 \text{ nm}$ ) was transported through a quartz optical fiber directly to the NMR tube containing a solution of the sample dissolved in air equilibrated  $\text{CD}_3\text{CN}$ . In Figure 5 are reported the time dependent variation of the  $\text{H}_\text{me}$  resonance integrals belonging to the  $E$  and  $Z$  isomers. The *magenta* trace represents the amount of the  $Z\text{-}1\text{H}^{2+}$  isomer while the *grey* trace is indicative of  $E\text{-}1\text{H}^{2+}$ . The

$E \rightarrow Z$  photoisomerization of  $E\text{-1H}^{2+}$  was completed in about 3 hours (Figure 5, *left*). Remarkably, at the photostationary state (PSS) the mixture was composed by 91 % of the  $Z$  isomer. The irradiated solution of the rotaxane was left in the dark, to follow the thermal  $Z \rightarrow E$  back isomerization reaction (Figure 5, *right*), which provided the  $E$  isomer quantitatively proving that no irreversible side photoreactions occurred during the irradiation.

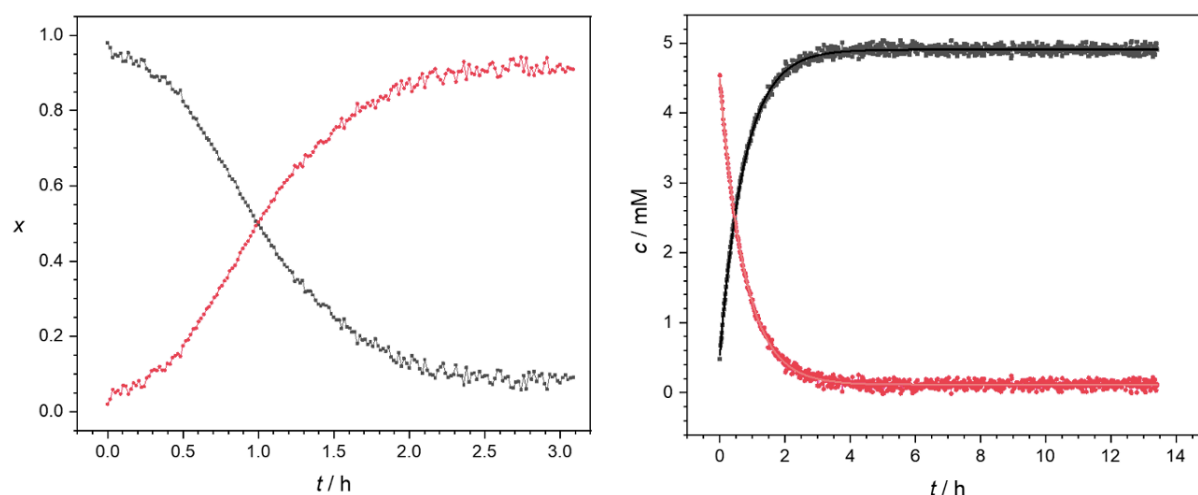


Figure 5. Left:  $\chi$  = molar fractions, kinetic profile of  $E \rightarrow Z$  photoisomerization process of  $E\text{-1H}^{2+}$  ( $\lambda_{\text{irr}} = 369 \pm 10$  nm), right: thermal back  $Z \rightarrow E$  isomerization process of  $Z\text{-1H}^{2+}$ . In both graphs, traces: magenta,  $Z$  isomer; grey,  $E$  isomer. Data obtained from  $^1\text{H-NMR}$  experiment,  $\text{CD}_3\text{CN}$ , 298K, 500 MHz.

It was surprising to observe that the  $E \rightarrow Z$  photoisomerization of the deprotonated rotaxane  $E\text{-1}^+$  was not accessible in the same experimental setup used for the previous experiment. This behavior could be explained in two possible ways, either a very fast  $Z \rightarrow E$  thermal back isomerization process, or a low  $E \rightarrow Z$  and/or very efficient  $Z \rightarrow E$  photoisomerization reaction. In the first case, the intensity of the light source used could represent a determinant aspect. The accumulation of the  $Z$  isomer would be inefficient if the thermal back reaction is faster than the photon flux provided.<sup>32</sup> For this reason, we further investigated the system by means of UV visible spectroscopy, indeed in this case more diluted sample can be used and the photon flux shouldn't be a limiting factor.

## 2.5.2. UV-vis photoisomerization and thermal back $Z \rightarrow E$ isomerization

The UV vis isomerization experiments were performed using a diode array spectrophotometer. The absorption spectrum of [2]rotaxane  $\mu\text{M}$  solutions in acetonitrile was recorded during irradiation with a mercury lamp endowed with a filter to select the 365 nm wavelength. The photoisomerization reaction of  $E\text{-1}^+$  was clearly observed under these experimental conditions. In particular, the PSS was composed of about 30% of the  $Z$  isomer (Figure 6, *left*), conversely the  $E \rightarrow Z$  photoisomerization of  $E\text{-1H}^{2+}$  provided about 70% of the metastable *cis* isomer (Figure 6, *right*).

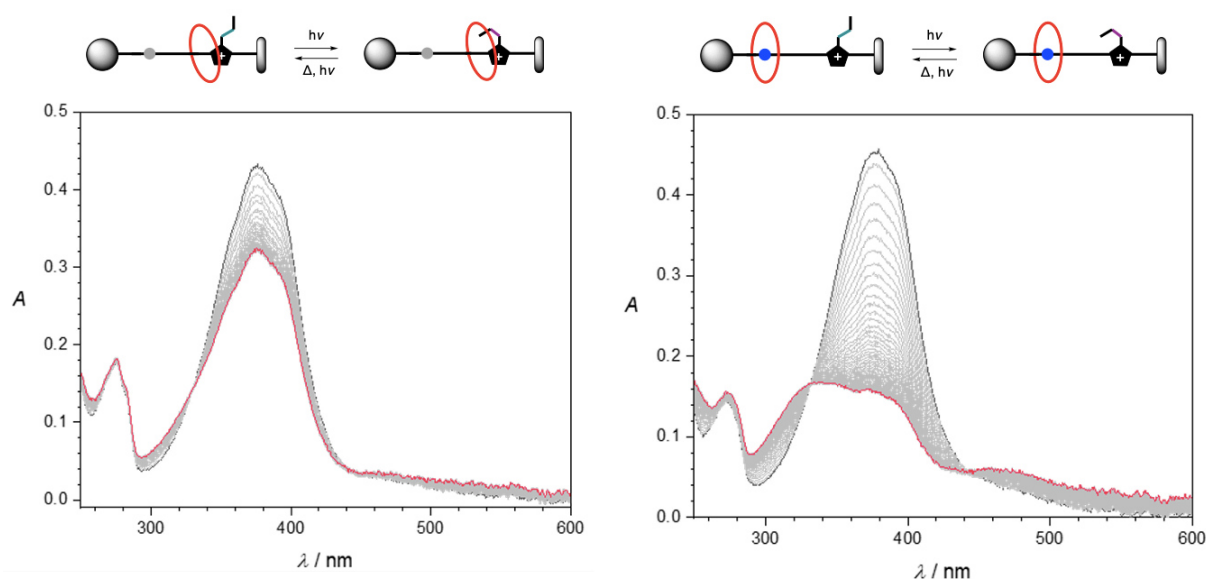


Figure 6. *Left*, absorption spectrum of  $E\text{-1}^+$ ,  $[E\text{-1}^+]_0 = 2.0 \times 10^{-5} \text{ M}$  (black line) and spectral changes upon irradiation with 365 nm light ( $E \rightarrow Z$  photoisomerization, gray lines) until reaching the photostationary state (magenta line). *Right*, absorption spectrum of  $E\text{-1H}^{2+}$ ,  $[E\text{-1H}^{2+}]_0 = 1.9 \times 10^{-5} \text{ M}$  (black line) and spectral changes upon irradiation with 365 nm light ( $E \rightarrow Z$  photoisomerization, gray lines) until reaching the photostationary state (magenta line). Solvent acetonitrile, 298 K

It is worth noting that a different composition of the PSS was obtained for  $E\text{-1H}^{2+}$  in the NMR experiments (PSS 91:9) and in the UV-vis experiments (PSS  $\sim$  70:30). This apparent discrepancy can be explained considering that, in the UV visible setup, the irradiation wavelength (365 nm) was selected using interference filters. On the contrary, the emission of the LED employed for the NMR irradiation experiment was not filtered. The maximum of the LED emission is at 369 nm with a full width at half maximum (FWHM) of  $\pm 15.56 \text{ nm}$ . The irradiation with polychromatic light irretrievably causes a different PSS.

Solutions of rotaxanes ( $E-1H^{2+}$ ,  $E-1^+$ ) and free threads ( $E-2H^{2+}$ ,  $E-2^+$ ) in acetonitrile were irradiated at 365 nm until the system reached a PSS (yellow background in *a*, *b*, *c* and *d*, Figure 7). The  $E \rightarrow Z$  photoisomerization process can be conveniently followed by measuring the absorbance at 375 nm that corresponds to the maxima of the  $\pi \rightarrow \pi^*$  band of the azoimidazolium moiety in  $E$  configuration (Figure 6). All the species reach the PSS in about 25 minutes. Subsequently, the profiles of the  $Z \rightarrow E$  thermal back reactions were obtained by monitoring the absorbance at 375 nm in the dark at 298 K (grey background in *a*, *b*, *c* and *d*, Figure 7).

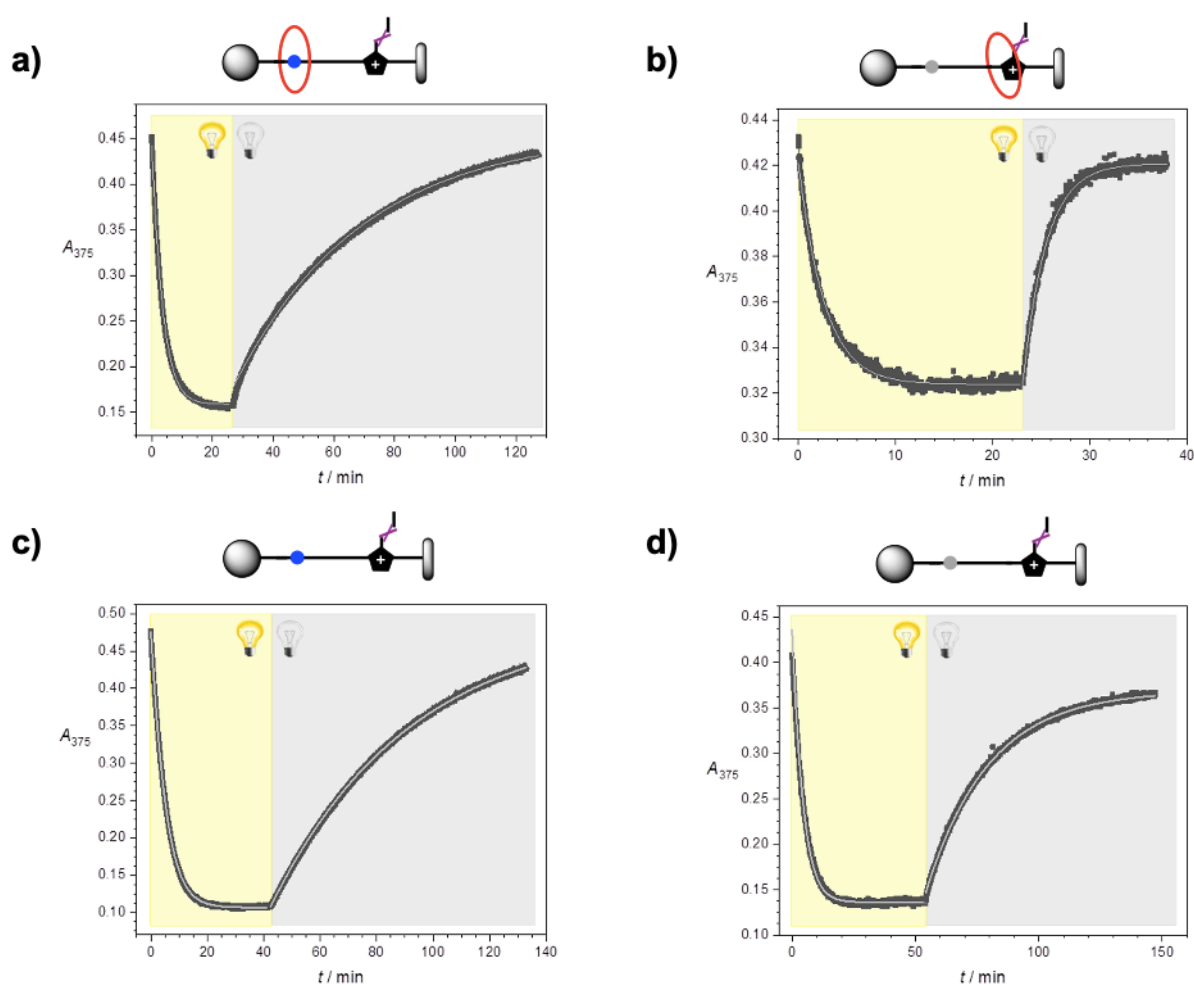


Figure 7. Changes in the absorbance at  $\lambda_{max} = 375$  nm during  $E \rightarrow Z$  isomerization (upon irradiation at 365 nm, yellow background in the graphs) and  $Z \rightarrow E$  back-isomerization (in the dark, grey background). a)  $E-1H^{2+}$ ,  $[E-1H^{2+}]_0 = 1.9 \times 10^{-5}$  M; b)  $E-1^+$ ,  $[E-1^+]_0 = 1.6 \times 10^{-5}$  M; c)  $E-2H^{2+}$ ,  $[E-2H^{2+}]_0 = 2 \times 10^{-5}$  M; d)  $E-2^+$ ,  $[E-2^+]_0 = 1.9 \times 10^{-5}$  M. Acetonitrile, 298 K.

The metastable  $Z$  isomer decays to the  $E$  form with a temperature dependent reaction. From the comparison of the back isomerization curves is clear that the rotaxane  $Z-1^+$  (Figure 7, *b*) has the fastest  $Z \rightarrow E$  isomerization kinetic, indeed the complete relaxation of the  $Z$  form to the  $E$  isomer occurs in about 15 minutes. In all the other cases, this process requires more than two

hours. The thermal back isomerization rate constants ( $k_A$ ) were determined through the fitting of the kinetic profiles with a first order model, the values determined are reported in Table 1.

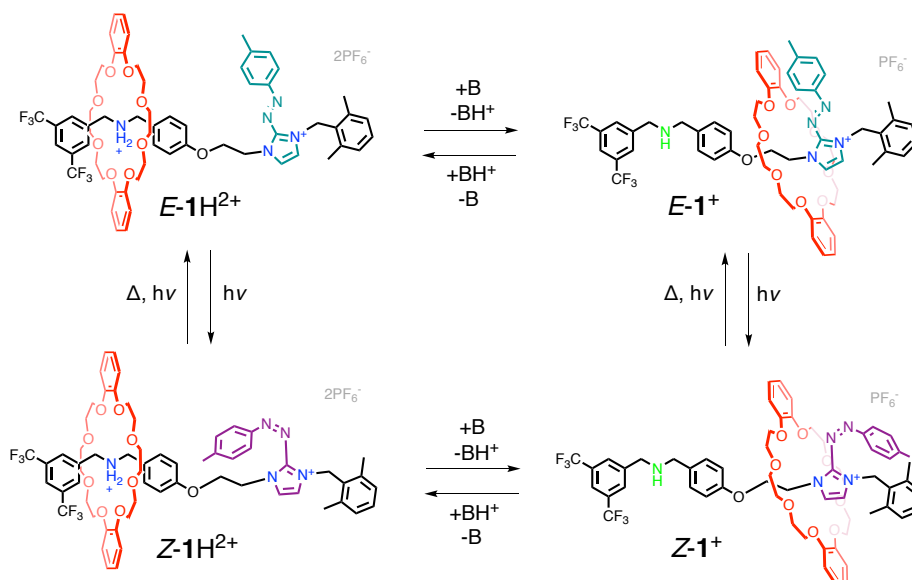
| Compound               | $\lambda_{\max}$ [nm] | $k_A$ [s <sup>-1</sup> ] <sup>a</sup> |
|------------------------|-----------------------|---------------------------------------|
| <b>1H<sup>2+</sup></b> | 375                   | $3.97 \pm 0,06 \cdot 10^{-4}$         |
| <b>1<sup>+</sup></b>   | 375                   | $6.96 \pm 0,02 \cdot 10^{-3}$         |
| <b>2H<sup>2+</sup></b> | 375                   | $2.70 \pm 0,01 \cdot 10^{-4}$         |
| <b>2<sup>+</sup></b>   | 375                   | $6.63 \pm 0,02 \cdot 10^{-4}$         |

*Table 1. Rates of thermal back isomerization of the rotaxane and free thread solutions in acetonitrile at 298 K.  
<sup>a</sup> The reported errors are relative to the fitting of the experimental data.*

The comparison of the  $k_A$  of the rotaxane and free thread is useful to study the effect of the macrocycle on the interlocked structure. The thermal back isomerization constant of *Z*-**1H<sup>2+</sup>** is about 20 times lower than the one of *Z*-**1<sup>+</sup>**, conversely the constant determined for the free thread *Z*-**2<sup>+</sup>** is “only” 2.5 folds compare to the one of *Z*-**1H<sup>+</sup>**. This means that in rotaxane *Z*-**1<sup>+</sup>**, in which the macrocycle encircles the photochromic unit, the rate of the thermal *Z*→*E* reaction is affected by the supramolecular interaction of the azoimidazolium with the ring. These results are significative since they prove that a photophysical parameter can be modulated in this family of [2]rotaxanes. Upon deactivation of the ammonium site, it is possible to switch from a slow relaxing *Z* isomer (*Z*-**1H<sup>2+</sup>**) to a faster decaying metastable isomer, as observed in *Z*-**1<sup>+</sup>**.

## 2.6. [2]rotaxane reaction network

The reported [2]rotaxane is composed of two stations with two accessible states (protonated/deprotonated for ammonium recognition site, *E/Z* for the azoimidazolium station); hence,  $2^2 = 4$  states are possible for this interlocked architecture (Scheme 3).



*Scheme 3. Network of acid-base (horizontal) and photochemical (vertical) reactions that interconnect the four accessible states of the rotaxane  $E-1H^{2+}$ .*

As detailed above, the addition of a base to  $E-1H^{2+}$  causes the deprotonation of the ammonium site to afford  $E-1^+$  in which the macrocycle encircles the azoimidazolium station, while irradiation with UV light induces the formation of the *Z* isomers (respectively  $Z-1H^{2+}$  and  $Z-1^+$ ). Another important feature of this scheme is that the photochemical properties of the protonated and deprotonated rotaxane are markedly different. By irradiation at 365 nm the PSS reached for  $E-1H^{2+}$  is composed of  $\sim 70\%$  of the *Z* isomer, while for  $E-1^+$  the PSS is composed of about 30% of the metastable *Z* isomer. This trend can be partially explained by a faster  $Z \rightarrow E$  thermal back isomerization of  $Z-1^+$  compared to  $Z-1H^{2+}$ .

Furthermore, we expected that a difference in the affinity for the DB24C8 between the two isomers (*E*, *Z*) of the photochromic recognition site should be reflected in the acid-base properties of the ammonium center.<sup>15</sup> In the next paragraphs will be reported the experiments performed to investigate the relative acidity of  $E-1H^{2+}$  and  $Z-1H^{2+}$ . Moreover, the operation of the reactions network will be investigated under condition of light irradiation.

### 2.6.1. Acid/base properties of the ammonium recognition site

$^1\text{H}$ -NMR titration experiments performed on rotaxane  $E\text{-}1\text{H}^{2+}$  by addition of a base allowed to determine the  $\text{p}K_{\text{a}}$  value of the ammonium site in deuterated acetonitrile, which resulted to be 20,74. Analogous titrations experiments were attempted on  $Z\text{-}1\text{H}^{2+}$  with the difference that the sample was maintained under continuous irradiation ( $\lambda_{\text{irr}} = 369 \pm 10 \text{ nm}$ ) in order to control the  $Z \rightarrow E$  thermal back relaxation of the species. These experiments provided an unexpected result: after the addition of a sub stoichiometric amount (0.1 equivalents) of base (1,8-diazabicyclo[5.4.0]undec-7-ene, DBU), the  $Z$  isomer was consumed instantaneously to yield a mixture of  $E\text{-}1\text{H}^{2+}$  and  $E\text{-}1^+$ . The corresponding  $^1\text{H}$  NMR spectrum is reported in Figure 8. The disappearance of the  $Z$  isomer can be deduced clearly from the lower field shift of the  $Z$  characteristic resonances  $\text{H}_{\text{B}}$  (from 4.38 ppm to 4.94 ppm) and  $\text{H}_{\text{E}}$  (from 4.26 ppm to 5.73 ppm) consistently with the formation of  $E\text{-}1\text{H}^{2+}$ .

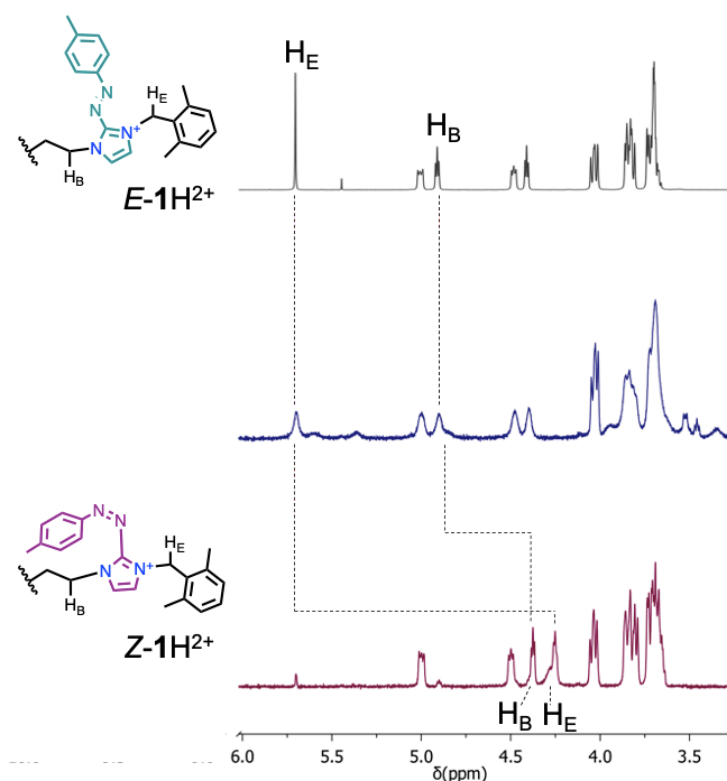


Figure 8. Stacked  $^1\text{H}$  NMR spectra: top, reference spectrum of  $E\text{-}1\text{H}^{2+}$ ; bottom, spectrum of  $Z\text{-}1\text{H}^{2+}$ ; middle, the same sample after the addition of 0.1 equivalents of DBU maintaining the sample under irradiation ( $\lambda_{\text{irr}} = 369 \pm 10 \text{ nm}$ ).  $\text{CD}_3\text{CN}$ , 298 K, 500 MHz.

The formation of  $Z-1^+$  upon deprotonation of  $Z-1H^{2+}$ , was not observed. This is not surprising considering the fast thermal back isomerization of the former (Table 1). However, this does not explain the complete disappearance of  $Z-1H^{2+}$  which is observed even while maintaining the system under constant irradiation.

The same experiment performed by UV-vis spectroscopy provided an even more interesting result. In a typical experiment, a  $\mu\text{M}$  solution of  $E-1H^{2+}$  was irradiated at 365 nm until the PSS ( $\text{PSS}_0$ , Figure 9) was reached ( $Z/E \sim 70:30$ ), then 0,1 equivalents of DBU were added while maintaining the system under constant irradiation. This resulted in an increase in the absorbance at 375 nm that kept increasing until the system reached a different PSS composition ( $\text{PSS}_{t1}$ , Figure 9), coherently with a situation in which the  $Z$  isomer is less abundant than at the beginning.

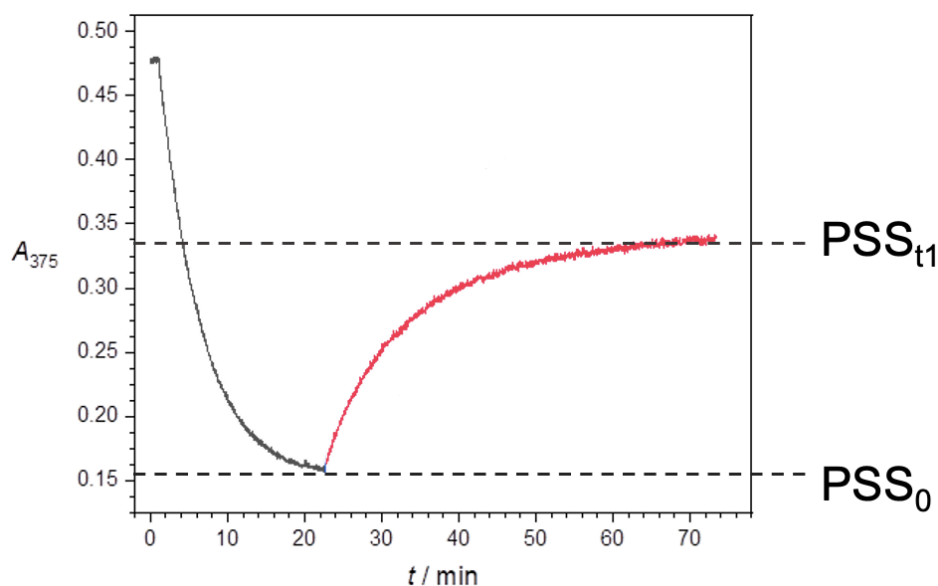


Figure 9. Changes in absorbance at 375 nm for a solution of  $E-1H^{2+}$  upon irradiation to the photostationary state (black curve) and subsequent addition of 0.1 equivalents of DBU (magenta curve).  $[E-1H^{2+}]_0 = 1.8 \cdot 10^{-5} \text{ M}$ .

This large variation in absorbance cannot be simply explained with the different PSS composition due to the formation of  $Z-1^+$ , because the quantity formed by deprotonation is too small to induce such an effect.

Due to these puzzling results, the determination of  $Z-1H^+$  apparent acidity was not possible either with NMR or UV-vis experiments. In fact, while in the first case the  $Z$  isomer was “lost” upon addition of the base, in the UV-vis experiments the addition of the base resulted in a different composition of the PSS.

## 2.6.2. Light-on/light-off experiment

In order to evaluate the relative acidity of  $E\text{-1H}^{2+}$  and  $Z\text{-1H}^+$  it was decided to use the deprotonated rotaxane  $E\text{-1}^+$  as an internal base for the deprotonation of  $Z\text{-1H}^+$ . This strategy avoids the use of external base/conjugated acid pairs, thus lower the number of involved species in the system. Experiments were performed by UV-vis spectroscopy by employing  $\mu\text{M}$  solutions of  $E\text{-1H}^{2+}$  irradiated ( $\lambda_{\text{irr}} = 365 \text{ nm}$ ) at the PSS (“light-on”, *yellow* background in Figure 10). Subsequently,  $E\text{-1}^+$  was added to the solution and the light was turned off to register the  $Z \rightarrow E$  thermal back isomerization (“light-off”, *grey* background in Figure 10). The experiment was repeated for different  $E\text{-1}^+/E\text{-1H}^{2+}$  molar ratio. This method provided information about the relative acidities of the rotaxane isomers, indeed in the case in which  $E\text{-1}^+$  was not able to deprotonate  $Z\text{-1H}^+$  the sole thermal back isomerization of  $Z\text{-1H}^+$  should be observed in the “light-off” part of the experiment.

In the first part of the graph (*yellow* background, Figure 10) the absorbance at 375 nm decreases until a PSS is reached consistently with the occurrence of  $E\text{-1H}^{2+}$  isomerization process.

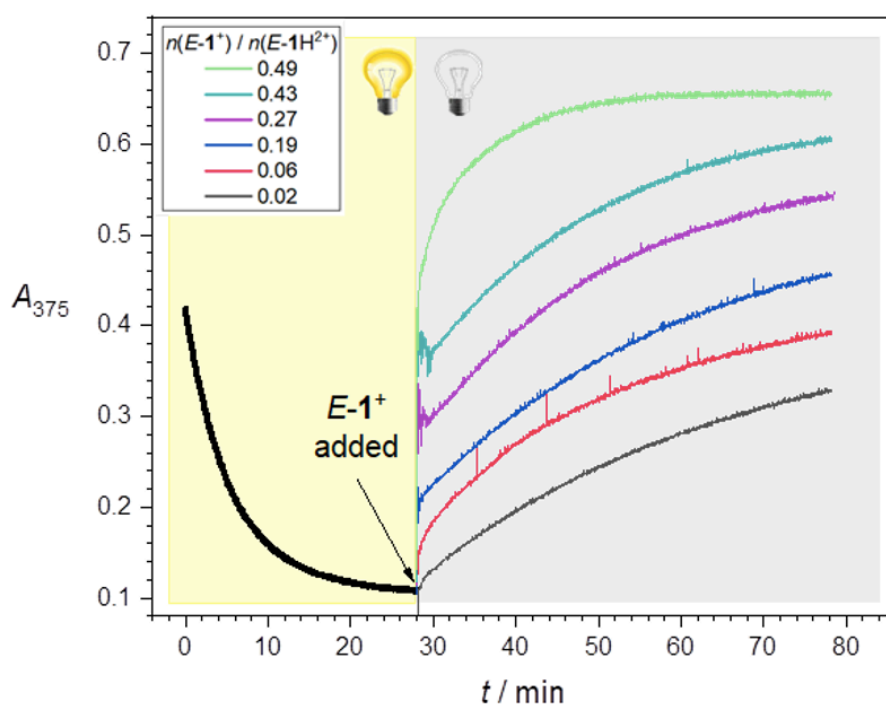


Figure 10. Time dependent absorption change at 375 nm: in the first part (*yellow* background) the rotaxane  $E\text{-1H}^{2+}$  was irradiated at 365 nm until the PSS was reached. In the second part (*grey* background), concomitant interruption of irradiation and addition of increasing amount of the rotaxane  $E\text{-1}^+$  (from grey to the green curve).  $[E\text{-1H}^{2+}]_0 = 1.8 \cdot 10^{-5} \text{ M}$ , acetonitrile, 298 K.

The situation observed in the “light-off” part of the experiment is much more interesting. The fitting of the time dependent profiles registered in the dark after the addition of  $E-1^+$  required a two-contribution kinetic model, the values of the rate constants found are reported in Table 2.

| $E-1^+/E-1H^{2+}$ | $k_A [s^{-1}]^a$                | $k_B [s^{-1}]^a$                |
|-------------------|---------------------------------|---------------------------------|
| 0.02              | $(5.31 \pm 0.20) \cdot 10^{-3}$ | $(3.03 \pm 0.02) \cdot 10^{-4}$ |
| 0.06              | $(6.85 \pm 0.07) \cdot 10^{-3}$ | $(5.20 \pm 0.06) \cdot 10^{-4}$ |
| 0.19              | $(7.16 \pm 0.20) \cdot 10^{-3}$ | $(2.84 \pm 0.10) \cdot 10^{-4}$ |
| 0.27              | $(1.10 \pm 0.01) \cdot 10^{-2}$ | $(1.43 \pm 0.02) \cdot 10^{-4}$ |
| 0.43              | $(1.17 \pm 0.01) \cdot 10^{-2}$ | $(5.20 \pm 0.02) \cdot 10^{-4}$ |
| 0.49              | $(1.47 \pm 0.02) \cdot 10^{-2}$ | $(2.46 \pm 0.40) \cdot 10^{-4}$ |

Table 2. Rate constants obtained from the fitting using a two contributions kinetic model of the back-isomerization in the dark of  $E-1H^{2+}$  and  $E-1^+$  mixtures with different molar ratios in acetonitrile at 298 K. <sup>a</sup> The errors reported for  $k_A$  and  $k_B$  are relative to the fitting of the experimental data

While  $k_B$  is a first order constant that correlates quite nicely with the thermal back isomerization rate of  $Z-1H^{2+}$  (See Table 1),  $k_A$  is an apparent pseudo first order constant that increases proportionally to the amount of  $E-1^+$  added.

A plausible explanation for these experimental data is depicted in the schematic representation of Figure 11. Upon addition of  $E-1^+$  to a solution containing  $Z-1H^{2+}$  a proton exchange between these species occur resulting in the formation of  $E-1H^{2+}$  and  $Z-1^+$  (curved arrows, Figure 11).

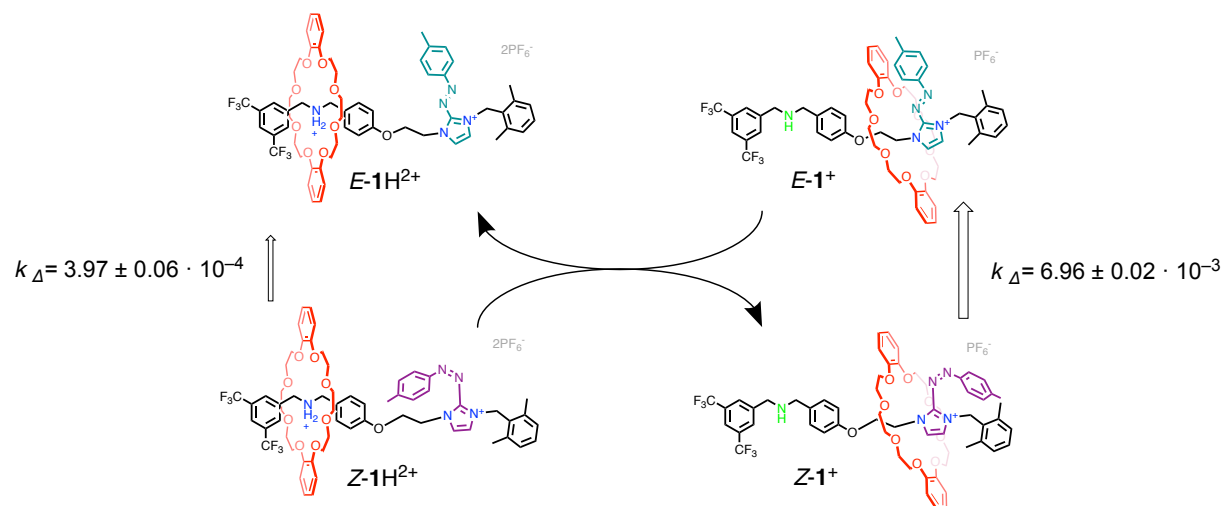
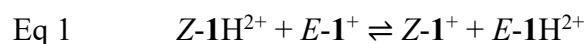


Figure 11. Schematical representation of the experimental data interpretation. The vertical arrows are depicted in different dimension to represent the difference in the  $k_A$  rate constants.

As described above, rotaxane  $Z-1^+$  is characterized by a fast thermal back isomerization ( $k_A$ , Table 1), this process quickly regenerates the base  $E-1^+$  (*big* vertical arrow, Figure 11). In a total balance,  $E-1^+$  is firstly consumed in the acid-base pre-equilibrium described by the Equation 1, and subsequently formed by the thermal back isomerization of  $Z-1^+$ . This process continues in a catalytic fashion until all  $Z-1H^{2+}$  is converted into  $E-1H^{2+}$ .



The consumption of  $Z-1H^{2+}$  occurs through two different paths: the thermal back isomerization of  $Z-1H^{2+}$  (described by  $k_B$  constants in Table 2) and, more rapidly, through the acid-base preequilibrium followed by thermal back isomerization of  $Z-1^+$  (described by  $k_A$  constants, Table 2). This hypothesis implies that the two isomers of  $E-1H^{2+}$  have different apparent acidity ( $Z-1H^{2+}$  would be more acidic than  $E-1H^{2+}$ ).

This difference in acidity between  $Z-1H^{2+}$  and  $E-1H^{2+}$  can possibly arise from a difference in the affinity of the crown macrocycle for the azoimidazolium station in the  $Z$  and  $E$  configurations. The same “light-on/light-off” experiment were performed with the simple thread  $2H^{2+}$  (Figure 12). In this case, the addition of the deprotonated axle  $2^+$  to a PSS solution of  $2H^{2+}$  didn't result in any significative time dependent changes in the absorbance at 375 nm (*purple* trace, Figure 12). This result means that the presence of the ring has a key role in determining the difference in  $pK_a$ .

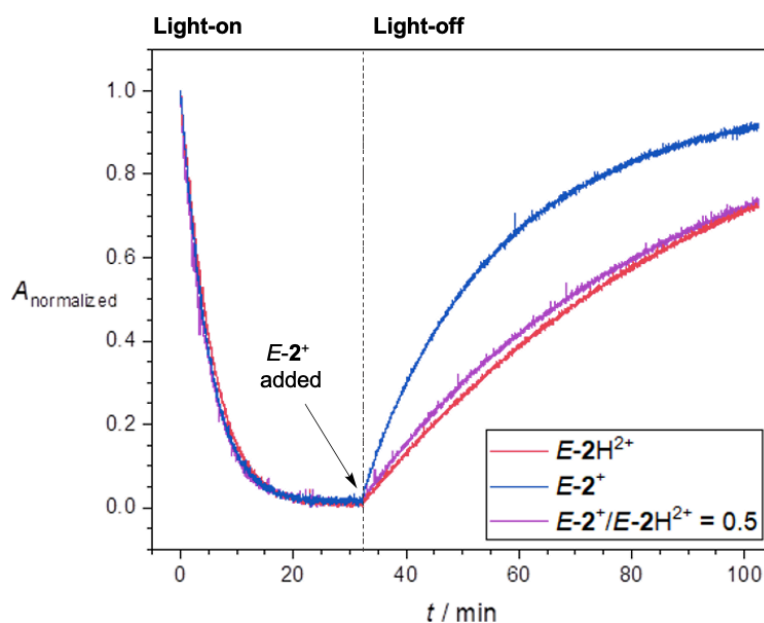


Figure 12. Light on-off experiment performed with the free axle  $2H^{2+}$ . Normalized absorption spectra. Change in the absorption at 375 nm: in the light-on part  $E-2H^{2+}$  (purple trace) was irradiated at 365 nm until the PSS was reached, the light-off part was recorded after the concomitant interruption of irradiation and addition of  $E-2^+$ . The blue and red traces belong respectively to  $E-2^+$  and  $E-2H^{2+}$ .

### 2.6.3. Out of equilibrium network operation

The reactions network (Scheme 3) that interconnects the rotaxanes can be also considered as the sum of photochemical reactions (Figure 13, a), and acid-base equilibria (Figure 13, b). From the experimental results presented, some important consideration can be done: the photoisomerization process occurs more efficiently for  $E-1H^{2+}$  (PSS  $Z/E \sim 70:30$ ) than  $E-1^+$  (PSS  $Z/E \sim 30:70$ ), furthermore the two isomeric rotaxanes present different acidities. This difference in the vertical processes (photochemical reaction, Figure 13, a) and in the horizontal ones (acid base equilibria, Figure 13, b) can be the driving force for the realization of an out of equilibrium reactions network (Figure 13, c). Furthermore, this system could also work in the presence of a base with suitable strength B (Scheme 3 and Figure 13, b).

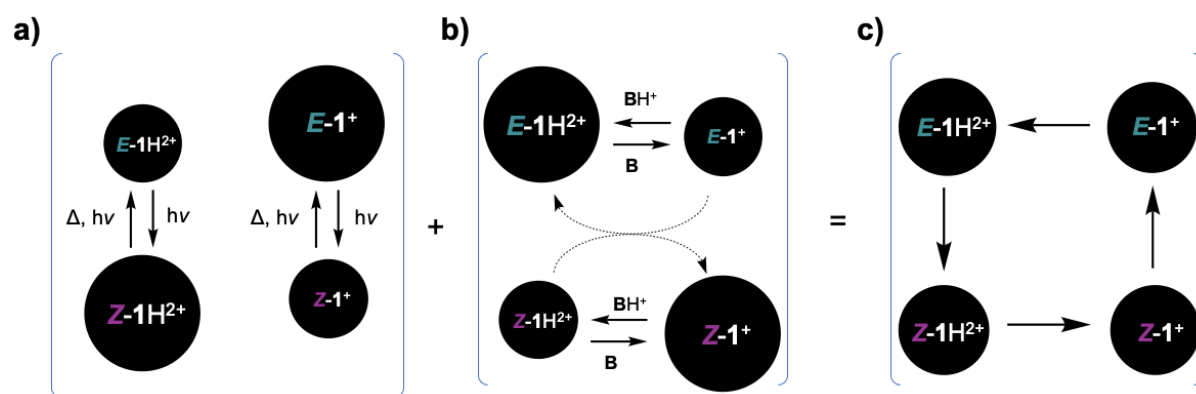


Figure 13. a) Representation of  $E-1H^{2+}$  and  $E-1^+$  photoisomerization reactions, b) acid base reactions that interconvert the protonated and deprotonated rotaxanes, c) anticlockwise direction of the cycle achieved during the out of equilibrium operation. The different dimensions of the circles were used to represent the difference in the PSS composition of  $E-1H^{2+}$  and  $E-1^+$  (a) and the formation of  $E-1H^{2+}$  and  $Z-1^+$  that occur from the reaction between  $E-1^+$  and  $Z-1H^{2+}$  (b).

The cycle can operate autonomously as long as light energy is furnished to the system. The described interplay between the photochemical and acid-base reactions results in an autonomous shuttling of the macrocycle. This out of equilibrium process is realized thanks to a light induced isomerization and proton transfer process that is due to the difference in acidity between  $Z-1H^{2+}$  and  $E-1H^{2+}$ .

A different type of light-on/light-off experiment (Figure 14) was attempted to directly observe the autonomous out of equilibrium cycle driven by light. Differently from the previous experiments, solutions of rotaxanes were prepared from the beginning with different relative ratio of  $E-1H^{2+}$  and  $E-1^+$ .

The solutions in acetonitrile at 298 K were irradiated ( $\lambda_{\text{irr}} = 365 \text{ nm}$ ) and the absorbance change at 375 nm was recorded. In all traces reported in Figure 14, a decrease in absorbance is firstly observed consistently with the  $E \rightarrow Z$  photoisomerization process. However, after about five minutes of irradiation, a second effect occur only in the solutions with a higher amount of  $E-1^+$  ( $E-1^+/E-1H^{2+} \geq 0.19$ , Figure 14). The initial decrease in absorbance is followed by an increase consistent with the accumulation of  $E$  species.

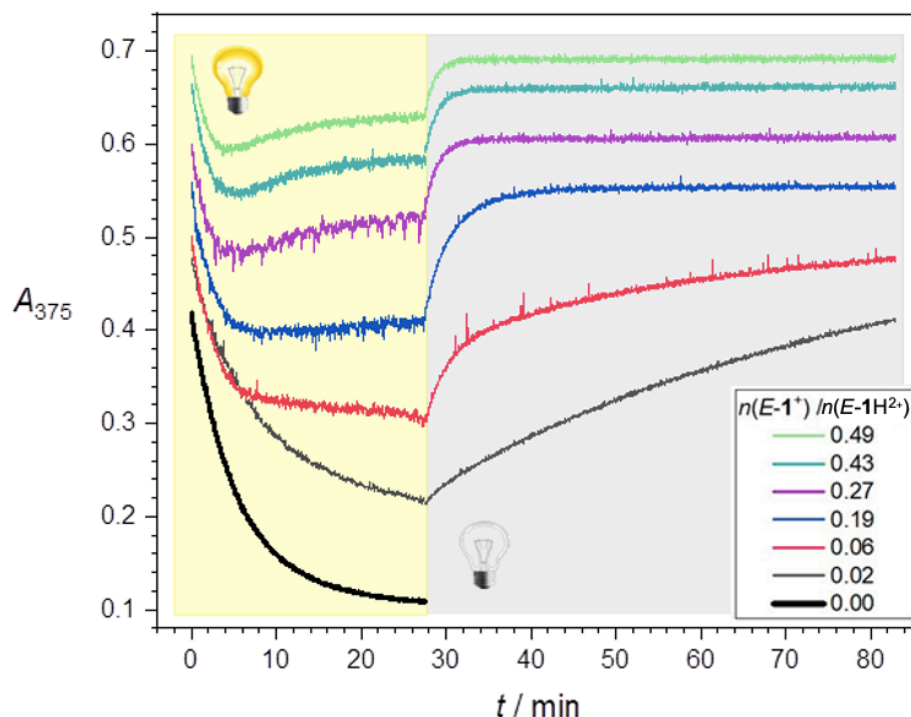


Figure 14. Time dependent absorption change at 375 nm of solutions containing  $E-1H^{2+}$  and  $E-1^+$  in different proportions, upon irradiation at 365 nm light (yellow background), and subsequent rest in the dark (grey background). Acetonitrile, 298 K.

This observation can be explained by the consumption of  $Z-1H^+$  which reacts with  $E-1^+$  to yield  $Z-1^+$ , the latter rapidly back-isomerizing to  $E-1^+$  in analogy with the behavior described in the previous paragraph. The acid-base reaction between  $E-1^+$  and  $Z-1H^{2+}$  is a bimolecular process and thus dependent on the concentration of the species. For this reason, the process is slower in the beginning, in which the photogenerated  $Z-1H^+$  is still at a very low concentration. The stage at which the acid-base reactions and the photochemical generation of the  $Z$  isomer is balanced is represented by the *plateau* reached by all the traces. This state corresponds to the photostationary dissipative state. When the light is turned off (Figure 14, grey background) the system relaxes to its global minimum composed by  $E-1^+$  and  $E-1H^+$ . The different rates observed for this process are again a result of the different amount of  $E-1^+$  present in solution

at the moment of the interruption of light irradiation. A further confirmation of this interpretation is obtained by experiments in which a mixture of the protonated and deprotonated free axle  $2\text{-H}^{2+}$  and  $2^+$  in acetonitrile at 298 K are irradiated ( $\lambda_{\text{irr}} = 365 \text{ nm}$ ). In this case, the *E-Z* isomerization profile obtained monitoring the absorbance at 375 nm (grey trace, Figure 15) does not show any peculiar effect.

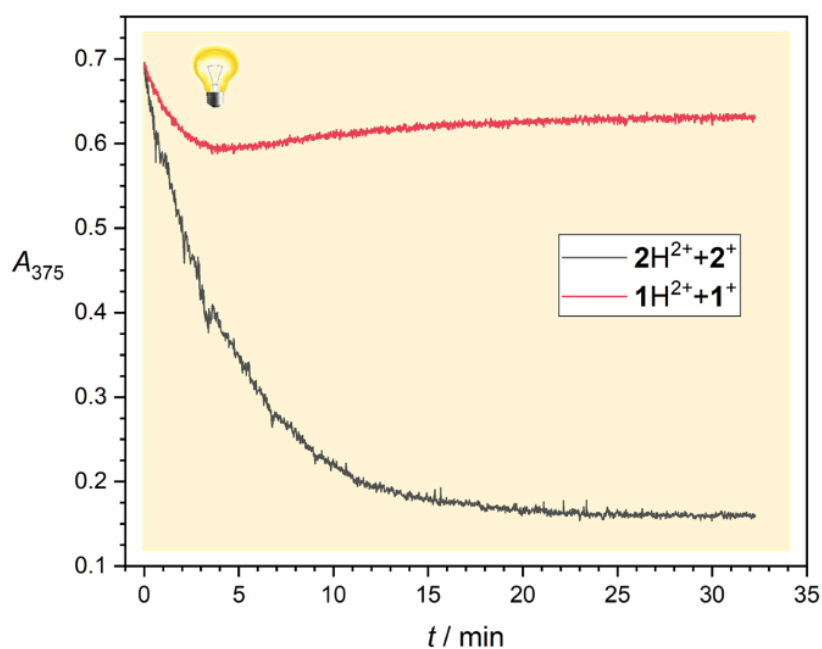


Figure 15. Changes in absorption at 375 nm for a solution containing *E-1H*<sup>2+</sup> and *E-1*<sup>+</sup> (red trace, *E-1*<sup>+</sup>/*E-1H*<sup>2+</sup> = 0.49) and a solution containing *E-2H*<sup>2+</sup> and *E-2*<sup>+</sup> (black trace, *E-2*<sup>+</sup>/*E-2H*<sup>2+</sup> = 0.49) upon irradiation at 365 nm.

## 2.7. Conclusion

In this chapter it was described the synthesis, NMR and UV visible characterization of a [2]rotaxane ( $E\text{-1H}^{2+}$ ) endowed with a novel azoimidazolium unit that acts as a recognition site for a crown ether macrocycle. The synthesis of this photo-responsive compound was articulated in eight total steps, furthermore a model free axle was also prepared. Interestingly the *stopping* reaction to afford the interlocked compound leads to the contemporary formation of the cationic center.

The behavior of the multi-responsive rotaxane was studied by  $^1\text{H}$  NMR and UV visible experiments. Deprotonation with a base results in the translation of the ring from the ammonium site to the azoimidazolium unit. The ability to respond to light stimuli was investigated in the protonated and deprotonated rotaxanes ( $E\text{-1}^+$ ). Importantly, the thermal back isomerization constant of the rotaxane, in which the ring is surrounding the photochromic unit, resulted to be 20 times bigger compared to the protonated rotaxane. The comparison with the model axle confirmed that this effect is due to the presence of the macrocycle.

The strength of the non-covalent interaction established between the macrocycle and the pH-insensitive station should determine a difference in the  $\text{pK}_a$  of the ammonium center.<sup>17</sup> The direct determination of the apparent  $\text{pK}_a$  of  $Z\text{-1H}^+$  was not possible in our experimental conditions. For this reason, the relative acidity of  $E\text{-1H}^{2+}$  and  $Z\text{-1H}^{2+}$  was investigated in specifically designed light-on/light-off experiments. Our data suggests that the *E* isomer is more acidic than the *Z* isomer.

This result is particularly significant because it enables the possibility to achieve a light-driven autonomous and reversible shuttling in this type of systems. The process is realized under condition of continuous irradiation by means of a photoinduced proton transfer. As a result, a preferential direction is realized in the cycle that interconvert the *E/Z* protonated and deprotonated rotaxanes forms. The directionality is achieved through both an energy<sup>33-35</sup> (the light stimulus changes the acidity constants) and information ratchet<sup>33-35</sup> mechanism (the position of the ring influences the *E-Z* interconversion).

The investigated system is very interesting since the development of photoresponsive molecular machines that operate away from equilibrium is a particularly challenging topic in the field of artificial molecular machines.<sup>36</sup>

## 2.8. Experimental Section

|  |            |
|--|------------|
| <b>Experimental Details</b>  | <b>106</b> |
| <b>2.9. Synthetic procedures</b>   | <b>108</b> |
| 2.9.1 Synthesis of the precursors <b>2a</b> and <b>1b</b>                            | <b>108</b> |
| Synthesis of <b>a</b>  | 109        |
| Synthesis of <b>1a</b>   | 109        |
| Synthesis of <b>2a</b>   | 110        |
| Synthesis of <b>b</b>  | 110        |
| Synthesis of <b>1b</b>   | 111        |
| 2.9.2. Synthesis of the [2]rotaxane  | <b>112</b> |
| Synthesis of <b>1c</b>   | 113        |
| Synthesis of <b>2c</b>   | 114        |
| Synthesis of <i>E</i> - <b>1H</b> <sup>2+</sup>                                      | 115        |
| Synthesis of <i>E</i> - <b>1</b> <sup>+</sup>  | 116        |
| 2.9.3. Synthesis of the model compound <i>E</i> - <b>2H</b> <sup>2+</sup>            | <b>118</b> |
| Synthesis of <b>1d</b>   | 119        |
| Synthesis of <i>E</i> - <b>2H</b> <sup>2+</sup>                                      | 120        |
| Synthesis of <i>E</i> - <b>2</b> <sup>+</sup>  | 121        |
| <b>2.10. NMR spectra</b>   | <b>122</b> |
| <sup>1</sup> H and <sup>13</sup> C NMR spectra of <i>E</i> - <b>1H</b> <sup>2+</sup> | 122        |
| HSQC and HMBC spectra of <i>E</i> - <b>1H</b> <sup>2+</sup>                          | 123        |
| <sup>1</sup> H and <sup>13</sup> C NMR spectra of <i>E</i> - <b>1</b> <sup>+</sup>   | 124        |
| HSQC and HMBC spectra of <i>E</i> - <b>1</b> <sup>+</sup>                            | 125        |
| <sup>1</sup> H and <sup>13</sup> C NMR spectra of <i>E</i> - <b>2H</b> <sup>2+</sup> | 126        |
| HSQC and HMBC spectra of <i>E</i> - <b>2H</b> <sup>2+</sup>                          | 127        |
| <sup>1</sup> H and <sup>13</sup> C NMR spectra of <i>E</i> - <b>2</b> <sup>+</sup>   | 128        |

### 2.8.1. Experimental details

Solvents and reagents 3,5-bis-(trifluoromethyl)benzylamine, 4-hydroxybenzaldehyde, sodium borohydride, di-*tert*-butyl-dicarbonate, potassium carbonate, 1,2-dibromoethane, 4-methylaniline, sodium nitrite, hexafluorophosphoric acid, Imidazole, dibenzo-24-crown-8, 2-(Bromomethyl)-1,3-dimethylbenzene, ammonium hexafluorophosphate, trifluoroacetic acid, polystyrene-supported DBU, were all used as supplied by Fluorochem, Sigma-Aldrich or VWR without further purification. Flash column chromatography was performed using Sigma Aldrich Silica 40 (230-400 mesh size or 40-63  $\mu\text{m}$ ) as the stationary phase. Gel permeation chromatography was performed using Biorad Biobeads SX-1 as the stationary phase. Thin layer chromatography was performed on TLC Silica gel 60 F254 coated aluminium plates from Merck.

### 2.8.2. NMR measurements

$^1\text{H}$  NMR spectra were recorded on an Agilent DD2 spectrometer operating at 500 MHz or a Varian Mercury spectrometer operating at 400 MHz;  $^{13}\text{C}$  NMR spectra were recorded on an Agilent DD2 spectrometer operating at 126 MHz or a Varian Mercury spectrometer operating at 101 MHz;  $^{19}\text{F}$  NMR spectra were recorded on an Agilent DD2 spectrometer operating at 470 MHz. Chemical shifts are quoted in ppm relative to tetramethylsilane ( $\text{SiMe}_4$ ,  $\delta = 0$  ppm), using the residual solvent peak as a reference standard; all coupling constants ( $J$ ) are expressed in Hertz (Hz). The samples were irradiated directly inside the thermostated NMR probe, using a 1 mm silica core optical fiber (Thorlabs) connected to a Prizmatix UHP-T-365-SR LED Illuminator (1.5 W,  $\lambda_{\text{max}} = 369$  nm, FWHM, 15.56 nm) through a FCA-SMA adaptor. At its other end, the protective coating of the optical fiber was removed (about 6 cm) and the exposed fiber was sanded to enable the diffusion of light from the fiber core into the solution. The fibre prepared in this way was immersed directly into the thermostated solution (550  $\mu\text{L}$  of 5 mM solution of the rotaxane/free thread) in the NMR tube. The obtained experimental data were processed using MestReNova software and OriginPro 2019. The photon flow at the end of the fiber was determined to be  $4 \times 10^{-8}$  Einstein  $\text{s}^{-1}$  using the ferrioxalate actinometry in its “microversion”.<sup>37</sup>

### 2.8.3. NMR acidity measurements

Deprotonation experiments were carried out in acetonitrile- $d_3$  using heterogeneous [**B1**, polystyrene-supported DBU], and homogeneous [**B2**, DBU,  $\text{p}K_a = 24.3$ ]<sup>38</sup> bases. The spectra

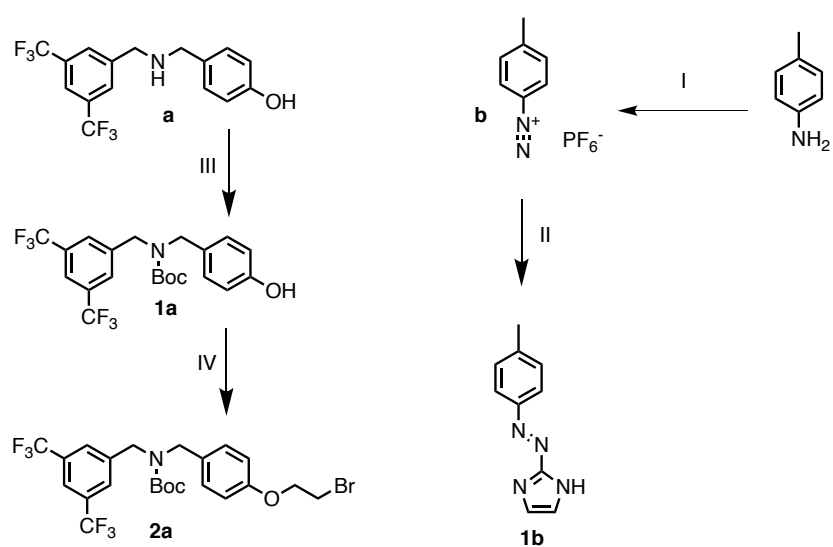
were acquired upon stepwise addition of the base directly into the NMR tube containing 550  $\mu\text{L}$  of  $c \approx 5 \text{ mM}$  solution of the sample. The experiments were performed in the dark or under continuous irradiation (using the set-up described in the previous paragraph) to assess the acidity of the *Z* moieties. Experimental data were processed using HypNMR from HYPERQUAD suite of programs<sup>39</sup> and OriginPro 2019. The error on the  $\text{p}K_a$  values is estimated to be  $\pm 0.1$  units, calculated as the average mean square root in the  $\text{p}K_a$  values of the ammonium stations investigated.

#### 2.8.4. UV irradiation experiments

The isomerization experiments were performed using a diode array spectrophotometer Avantes StarLine AvaSpec-ULS2048CL-EVO-RS equipped with an optical fiber which enables the fast acquisition of UV/Vis spectra (ms) and concomitant *in situ* irradiation. About 3 ml of a solution  $\approx 2 \times 10^{-5} \text{ mol dm}^{-3}$  of the rotaxane/free thread in a 10mm pathlength quartz cuvette was continuously irradiated by a medium pressure Hg lamp (200 W) at room temperature. The irradiation wavelength was selected using interference filters and the intensity of the incident light was regulated with a pinhole of opportune diameter. The photon flow was determined by the “microversion” of the ferrioxalate actinometer<sup>37</sup> and resulted to be  $\approx 1.5 \times 10^{-9} \text{ Einstein s}^{-1}$ . The acquisition of the spectra was prolonged after interrupting the irradiation of the sample, in order to study the thermal back-isomerization processes. The rate constants for thermal back-isomerization were obtained by fitting the back-isomerization spectral data at the wavelength of the maximum against time using a first-order kinetics (exponential) model in OriginPro 2019.

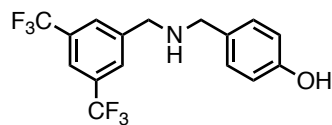
## 2.9. Synthetic procedures

### 2.9.1 synthesis of the precursors **2a** and **1b**



Scheme 4. I)  $\text{HPF}_6$ ,  $\text{NaNO}_2$ ,  $\text{H}_2\text{O}$ , 0-20 °C II) Imidazole,  $\text{K}_2\text{CO}_3$ ,  $\text{H}_2\text{O}$ , 0-20 °C. 23% III)  $\text{Boc}_2\text{O}$ , THF. 87% IV)  $\text{BrCH}_2\text{CH}_2\text{Br}$ ,  $\text{K}_2\text{CO}_3$ ,  $\text{CH}_3\text{CN}$ . 45%

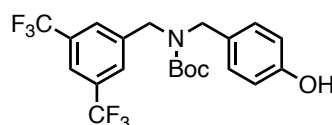
## Synthesis of **a**



An ethanol solution (200 mL) of 3,5-trifluoromethyl-benzylamine (19.45 g, 80.0 mmol) and 4-hydroxybenzaldehyde (9.77 g, 80.0 mmol) was stirred at 40 °C under reduced pressure to remove the solvent. The procedure was repeated three times providing the imine intermediate product, which was re-dissolved in Ethanol (200 mL). NaBH<sub>4</sub> (6.66 g, 176 mmol) was added portionwise and the resulting mixture was stirred at room temperature for 18 h. Removal of the solvent under reduced pressure provided a colourless oil which was dissolved in ethyl acetate (100 mL), washed with water (3×100 mL) and dried over MgSO<sub>4</sub>. Filtration and removal of the solvent under reduced pressure afforded the crude product which, was purified by flash chromatography (Chloroform, R<sub>f</sub> = 0.06) to obtain **a** as a pale-yellow solid (21.45 g, 77%).

<sup>1</sup>H NMR (500 MHz, CDCl<sub>3</sub>, 298 K) δ 7.81 (s, 2H), 7.77 (s, 1H), 7.14 (d, *J* = 8.1 Hz, 2H), 6.70 (d, *J* = 8.1 Hz, 2H), 3.93 (s, 2H), 3.76 (s, 2H). <sup>13</sup>C NMR (126 MHz, CDCl<sub>3</sub>, 298 K) δ 155.64, 141.97, 131.85 (q, *J* = 32.8 Hz) 130.36, 129.93, 128.68, 128.65, 128.62, 128.59, 123.44 (q, *J* = 273.4 Hz), 121.38 (p, *J* = 3.8 Hz), 115.90, 52.73, 52.02. <sup>19</sup>F NMR (470 MHz, CDCl<sub>3</sub>, 298 K) δ -62.90 (s, 6F).

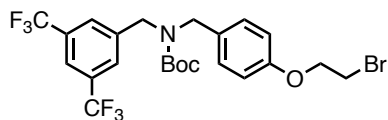
## Synthesis of **1a**



A solution of **a** (19.55 g, 55.97 mmol) and di-*tert*-butyl-dicarbonate (12.21 g, 55.97 mmol) in tetrahydrofuran (600 mL) was stirred at room temperature for 18 h. Removal of the solvent under reduced pressure provided the product as a crude oil which was purified by flash chromatography (Chloroform, R<sub>f</sub> = 0.1) to obtain product **1a** as an off-white solid (21.96 g, 87%).

<sup>1</sup>H NMR (500 MHz, CDCl<sub>3</sub>, 298 K) δ 7.74 (s, 1H), 7.57 (s, 2H), 7.04 (m, 2H), 6.77 (d, *J* = 8.0 Hz, 2H), 6.42 (s, 1H, OH), 4.42 (m, 4H), 1.46 (s, 9H). <sup>13</sup>C NMR (126 MHz, CDCl<sub>3</sub>, 298 K) δ 156.2 (d, *J* = 53.3 Hz), 155.9, 141.0 (d, *J* = 53.3 Hz), 131.9 (q, *J* = 33.3 Hz), 129.5 (d, *J* = 65.4 Hz), 128.75 (d, *J* = 10.5 Hz), 127.7, 123.4 (q, *J* = 273.4 Hz), 121.3, 115.8, 81.5, 50.2, 49.1 (d, *J* = 68.8 Hz), 28.5. <sup>19</sup>F NMR (470 MHz, CDCl<sub>3</sub>, 298 K) δ -62.98 (s, 6F).

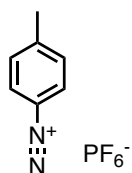
## Synthesis of **2a**



A solution of **1a** (449 mg, 1.00 mmol), 1,2-dibromoethane (2.15 mL, 25.00 mmol) and cesium carbonate (815 mg, 2.50 mmol) in dry acetonitrile (25 mL) was stirred at 80 °C for 18 h under a nitrogen atmosphere. The solution was cooled down to room temperature and the solvent removed under reduced pressure to provide a crude mixture which was dissolved in dichloromethane (50 mL), washed with water (3×50 mL) and dried over anhydrous MgSO<sub>4</sub>. The crude compound was purified by flash chromatography (Chloroform, R<sub>f</sub> = 0.6) to provide the product **2a** as a colorless oil (250 mg, 45%).

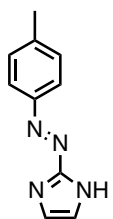
<sup>1</sup>H NMR (500 MHz, CDCl<sub>3</sub>, 298 K) δ 7.74 (s, 1H), 7.56 (bs, 2H), 7.13 (bd, *J* = 25.9 Hz, 2H), 6.85 (d, *J* = 8.3 Hz, 2H), 4.60 - 4.30 (m, 4H), 4.27 (t, *J* = 6.3 Hz, 2H), 3.63 (t, *J* = 6.3 Hz, 2H), 1.49 (m, 9H). <sup>13</sup>C NMR (126 MHz, CDCl<sub>3</sub>, 298 K) δ 157.8, 155.8 (d, *J* = 29.8 Hz), 141.3 (d, *J* = 34.9 Hz), 131.8 (q, *J* = 33.2 Hz), 130.3, 129.5 (d, *J* = 74.8 Hz), 127.7 (d, *J* = 25.2 Hz), 123.4 (q, *J* = 273.4 Hz), 121.2, 115.1, 81.0, 68.1, 50.1, 49.2 (d, *J* = 55.1 Hz), 29.1, 28.4. <sup>19</sup>F NMR (470 MHz, CDCl<sub>3</sub>, 298 K) δ -62.94 (s, 6F).

## Synthesis of **b**



To a water suspension (150 mL) of *p*-toluidine 4.52 g (42.2 mmol) cooled to 0 °C, 16.8 mL of HPF<sub>6</sub> (60% in water) (105.1 mmol) were added dropwise, resulting into a pale-yellow solution. Keeping the solution at 0 °C, 8.74 g NaNO<sub>2</sub> (126.6 mmol) were added portionwise to the mixture maintained at 0 °C, the reaction was stirred for 2 hours at room temperature. The white solid precipitated was collected by filtration, washed with Et<sub>2</sub>O and dried under vacuum. The product was directly employed in the next reaction step.

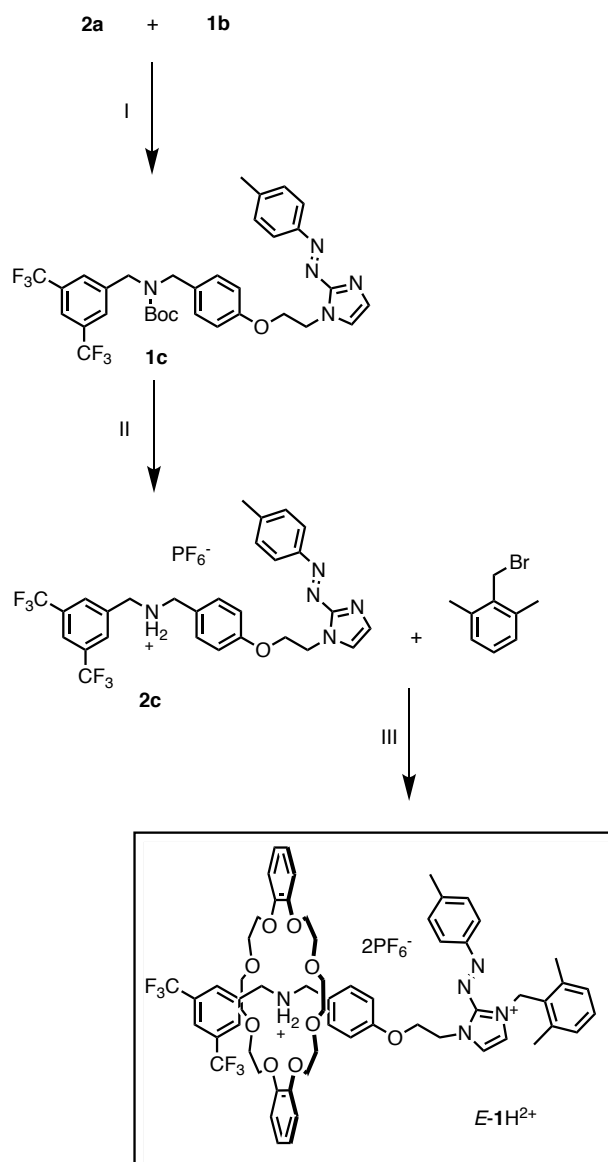
## Synthesis of **1b**



The product was prepared by modifying a previously reported procedure.<sup>28</sup> Imidazole (2.50 g, 36.70 mmol) was added to a solution of  $K_2CO_3$  (5.07 g, 36.70 mmol) in water (80 mL). The solution was cooled down to 0 °C and 4-methylphenyldiazonium hexafluorophosphate (**b**) (9.69 g, 36.7 mmol) was added portionwise and the resulting solution left to warm up to room temperature and stirred for 18 h. The red-brownish precipitate was collected and dissolved in 1 M HCl and the undissolved dark brown byproduct filtered off. The solution was neutralized with NaOH and the yellow precipitate collected by filtration. Recrystallization from ethanol provided the pure product **1b** as dark orange crystals (1.56 g, 23%).

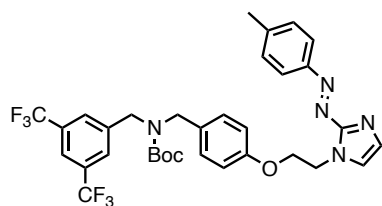
$^1H$  NMR (500 MHz,  $(CD_3)_2SO$ , 298 K)  $\delta$  12.91 (s, 1H, NH), 7.76 (d,  $J = 8.1$  Hz, 2H), 7.39 (d,  $J = 8.1$  Hz, 2H), 7.33 (s, 2H), 2.39 (s, 3H).  $^{13}C$  NMR (126 MHz,  $(CD_3)_2SO$ , 298 K)  $\delta$  154.60, 150.10, 141.77, 130.07, 122.30, 21.04.

## 2.9.2. Synthesis of the [2]rotaxane



Scheme 5. I)  $\text{K}_2\text{CO}_3$ ,  $\text{CH}_3\text{CN}$ , reflux. 63% II)  $\text{HPF}_6$ ,  $\text{THF}$ . 52% II)  $\text{DB24C8}$ , *o*- $\text{Me}_2$ - $\text{BnBr}$ , microwave reactor,  $\text{CH}_3\text{CN}$ ,  $80^\circ\text{C}$ . 65%.

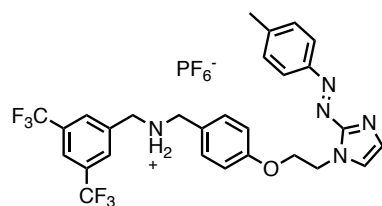
## Synthesis of **1c**



Intermediate **2a** (1.50 g, 2.70 mmol), 1-methyl-2-(phenylazo)imidazole **1b** (502 mg, 2.70 mmol), 18-crown-6 (210 mg, 0.81 mmol) and potassium carbonate (750 g, 5.40 mmol) were suspended in dry acetonitrile (100 mL) and stirred at 80 °C for 24 h under a nitrogen atmosphere. The solvent was removed under reduced pressure and the crude mixture dissolved in ethyl acetate (100 mL), washed with water (3×50 mL) and dried over MgSO<sub>4</sub>. Filtration and removal of the solvent under reduced pressure provided a red-brownish oil which was purified by flash chromatography (Chloroform, R<sub>f</sub> = 0.1) to obtain the product **1c** as a yellow crystalline solid (1.10 g, 63%).

<sup>1</sup>H NMR (500 MHz, CDCl<sub>3</sub>, 298 K) δ 7.88 (d, *J* = 8.3 Hz, 2H), 7.72 (s, 1H), 7.54 (m, 2H), 7.35 - 7.27 (m, 4H), 7.11 (m, 2H), 6.79 (d, *J* = 8.3 Hz, 2H), 4.81 (t, *J* = 5.2 Hz, 2H), 4.54 - 4.24 (m, 6H), 2.43 (s, 3H), 1.60 - 1.37 (m, 9H). <sup>13</sup>C NMR (126 MHz, CDCl<sub>3</sub>, 298 K) δ 157.71, 155.78, 152.23, 151.29, 142.66, 131.70 (q, *J* = 33.2 Hz), 130.37, 130.26, 129.92, 129.75, 129.68, 129.12, 127.61, 123.56, 123.37, 123.33 (q, *J* = 273.4 Hz), 121.16, 114.84, 81.01, 67.41, 50.04, 49.36, 48.97, 45.41, 28.40, 21.69. <sup>19</sup>F NMR (470 MHz, CDCl<sub>3</sub>, 298 K) δ -62.92 (s, 6F).

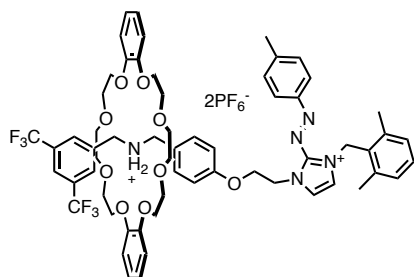
## Synthesis of **2c**



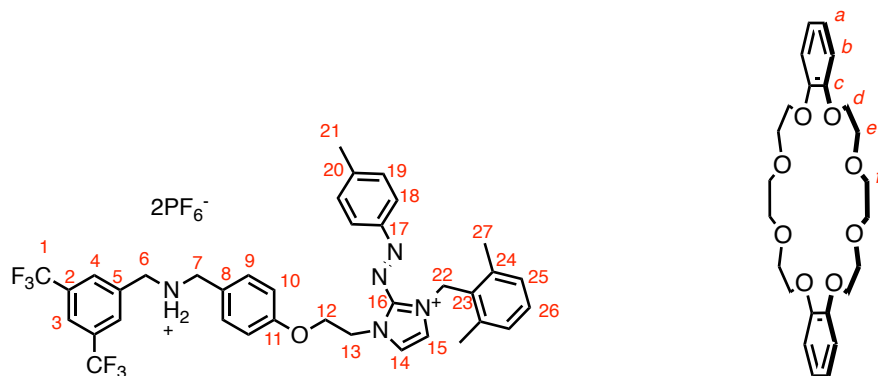
A solution of **1c** (1.00 g, 1.51 mmol) and HPF<sub>6</sub> (60%<sub>w/w</sub> in H<sub>2</sub>O, 1.33 mL, 15.1 mmol) in tetrahydrofuran (100 mL) was stirred at room temperature for 3 h. The solvent was removed under reduced pressure and the residue dissolved in dichloromethane (100 mL) and washed with a saturated aqueous solution of ammonium hexafluorophosphate (3×100 mL). The organic phases were dried over anhydrous MgSO<sub>4</sub>, filtration and removal of the solvent under reduced pressure provided the product **2c** as an orange solid (555 mg, 52%).

<sup>1</sup>H NMR (500 MHz, (CD<sub>3</sub>)<sub>2</sub>SO, 298 K) δ 8.16 (s, 2H), 8.11 (s, 1H), 7.75 (d, *J* = 8.0 Hz, 2H), 7.68 (s, 1H), 7.36 (d, *J* = 8.1 Hz, 2H), 7.32 (d, *J* = 8.3 Hz, 2H), 7.25 (s, 1H), 6.92 (d, *J* = 8.3 Hz, 2H), 4.82 (t, *J* = 5.2 Hz, 2H), 4.40 (t, *J* = 5.2 Hz, 2H), 4.25 (s, 2H), 4.03 (s, 2H), 2.39 (s, 3H). <sup>13</sup>C NMR (126 MHz, (CD<sub>3</sub>)<sub>2</sub>SO, 298 K) δ 158.14, 151.89, 150.81, 141.88, 141.79, 131.09, 130.63, 130.13 (q, *J* = 33.2 Hz), 130.07, 129.95, 129.90, 129.86, 124.62, 123.26 (q, *J* = 273.4 Hz), 122.57, 122.31, 114.55, 67.17, 50.46, 49.22, 44.85, 21.03. <sup>19</sup>F NMR (470 MHz, CD<sub>3</sub>CN, 298 K) δ -63.63 (s, 6F), -72.54 (d, *J* = 707.4 Hz, PF<sub>6</sub>).

## Synthesis of $E-1H^{2+}$



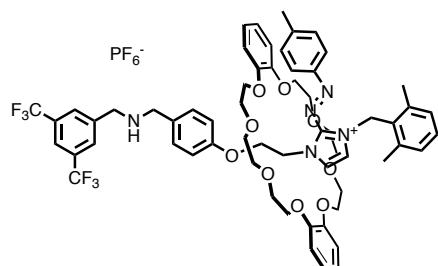
A solution of **2c** (230 mg, 0.326 mmol) and DB24C8 (292 mg, 0.652 mmol) in acetonitrile (15 mL) was stirred at room temperature for 30 min. Neat 2-(bromomethyl)-1,3-dimethylbenzene (325 mg, 1.63 mmol) was then added and the resulting mixture stirred at 80 °C in a microwave reactor for 2 h. The solution was cooled down to room temperature and the solvent removed under reduced pressure to provide a crude mixture which was dissolved in dichloromethane (50 mL), washed with water (3×50 mL) and a saturated aqueous solution of potassium hexafluorophosphate (3×20 mL) and dried over anhydrous MgSO<sub>4</sub>. The crude compound was purified by flash chromatography (dichloromethane, then 90:10 dichloromethane:methanol, then 0.1 M H<sub>4</sub>NPF<sub>6</sub> in methanol) and repeated Gel Permeation Chromatography (dichloromethane) to provide the product  $E-1H^{2+}$  as a bright orange solid (274 mg, 65%).



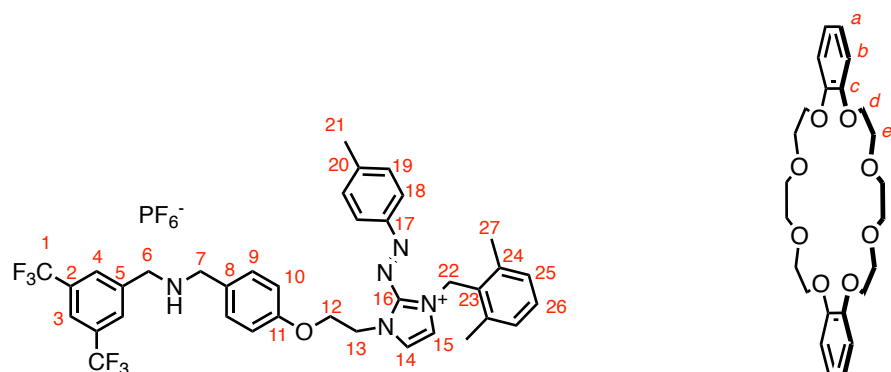
<sup>1</sup>H NMR (500 MHz, CD<sub>3</sub>CN, 298 K) δ 8.04 (d,  $J$  = 8.3 Hz, 2H, **18**), 7.85 (d,  $J$  = 1.7 Hz, 2H, **4**), 7.74 (s, 2H, NH<sub>2</sub>), 7.65 (d,  $J$  = 2.2 Hz, 1H, **14**), 7.51 (d,  $J$  = 8.2 Hz, 2H, **19**), 7.39 (d,  $J$  = 8.3 Hz, 2H, **9**), 7.34 - 7.27 (m, 2H, **3+26**), 7.20 (d,  $J$  = 7.6 Hz, 2H, **25**), 6.93 (d,  $J$  = 2.2 Hz, 1H, **15**), 6.87 (d,  $J$  = 8.3 Hz, 2H, **10**), 6.68 (dd,  $J$  = 6.1, 3.5 Hz, 4H, **b**), 6.59 (dd,  $J$  = 6.0, 3.6 Hz, 4H, **a**), 5.70 (s, 2H, **22**), 5.03 - 4.97 (m, 2H, **6**), 4.90 (t,  $J$  = 4.8 Hz, 2H, **13**), 4.50 - 4.46 (m, 2H, **7**), 4.40 (t,  $J$  = 4.8 Hz, 2H, **12**), 4.03 (ddd,  $J$  = 11.3, 7.9, 1.5 Hz, 4H, **d**), 3.87 - 3.79 (m, 8H, **d+e**), 3.74 - 3.65 (m, 12H, **e+f**), 2.50 (s, 3H, **21**), 2.28 (s, 6H, **27**). <sup>13</sup>C NMR (126 MHz, CD<sub>3</sub>CN, 298 K) δ 159.85 (**11**), 151.97 (**17**), 149.28 (**20**), 147.55 (**c**), 144.86 (**16**), 139.84 (**24**), 136.14 (**5**), 132.34 (**9**), 131.70 (**19**), 131.21 (q,  $J$  = 32.8 Hz, **2**), 131.04 (**4**), 130.99 (**26**), 130.01 (**25**), 129.67 (**23**), 125.60 (**14**), 125.54 (**18**), 125.04 (**8**), 124.09 (q,  $J$  = 273.4 Hz, **1**), 122.54 (m, **3**), 122.06 (**15**),

122.01 (**b**), 115.97 (**10**), 112.76 (**a**), 71.62 (**f**), 71.03 (**e**), 68.48 (**d**), 67.01 (**12**), 53.30 (**7**), 51.68 (**6**), 49.93 (**13**), 49.26 (**22**), 22.12 (**21**), 19.85 (**27**).  $^{19}\text{F}$  NMR (470 MHz,  $\text{CD}_3\text{CN}$ , 298 K)  $\delta$  – 63.00 (s, 6F, **1**), –72.89 (d,  $J = 706.5$  Hz, 12F,  $\text{PF}_6^-$ ). HRMS-ESI ( $m/z$ ): calcd for  $[\text{C}_{61}\text{H}_{69}\text{N}_5\text{O}_9\text{PF}_{12}]$ , 1274.4641; found 1274.4641  $[(\text{1H})(\text{PF}_6)]^+$ .

### Synthesis of $E\text{-1}^+$



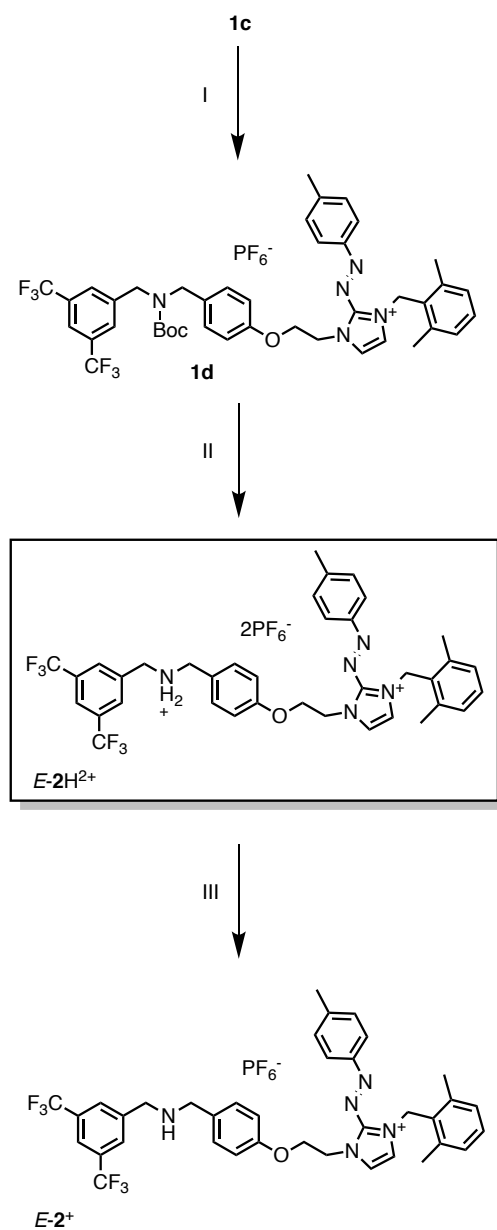
A solution of  $E\text{-1H}^{2+}$  (15 mg, 0.013 mmol) in  $\text{CD}_3\text{CN}$  (500  $\mu\text{L}$ ) was reacted with **B1** (20 mg) inside an NMR tube. The suspension was agitated for fixed time intervals and the reaction progress monitored by  $^1\text{H}$  NMR spectroscopy. Upon complete disappearance of the peaks of  $E\text{-1H}^{2+}$ , the mixture was filtered through a pad of Celite to isolate the solution containing  $E\text{-1}^+$ .



$^1\text{H}$  NMR (500 MHz,  $\text{CD}_3\text{CN}$ , 298 K)  $\delta$  8.57 (d,  $J = 2.2$  Hz, 1H, **14**), 8.25 (d,  $J = 8.1$  Hz, 2H, **18**), 7.94 (s, 2H, **4**), 7.87 (s, 1H, **3**), 7.43 (d,  $J = 8.0$  Hz, 2H, **19**), 7.26 (t,  $J = 7.6$  Hz, 1H, **26**), 7.13 (d,  $J = 7.6$  Hz, 2H, **25**), 7.03 (d,  $J = 8.1$  Hz, 2H, **9**), 6.80 (ddt,  $J = 22.3, 6.3, 3.7$  Hz, 8H, **b+a**), 6.71 (d,  $J = 2.2$  Hz, 1H, **15**), 6.61 (d,  $J = 8.1$  Hz, 2H, **10**), 5.60 (t,  $J = 7.9$  Hz, 2H, **13**), 5.36 (s, 2H, **22**), 4.84 (t,  $J = 7.9$  Hz, 2H, **12**), 4.05 - 3.92 (m, 8H, **d**), 3.86 (s, 2H, **6**), 3.66 (m, 10H, **7+e**), 3.43 (ddd,  $J = 87.5, 10.9, 6.5$  Hz, 8H, **f**), 2.47 (s, 3H, **21**), 2.08 (s, 6H, **27**).  $^{13}\text{C}$  NMR (126 MHz,  $\text{CD}_3\text{CN}$ , 298 K)  $\delta$  158.85 (**11**), 152.02 (**17**), 148.86 (**c**), 148.34 (**20**), 145.70 (**5**), 144.36 (**16**), 139.49 (**24**), 133.03 (**8**), 131.71 (q,  $J = 32.8$  Hz, **2**), 131.37 (**19**), 130.71 (**26**), 130.33 (**23**), 129.93 (**9**), 129.85 (**25**), 129.52 (**4**), 126.99 (**14**), 126.06 (**18**), 124.84 (q,  $J = 273.4$  Hz, **1**), 121.83 (**b**), 121.47 (**3**), 120.93 (**15**), 115.20 (**10**), 112.91 (**a**), 71.59 (**f**), 70.92 (**e**), 69.09 (**d**), 65.57 (**12**), 53.00 (**7**), 52.29 (**6**), 49.44 (**22**), 47.77 (**13**), 22.03 (**21**), 19.92 (**27**).  $^{19}\text{F}$  NMR

(470 MHz, CD<sub>3</sub>CN, 298 K)  $\delta$  -63.25 (s, 6F, **1**), -72.97 (d,  $J = 706.3$  Hz, 6F, PF<sub>6</sub>). HRMS-ESI (m/z): calcd for [C<sub>61</sub>H<sub>68</sub>N<sub>5</sub>O<sub>9</sub>], 1128.4921; found 1128.4921 [**1**]<sup>+</sup>.

### 2.9.3. Synthesis of the model compound $E-2H^{2+}$

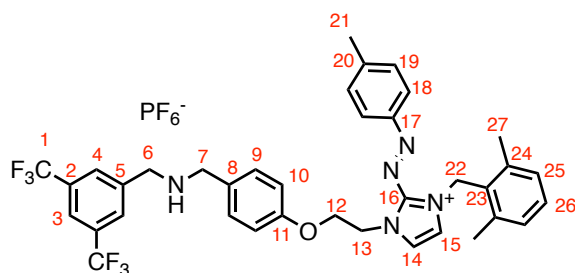


Scheme 6. I) a. *o*-Me<sub>2</sub>-BnBr, CH<sub>3</sub>CN, reflux. b. NH<sub>4</sub>PF<sub>6</sub> 93% II) HPF<sub>6</sub>, THF. 41% III) Base, CH<sub>3</sub>CN.





## Synthesis of E-2<sup>+</sup>



A solution of *E*-2H<sup>2+</sup> (25 mg, 0.026 mmol) in acetonitrile (5 mL) was loaded on a silica pad and eluted with 20 mL of solvent. Removal of the solvent under reduced pressure provided the product as an orange solid (21 mg, quantitative).

<sup>1</sup>H NMR (500 MHz, CD<sub>3</sub>CN, 298 K) δ 8.01 (d, *J* = 8.3 Hz, 2H, **18**), 7.91 (d, *J* = 1.6 Hz, 2H, **4**), 7.85 (s, 1H, **3**), 7.64 (d, *J* = 2.2 Hz, 1H, **14**), 7.49 (d, *J* = 8.3 Hz, 2H, **19**), 7.31 (dd, *J* = 8.1, 7.1 Hz, 1H, **26**), 7.22 - 7.17 (m, 4H, **25+9**), 6.90 (d, *J* = 2.2 Hz, 1H, **15**), 6.80 (d, *J* = 8.3 Hz, 2H, **10**), 5.68 (s, 2H, **22**), 4.88 (t, *J* = 6.3 Hz, 2H, **13**), 4.41 (t, *J* = 6.3 Hz, 2H, **12**), 3.85 (s, 2H, **6**), 3.64 (s, 2H, **7**), 2.49 (s, 3H, **21**), 2.28 (s, 6H, **27**). <sup>13</sup>C NMR (126 MHz, CD<sub>3</sub>CN, 298 K) δ 157.85, 151.96, 149.19, 145.62, 144.83, 139.85, 134.64, 131.86, 131.66, 131.60, 130.98, 130.44, 129.99, 129.65, 129.46, 125.57, 125.49, 121.96, 121.49, 115.25, 68.30, 66.87, 52.95, 52.40, 50.05, 49.25, 26.26, 22.08, 19.82. <sup>19</sup>F NMR (470 MHz, CD<sub>3</sub>CN, 298 K) δ -63.31 (s, 6F, **1**), -72.96 (d, *J* = 706.3 Hz, 6F, PF<sub>6</sub>). HRMS-ESI (*m/z*): calcd for [C<sub>37</sub>H<sub>36</sub>N<sub>5</sub>OF<sub>6</sub>], 680.2824; found 680.2824 [**2**]<sup>+</sup>.

## 2.10. NMR spectra

$^1\text{H}$  and  $^{13}\text{C}$  NMR spectra of  $E\text{-}1\text{H}^{2+}$

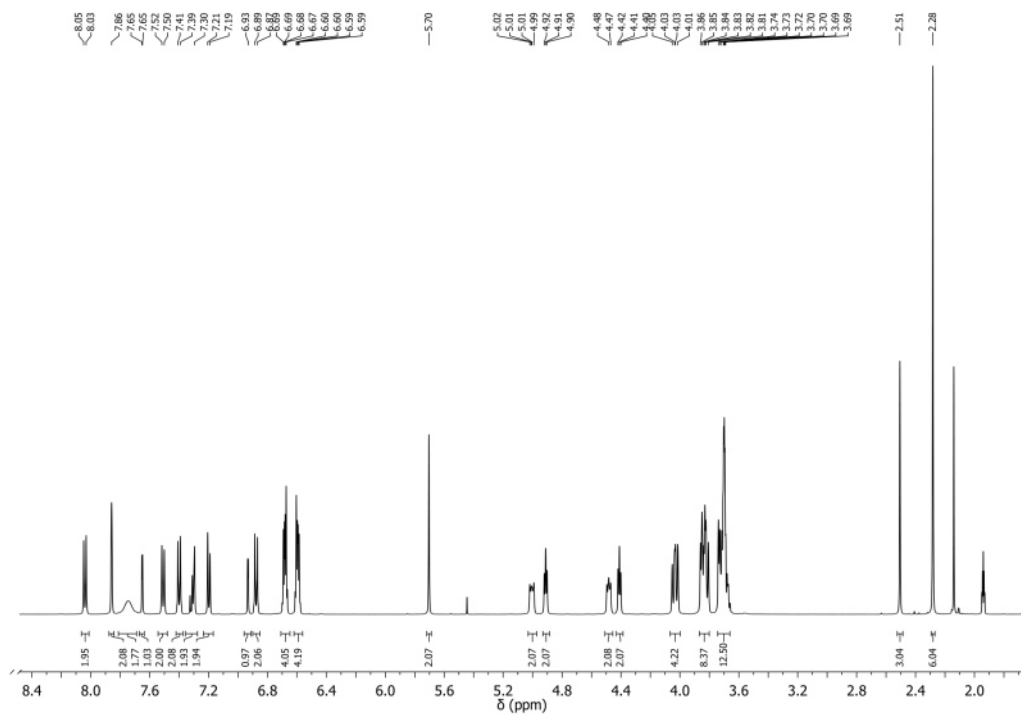


Figure 16.  $^1\text{H}$  NMR spectrum of  $E\text{-}1\text{H}^{2+}$  ( $\text{CD}_3\text{CN}$ , 298 K, 500 MHz).

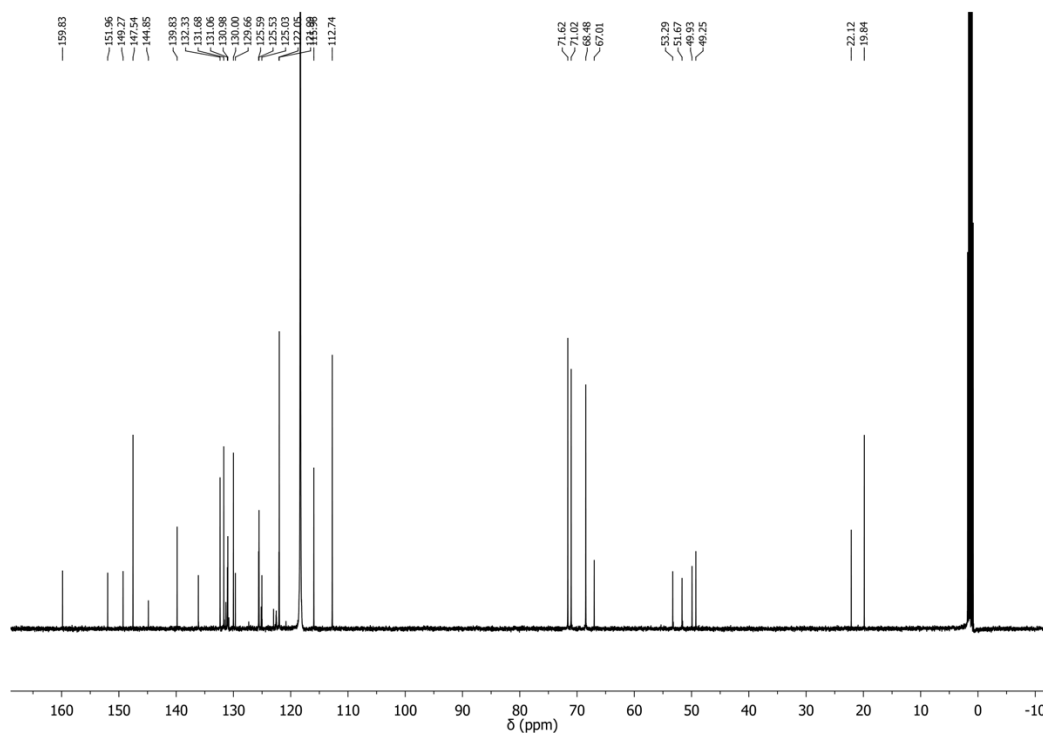


Figure 17.  $^{13}\text{C}$  NMR spectrum of  $E\text{-}1\text{H}^{2+}$  ( $\text{CD}_3\text{CN}$ , 298 K, 126 MHz).

## HSQC and HMBC spectra of $E-1H^{2+}$

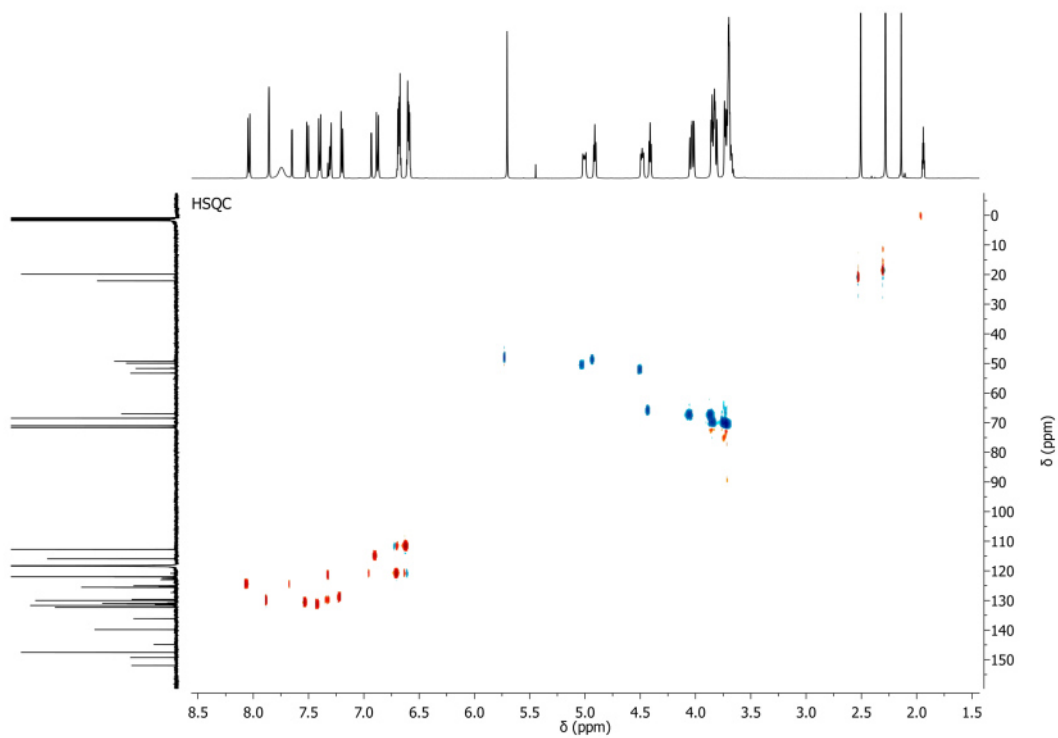


Figure 18. Heteronuclear Single Quantum coherence Spectroscopy (HSQC).  $E-1H^{2+}$ ,  $f1$ :  $^{13}C$  NMR,  $f2$ :  $^1H$  NMR, ( $CD_3CN$ , 298 K, 126 MHz, 500 MHz).

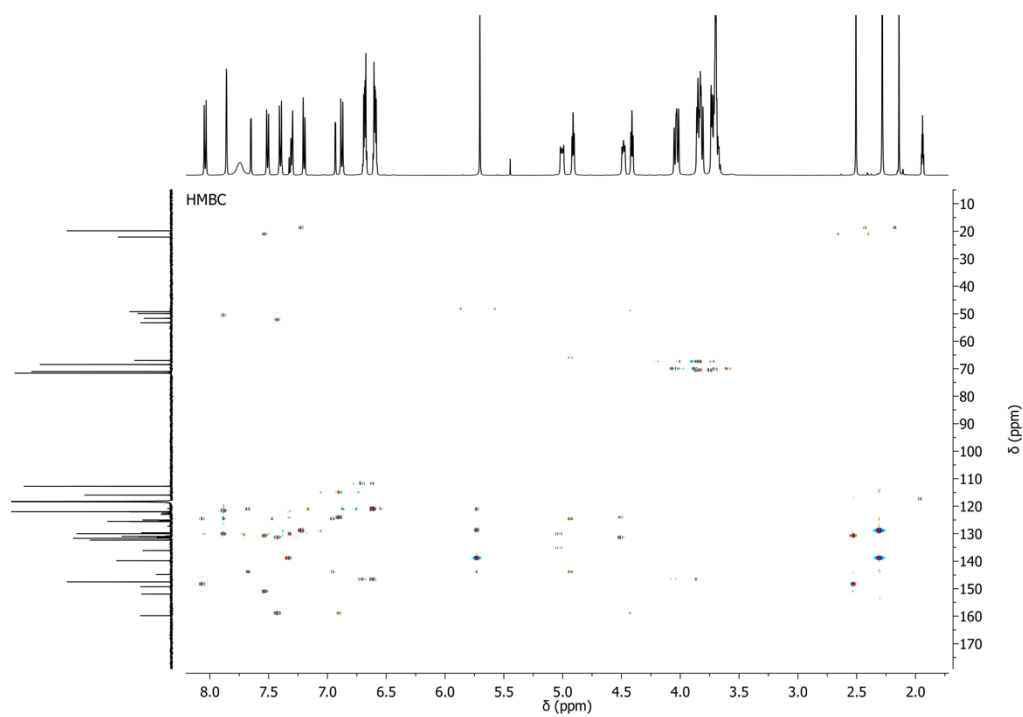


Figure 19. Heteronuclear Multiple Bond Correlation (HMBC).  $E-1H^{2+}$ ,  $f1$ :  $^{13}C$  NMR,  $f2$ :  $^1H$  NMR, ( $CD_3CN$ , 298 K, 126 MHz, 500 MHz).

$^1\text{H}$  and  $^{13}\text{C}$  NMR spectra of  $E-1^+$

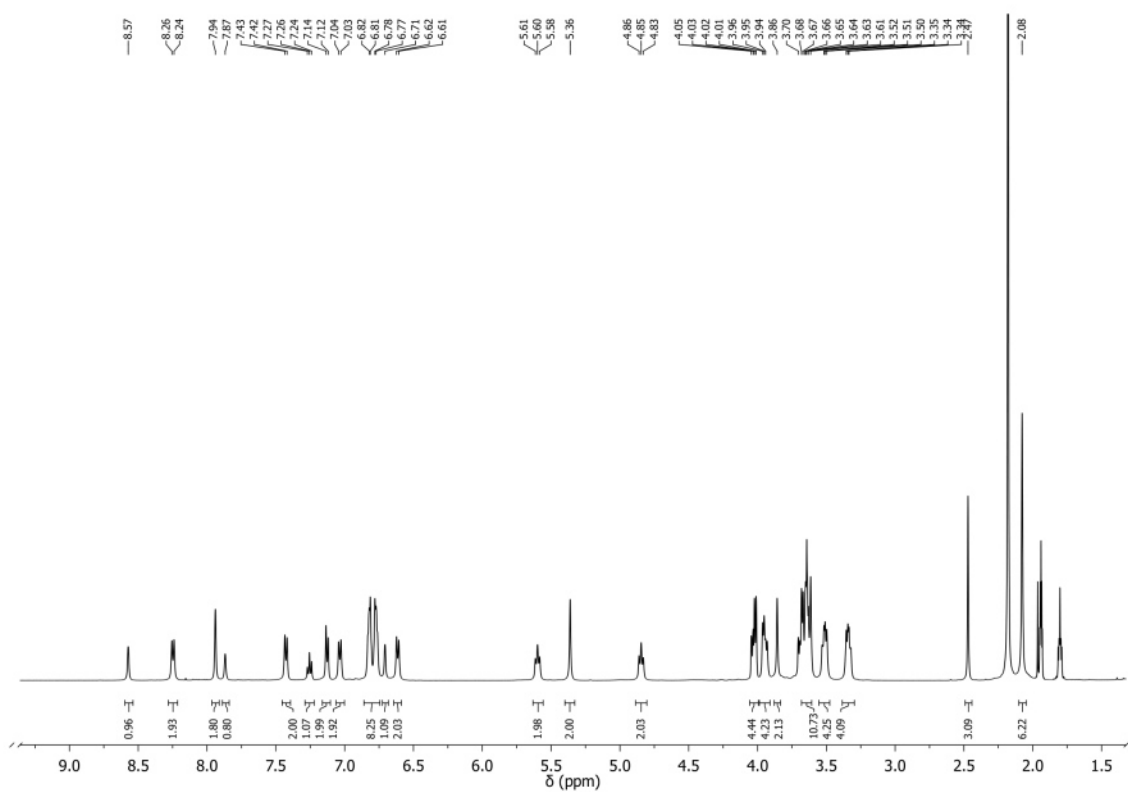


Figure 20.  $^1\text{H}$  NMR spectrum of  $E-1^+$  ( $\text{CD}_3\text{CN}$ , 298 K, 500 MHz).

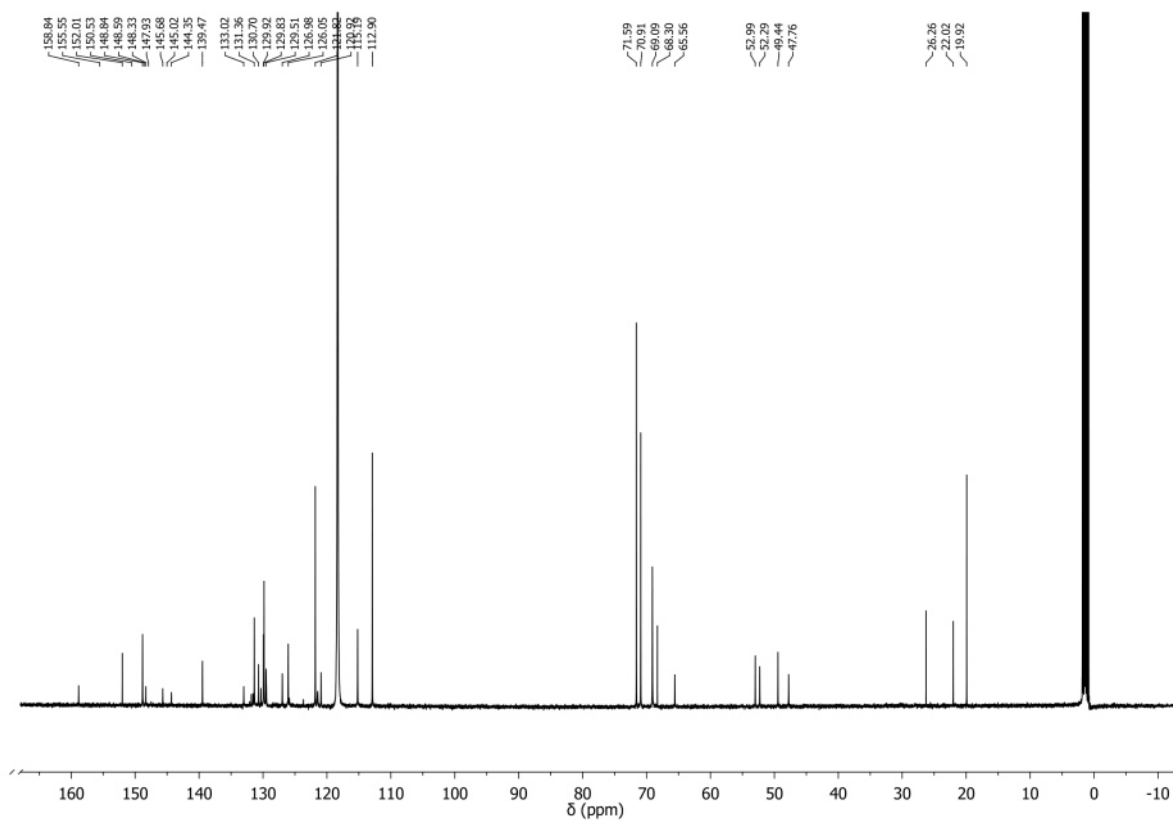


Figure 21.  $^{13}\text{C}$  NMR spectrum of  $E-1^+$  ( $\text{CD}_3\text{CN}$ , 298 K, 126 MHz).

## HSQC and HMBC spectra of $E-1^+$

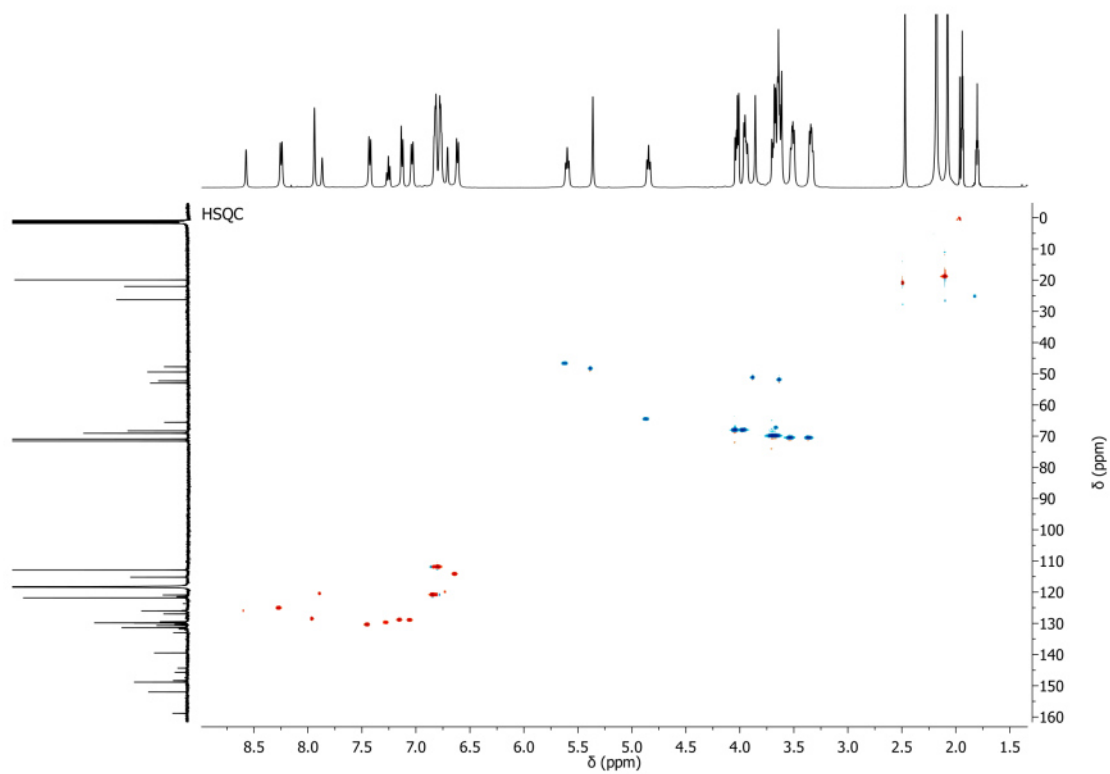


Figure 22. Heteronuclear Single Quantum coherence Spectroscopy (HSQC).  $E-1^+$ ,  $f1$ :  $^{13}\text{C}$  NMR,  $f2$ :  $^1\text{H}$  NMR, ( $\text{CD}_3\text{CN}$ , 298 K, 126 MHz, 500 MHz).

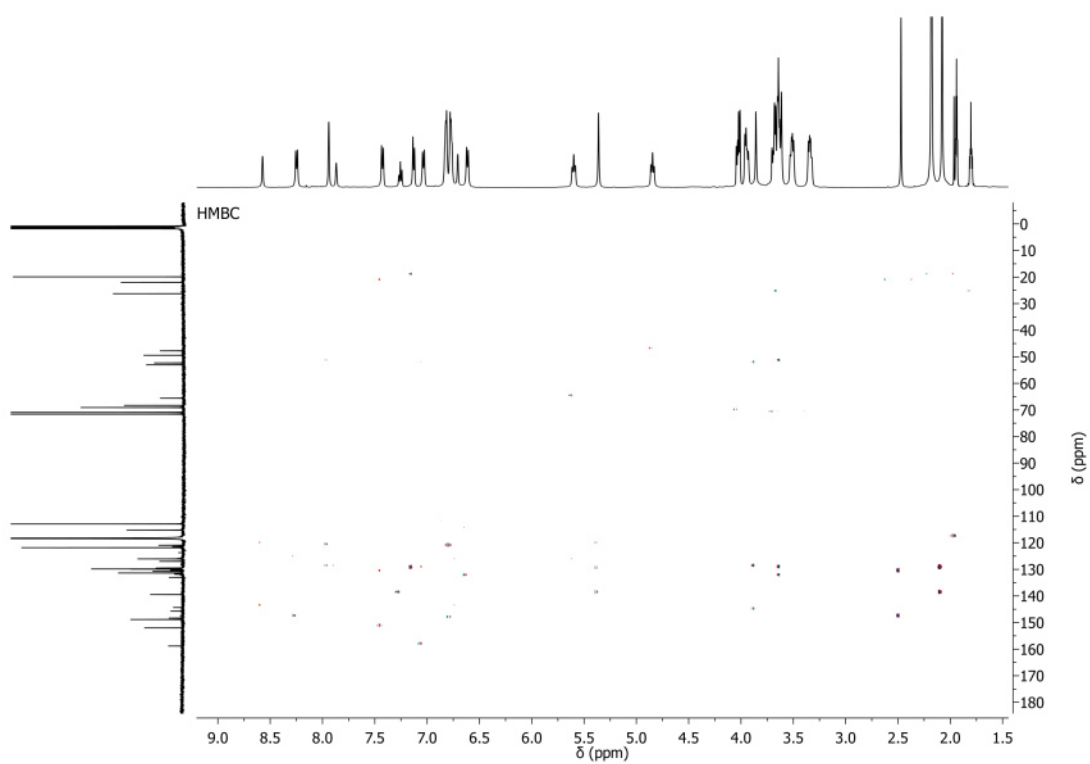


Figure 23. Heteronuclear Multiple Bond Correlation (HMBC).  $E-1^+$ ,  $f1$ :  $^{13}\text{C}$  NMR,  $f2$ :  $^1\text{H}$  NMR, ( $\text{CD}_3\text{CN}$ , 298 K, 126 MHz, 500 MHz).

# $^1\text{H}$ and $^{13}\text{C}$ NMR spectra of $E\text{-}2\text{H}^{2+}$

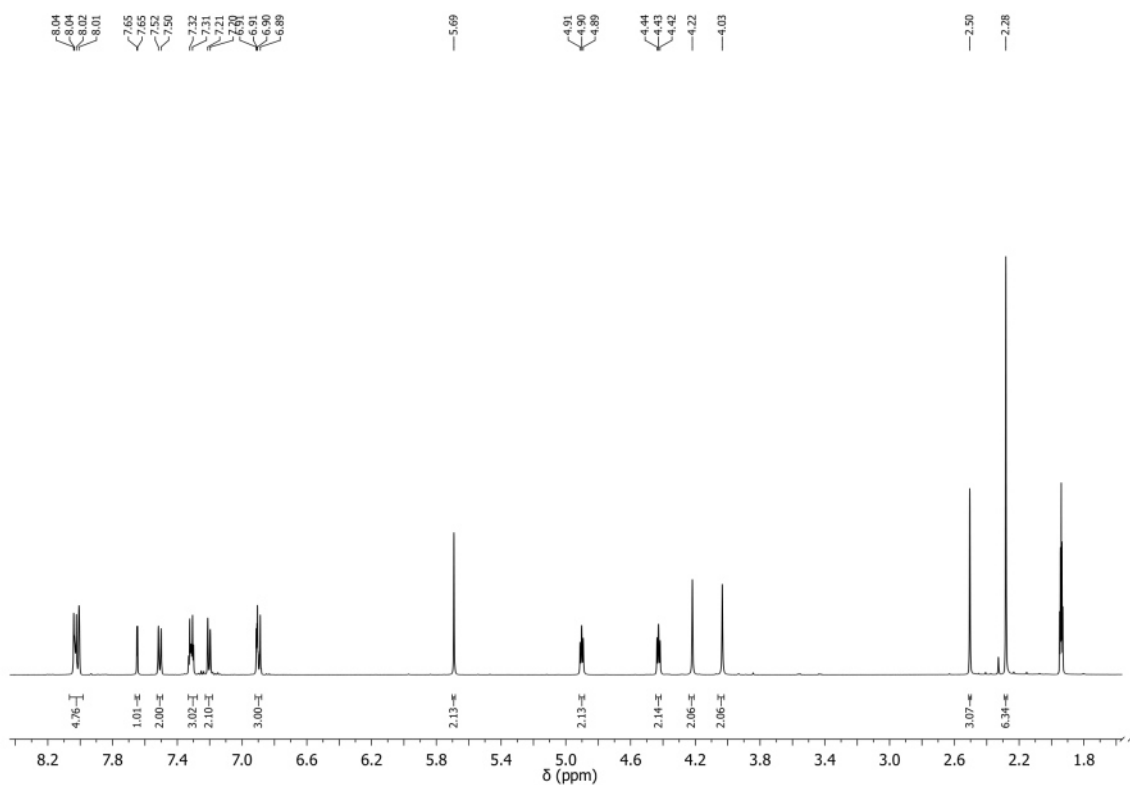


Figure 24.  $^1\text{H}$  NMR spectrum of  $E\text{-}2\text{H}^{2+}$  ( $\text{CD}_3\text{CN}$ , 298 K, 500 MHz).

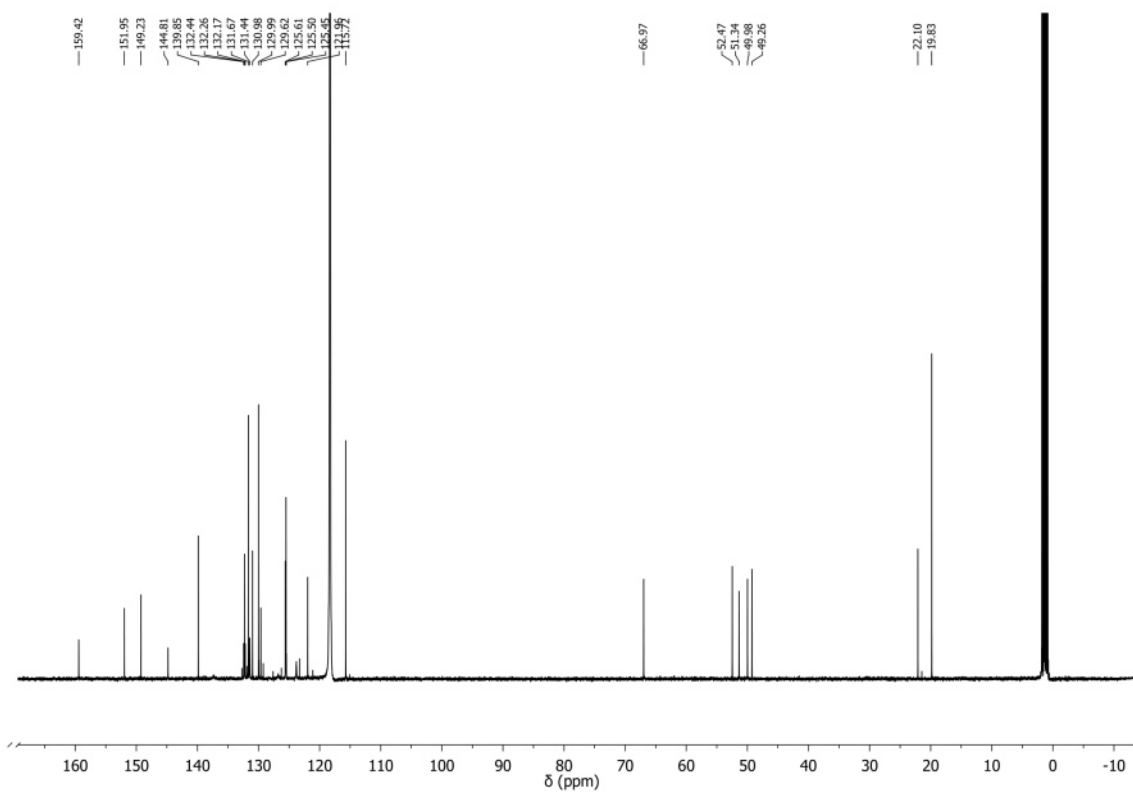


Figure 25.  $^{13}\text{C}$  NMR spectrum of  $E\text{-}2\text{H}^{2+}$  ( $\text{CD}_3\text{CN}$ , 298 K, 126 MHz).

## HSQC and HMBC spectra of $E\text{-}2\text{H}^{2+}$

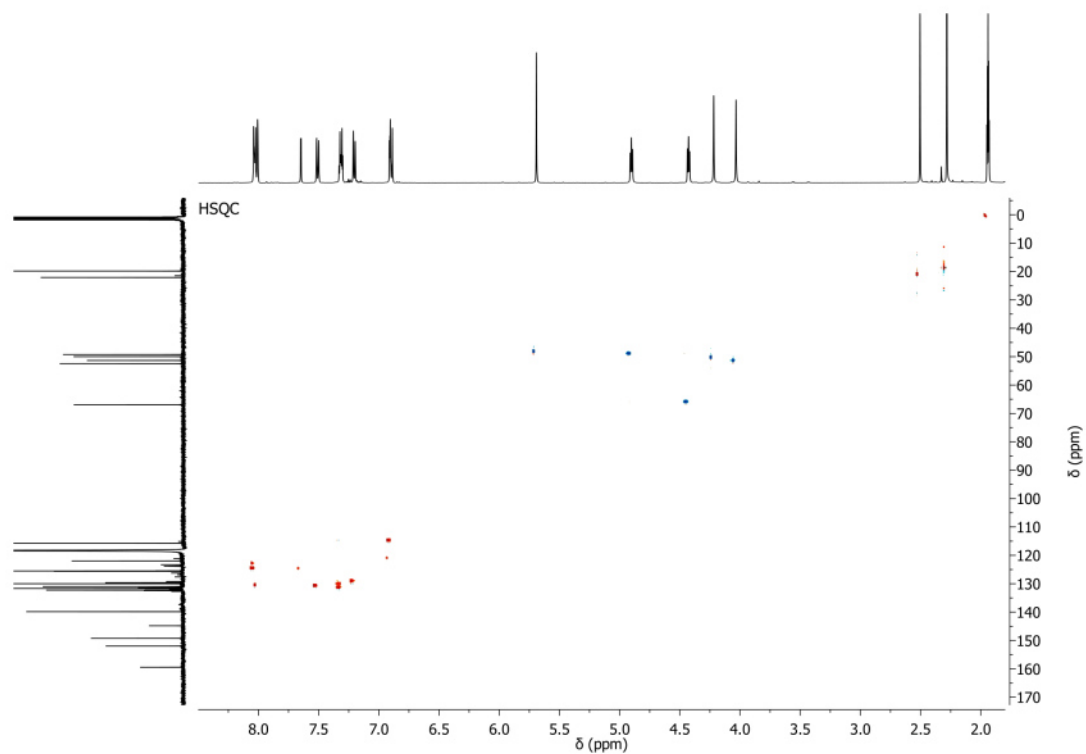


Figure 26. Heteronuclear Single Quantum coherence Spectroscopy (HSQC).  $E\text{-}2\text{H}^{2+}$ ,  $f1$ :  $^{13}\text{C}$  NMR,  $f2$ :  $^1\text{H}$  NMR, ( $\text{CD}_3\text{CN}$ , 298 K, 126 MHz, 500 MHz).

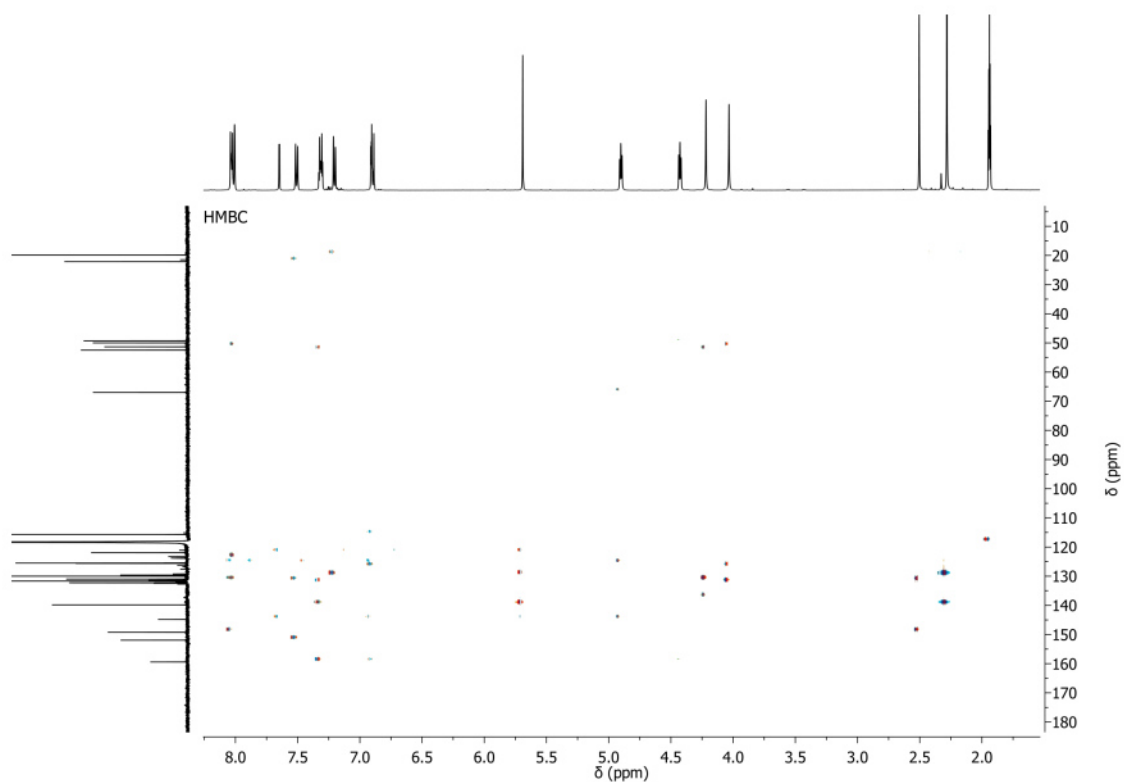


Figure 27. Heteronuclear Multiple Bond Correlation (HMBC).  $E\text{-}2\text{H}^{2+}$ ,  $f1$ :  $^{13}\text{C}$  NMR,  $f2$ :  $^1\text{H}$  NMR, ( $\text{CD}_3\text{CN}$ , 298 K, 126 MHz, 500 MHz).

$^1\text{H}$  and  $^{13}\text{C}$  NMR spectra of  $E\text{-}2^+$

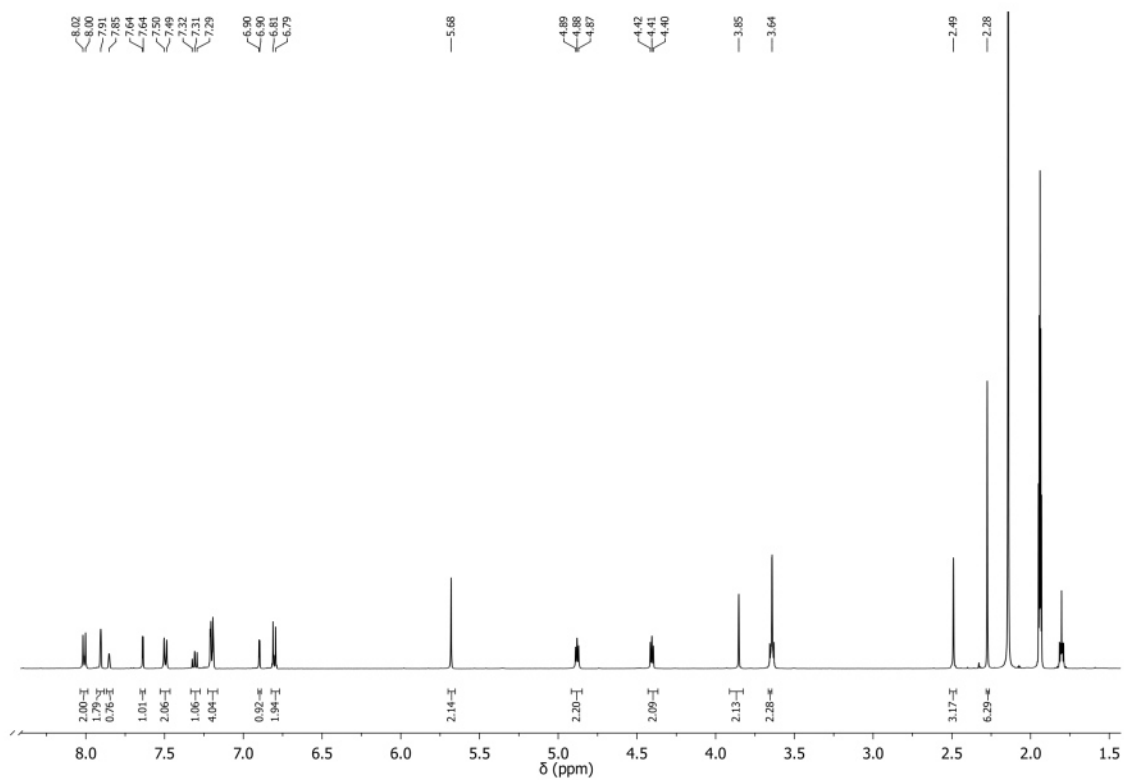


Figure 28.  $^1\text{H}$  NMR spectrum of  $E\text{-}2^+$  ( $\text{CD}_3\text{CN}$ , 298 K, 500 MHz).

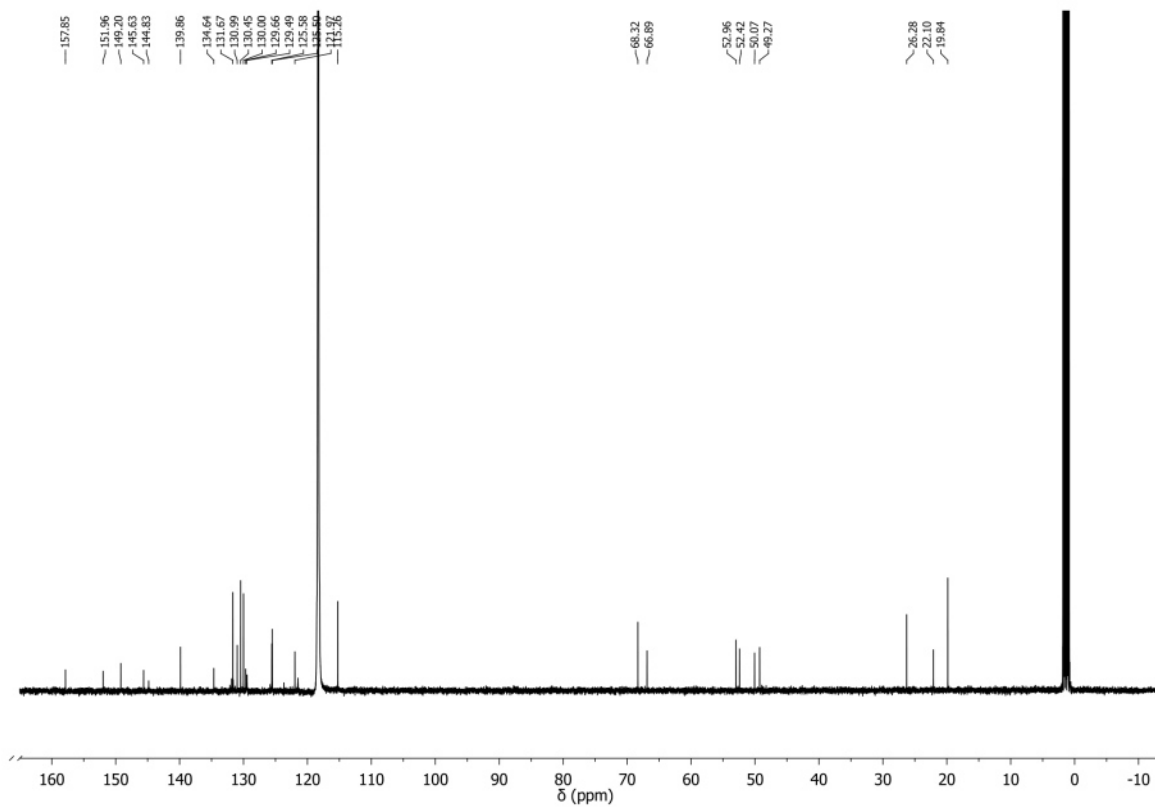


Figure 29.  $^{13}\text{C}$  NMR spectrum of  $E\text{-}2^+$  ( $\text{CD}_3\text{CN}$ , 298 K, 126 MHz).

## 2.11. References

1. M. V. Martínez-Díaz, N. Spencer & J. F. Stoddart, *Angew. Chem. Int. Ed. Eng.*, **1997**, *36*(17), 1904-1907.
2. H. Y. Zhou, Y. Han & C. F. Chen, *Mater. Chem.*, **2020**, *4*(1), 12-28.
3. D. Thibeault & J. F. Morin, *Molecules*, **2010**, *15*(5), 3709-3730.
4. V. Blanco, A. Carlone, K. D. Hänni, D. A. Leigh & B. Lewandowski, *Angew. Chem. Int. Ed.*, **2012**, *51*, 5166-5169.
5. C. S. Kwan, A. S. Chan & K. C. F. Leung, *Org. Lett.*, **2016**, *18*(5), 976-979.
6. A. Goujon, T. Lang, G. Mariani, E. Moulin, G. Fuks, J. Raya, E. Buhler & N. Giuseppone, *J. Am. Chem. Soc.*, **2017**, *139*(42), 14825-14828.
7. C. J. Bruns & J. F. Stoddart, *Acc. Chem. Res.*, **2014**, *47*(7), 2186-2199.
8. F. Coutrot & E. Busseron, *Chem. – Eur. J.*, **2008**, *14*, 4784.
9. C. Schäfer, G. Ragazzon, B. Colasson, M. La Rosa, S. Silvi & A. Credi, *ChemistryOpen*, **2016**, *5*(2), 120.
10. K. Zhu, G. Baggi & S. J. Loeb, *Nat. Chem.* **2018**, *10*, 625- 630.
11. A. C. Fahrenbach, C. J. Bruns, D. Cao & J. F. Stoddart, *Acc. Chem. Res.*, **2012**, *45*(9), 1581-1592.
12. M. Curcio, F. Nicoli, E. Paltrinieri, E. Fois, G. Tabacchi, L. Cavallo, S. Silvi, M. Baroncini & A. Credi, *J. Am. Chem. Soc.*, **2021**, *143*(21), 8046-8055.
13. M. Cesario, C. O. Dietrich, A. Edel, J. Guilhem, J. P. Kintzinger, C. Pascard & J. P. Sauvage, *J. Am. Chem. Soc.*, **1986**, *108*(20), 6250-6254.
14. N. Kihara, Y. Tachibana, H. Kawasaki & T. Takata, *Chem. Lett.*, **2000**, *29*(5), 506-507.
15. G. Ragazzon, C. Schäfer, P. Franchi, S. Silvi, B. Colasson, M. Lucarini & A. Credi, *PNAS*, **2018**, *115*(38), 9385-9390.
16. V. Balzani, A. Credi & M. Venturi, *Chem. Soc. Rev.*, **2009**, *38*(6), 1542-1550.
17. E. Moulin, L. Faour, C. C. Carmona-Vargas & N. Giuseppone, *Adv. Mat.*, **2020**, *32*(20), 1906036.
18. P. Ceroni, A. Credi, M. Venturi, *Chem. Soc. Rev.* **2014**, *43*, 4068-4083.
19. M. Baroncini, S. Silvi & A. Credi, *Chem. Rev.* **2020**, *120*, 200-268.
20. S. Corrà, M. Curcio, M. Baroncini, S. Silvi & Credi, *Adv. Mater.* **2020**, *32*, 1906064.
21. V. García-López, F. Chen, L. G. Nilewski, G. Duret, A. Aliyan, A. B. Kolomeisky, J. T. Robinson, G. Wang, R. Pal, J. M. Tour, *Nature*, **2017**, *548*, 567- 572.

22. W. Danowski, T. van Leeuwen, S. Abdolazadeh, D. Roke, W. R. Browne, S. J. Wezenberg, B. L. Feringa, *Nat. Nanotechnol.* **2019**, *14*, 488-494.
23. Y. Zheng, M. K. L. Han, R. Zhao, J. Blass, J. Zhang, D. W. Zhou, J.-R. Colard-Itte, D. Dattler, A. Colak, M. Hoth, A. J. Garcia, B. Qu, R. Bennewitz, N. Giuseppone, A. del Campo, *Nat. Commun.* **2021**, *12*, 3580.
24. L. Andreoni, M. Baroncini, J. Groppi, S. Silvi, C. Taticchi & A. Credi, *Energy & Fuels*, **2021**, *35*(23), 18900-18914.
25. D. Prischich, A. M. J. Gomila, S. Milla-Navarro, G. Sangüesa, R. Diez-Alarcia, B. Preda, C. Matera, M. Batlle, L. Ramírez, E. Giralt, J. Hernando, E. Guasch, J. J. Meana, P. de la Villa, P. Gorostiza, *Angew. Chem. Int. Ed.* **2021**, *60*, 3625-3631.
26. T. Asaka, N. Akai, A. Kawai, K. Shibuya, *J. Photochem. Photobiol. A* **2010**, *209*, 12-18.
27. A. Kawai, D. Kawamori, T. Monji, T. Asaka, N. Akai, K. Shibuya, *Chem. Lett.*, **2010**, *39*, 230-231.
28. D. Mallick, A. Nandi, S. Datta, K. K. Sarker, T. K. Mondal, C. Sinha, *Polyhedron* **2012**, *31*, 506-514.
29. *Comprehensive Heterocyclic Chemistry III*, Volume 4, **2008**, Pages 143-364
30. M. Baroncini, S. Silvi, M. Venturi & A Credi, *Chem. Eur. J.*, **2010**, *16*, 11580–11587.
31. a) C. Feldmeier, H. Bartling, E. Riedle, R. M. Gschwind, *J. Magn. Reson.* **2013**, *232*, 39-44; b) P. Nitschke, N. Lokesh, R. M. Gschwind, *Prog. Nucl. Magn. Reson. Spectrosc.* **2019**, *114*, 86-134.
32. M. Dong, A. Babalhavaeji, S. Samanta, A. A. Beharry & G. A. Woolley, *Acc. Chem. Res.*, **2015**, *48*(10), 2662-2670.
33. S. Erbas-Cakmak, A.D. Leigh, C. T. McTernan & A. L. Nussbaumer. *Chem. Rev.*, **2015**, *115*(18), 10081-10206.
34. M. Baroncini, S. Silvi & A. Credi, *Chem. Rev.*, **2019**, *120*(1), 200-268.
35. P. Reimann, *Phys. Rep.* **2002**, *361*, 57–265.
36. S. Amano, S. Borsley, D. A. Leigh & A. Sun, *Nat. Nanotech.*, **2021**, *16*(10), 1057-1067.

**Chapter 3:** *Chemical induced mismatch of rings and stations in a [3]rotaxane*

### 3.1. Introduction

Mechanically interlocked molecules such as rotaxanes have found their application in disparate fields of chemistry such as structural and functional materials,<sup>1-5</sup> catalysis,<sup>6,7</sup> nanomedicine,<sup>8</sup> molecular electronics,<sup>9,10</sup> and molecular machines.<sup>11-13</sup> The interest about these molecules is often addressed to their peculiar structural and dynamic properties;<sup>14,15</sup> indeed, specific functions can be achieved through the control of the relative arrangement of the components. As an example, the localization of the ring along the axle can be controlled through the application of external stimuli. This task is achieved through the modulation of the supramolecular interactions between rings and recognition sites (or stations) present on the axle moiety. Importantly, in the design of rotaxanes, the balance between the number of stations ( $n_S$ ) and rings ( $n_R$ ) can result in markedly different properties. Figure 1 depicts all the possibilities that can be obtained by varying the number of stations ( $n_S$ ) in relation to the number of rings ( $n_R$ ) in a rotaxane architecture.

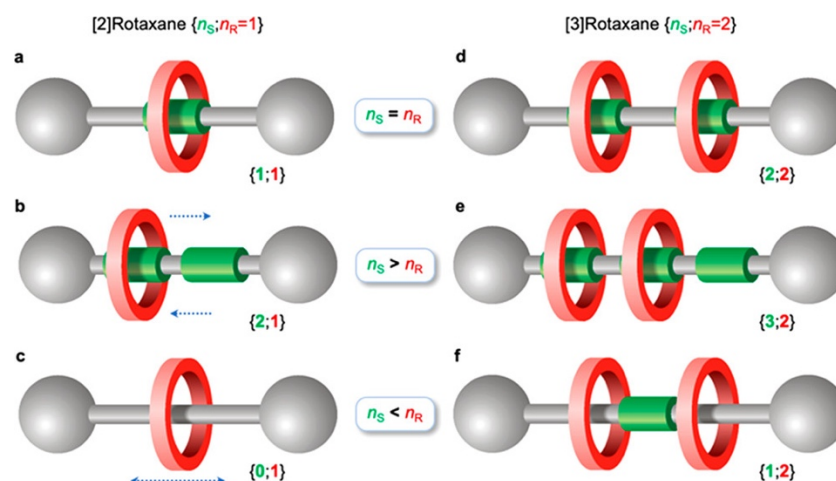


Figure 1. Graphical representation of [2]rotaxanes (left) and [3]rotaxanes (right). The number of recognition sites, or stations ( $n_S$ ), is respectively (a, d) equal to, (b, e) higher than, and (c, f) lower than the number of macrocyclic rings ( $n_R$ ). The blue arrows in b and c highlight the kind of translational movements that are typically observed in these rotaxanes. Reproduced with permission from reference 16.

The case in which  $n_S = n_R$  is quite common, in this situation, each ring sits on a recognition site. Conversely, when  $n_S > n_R$  the ring shuttles between the two stations, the translation can occur randomly or can be controlled with chemical or physical stimuli.<sup>5,6,9,10,14,15</sup> When  $n_S < n_R$  a much more interesting situation is realized. Indeed, in this case, the rings are forced to compete between them to accommodate a recognition site, thus dynamic effects are expected to emerge.<sup>17-21</sup> In particular, in a [3]rotaxane the case in which  $n_S < n_R$  results in a frustrated structure where two rings interact with a single station.<sup>22</sup> The competition between the two rings can lead to a highly dynamic system characterized by an equilibrium between several different conformations.

### 3.1.2. Objective of the project and $\text{RotH}_2^{3+}$ structure

In this chapter is described the design, synthesis and investigation of [3]rotaxane  $\text{RotH}_2^{3+}$  (Figure 2, top) in which the number of recognition sites can be changed upon application of an external stimulus. This interlocked molecule is composed by two DB24C8 macrocycles and is endowed with two lateral ammonium recognition sites and one central triazolium station in its linear component. The mono-deprotonation of one ammonium site in  $\text{RotH}_2^{3+}$  switches from the case  $n_S > n_R$  to the state  $n_S = n_R$ , in which macrocycles and recognition sites are in equal number.

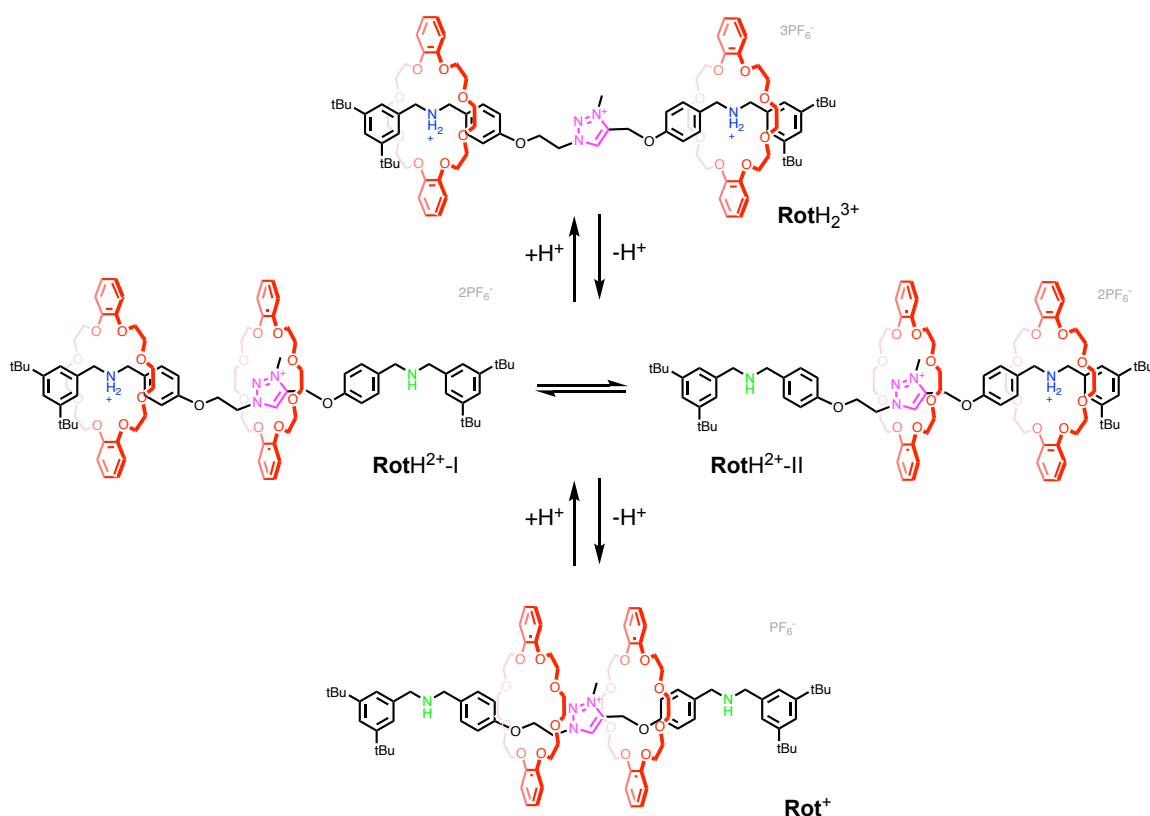


Figure 2. Structural formulas and network of [3]rotaxanes interconverted from acid-base reactions.

The two rotaxanes  $\text{RotH}^{2+}$ -I and  $\text{RotH}^{2+}$ -II formed upon mono deprotonation exist as isomers because of the non-symmetrical nature of the axle. Moreover, they are interconverted by a combination of ring shuttling and proton exchange. Upon addition of a further equivalent of base, the monocationic  $\text{Rot}^+$  is formed. This species is particularly interesting because the two macrocycles compete for the only remaining triazolium station ( $n_S < n_R$ ). Furthermore, it has to be noted that the  $pK_a$  of an ammonium station in a rotaxane is affected by the supramolecular interaction with the ring.<sup>23-25</sup> Considering these premises a peculiar behavior was expected for

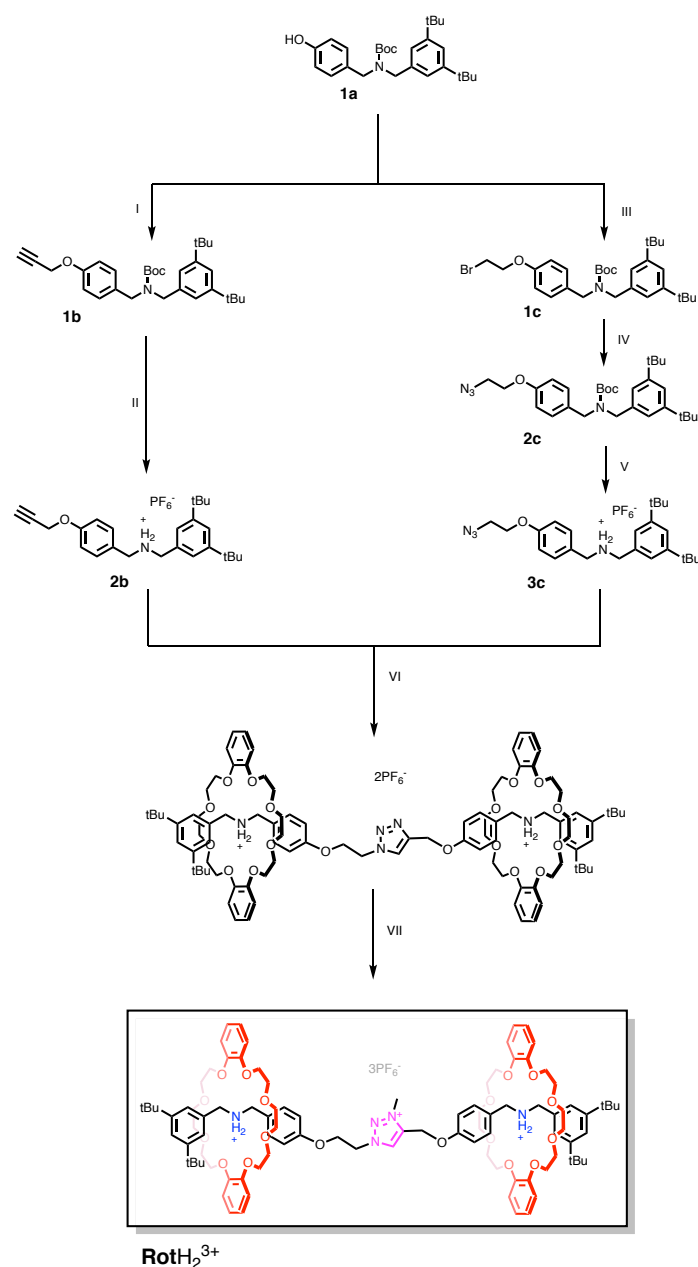
this rotaxane upon treatment with a base. The attention was also focused on the properties of the isomeric rotaxanes **RotH**<sup>2+</sup>. To conclude, the dynamic properties of the fully deprotonated rotaxane **Rot**<sup>+</sup> were investigated. The entire set of species depicted in Figure 2 was studied by UV-visible and NMR spectroscopy in combination with computational techniques.

The study of this system is relevant for the investigation of the unconventional chemical reactions that occur in rotaxanes. Furthermore, this project contributed to increase our knowledge about switchable [3]rotaxanes, indeed, despite their huge potential,<sup>26,27</sup> these compounds are still less investigated than [2]rotaxane.<sup>28</sup>

## 3.2. Synthesis of $\text{RotH}_2^{3+}$ and model compound **1**

### 3.2.1. Synthesis of $\text{RotH}_2^{3+}$

The preparation of [3]rotaxane  $\text{RotH}_2^{3+}$  followed a convergent strategy. Starting from Boc-protected precursor **1a** (Scheme 1), two different synthetic routes were followed to afford compounds **2b** and **3c** that were finally reacted in a last convergent step (VI).

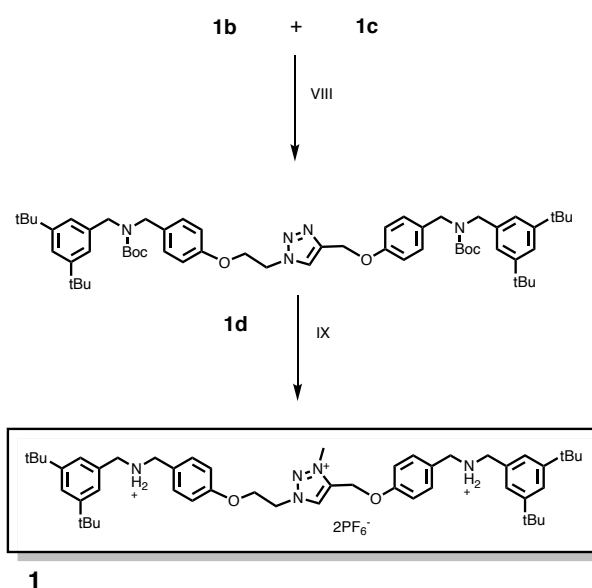


Scheme 1. Synthetic Route to the precursor  $\text{RotH}_2^{3+}$ : I)  $\text{BrCH}_2\text{CCH}$ ,  $\text{K}_2\text{CO}_3$ , MeCN. 94% II)  $\text{HPF}_6$ , THF. 75% III)  $\text{BrC}_2\text{H}_4\text{Br}$ ,  $\text{K}_2\text{CO}_3$ , MeCN. 42% IV)  $\text{NaN}_3$ , DMF. 83% V)  $\text{HPF}_6$ , THF. 72%. VI) DB24C8,  $[(\text{MeCN})_4\text{Cu}][\text{PF}_6]$ , DCM. 78% VII) MeI,  $\text{KPF}_6$ . 91%.

The nucleophilic substitution of **1a** provided the alkyne derivative **1b** in excellent yield. Successively, deprotection of **1b** with hexafluorophosphoric acid afforded the final dibenzyl

ammonium salt **2b**. The hexafluorophosphate salt of **3c** was obtained in three steps: firstly, compound **1c** was prepared through a nucleophilic substitution of **1a** with dibromoethane, then the azido precursor **2c** was synthesized. Deprotection of the latter in hexafluorophosphoric acid provided salt **3c**. The title [3]rotaxane was obtained by exploiting the strong supramolecular interaction between dibenzylammonium hexafluorophosphate salts and 24-crown-8 ethers in apolar solvent such as dichloromethane (DCM),<sup>15</sup> A mixture of compound **2b** and **3c** with an excess of DB24C8 were dissolved in DCM, the addition of Cu (I) catalyzed the azido-alkyne coupling reaction (CuAAC) of the two self-assembled pseudorotaxane halves affording the interlocked [3]rotaxane. In the last synthetic step, methylation of the triazole moiety was performed in neat methyl iodide. Subsequent anion exchange with ammonium hexafluorophosphate provided the final product (**RotH<sub>2</sub><sup>3+</sup>**).

### 3.2.2 Synthesis of the free axle **1**



*Scheme 2. Synthetic Route to the model axle **1**: VII) [(MeCN)<sub>4</sub>Cu][PF<sub>6</sub>], DCM. 84% IX) a. MeI, a. TFA/Na<sub>2</sub>CO<sub>3</sub> c. HCl/NH<sub>4</sub>PF<sub>6</sub>. 41%.*

The compounds **1b** and **1c** were also employed for the synthesis of the model axle **1** in which no rings are interlocked on the linear molecule (Scheme 2). Compound **1d** was obtained by means of a CuAAC reaction followed by methylation of the triazole unit. In the final step, the doubly Boc-protected compound was reacted in trifluoroacetic acid to remove the protecting groups. Successively, the axle was protonated with hydrochloric acid and the anion was exchanged using a saturated solution of ammonium hexafluorophosphate to yield the model compound **1**.

### 3.3. $^1\text{H}$ NMR characterization of $\text{RotH}_2^{3+}$

The resonances of the proton and carbon nuclei of the tricationic  $\text{RotH}_2^{3+}$  were assigned through a combination of 1D and 2D NMR experiments ( $^{13}\text{C}$ -NMR, HSQC, HMBC are reported in the experimental section Paragraph 3.11.). The  $^1\text{H}$ -NMR spectrum recorded in  $\text{CD}_2\text{Cl}_2$  at 298 K is reported in Figure 3.

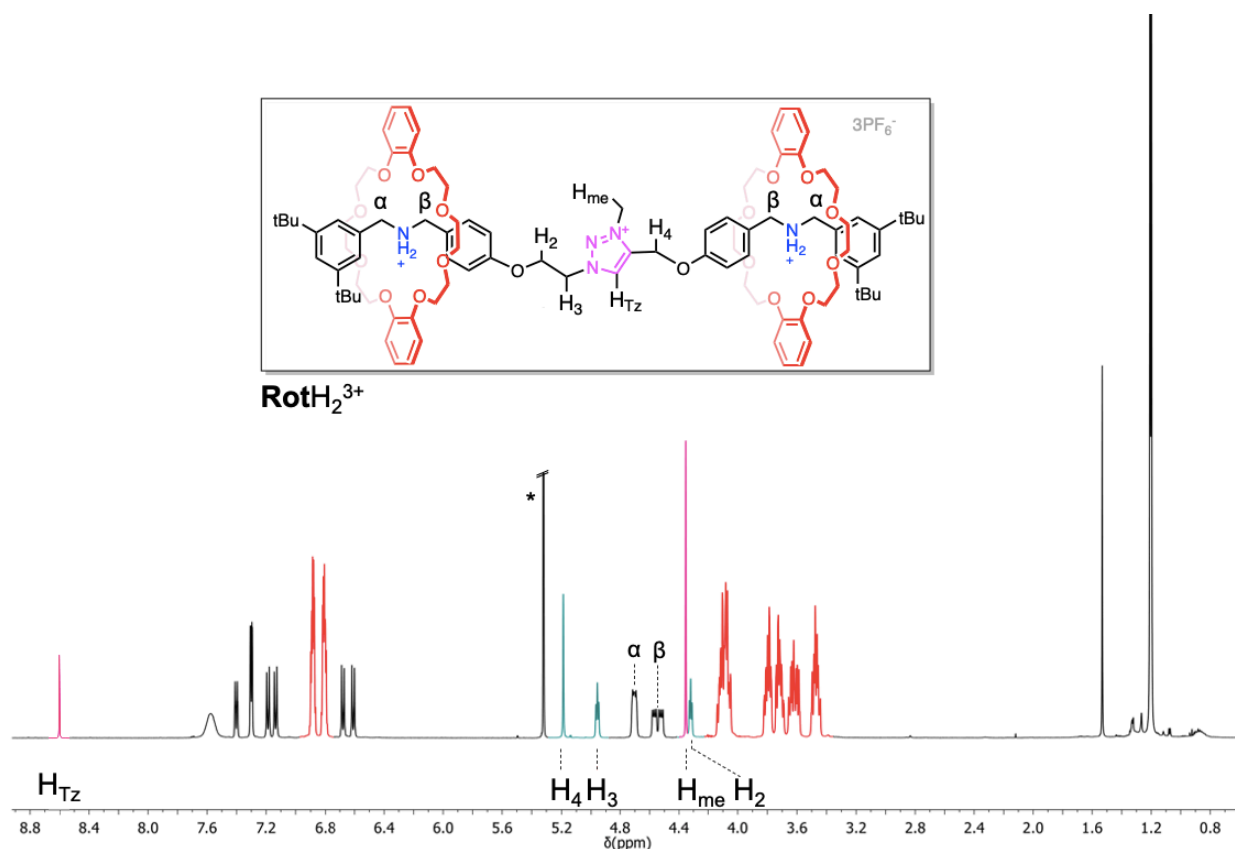


Figure 3.  $\text{RotH}_2^{3+}$ ,  $^1\text{H}$ -NMR  $\text{CD}_2\text{Cl}_2$ , 298 K, 500 MHz. The peak labeled with an asterisk is the residual signal of the deuterated solvent.

The peaks in red belong to the DB24C8 macrocycles, in particular the resonances at 6.85 ppm correspond to the aromatic protons, while the signals between 4.13 ppm and 3.41 ppm are attributed to the protons present on the glycolic chains. The hydrogen bond interactions established between the ammonium centers and the macrocycles cause the deshielding of the  $\alpha$  and  $\beta$  benzylic signals (in respect of the typical dibenzylamine resonances in analogous nuclei) and the appearance of a peculiar multiplicity.<sup>29</sup> The signals colored in magenta are indicative of the resonances of the central triazolium station: the methyl singlet resonates at 4.35 ppm while the triazolium proton is the most deshielded peak at 8.60 ppm. To conclude, the signals colored in cyan correspond to the resonances of the ethylene ( $\text{H}_2$ ,  $\text{H}_3$ ) and methylene ( $\text{H}_4$ ) bridges that connect the triazolium with the lateral ammonium stations.

### 3.4. Acid/base switching study

#### 3.4.1. Deactivation of one ammonium site ( $n_S = n_R$ )

The rotaxanes **RotH<sup>2+</sup>-I** and **RotH<sup>2+</sup>-II** are interconverted by the shuttling of the crown ether rings, this process is slow in the <sup>1</sup>H NMR timescale and thus the two species can singularly be observed. A polystyrene supported phosphazene base was added to a solution of **RotH<sub>2</sub><sup>3+</sup>** in deuterated acetonitrile and the process of deprotonation was monitored through <sup>1</sup>H NMR spectroscopy. The partial arrayed spectra recorded over time until the mono deprotonation occurred are reported in Figure 4.

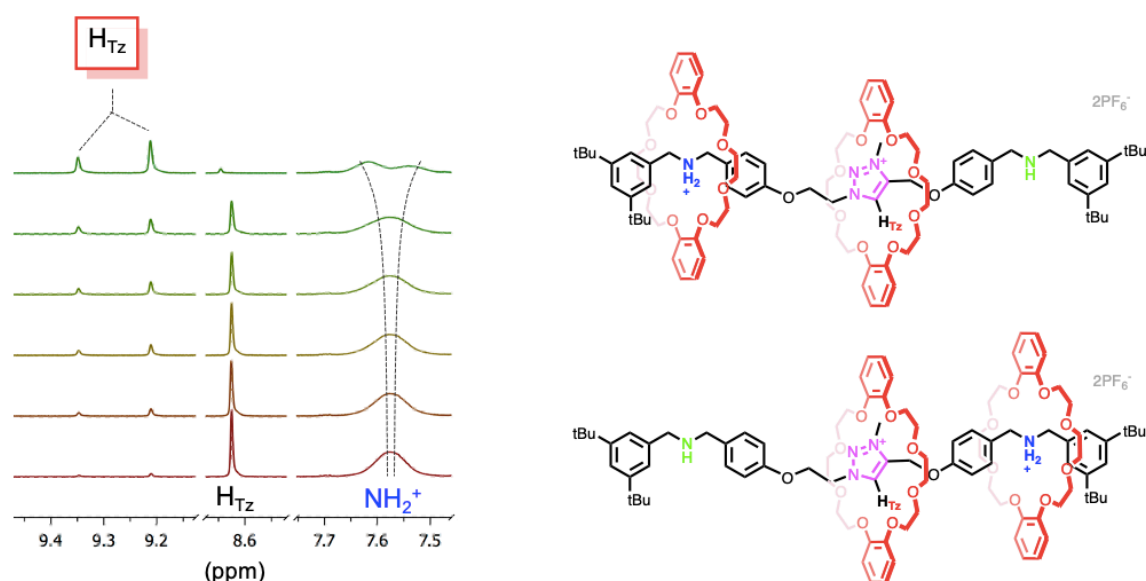


Figure 4. Deprotonation process of **RotH<sub>2</sub><sup>3+</sup>**. *Left*, partial arrayed <sup>1</sup>H NMR spectra recorded after the addition of the heterogenous base. The last green spectrum corresponds to the deprotonation one ammonium site. *Right*, chemical structures of the two isomers **RotH<sup>2+</sup>-II** and **RotH<sup>2+</sup>-I**.  $CH_2Cl_2$ , 298 K, 500 MHz.

The formation of **RotH<sup>2+</sup>-II** and **RotH<sup>2+</sup>-I** was indicated by the progressive disappearance of the **RotH<sub>2</sub><sup>3+</sup>** triazolium peak (labeled as  $H_{Tz}$ , Figure 4) and the concomitant observation of two new deshielded triazolium frequencies ( $H_{Tz}$  in the red square, Figure 4). The broadened peak, labeled as  $NH_2^+$ , (Figure 4) belongs to the acidic proton nuclei of the ammonium centers, which present a splitting of the signal into two different ones. The higher field shift of the triazolium protons is attributed to their interaction with the oxygen atoms of the crown ether cavity. Interestingly, the two dicationic rotaxanes were formed in a different relative ratio, this observation suggests a difference in the acidity of the two ammonium stations that will be discussed in detail in the next paragraphs.

### 3.4.2. Deactivation of two ammonium sites ( $n_S < n_R$ )

The complete deprotonation of  $\text{RotH}_2^{3+}$  afforded the monocationic  $\text{Rot}^+$  in which the number of station  $n_S$  is lower than the number of rings  $n_R$ . In Figure 5 are reported the  $^1\text{H}$  NMR spectra obtained upon deprotonation of one ammonium site (Figure 5, *b*), and the spectrum of  $\text{Rot}^+$  in which the ammonium sites are fully deprotonated (Figure 5, *c*). Upon complete deprotonation, the resonances of the isomeric rotaxanes converge into the ones observed in the spectrum of  $\text{Rot}^+$ .

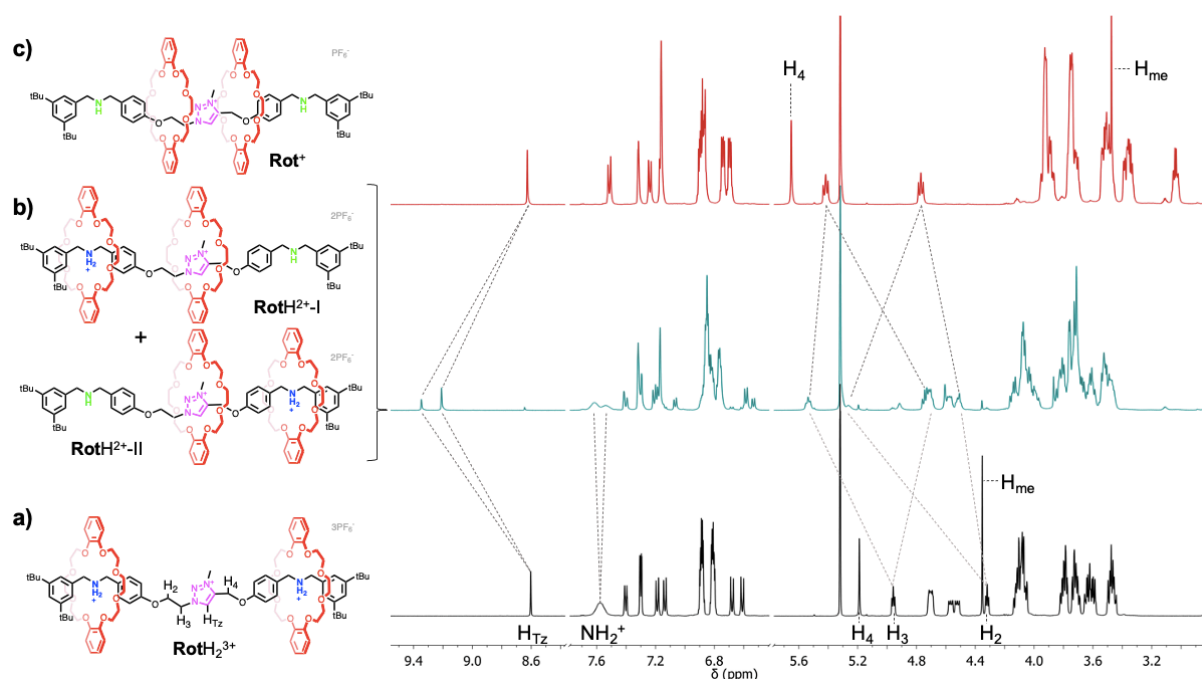


Figure 5.  $^1\text{H}$ -NMR,  $\text{CD}_2\text{Cl}_2$ , 298 K, 500 MHz. *a*)  $\text{RotH}_2^{3+}$  (black trace), *b*) isomeric mixture of mono deprotonated rotaxanes  $\text{RotH}_2^{2+}\text{-I}$  and  $\text{RotH}_2^{2+}\text{-II}$ , *c*) deprotonated rotaxane  $\text{Rot}^+$ .

The triplets  $\text{H}_3$  and  $\text{H}_2$ , belonging to the ethylene *bridge*, and the methylene peak  $\text{H}_4$  are deshielded in comparison to those of  $\text{RotH}_2^{3+}$  and  $\text{Rot}^+$ . This is particularly significant since it is indicative of a shuttling of the ring toward the central triazolium moiety. Another confirmation of this rearrangement is given by the triazolium methyl signal ( $\text{H}_{\text{me}}$ ) which is shielded in  $\text{Rot}^+$ . These peculiar spectral changes are reported in the literature for analogous interlocked systems and are associated with the complexation of a triazolium moiety with a crown ether.<sup>30-32</sup> To conclude, the triazolium signal  $\text{H}_{\text{Tz}}$  remains at the same chemical shift, going from  $\text{RotH}_2^{3+}$  to  $\text{Rot}^+$ .

### 3.4.3. Functionalization of the deprotonated [3]rotaxane $\text{Rot}^+$

The presence of a macrocycle encircling a functional group in a rotaxane can result in a poor reactivity of the latter.<sup>17,23,33,34</sup> To have a further confirmation about the translation of the ring, the monocationic rotaxane  $\text{Rot}^+$  was reacted with di-*tert*-butyl-dicarbonate ( $\text{Boc}_2\text{O}$ ). The bis carbamate product  $\text{RotBoc}_2^+$  was easily obtained, more interestingly the  $^1\text{H-NMR}$  spectrum of this compound resulted to be similar to the one of  $\text{Rot}^+$  (Figure 6).

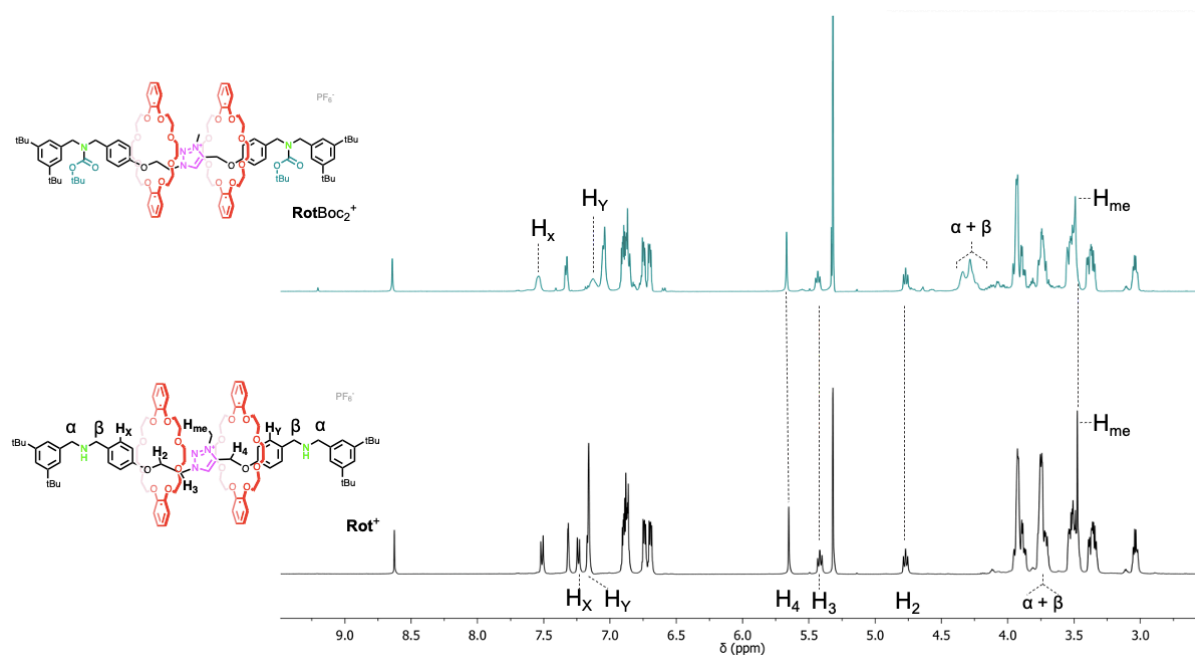
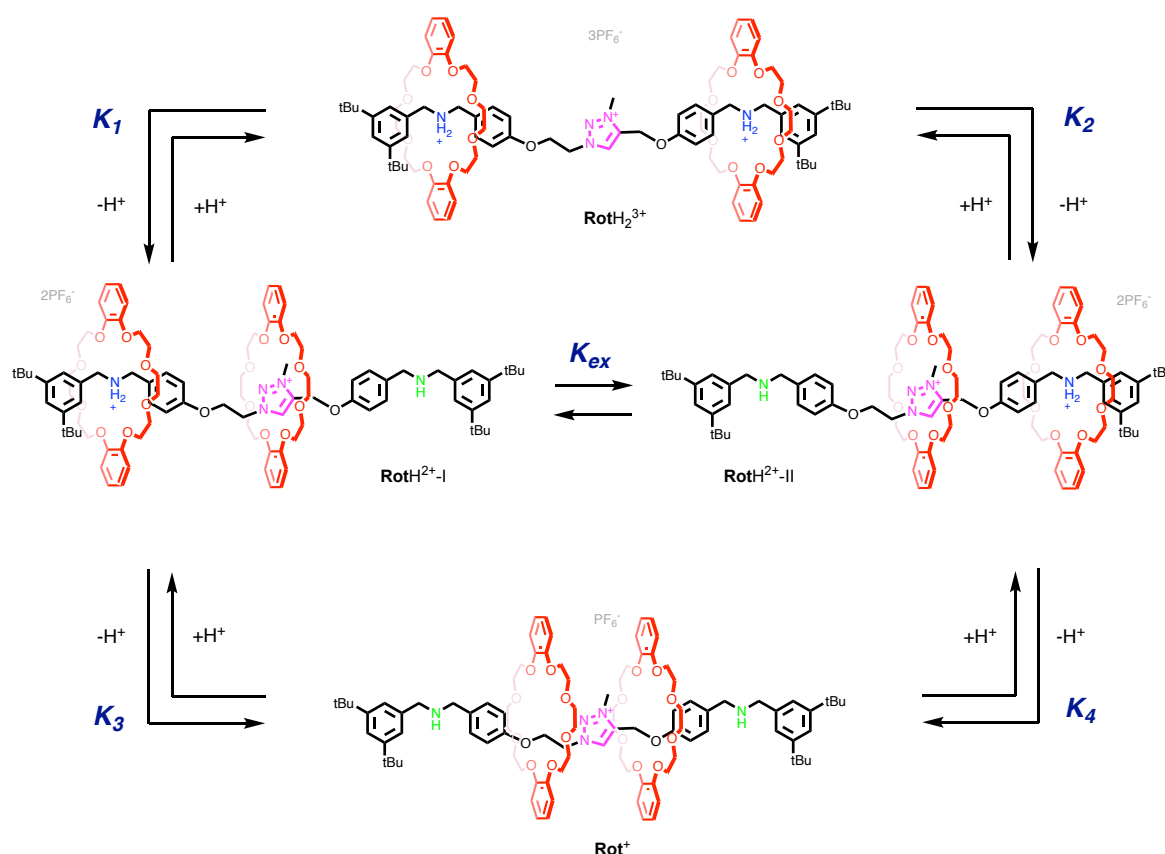


Figure 6.  $^1\text{H-NMR}$ ,  $\text{CD}_2\text{Cl}_2$ , 298 K, 500 MHz. Bottom, spectrum of  $\text{Rot}^+$ , top, spectrum of the bis carbamate rotaxane  $\text{RotBoc}_2^+$ .

In particular, the resonances of the nuclei in proximity of the triazolium station (ethylene *bridge*,  $\text{H}_2$  and  $\text{H}_3$ , and methylene *bridge*  $\text{H}_4$ ) are unaltered. The only differences observed in the spectrum are relative to the nuclei influenced by the presence of the bulky *tert*-butoxy carbonyl groups (Boc). The  $\alpha$  and  $\beta$  benzylic protons peaks resulted to be broadened in  $\text{RotBoc}_2^+$ , the same effect is observed for the aromatic nuclei  $\text{H}_X$  and  $\text{H}_Y$ . This behavior is due to the restricted rotation of the carbamate group that is slow in the NMR timescale. The fact that the reactivity of the secondary amine group of  $\text{Rot}^+$  is not hindered by the macrocycles is an indirect confirmation that, in the monocationic rotaxane, the rings encircle the triazolium station.

### 3.5. Thermodynamic analysis of the deprotonation reaction

The stepwise deprotonation of  $\text{RotH}_2^{3+}$  yield three different species: the dicationic rotaxanes  $\text{RotH}^{2+}$ -I and  $\text{RotH}^{2+}$ -II, and the monocationic  $\text{Rot}^+$  (Scheme 3). The acidity of the dibenzyl ammonium site in a rotaxane is strongly influenced by coordination with a crown-ether resulting in a decreased acidity<sup>23-25</sup>. For this reason, it was expected that the different positions of the macrocycles on the axle would result in distinct acid/base properties for these interlocked species.



Scheme 3. Scheme of the equilibria involved in the interconversion between  $\text{RotH}_2^{3+}$ ,  $\text{RotH}^{2+}$  (I and II), and  $\text{Rot}^+$ .

The constants  $K_1$  and  $K_2$  are related to the deprotonation processes that from the tricationic  $\text{RotH}_2^{3+}$  leads to the formation of the isomeric rotaxanes  $\text{RotH}^{2+}$  (I and II); analogously, the constants  $K_3$  and  $K_4$  are relative to the converging equilibria toward the species  $\text{Rot}^+$ . The exchange constant  $K_{ex}$  is relative to the interconversion of  $\text{RotH}^{2+}$ -I and  $\text{RotH}^{2+}$ -II that occurs through shuttling of the rings. Through the combination of  $^1\text{H}$ -NMR and UV-vis experiments, it was possible to measure the acid-base constants of this rather complex set of reactions.

A solution of **RotH<sub>2</sub><sup>3+</sup>** in acetonitrile was titrated with a phosphazene base (P<sub>1</sub>-tBu). The deprotonation process was followed by recording the absorbance variation at 275 nm (*left*, Figure 7). The profile of the titration curve (*right*, Figure 7) reached a plateau after two equivalents of base added, confirming the complete deprotonation of the rotaxane.

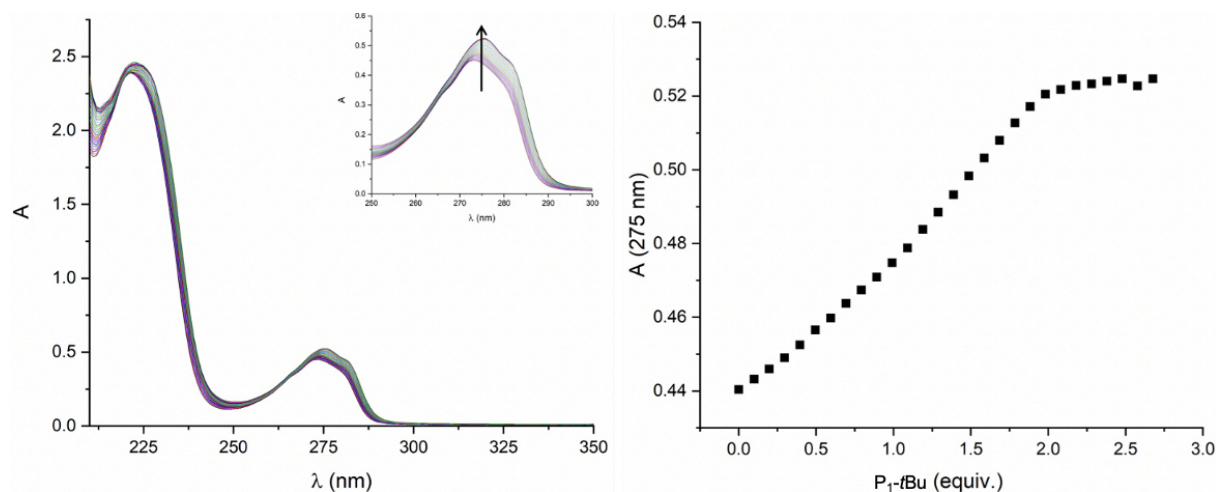


Figure 7. UV-vis titration of **RotH<sub>2</sub><sup>3+</sup>** with P1-tBu in acetonitrile [**RotH<sub>2</sub><sup>3+</sup>**]<sub>0</sub>=3,96·10<sup>-5</sup>M, 298 K.

The fitting of the curve reported provided the values of the two constants ( $K_{obs}^I$  and  $K_{obs}^{II}$ ), that correspond respectively to the sum of the first two acid base constants ( $K_1+K_2$ ) and the second two ( $K_3+K_4$ ). At the equilibrium, the network of reactions described in Scheme 3 respects the following system of equations (1):

$$1. \begin{cases} K_{ex} = \frac{K_2}{K_1} = \frac{K_3}{K_4} \\ K_{obs}^I = K_1 + K_2 \\ K_{obs}^{II} = K_3 + K_4 \end{cases}$$

The constant  $K_{ex}$  can be determined by <sup>1</sup>H NMR by analyzing the spectrum of the dicationic mixture of rotaxanes (**RotH<sup>2+</sup>-I** and **RotH<sup>2+</sup>-II**). The two species are in slow equilibrium in the NMR time scale (Figure 5, b). This is most likely because the removal of a proton from a complexed ammonium site is kinetically hindered, moreover the proton exchange between the two species implies the displacement of the two rings. The integration of the proton signals relative to the two isomers **RotH<sup>2+</sup>-II** and **RotH<sup>2+</sup>-I** provided their ratio at equilibrium and thus the value of the constant  $K_{ex}=2.3$ . With this data in hands, the system of equations 1 could be

solved assuming that the molar absorption coefficient ( $\epsilon$ ) of **RotH**<sup>2+</sup>-I and **RotH**<sup>2+</sup>-II at the observed wavelength is identical. This assumption is reasonable since the two rotaxanes differ for the sole position of the crown ether in respect to the triazolium station, moreover the UV visible spectrum is not affected by the DB24C8-dibenzylammonium interactions.<sup>35</sup> The negative logarithm ( $pK$ ) of the constants values determined are reported in Table 1.

|        |                   |
|--------|-------------------|
| $pK_1$ | 23.5 <sup>a</sup> |
| $pK_2$ | 23.2 <sup>a</sup> |
| $pK_3$ | 24.2 <sup>a</sup> |
| $pK_4$ | 24.5 <sup>a</sup> |

*Table 1. Negative logarithm of the acidity constants determined by a combination of UV vis and NMR experiments. <sup>a</sup> The error on the  $pK_a$  estimated is  $\pm 0.1$  units, calculated as the average mean square root in the  $pK_a$  values of the ammonium stations investigated.*

From these data, it can be concluded that the ammonium on the ethylene bridge side is two times easier to deprotonate with respect to the one residing on the methylene bridge ( $pK_2 < pK_1$ ). A difference in the acidity of the two ammonium centers was observed also for the free axle **1** for which  $pK_1' = 16.9$  and  $pK_2' = 17.5$ . The two ammonium units of both **RotH**<sub>2</sub><sup>3+</sup> and **1** are not chemically identical because of the different length of the ethylene and methylene *bridge* on the triazolium sides. However, the axle is a simple diprotic acid for which the two mono-deprotonated species are not observed in <sup>1</sup>H NMR because of their fast exchange. In light of this, the macrocycles have a determinant role in the expression of the acidity difference between the ammonium sites since **RotH**<sup>2+</sup>-I and **RotH**<sup>2+</sup>-II can be singularly observed. More interestingly,  $pK_1 < pK_4$ , even though these constants are referred to the deprotonation of the same ammonium site, this process is clearly favored when the triazolium unit is un-occupied ( $K_1$ ). This means that the presence of a ring on the triazolium station affects the acidity of the nearby complexed ammonium site, disfavoring the shuttling motion of the ring. The same trend is observed also for the methylene side ammonium station ( $K_3 < K_2$ ). These observations prove that the macrocycles have a crucial role in the determination of the acid base properties of the equilibrium network. This is evident also in the  $\Delta pK_a$  difference of the two successive deprotonation for the axle ( $\Delta pK_a = 0.6$  units) and for the [3]rotaxane ( $\Delta pK_a = 1.0$  units).

### 3.6. Variable-Temperature NMR experiments

In the cationic **Rot**<sup>+</sup> the number of rings is greater than the number of stations, resulting in a frustrated structure in which two rings are forced to share a single triazolium site. The rotaxane was investigated by a Variable-Temperature (VT) <sup>1</sup>H NMR experiments. Indeed, a high dynamicity was expected since the two crown ethers are held around the triazolium station only by weak ion-dipole interactions. A series of <sup>1</sup>H NMR spectra of **Rot**<sup>+</sup> were recorded at different temperatures (from 233 K to 343 K) in acetonitrile (Figure 8).

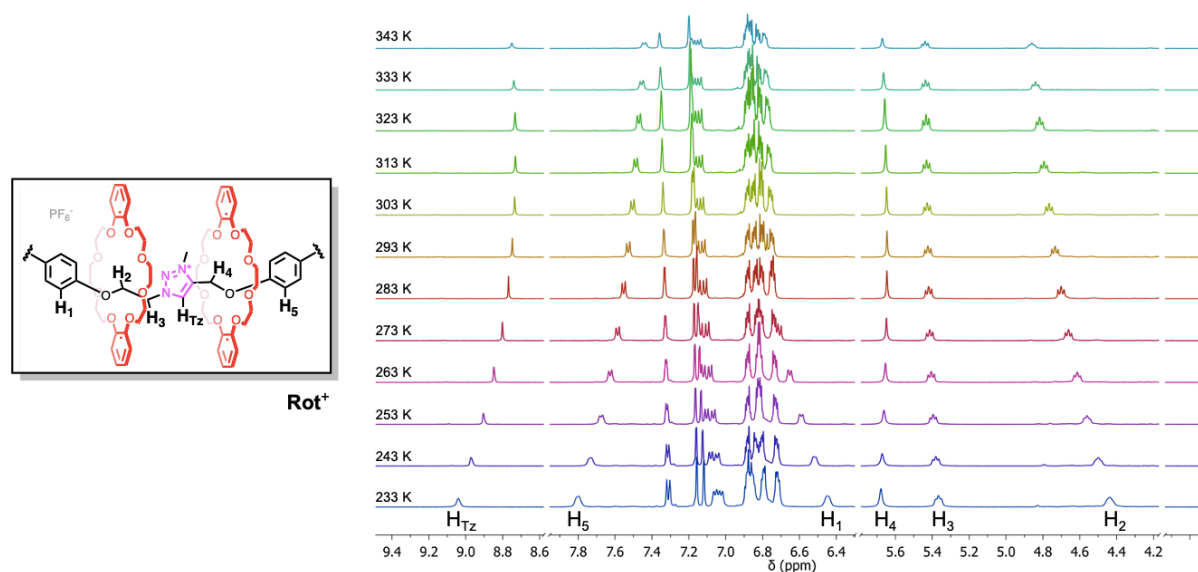


Figure 8. Portion of the variable-temperature <sup>1</sup>H NMR spectra of **Rot**<sup>+</sup> (500 MHz, CD<sub>3</sub>CN). Left, chemical structure of **Rot**<sup>+</sup>, the lateral dibenzylamine sites were omitted for clarity.

The experiment provided interesting results, indeed, by increasing the temperature, a shielding effect is observed for the methylene side peak H<sub>5</sub> while the ethylene side proton H<sub>1</sub> and H<sub>2</sub> are deshielded. These changes are indicative of the the movement of the rings toward the ethylene bridge. The chemical shift of the peaks closest to the triazolium site H<sub>4</sub> and H<sub>3</sub> didn't show any significant change upon temperature variation, meaning that the local chemical environment of this nuclei remains basically unaltered. Most interestingly the triazolium aromatic signal H<sub>Tz</sub> present a peculiar trend. In fact, their resonances shift from 9.04 ppm at 233K to 8.73 ppm at 313 K, while a further increase of the temperature causes a deshielding of the peak that resonates at 8.76 ppm at 343K (Figure 9).

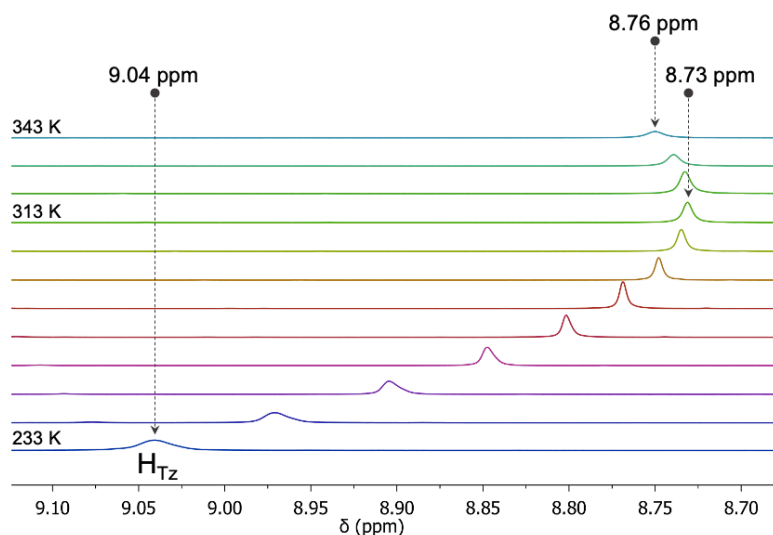


Figure 9. Portion of the variable-temperature  $^1\text{H}$  NMR spectra of **Rot**<sup>+</sup> (500 MHz,  $\text{CD}_3\text{CN}$ ). Chemical shift variation of the triazolium aromatic peak upon variation of the temperature.

The observed changes can be explained by the presence of a dynamic system in which multiple co-conformations are involved, whose population distribution is highly dependent on temperature. The same experiment performed on axle **1** (Figure 10) showed only linear variation of the peaks chemical shift with temperature. This clearly proves that it is the displacement of the rings along the axle which causes the peculiar temperature-dependent spectral features in **Rot**<sup>+</sup>. The details about the co-conformation explored by the system could be deduced from theoretical modelling studies.

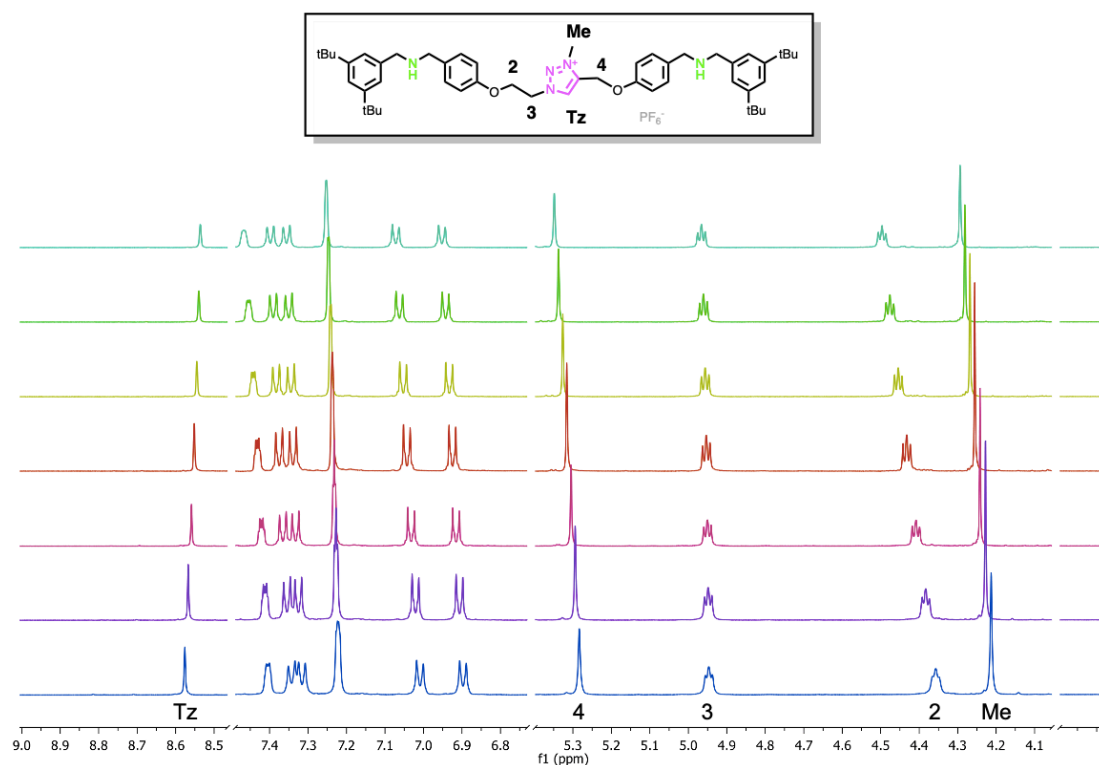


Figure 10. Portion of the variable-temperature  $^1\text{H}$  NMR spectra of the free axle **1** (500 MHz,  $\text{CD}_3\text{CN}$ ). Top, chemical structure and labeled nuclei of **1**.

### 3.7. Molecular Modelling

The part described in this paragraph was performed by our collaborators from the University of Insubria Prof. Ettore Fois and Prof. Gloria Tabacchi, I am very grateful to them for the interesting results provided. For further insight, the reader can refer to the published article.<sup>16</sup> Detailed information about the co-conformation explored by the system can be obtained from modelling studies. A geometry optimization was performed by applying density functional theory (DFT) method for the three different rotaxanes **RotH<sub>2</sub><sup>3+</sup>**, **RotH<sup>2+</sup>-I** and **RotH<sup>2+</sup>-II**. The geometry optimization of the two isomeric rotaxanes **RotH<sup>2+</sup>-I** and **RotH<sup>2+</sup>-II** leads to the conclusion that the second one is more stable than the first by 1.4 kcal mol<sup>-1</sup>. The optimized structures are reported in Figure 11. In both **RotH<sup>2+</sup>** isomers the macrocycle migrated on the triazolium site and established a hydrogen bond with the triazolium proton. However, the structure of **RotH<sup>2+</sup>-II** has a greater conformation flexibility since the translation of the ring is accompanied by a rearrangement of the ethylene side axle.

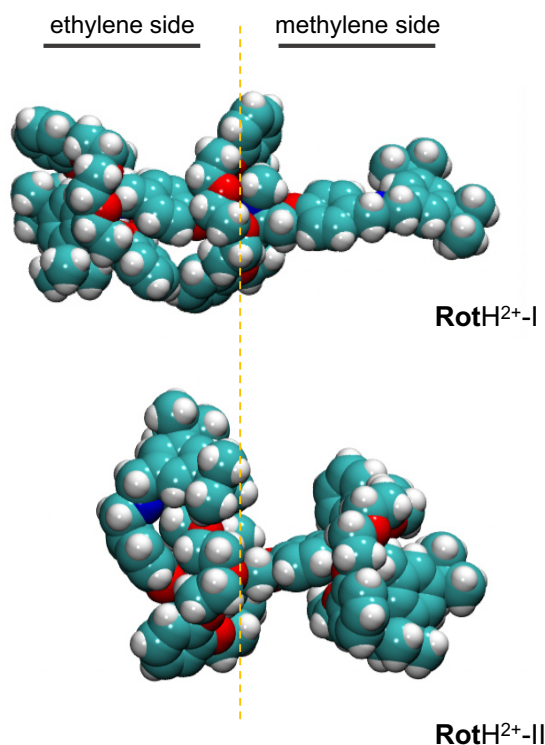


Figure 11. Optimized geometry of **RotH<sup>2+</sup>-I** (top) and **RotH<sup>2+</sup>-II** (bottom), the orange dashed line indicates the position of the triazolium station. Color code: C, cyan; N, blue; O, red; H, white.

The rotaxane **Rot<sup>+</sup>** was investigated *via* a finite temperature DFT-metadynamics (MTD) approach,<sup>36-40</sup> indeed in this case the two macrocycles compete for the triazolium station resulting in a highly dynamic system. The free energy profile reported in Figure 12 refers to the shuttling of the rings with respect to the central triazolium site. The profile was obtained by

forcing alternatively each one of the rings to transit along the axle, the collective variable CV (in Å) represents the displacement of an oxygen atom of the ring with respect of a nitrogen atom of the triazolium.

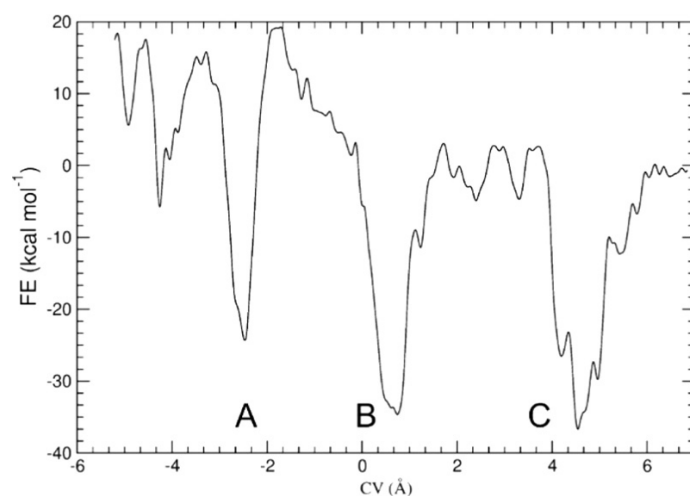


Figure 12. Free energy profile for the shuttling of the two rings along the axle of **Rot**<sup>+</sup>.

The three free energy minima found were labeled as A, B and C and correspond to different co-conformations explored by **Rot**<sup>+</sup>. The profile was calculated in vacuum because of the large dimension of the system. However, previous studies on rotaxanes showed that even if the barriers are overestimated by about 15 kcal mol<sup>-1</sup>, the transition state of the structures do not change appreciably.<sup>41</sup>

The representative structures of the three energy minima are reported in Figure 13. In the structure B the two macrocycles are close to the triazolium station, in C one of the two macrocycle is close to the triazolium and the other is placed on the methylene bridge side. In the co-conformer of higher energy A one ring is close to the triazolium and the other sits on the ethylene bridge side.

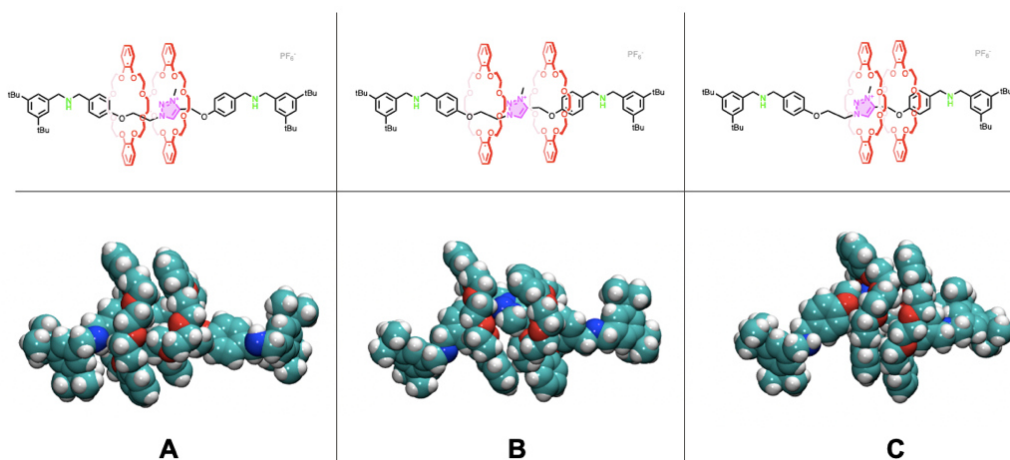


Figure 13. Graphical representations of the three coconformations extracted from the combined Metadynamics-DFT simulation of **Rot**<sup>+</sup> at room temperature. The reported coconformations are representative of the three free energy minima labeled A, B, and C. Color code: C, cyan; N, blue; O, red; H, white. The chemical formulas on top were reported for clarity.

Clearly, the displacement of the crown ether on the axle causes a variation of the nuclei chemical shift surrounded by the ring cavity. In the simulated  $^1\text{H}$  NMR spectra of the co-conformers A, B and C a deshielding of the triazolium proton signal (labeled as *i*, blue arrow in Figure 14) is observed in the computed spectra for C and A (black and green spectra, in Figure 14) consistently with the very close localization of the ring on the triazolium unit in these structures. On the contrary in B (red spectrum, Figure 14) the two macrocycles are relatively distant from the triazolium, and the signal is not deshielded.

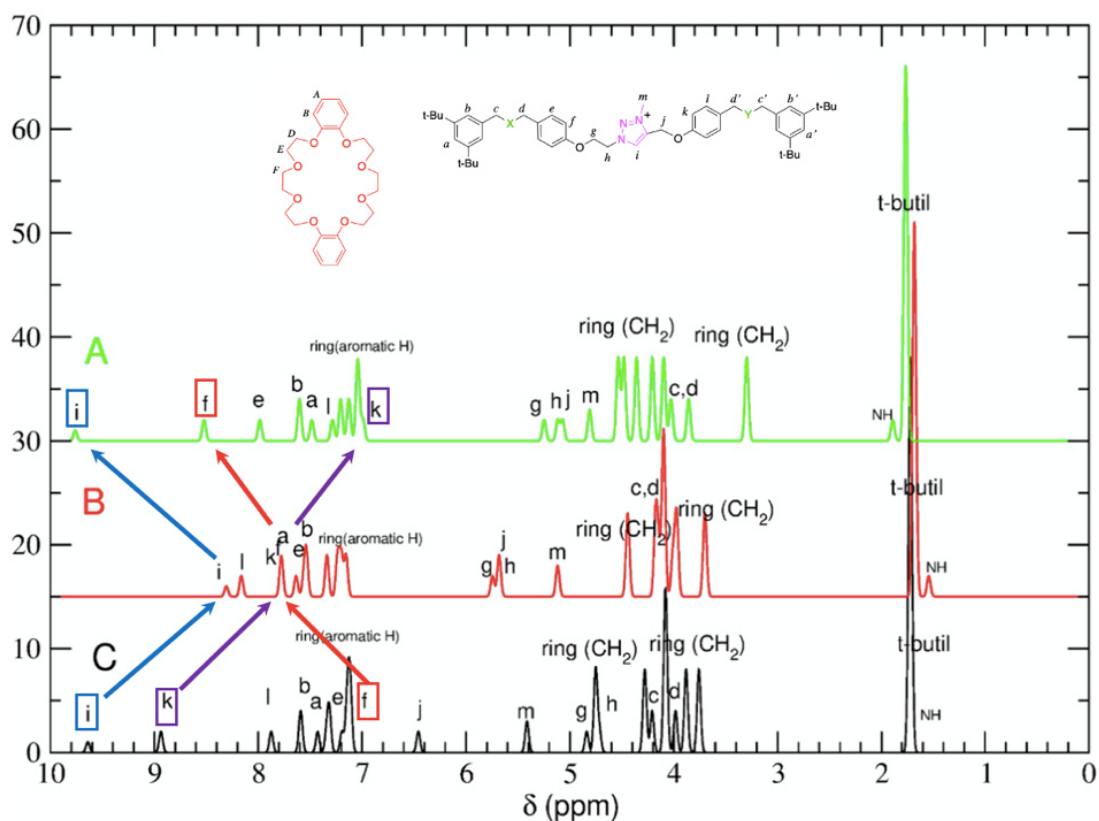


Figure 14 Simulated  $^1\text{H}$ -NMR spectra for the free energy minima A (top panel, green line); B (middle panel, red line); C (bottom panel, black line).

The simulated NMR spectra agree with the chemical shift variation of  $\text{H}_{\text{Tz}}$  observed experimentally by increasing the temperature in the VT NMR experiment. A further analogy with the VT experimental data is given by the calculated chemical shift of the nuclei *f* and *k* corresponding to  $\text{H}_1$  and  $\text{H}_5$  that are respectively deshielded and shielded going from C to A (red and purple arrows, Figure 14). The simulated NMR spectra of A, B and C correlate with the trend observed in the VT NMR experiment. This supports the hypothesis that at low temperature the structure C is predominant, at intermediate temperature B and C are present, while the increase of the population of A requires higher temperatures.

To conclude, the higher barrier for the  $B \rightarrow A$  path respect to the  $B \rightarrow C$  one (Figure 15) can be related to the asymmetry of the triazolium group. In the path from B to C the macrocycle should first pass through the flat rigid ring represented by the triazolium unit (Figure 15), thus hindering rotation of the latter. Whereas in the other path ( $B \rightarrow A$ ) the macrocycle must first impact with the methyl group causing the rotation of the  $C_{\alpha}$ - $C_{\beta}$  single bond, this result in a hampering of the macrocycle transit and thus in a greater free energy cost.

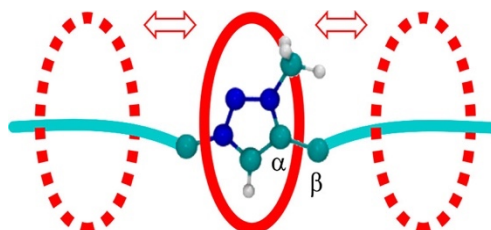


Figure 15. Representation of a triazolium unit encircled by a macrocycle (red oval). Color code: C, cyan; N, blue; H, white. The red arrows represent two nonequivalent shuttling directions for the macrocycle. Reproduced with permission from reference 16.

### 3.8. Conclusion

In this chapter was described the synthesis and characterization of a [3]rotaxane (**RotH<sub>2</sub><sup>3+</sup>**) endowed with two lateral ammonium stations and one central triazolium recognition site. The synthesis started from a common precursor and was accomplished by a convergent approach. The coupling reaction between two pseudorotaxanes halves provided the final interlocked compound.

This [3]rotaxane is interesting because the relative number of stations ( $n_S$ ) in respect of the number of rings ( $n_R$ ) can be changed on command, giving access to a family of compounds (**RotH<sup>2+</sup>-I**, **RotH<sup>2+</sup>-II** and **Rot<sup>+</sup>**). In compound **RotH<sub>2</sub><sup>3+</sup>** the acidity of the ammonium centers is influenced by the presence of the crown ethers, furthermore the two sites have different acidity because of the asymmetry of the axle. The two isomeric rotaxanes **RotH<sup>2+</sup>-I** and **RotH<sup>2+</sup>-II** are formed upon deactivation of one ammonium site, these two species differ for the position of the ring-complexed ammonium site in respect to the central triazolium. The direct observation of all **RotH<sup>2+</sup>** isomers is possible by <sup>1</sup>H NMR since the presence of the rings induces a slow proton exchange between these different species. On the contrary, mono deprotonation of the free axle results in a mixture of isomers in fast equilibrium. The acid-base properties of the **RotH<sup>2+</sup>** were studied in detail by combining UV-vis and NMR experiments, revealing the peculiar effect of the rings movement on the ammonium sites' acidity.

The monocationic rotaxane **Rot<sup>+</sup>** belongs to a rarely reported class of rotaxane in which  $n_S < n_R$ . We expected that this peculiar arrangement would cause a frustrated, highly dynamic system in which the two rings would compete for the remaining triazolium station. Variable-temperature NMR confirmed this behavior. VT-NMR experimental data were interpreted with the help of computational studies. In particular, the simulated NMR spectra of **Rot<sup>+</sup>** stable conformations were useful to this purpose. An interesting observation is that the transit of a macrocycle over a triazolium unit occurs with different energy barriers. This effect is caused by the presence of the asymmetrically installed methyl substituent that differentiates the ring approaches from the two directions of the axle.

The rotaxane described proves that unusual thermodynamic and kinetic phenomena can emerge when interlocking more than one macrocycle on a linear axle and inducing a mismatch between rings and stations. The study is relevant in the field of higher order rotaxanes, in particular in the perspective to exploit the peculiar properties of MIMs in nanostructured devices and materials.

### 3.9. Experimental Section

|   |            |
|---|------------|
| <b>Experimental Details</b>   | <b>152</b> |
| <b>3.10. Synthetic procedures</b>   | <b>155</b> |
| 3.10.1 Synthesis of the precursors <b>2b</b> and <b>3c</b>  | <b>155</b> |
| Synthesis of <b>a</b>   | 156        |
| Synthesis of <b>1a</b>  | 156        |
| Synthesis of <b>1b</b>  | 157        |
| Synthesis of <b>2b</b>  | 157        |
| Synthesis of <b>1c</b>  | 158        |
| Synthesis of <b>2c</b>  | 159        |
| Synthesis of <b>3c</b>  | 159        |
| 3.10.2. Synthesis of the model compound <b>1H<sub>2</sub><sup>3+</sup></b>                        | <b>160</b> |
| Synthesis of <b>1d</b>  | 161        |
| Synthesis of <b>1H<sub>2</sub><sup>3+</sup></b>   | 162        |
| Synthesis of <b>1<sup>+</sup></b>   | 163        |
| 3.10.3. Synthesis of the [3]rotaxane  | <b>164</b> |
| Synthesis of <b>1e</b>  | 165        |
| Synthesis of <b>RotH<sub>2</sub><sup>3+</sup></b>   | 166        |
| General procedure for the stepwise deprotonation of compound <b>RotH<sub>2</sub><sup>3+</sup></b> | 168        |
| Synthesis of <b>Rot<sup>+</sup></b>   | 168        |
| <b>3.11. NMR spectra</b>  | <b>170</b> |
| <sup>1</sup> H and <sup>13</sup> C NMR spectra of <b>1-H<sub>2</sub><sup>3+</sup></b>             | 170        |
| <sup>1</sup> H and <sup>13</sup> C NMR spectra of <b>1<sup>+</sup></b>                            | 171        |
| <sup>1</sup> H and <sup>13</sup> C NMR spectra of <b>RotH<sub>2</sub><sup>3+</sup></b>            | 172        |
| HSQC and HMBC spectra of <b>RotH<sub>2</sub><sup>3+</sup></b>                                     | 173        |
| <sup>1</sup> H and <sup>13</sup> C NMR spectra of <b>Rot<sup>+</sup></b>                          | 174        |
| HSQC and HMBC spectra of <b>Rot<sup>+</sup></b>   | 175        |

### 3.9.1. Experimental details

Solvents and reagents [3,5-di-*tert*-butyl-benzyl bromide, sodium azide, 4-hydroxybenzaldehyde, sodium borohydride, di-*tert*-butyl-dicarbonate, 1,2-dibromoethane, propargyl bromide, hexafluorophosphoric acid, dibenzo-24-crown-8, methyl iodide, ammonium hexafluorophosphate, [polystyrene-supported BEMP, P1-*t*-Bu] and triethylamine were all used as supplied by Fluorochem, Sigma-Aldrich or VWR without further purification. Flash column chromatography was performed using Sigma Aldrich Silica 40 (230-400 mesh size or 40-63  $\mu\text{m}$ ) as the stationary phase. Size exclusion chromatography was performed using Biorad Biobeads SX-3 as the stationary phase. Thin layer chromatography was performed on TLC Silica gel 60 F254 coated aluminium plates from Merck. Hydrogenation reactions were carried out in a H-Cube flow reactor equipped with a 10 % Pd/C catalyst at a H<sub>2</sub> pressure of 10 bar and a flow rate of 1 mL min<sup>-1</sup> using methanol as the solvent.

### 3.9.2. NMR measurements

<sup>1</sup>H NMR spectra were recorded on an Agilent DD2 spectrometer operating at 500 MHz or a Varian Mercury spectrometer operating at 400 MHz; <sup>13</sup>C NMR spectra were recorded on an Agilent DD2 spectrometer operating at 126 MHz or a Varian Mercury spectrometer operating at 101 MHz. Chemical shifts are quoted in ppm relative to tetramethylsilane (SiMe<sub>4</sub>,  $\delta = 0$  ppm), using the residual solvent peak as a reference standard; all coupling constants (*J*) are expressed in Hertz (Hz). Exchange rate constant quantification was carried out using the MestreLab EXSYCalc software.

### 3.9.3. Determination of thermodynamic constants

Deprotonation experiments were carried out in acetonitrile using triethylamine ( $\text{p}K_a = 18.8$ ) or phosphazene compounds as heterogeneous [**B1**, polystyrene-supported BEMP] and homogeneous [ (P1-*t*-Bu),  $\text{p}K_a = 26.9$ ] bases. The  $\text{p}K_a$  values for the ammonium stations were calculated based on the titration curve fitting, carried out on the HyperSpec suite. The error on the  $\text{p}K_a$  values is estimated to be  $\pm 0.1$  units, calculated as the average mean square root in the  $\text{p}K_a$  values of the ammonium stations investigated.

## Computational Details

### *Quantum chemical calculations*

A model structure of the complex **RotH<sub>2</sub><sup>3+</sup>**, consisting of two identical dibenzo-24-crown-8 (DB24C8) rings interlocked with an axle containing two lateral dibenzylammonium (Am) and one central triazolium (Tz) stations, was optimized by adopting the D95(d,p)<sup>42</sup> basis set and the range-separated hybrid functional  $\omega$ B97XD<sup>43</sup> as density functional approximation to DFT.

From this optimized structure, two different starting geometries for the **RotH<sup>2+</sup>** model were created by removing one proton from one of the two lateral dibenzylammonium stations. These computational models correspond to the two isomers **RotH<sup>2+</sup>-I** and **RotH<sup>2+</sup>-II**, formed upon mono-deprotonation of the parent compound **RotH<sub>2</sub><sup>3+</sup>**. In particular, the starting structures for **RotH<sup>2+</sup>-I** and **RotH<sup>2+</sup>-II** were obtained by deprotonating the Am on the methyl group side, and the Am on the ethyl group side, respectively. These two geometries were optimized at the same level of theory as **RotH<sub>2</sub><sup>3+</sup>** - namely,  $\omega$ B97XD/D95(d,p).

The calculations of the NMR spectra of the above-mentioned optimized structures of **RotH<sub>2</sub><sup>3+</sup>**, **RotH<sup>2+</sup>-I** and **RotH<sup>2+</sup>-II**, were performed by using as basis set a QZP (quadruple- $\zeta$  with polarization) for all the protons<sup>44</sup> and cc-pCVDZ (double- $\zeta$  with polarization and tight-core) for the heavy atoms<sup>45</sup> (O, C, N) and adopting a DFT approximation optimized for proton NMR chemical shifts<sup>46</sup>. The chemical shifts of all the protons were calculated by taking as a reference the chemical shift of the protons of tetrametilsilane (TMS). The chemical shifts of the protons reported in this work were calculated from the average over equivalent protons.

The above calculations were performed with the Gaussian 09 code<sup>47</sup> using an implicit solvent model for CH<sub>2</sub>Cl<sub>2</sub> or CH<sub>3</sub>CN.<sup>48</sup>

### *Ab initio molecular dynamics and Metadynamics calculations*

The finite-temperature behavior of **Rot<sup>+</sup>** was modelled via *ab initio* molecular dynamics,<sup>49</sup> combined with statistical sampling according to the *ab initio* metadynamics<sup>50,51</sup> scheme.

A Generalized Gradient Approximation to density functional theory (DFT) was used to describe electron-electron interactions – in particular, the PBE functional in combination with empirical dispersion corrections (*i.e.* PBE-D2).<sup>52,53</sup> Ion cores-electron interactions were treated with ultra-soft pseudopotentials.<sup>54</sup> Plane-waves (PW) were used as basis set. The cutoffs for the PW expansion of the wavefunctions and density were 25 Ry and 200 Ry, respectively. Calculations were performed using periodic boundary conditions, which were applied to a simulation cell of size 70×30×30 Å. Such a size is sufficiently large to allow for a  $\Gamma$ -point-only sampling, and to minimize interactions of the rotaxane with periodic images.

Each simulation system was constituted by the neutral ring DB24C8 and by the positively charged axle. In all cases, the simulation cell contained a total of 255 atoms.

A guess configuration was obtained by removing one proton from both the two lateral dibenzylammonium stations of the parent compound. *Ab initio* molecular dynamics (AIMD) equilibration (elapsed time: 10 ps) was performed at 300K (27 °C). This temperature was chosen in order to favor a faster equilibration of the system. Additionally, it corresponds roughly to the central part of the temperature conditions at which the variable temperature NMR experiments were conducted (T = from -40 to 70 °C).

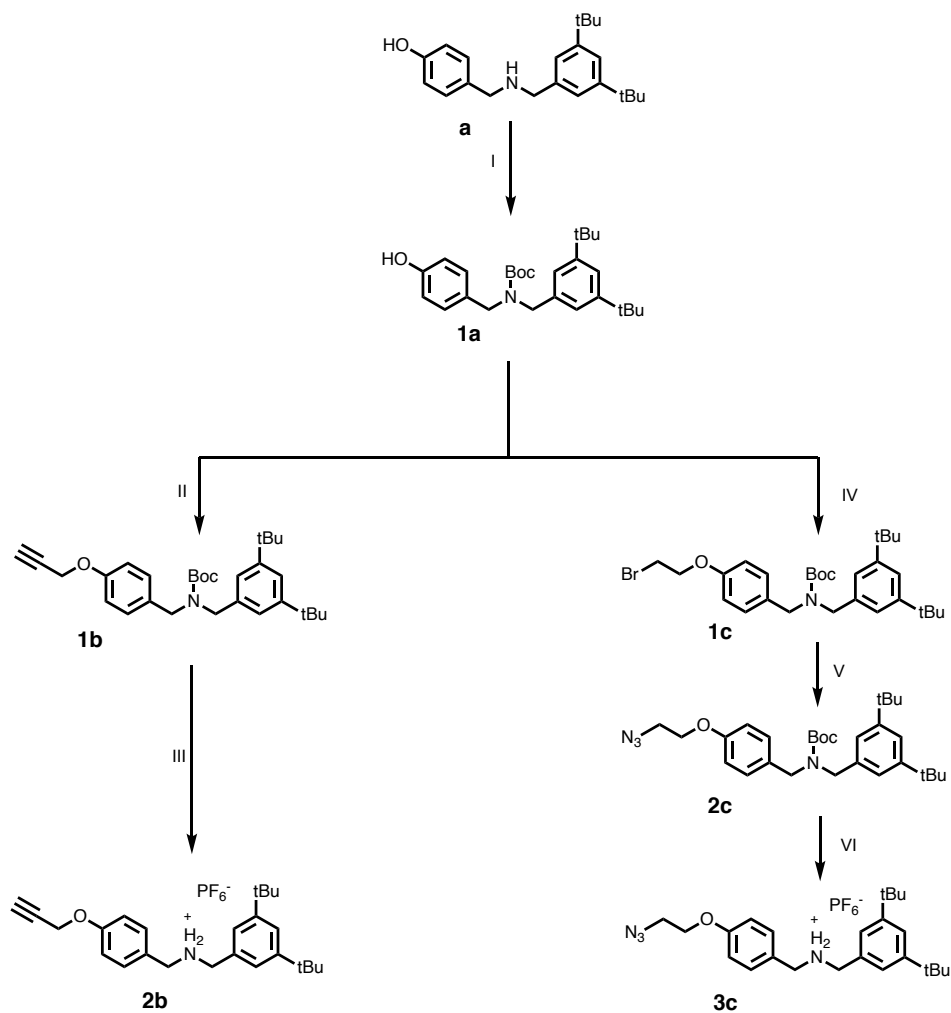
The simulations were carried out in the canonical NVT ensemble and with Nose-Hoover chain thermostats for the ionic degrees of freedom.<sup>55,56</sup> The AIMD equations<sup>49,57</sup> were integrated with a time step of 5 atomic units (a.u.), *i.e.* 0.121 fs. The (fictitious) mass of the wavefunction's coefficients was 500 a.u.

The shuttling process was explored by performing two *ab initio* metadynamics (MTD). In the first run, we selected as collective variable (CV), the displacement of the 8 oxygen atoms of the DB24C8 macrocycle on the side of the ethylene bridge, with respect to the nitrogen atoms of the Tz station (see path B→C in Figure 10, main text). In the second run, we adopted as CV the displacement of the 8 oxygen atoms of the ring on the methylene bridge side with respect to the Tz nitrogen atoms (see path B→A in Figure 10, main text). For the evolution of the CV, we employed the Lagrange-Langevin dynamics with friction of 0.001 a.u. The selected target temperature was 300 K as in the equilibration runs. The metadynamics parameters adopted for the gaussian hills in the production simulations were the following in all the methadynamics runs: perpendicular width = 0.02 a.u., height = 0.002 a.u. The sampling was accomplished in ~3000 metadynamics steps.

Due to the size of the simulation cell, all the PW simulations were performed in the gas phase. All PW calculations were carried out with the CPMD (Car-Parrinello-Molecular-Dynamics) computer program<sup>58</sup> running on the Shaheen II supercomputer at Kaust.

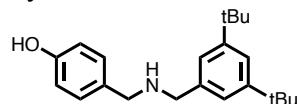
### 3.10. Synthetic procedures

#### 3.10.1 synthesis of the precursors **2b** and **3c**



Scheme 4. I)  $\text{Boc}_2\text{O}$ , THF, 87% II)  $\text{BrCH}_2\text{CCH}$ ,  $\text{K}_2\text{CO}_3$ ,  $\text{CH}_3\text{CN}$ , 94% III)  $\text{HPF}_6$ , THF, 75% IV)  $\text{BrC}_2\text{H}_4\text{Br}$ ,  $\text{K}_2\text{CO}_3$ ,  $\text{CH}_3\text{CN}$ , 42% V)  $\text{NaN}_3$ , DMF, 83% VI)  $\text{HPF}_6$ , THF, 72%.

### Synthesis of **a**

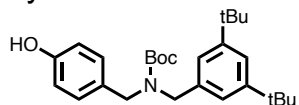


An ethanol solution (200 mL) of 3,5-di-*tert*-butylphenyl)methanamine\* (3.11 g, 14.16 mmol) and 4-hydroxybenzaldehyde (1.73 g, 14.16 mmol) was dried azeotropically at the rotary evaporator. The procedure was repeated three times, affording the imine intermediate, which was re-dissolved in ethanol (200 mL) and reduced by portionwise addition of NaBH<sub>4</sub> (1.18 g, 17.00 mmol) providing a vigorous effervescence and a final light-yellow solution. Once the effervescence terminated, the solution was heated to reflux for 30 min, then cooled down to room temperature and the solvent removed under reduced pressure. The crude product was dissolved in ethyl acetate (150 mL), washed with water (3×150 mL) and dried over MgSO<sub>4</sub>. Filtration and removal of the solvent under reduced pressure provided an off-white solid which was purified by recrystallisation from cyclohexane to obtain the product **a** as a colourless solid (3.79 g, 82%).

<sup>1</sup>H NMR (400 MHz, CDCl<sub>3</sub>, 298 K) δ 7.34 (t, *J* = 1.8 Hz, 1H), 7.18 (d, *J* = 1.8 Hz, 2H), 7.13 - 7.07 (m, 2H), 6.63 - 6.57 (m, 2H), 3.85 (s, 2H), 3.76 (s, 2H), 1.31 (s, 18H). <sup>13</sup>C NMR (101 MHz, CDCl<sub>3</sub>, 298 K) δ 156.24, 151.13, 138.15, 130.04, 129.94, 122.79, 121.44, 115.99, 53.86, 52.83, 34.94, 31.59.

\*For the synthesis of this compound refer to the experimental section of chapter 1 paragraph 1.11.2.

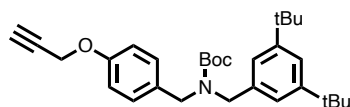
### Synthesis of **1a**



A tetrahydrofuran solution (100 mL) of di-*tert*-butyl dicarbonate (2.65 mL, 11.52 mmol) was added dropwise to a tetrahydrofuran solution (500 mL) of **a** (3.75 g, 11.52 mmol). The resulting mixture was stirred at room temperature for 16 h. Upon reaction completion, the solvent was removed under reduced pressure and the residue dissolved in ethyl acetate (150 mL), washed with water (3×150 mL) and dried over MgSO<sub>4</sub>. Filtration and removal of the solvent under reduced pressure provided a yellow solid which was purified by flash chromatography (hexane:ethyl acetate 70:30, R<sub>f</sub> = 0.65) to obtain the product **1a** as a colourless solid (4.275 g, 87%).

$^1\text{H}$  NMR (400 MHz,  $\text{CDCl}_3$ , 298 K)  $\delta$  7.33 (t,  $J = 1.7$  Hz, 1H), 7.05 (m, 4H), 6.79 (m, 2H), 6.29 (s, 1H, OH), 4.34 (dd,  $J = 20.9, 18.6$  Hz, 4H), 1.53 (s, 9H), 1.32 (s, 18H).  $^{13}\text{C}$  NMR (101 MHz,  $\text{CDCl}_3$ , 298 K)  $\delta$  155.62, 150.91, 137.10, 136.70, 129.41, 129.10, 128.91, 122.29, 121.91, 121.18, 115.51, 80.34, 49.91, 49.41, 48.90, 48.68, 34.79, 31.50, 28.56.

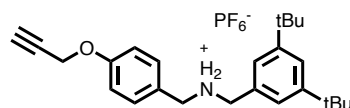
### Synthesis of **1b**



A dry acetonitrile (250 mL) suspension containing compound **1a** (1.20 g, 2.82 mmol), propargyl bromide (911  $\mu\text{L}$ , 8.46 mmol) and  $\text{K}_2\text{CO}_3$  (780 mg, 5.64 mmol) was stirred at 50  $^\circ\text{C}$  for 96 h under a dinitrogen atmosphere. The mixture was then cooled down to room temperature and the solvent removed under reduced pressure. The residue was dissolved in dichloromethane (100 mL), washed with water (3 $\times$ 100 mL) and dried over  $\text{MgSO}_4$ . Filtration and removal of the solvent under reduced pressure provided an orange oil which was purified by flash chromatography (hexane:ethyl acetate 85:15,  $R_f = 0.37$ ) to obtain the product **1b** as a brown/orange oil (1.23 g, 94%).

$^1\text{H}$  NMR (400 MHz,  $\text{CDCl}_3$ , 298 K)  $\delta$  7.32 (t,  $J = 1.8$  Hz, 1H), 7.22 - 6.98 (m, 4H), 6.93 (d,  $J = 8.6$  Hz, 2H), 4.69 (d,  $J = 2.4$  Hz, 2H), 4.47 - 4.17 (m, 4H), 2.52 (t,  $J = 2.4$  Hz), 1.51 (s, 9H), 1.31 (s, 18H).  $^{13}\text{C}$  NMR (101 MHz,  $\text{CDCl}_3$ , 298 K)  $\delta$  156.91, 156.10, 150.97, 137.39, 137.12, 131.38, 129.51, 128.95, 122.41, 122.01, 121.23, 114.99, 79.93, 78.75, 75.62, 55.97, 50.04, 49.55, 48.90, 48.63, 34.90, 31.61, 28.63.

### Synthesis of **2b**

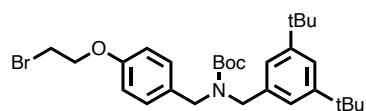


A tetrahydrofuran solution (1 mL) of  $\text{HPF}_6$  (1.3 mL of a 55% aqueous solution, 9.00 mmol) was added to a tetrahydrofuran solution (10 mL) of compound **1b** (1.40 g, 3.02 mmol) and the resulting mixture stirred at room temperature for 4 h. The solvent was removed under reduced pressure, water (50 mL) was then added and the mixture was extracted with dichloromethane (3 $\times$ 50 mL) and the combined organic phases washed with water (3 $\times$ 50 mL). The solvent was

removed under reduced pressure providing a light brown crude product that was purified by recrystallisation from cyclohexane, obtaining the product **2b** as a colourless solid (1.15 g, 75%).

$^1\text{H}$  NMR (500 MHz,  $\text{CDCl}_3$ , 298 K)  $\delta$  7.47 (s, 1H), 7.30 - 7.25 (m, 2H), 7.17 (d,  $J = 1.8$  Hz, 2H), 6.98 (d,  $J = 8.5$  Hz, 2H), 4.63 (d,  $J = 2.1$  Hz, 2H), 4.11 (d,  $J = 21.6$  Hz, 4H), 2.51 (m, 1H), 1.31 (s, 18H).  $^{13}\text{C}$  NMR (126 MHz,  $\text{CDCl}_3$ , 298 K)  $\delta$  158.88, 152.67, 131.59, 128.40, 124.25, 124.04, 122.12, 115.91, 78.07, 76.14, 55.91, 51.77, 50.52, 35.10, 31.39.  $^{19}\text{F}$  NMR (470 MHz,  $\text{CDCl}_3$ , 298 K)  $\delta$  -70.47 (d,  $J = 715.4$  Hz, 6F).

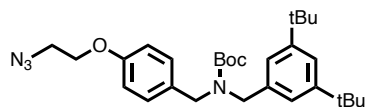
### Synthesis of **1c**



Compound **1a** (1.57 g, 3.68 mmol), 1,2-dibromoethane (5 mL, 58 mmol), KI (30 mg, 0.18 mmol) and  $\text{K}_2\text{CO}_3$  (1.27 g, 9.20 mmol) were suspended in dry acetonitrile (10 mL) under a dinitrogen atmosphere and stirred at 70 °C for 5 days. The mixture was then cooled down to room temperature and ethyl acetate (20 mL) was added. The organic phase was washed with water (3×50 mL), dried over  $\text{MgSO}_4$ . Filtration and removal of the solvent under reduced pressure provided a pale yellow solid which was purified by flash chromatography (hexane:ethyl acetate 90:10) to obtain the product **1c** as a colorless solid (820 mg, 42%).

$^1\text{H}$  NMR (400 MHz,  $\text{CDCl}_3$ , 298 K)  $\delta$  7.32 (s, 1H), 7.24 - 6.96 (m, 4H), 6.86 (d,  $J = 8.4$  Hz, 2H), 4.44 - 4.23 (m, 6H), 3.64 (t,  $J = 6.3$  Hz, 2H), 1.51 (s, 9H), 1.31 (s, 18H).  $^{13}\text{C}$  NMR (126 MHz,  $\text{CDCl}_3$ , 298 K)  $\delta$  157.28, 155.98, 150.84, 137.25, 131.13, 129.51, 128.91, 122.26, 121.87, 121.10, 114.75, 79.82, 67.94, 49.89, 49.42, 48.47, 34.77, 31.47, 29.10, 28.50.

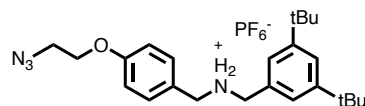
## Synthesis of **2c**



Compound **1c** (1.28 g, 2.40 mmol) and sodium azide (200 mg, 3.10 mmol) were suspended in dry dimethylformamide (20 mL) under a dinitrogen atmosphere and stirred at 70 °C for 3 h. The mixture was then cooled down to room temperature and water (20 mL) was added, followed by extraction with diethyl ether (3×30 mL). The combined organic phases were washed with water (3×30 mL) and dried over MgSO<sub>4</sub>. Filtration and removal of the solvent under reduced pressure provided the product **2c** as a colourless solid (980 mg, 83%).

<sup>1</sup>H NMR (500 MHz, CDCl<sub>3</sub>, 298 K) δ 7.33 (s, 1H), 7.25 - 6.97 (m, 4H), 6.88 (d, *J* = 8.4 Hz, 2H), 4.46 - 4.24 (m, 4H), 4.16 (t, *J* = 5.0 Hz, 2H), 3.61 (t, *J* = 4.9 Hz, 2H), 1.52 (s, 9H), 1.32 (s, 18H). <sup>13</sup>C NMR (126 MHz, CDCl<sub>3</sub>, 298 K) δ 157.58, 156.13, 150.99, 137.40, 131.18, 129.62, 128.99, 122.43, 122.06, 121.26, 114.72, 79.97, 67.17, 50.34, 50.02, 49.56, 48.92, 48.62, 34.92, 31.62, 28.65.

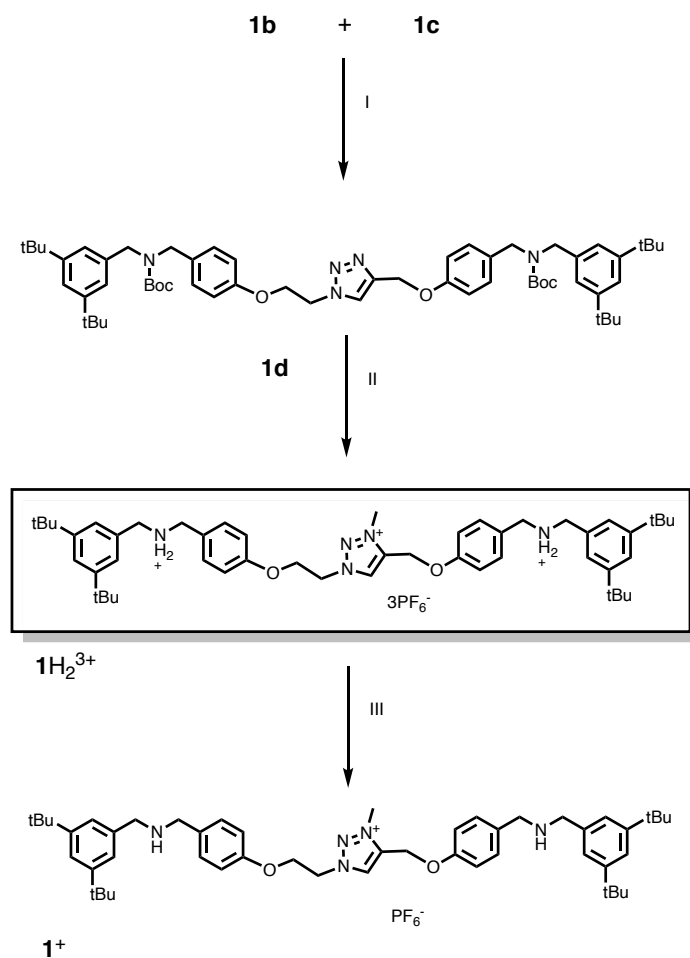
## Synthesis of **3c**



A tetrahydrofuran solution (1 mL) of HPF<sub>6</sub> (1.3 mL of a 55% aqueous solution, 9.00 mmol) was added to a tetrahydrofuran solution (10 mL) of compound **2c** (930 mg, 1.90 mmol) and the resulting mixture stirred at room temperature for 4 h. Water (50 mL) was then added and the mixture was extracted with dichloromethane (3×50 mL) and the combined organic phases washed with water (3×50 mL). The solvent was removed under reduced pressure providing a light brown crude product that was purified by recrystallisation from cyclohexane, obtaining the product **3c** as a colourless solid (741 mg, 72%).

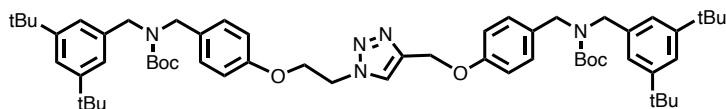
<sup>1</sup>H NMR (500 MHz, CDCl<sub>3</sub>, 298 K) δ 7.47 (s, 1H), 7.30 - 7.25 (m, 2H), 7.18 (m, 2H), 6.92 (d, *J* = 8.5 Hz, 2H), 4.18 - 4.06 (m, 6H), 3.57 (t, *J* = 4.8 Hz, 2H), 1.31 (s, 18H). <sup>13</sup>C NMR (126 MHz, CDCl<sub>3</sub>, 298 K) δ 159.62, 152.72, 131.69, 128.36, 124.29, 124.00, 121.86, 115.58, 67.10, 51.83, 50.63, 50.18, 35.10, 31.38. <sup>19</sup>F NMR (470 MHz, CDCl<sub>3</sub>, 298 K) δ -70.47 (d, *J* = 715.4 Hz, 6F).

### 3.10.2. Synthesis of the model compound $1H_2^{3+}$



Scheme 5. I)  $[(MeCN)_4Cu][PF_6]$ , DCM, 84% II) a.  $CH_3I$ , b.  $TFA/Na_2CO_3$  c.  $HCl/NH_4PF_6$ , 41%. III)  $Na_2CO_3$ ,  $KPF_6$ , 96%.

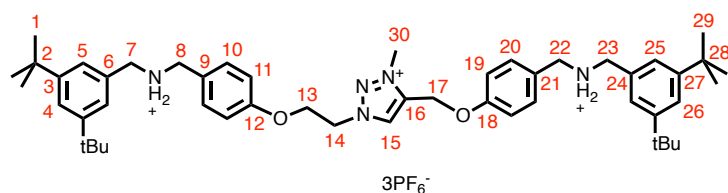
## Synthesis of **1d**



Compound **1b** (110 mg, 0.30 mmol), compound **2c** (113 mg, 0.30 mmol) and  $[\text{Cu}(\text{MeCN})_4][\text{PF}_6]$  (224 mg, 0.60 mmol) were dissolved in dry dichloromethane (20 mL) and stirred at room temperature for 48 h. The mixture was then diluted with dichloromethane (50 mL) and washed with sodium ethylenediaminetetraacetate (0.1 M in  $\text{H}_2\text{O}$ ,  $3 \times 25$  mL), water ( $3 \times 25$  mL) and dried over  $\text{MgSO}_4$ . Filtration and removal of the solvent under reduced pressure provided a pale-yellow solid which was purified by Flash Chromatography (chloroform,  $R_f = 0.2$ ) to obtain the product **1d** as a colourless solid (241 mg, 84%).

$^1\text{H}$  NMR (500 MHz,  $\text{CD}_2\text{Cl}_2$ , 298 K)  $\delta$  7.90 (s, 1H), 7.38 - 7.33 (m, 2H), 7.21 (bs, 4H), 7.08 (m, 4H), 7.00 (d,  $J = 8.5$  Hz, 2H), 6.89 (d,  $J = 8.5$  Hz, 2H), 5.21 (s, 2H), 4.79 (d,  $J = 5.0$  Hz, 2H), 4.45 - 4.30 (m, 10H), 1.53 (d,  $J = 3.9$  Hz, 18H), 1.35 (d,  $J = 6.1$  Hz, 36H).  $^{13}\text{C}$  NMR (126 MHz,  $\text{CD}_2\text{Cl}_2$ , 298 K)  $\delta$  158.03, 157.56, 156.19, 156.18, 151.32, 144.41, 137.91, 132.07, 131.54, 129.77, 129.67, 129.47, 124.41, 122.29, 122.26, 121.46, 115.11, 114.92, 80.01, 66.92, 62.38, 54.24, 50.52, 50.25, 50.05, 49.62, 49.06, 35.11, 35.10, 31.69, 31.68, 28.68.

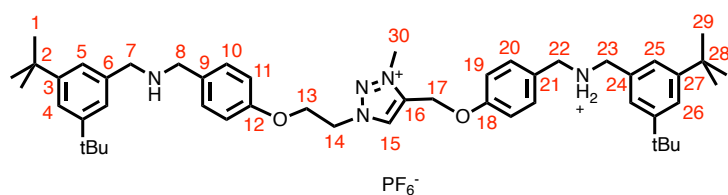
## Synthesis of $1\text{H}_2^{3+}$



Under a dinitrogen atmosphere, compound **1d** (241 mg, 0.25 mmol) was dissolved in iodomethane (15 mL) and the resulting solution was stirred for 48 h at room temperature under exclusion of light. Upon reaction completion, the solvent was removed under reduced pressure providing a yellow solid, which was dissolved in dichloromethane (30 mL) and washed with  $\text{KPF}_6(\text{aq})$  ( $3 \times 15$  mL). The organic fraction was isolated, the solvent removed under reduced pressure and the residue dissolved in trifluoroacetic acid (10 mL) and stirred at room temperature for 16 h. The acid was removed under reduced pressure and the crude product suspended in ethyl acetate (30 mL) and washed with  $\text{Na}_2\text{CO}_3(\text{aq})$  ( $3 \times 30$  mL). Removal of the solvent from the organic fraction provided a solid that was dissolved in the minimum volume of methanol (1 mL) and reacted with 37% HCl (few drops). Addition of a saturated methanol solution of  $(\text{H}_4\text{N})\text{PF}_6$  (3 mL), followed by precipitation through dropwise addition of water provided a colourless solid which was filtered and purified by sonication in diethyl ether to obtain the product  $1\text{H}_2^{3+}$  as a colourless solid (124 mg, 41%).

$^1\text{H}$  NMR (500 MHz,  $\text{CD}_3\text{CN}$ , 298 K)  $\delta$  8.57 (s, 1H, **15**), 7.53 (m, 2H, **4+26**), 7.50 - 7.45 (d,  $J = 8.3$  Hz, 2H, **20**), 7.44 - 7.39 (d,  $J = 8.3$  Hz, 2H, **10**), 7.30 (m, 4H, **5+25**), 7.15 - 7.09 (d,  $J = 8.3$  Hz, 2H, **19**), 7.08 - 6.81 (m, 6H,  $\text{NH}_2$ +**11**), 5.33 (s, 2H, **17**), 4.98 (t,  $J = 4.9$  Hz, 2H, **14**), 4.47 (t,  $J = 4.9$  Hz, 2H, **13**), 4.27 (d,  $J = 1.0$  Hz, 3H, **30**), 4.22 - 4.13 (m, 8H, **7+8+22+23**), 1.32 (s, 36H, **1+29**).  $^{13}\text{C}$  NMR (126 MHz,  $\text{CD}_3\text{CN}$ , 298 K)  $\delta$  159.66, 159.18, 152.85, 152.84, 140.49, 133.20, 133.09, 131.39, 130.75, 125.35, 125.21, 124.69, 124.67, 124.50, 116.17, 115.98, 66.08, 59.09, 54.46, 52.81, 52.75, 51.83, 51.78, 39.62, 35.65, 31.55.  $^{19}\text{F}$  NMR (470 MHz,  $\text{CD}_3\text{CN}$ , 298 K)  $\delta$  -72.89 (dd,  $J = 705.9, 4.9$  Hz, 18F). HRMS-ESI ( $m/z$ ): calcd for  $[\text{C}_{50}\text{H}_{73}\text{N}_5\text{O}_2\text{P}_2\text{F}_{12}]$ , 1065.5048; found 1064.4969 [**(9-H)**( $\text{PF}_6$ ) $_2$ ] $^+$ .

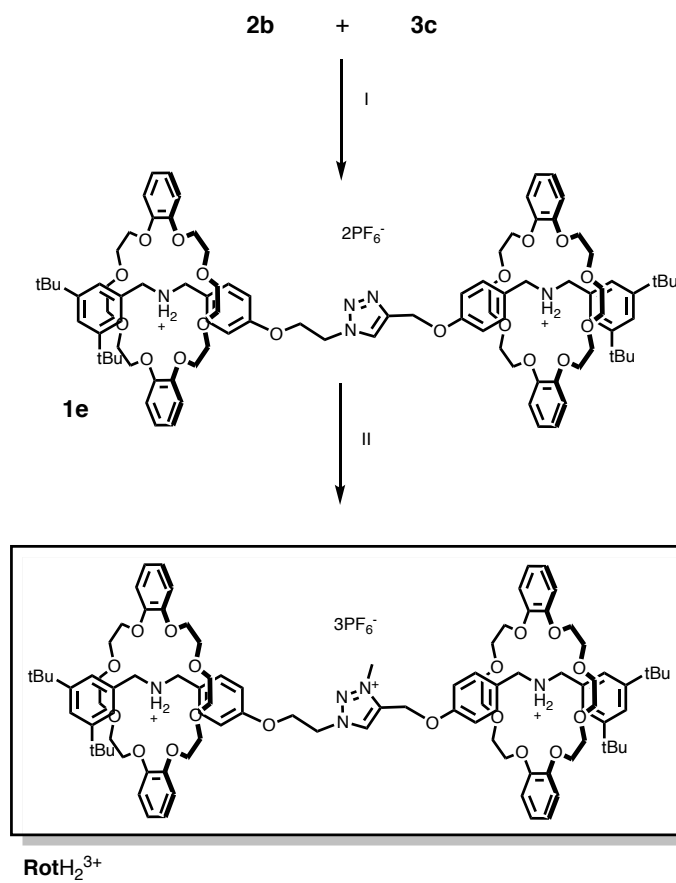
## Synthesis of **1**<sup>+</sup>



A solution of **1H**<sub>2</sub><sup>3+</sup> (124 mg, 0.10 mmol) in dichloromethane (30 mL) was washed with Na<sub>2</sub>CO<sub>3(aq)</sub> (3×30 mL) and dried over MgSO<sub>4</sub>. Filtration and removal of the solvent under reduced pressure provided the product **1**<sup>+</sup> as a crystalline colourless solid (90 mg, 96%).

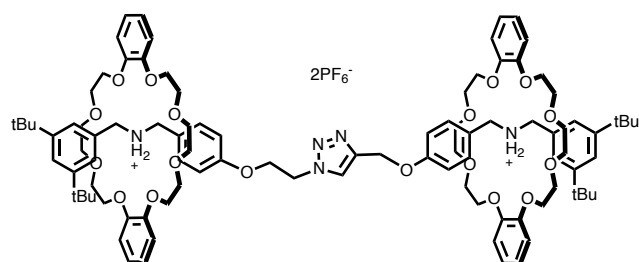
<sup>1</sup>H NMR (500 MHz, CD<sub>3</sub>CN, 298 K) δ 8.55 (s, 1H, **15**), 7.45 - 7.41 (m, 2H, **4+26**), 7.36 (m, 4H, **20+10**), 7.24 (s, 4H, **5+25**), 7.04 (d, *J* = 8.7 Hz, 2H, **19**), 6.92 (d, *J* = 8.6 Hz, 2H, **11**), 5.32 (s, 2H, **17**), 4.98 - 4.92 (t, *J* = 4.9 Hz, 2H, **14**), 4.46 - 4.41 (t, *J* = 4.9 Hz, 2H, **13**), 4.26 (s, 3H, **30**), 3.94 - 3.88 (m, 8H, **7+8+22+23**), 1.31 (s, 36H, **1+29**). <sup>13</sup>C NMR (126 MHz, CD<sub>3</sub>CN, 298 K) δ 158.66, 157.96, 152.30, 152.22, 140.71, 131.86, 131.75, 131.35, 124.38, 124.22, 123.30, 123.08, 115.93, 115.71, 66.10, 59.11, 54.51, 53.48, 53.34, 52.34, 52.32, 39.60, 35.55, 31.66, 31.64. <sup>19</sup>F NMR (470 MHz, CD<sub>3</sub>CN, 298 K) δ -72.89 (d, *J* = 706.5 Hz, 6F). HRMS-ESI (*m/z*): calcd for [C<sub>50</sub>H<sub>71</sub>N<sub>5</sub>O<sub>2</sub>], 773.5608; found 772.5530 [**10-H**]<sup>+</sup>.

### 3.10.3. Synthesis of the [3]rotaxane

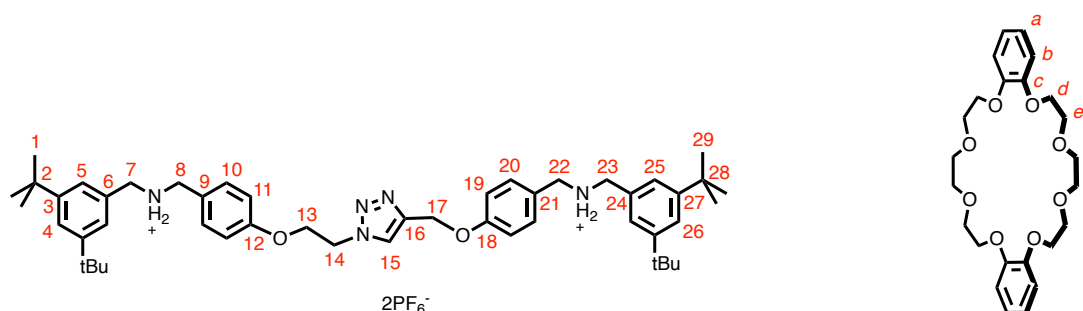


Scheme 6. I) DB24C8,  $[(\text{CH}_3\text{CN})_4\text{Cu}][\text{PF}_6]$ , DCM. 78% II) MeI,  $\text{KPF}_6$ . 91%.

## Synthesis of **1e**

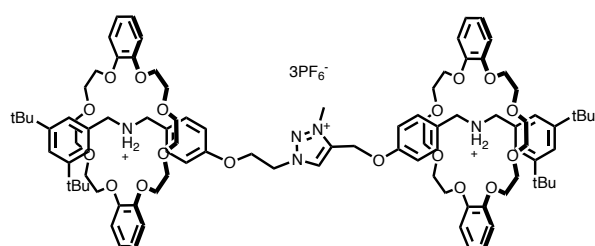


Compound **3c** (150 mg, 0.28 mmol), compound **2b** (143 mg, 0.28 mmol) and DB24C8 (630 mg, 1.40 mmol) were dissolved in dry dichloromethane (20 mL) and stirred for 10 min at room temperature under a dinitrogen atmosphere. The catalyst  $[\text{Cu}(\text{MeCN})_4][\text{PF}_6]$  (59 mg, 0.61 mmol) was then added and the resulting mixture stirred at room temperature for 48 h. The mixture was then diluted with dichloromethane (50 mL) and washed with sodium ethylenediaminetetraacetate (0.1 M in  $\text{H}_2\text{O}$ ,  $3 \times 25$  mL), water ( $3 \times 25$  mL) and dried over  $\text{MgSO}_4$ . Filtration and removal of the solvent under reduced pressure provided a pale-yellow solid which was purified by Size-Exclusion Chromatography (dichloromethane) to obtain the product **1e** as a colourless solid (425 mg, 78%).

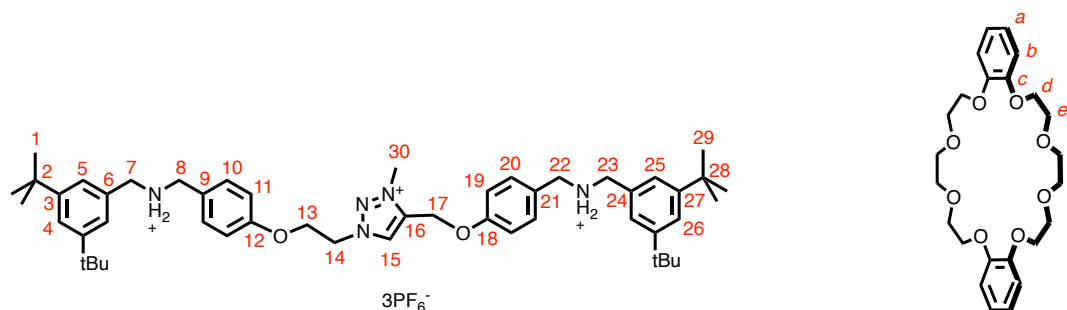


$^1\text{H}$  NMR (500 MHz,  $\text{CD}_2\text{Cl}_2$ , 298 K)  $\delta$  7.94 (s, 1H, **15**), 7.53 (s, 4H,  $\text{NH}_2$ ), 7.42 - 7.37 (m, 2H, **4+26**), 7.29 (m, 4H, **5+25**), 7.12 (d,  $J = 8.7$  Hz, 2H, **20**), 7.11 (d,  $J = 8.7$  Hz, 2H, **10**), 6.92 - 6.80 (m, 8H, **a**), 6.84 - 6.75 (m, 8H, **b**), 6.67 (d,  $J = 8.6$  Hz, 2H, **19**), 6.53 (d,  $J = 8.6$  Hz, 2H, **11**), 5.02 (s, 2H, **17**), 4.76 - 4.68 (m, 6H, **14+7+23**), 4.52 (dd,  $J = 6.8, 3.2$  Hz, 4H, **8+22**), 4.20 (t,  $J = 5.1$  Hz, 2H, **13**), 4.14 - 4.03 (m, 16H, **d**), 3.83 - 3.68 (m, 16H, **e**), 3.66 - 3.43 (m, 16H, **f**), 1.20 (s, 36H, **1+29**).  $^{13}\text{C}$  NMR (126 MHz,  $\text{CD}_2\text{Cl}_2$ , 298 K)  $\delta$  159.33, 158.80, 151.94, 151.90, 147.88, 147.82, 143.7, 131.85, 131.23, 131.21, 124.83, 124.48, 124.10, 123.96, 123.92, 123.71, 121.94, 121.86, 114.86, 114.59, 112.93, 112.85, 71.01, 70.98, 70.61, 70.60, 68.36, 68.28, 66.54, 61.91, 53.22, 52.70, 52.60, 50.01, 35.15, 35.14, 31.46, 31.45.  $^{19}\text{F}$  NMR (470 MHz,  $\text{CD}_3\text{CN}$ , 298 K)  $\delta$  -72.89 (d,  $J = 706.5$  Hz, 12F). HRMS-ESI ( $m/z$ ): calcd for  $[\text{C}_{97}\text{H}_{133}\text{N}_5\text{O}_{18}]$ , 828.4862; found 828.9901  $[\text{7+H}]^{2+}$ .

## Synthesis of $\text{RotH}_2^{3+}$



Under a dinitrogen atmosphere, compound **1e** (254 mg, 0.13 mmol) was dissolved in iodomethane (13 mL) and the resulting solution was stirred for 48 h at room temperature under exclusion of light. Upon reaction completion, the solvent was removed under reduced pressure providing a yellow solid, which was dissolved in the minimum amount of acetonitrile. Addition of a saturated aqueous solution of ammonium hexafluorophosphate led to the precipitation of a yellow solid, which was isolated, dissolved in dichloromethane and washed with a saturated aqueous solution of ammonium hexafluorophosphate (3×5 mL) and water (3×5 mL) and dried over  $\text{MgSO}_4$ . Filtration and removal of the solvent under reduced pressure provided the product  $\text{RotH}_2^{3+}$  as a yellow solid (246 mg, 91%).



$^1\text{H}$  NMR (500 MHz,  $\text{CD}_2\text{Cl}_2$ , 298 K)  $\delta$  8.59 (s, 1H, **15**), 7.58 (s, 4H,  $\text{NH}_2$ ), 7.41 (d,  $J = 6.9$  Hz, 2H, **4+26**), 7.35 - 7.27 (m, 4H, **5+25**), 7.20 (d,  $J = 8.6$  Hz, 2H, **20**), 7.14 (d,  $J = 8.6$  Hz, 2H, **10**), 6.85 (m, 16H, **a+b**), 6.69 (d,  $J = 8.6$  Hz, 2H, **19**), 6.61 (d,  $J = 8.6$  Hz, 2H, **11**), 5.19 (s, 2H, **17**), 4.99 - 4.93 (t,  $J = 5.1$  Hz, 2H, **14**), 4.75 - 4.68 (m, 4H, **7+23**), 4.61 - 4.50 (m, 4H, **8+22**), 4.36 (s, 3H, **30**), 4.34 - 4.30 (t,  $J = 5.1$  Hz, 2H, **13**), 4.10 (dtd,  $J = 15.9, 10.9, 6.3$  Hz, 16H, **d**), 3.77 (ddt,  $J = 41.8, 11.7, 6.1$  Hz, 16H, **e**), 3.68 - 3.44 (m, 16H, **f**), 1.21 (d,  $J = 4.5$  Hz, 36H, **1+29**).

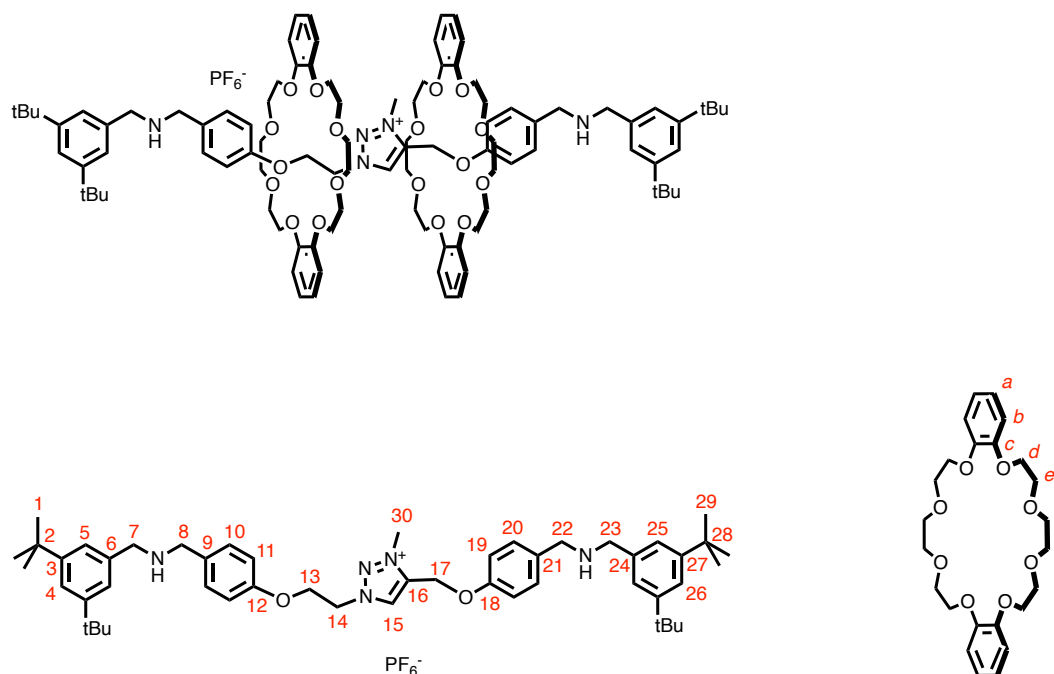
$^{13}\text{C}$  NMR (126 MHz,  $\text{CD}_2\text{Cl}_2$ , 298 K)  $\delta$  158.23 (**12**), 157.75 (**18**), 151.95 (**3** or **26**), 151.90 (**26** or **3**), 147.84 (**c**), 140.31 (**16**), 131.79 (**6+24**), 131.53 (**20**), 131.29 (**10**), 130.49 (**15**), 125.74 (**21**), 125.06 (**9**), 123.96 (**5** or **25**), 123.92 (**25** or **5**), 123.71 (**4+27**), 121.89 (**a**), 114.93 (**11**), 114.84 (**19**), 112.93 (**b**), 70.98 (**f**), 70.60 (**e**), 68.30 (**d**), 64.96 (**13**), 58.31 (**17**), 53.97 (**14**), 53.25

(7+23), 52.57 (8), 52.48 (22), 39.24 (30), 35.14 (2+28), 31.45 (1+29).  $^{19}\text{F}$  NMR (470 MHz,  $\text{CD}_3\text{CN}$ , 298 K)  $\delta$  -72.83 (d,  $J = 706.6$  Hz, 18F). HRMS-ESI ( $m/z$ ): calcd for  $[\text{C}_{98}\text{H}_{136}\text{N}_5\text{O}_{18}\text{P}_2\text{F}_{12}]$ , 1960.9164; found 1960.9164 [(RotH<sub>2</sub>)(PF<sub>6</sub>)<sub>2</sub>]<sup>+</sup>.

## General procedure for the stepwise deprotonation of compound **RotH<sub>2</sub><sup>3+</sup>**

A solution of **RotH<sub>2</sub><sup>3+</sup>** (38 mg, 0.018 mmol) in CD<sub>2</sub>Cl<sub>2</sub> (500 μL) was reacted with the phosphazene base (20 mg) inside an NMR tube. The suspension was mixed for fixed time intervals and the reaction progress monitored by <sup>1</sup>H NMR spectroscopy. Upon disappearance of the peaks of **RotH<sub>2</sub><sup>3+</sup>**, the mixture was filtered through a pad of Celite to isolate the solution containing the dicationic compounds **RotH<sub>2</sub><sup>+</sup>-I** and **RotH<sub>2</sub><sup>+</sup>-II**. An analogous protocol, comprising the addition of the base **B1** to the solution containing the intermediates **RotH<sub>2</sub><sup>+</sup>-I** and **RotH<sub>2</sub><sup>+</sup>-II**, agitation and filtration provided the monocation **Rot<sup>+</sup>**.

## Synthesis of **Rot<sup>+</sup>**



Yield: 33 mg, quantitative. <sup>1</sup>H NMR (500 MHz, CD<sub>2</sub>Cl<sub>2</sub>, 298 K) δ 8.63 (s, 1H, **15**), 7.51 (d, *J* = 8.5 Hz, 2H, **19**), 7.32 (m, 2H, **4+26**), 7.24 (d, *J* = 8.3 Hz, 2H, **20**), 7.16 (m, 6H, **5+25+10**), 6.88 (m, 10H, **a+11**), 6.72 (m, 8H, **b**), 5.65 (s, 2H, **17**), 5.42 (t, *J* = 8.1 Hz, 2H, **14**), 4.77 (t, *J* = 8.1 Hz, 2H, **13**), 3.98 - 3.84 (m, 16H, **d**), 3.79 - 3.67 (m, 16H, **8+22+7+23+e**), 3.57 - 3.44 (m, 15H, **30+e+f**), 3.36 (ddt, *J* = 14.2, 5.8, 3.5 Hz, 8H, **e+f**), 3.04 (tt, *J* = 6.5, 3.3 Hz, 4H, **f**), 1.31 (d, *J* = 2.3 Hz, 36H, **1+29**). <sup>13</sup>C NMR (126 MHz, CD<sub>2</sub>Cl<sub>2</sub>, 298 K) δ 158.23 (**12**), 158.06 (**18**), 151.17 (**3** or **26**), 151.15 (**26** or **3**), 148.68 (**c**), 148.58 (**c**), 140.22 (**6** or **24**), 140.18 (**24** or **6**), 139.05 (**16**), 133.15 (**9**), 133.08 (**21**), 132.55 (**15**), 129.56 (**10**), 128.63 (**20**), 122.80 (**5** or **25**), 122.68 (**25** or **5**), 121.49 (**a** or **b**), 121.47 (**a** or **b**), 121.23 (**4** or **27**), 121.19 (**27** or **4**), 116.71

(**19**), 114.73 (**11**), 112.86 (**b** or **a**), 112.49 (**b** or **a**), 71.51 (**f**), 71.25 (**f**), 70.66 (**e**), 70.37 (**e**), 69.00 (**d**), 68.89 (**d**), 65.02 (**13**), 56.82 (**17**), 54.15 (**7+23**), 53.26 (**22**), 53.20 (**8**), 52.12 (**14**), 37.35 (**30**), 35.08 (**2+28**), 31.65 (**1+29**). <sup>19</sup>F NMR (470 MHz, CD<sub>3</sub>CN, 298 K) δ -72.91 (d, *J* = 706.6 Hz, 6F). HRMS-ESI (*m/z*): calcd for [C<sub>98</sub>H<sub>135</sub>N<sub>5</sub>O<sub>18</sub>], 1669.9802; found 1669.9802 [Rot]<sup>+</sup>.

### 3.11. NMR spectra

$^1\text{H}$  and  $^{13}\text{C}$  NMR spectra of  $1\text{-H}_2^{3+}$

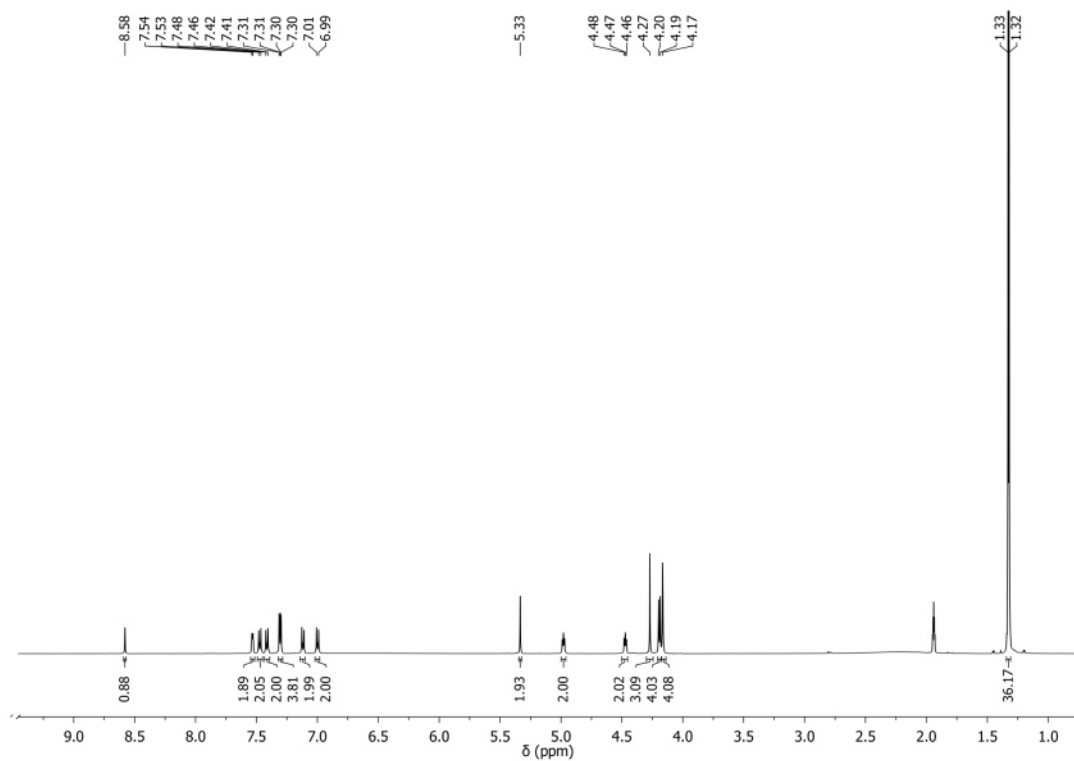


Figure 16.  $^1\text{H}$  NMR spectrum of  $1\text{H}_2^{3+}$  ( $\text{CD}_3\text{CN}$ , 298 K, 500 MHz).

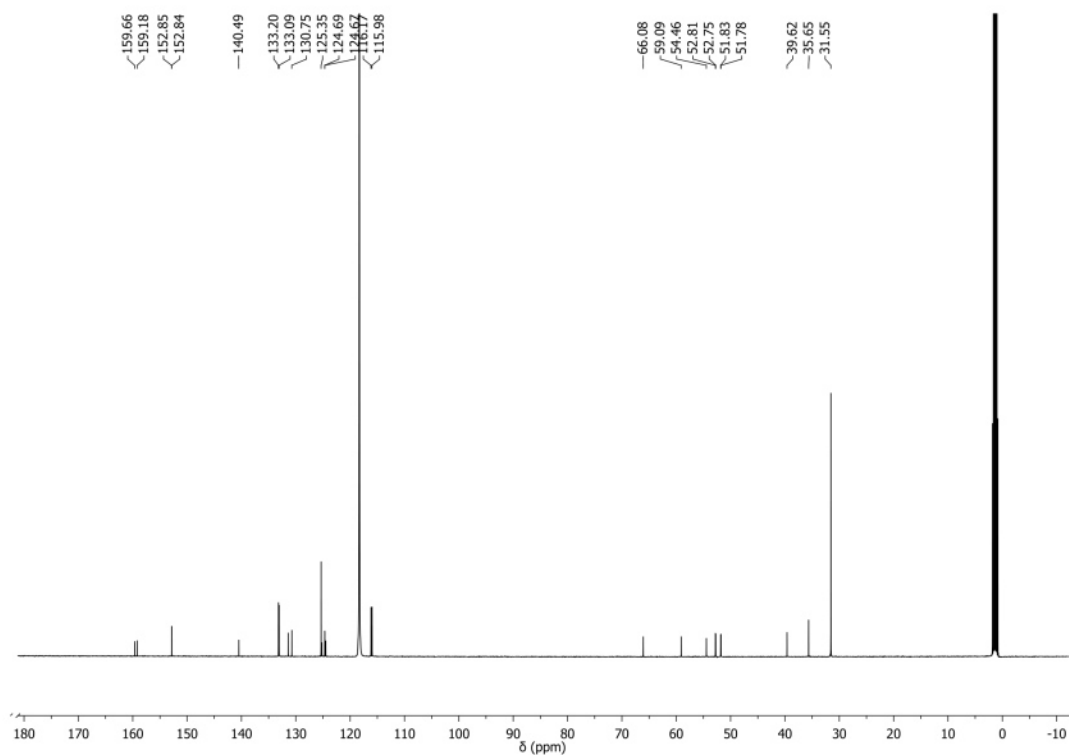


Figure 17.  $^{13}\text{C}$  NMR spectrum of  $1\text{H}_2^{3+}$  ( $\text{CD}_3\text{CN}$ , 298 K, 126 MHz).

$^1\text{H}$  and  $^{13}\text{C}$  NMR spectra of  $1^+$

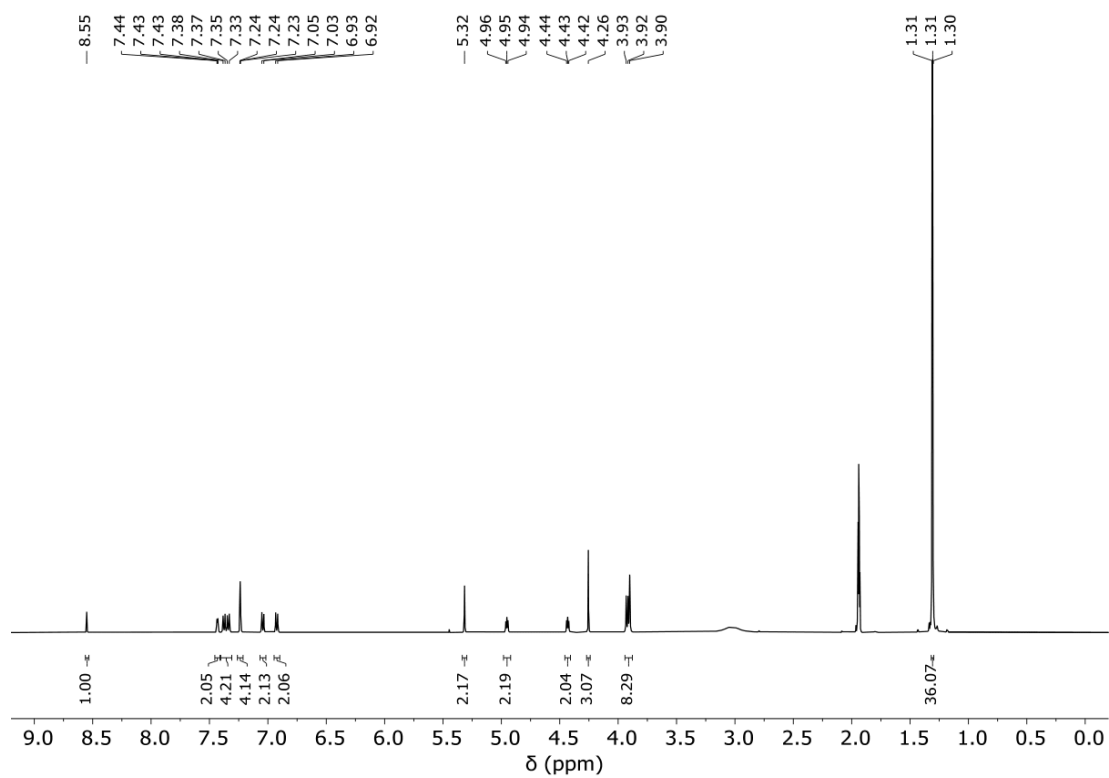


Figure 18.  $^1\text{H}$  NMR spectrum of  $1^+$  ( $\text{CD}_3\text{CN}$ , 298 K, 500 MHz).

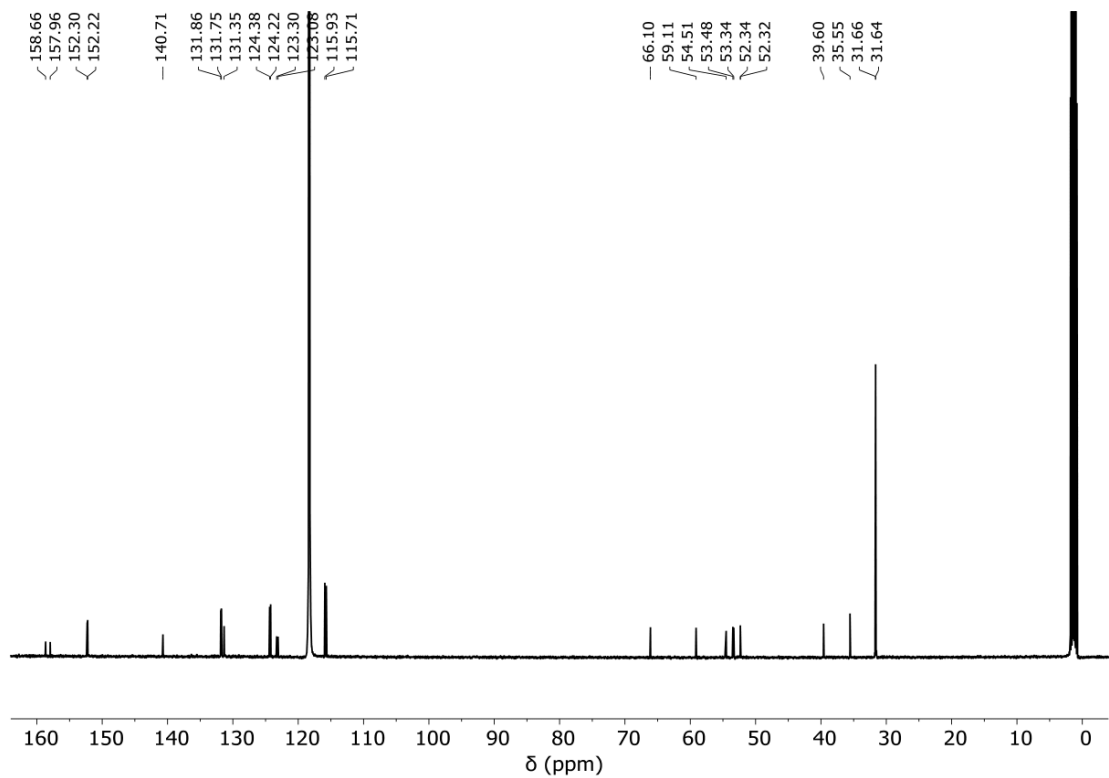


Figure 19.  $^{13}\text{C}$  NMR spectrum of  $1^+$  ( $\text{CD}_3\text{CN}$ , 298 K, 126 MHz).

$^1\text{H}$  and  $^{13}\text{C}$  NMR spectra of  $\text{RotH}_2^{3+}$

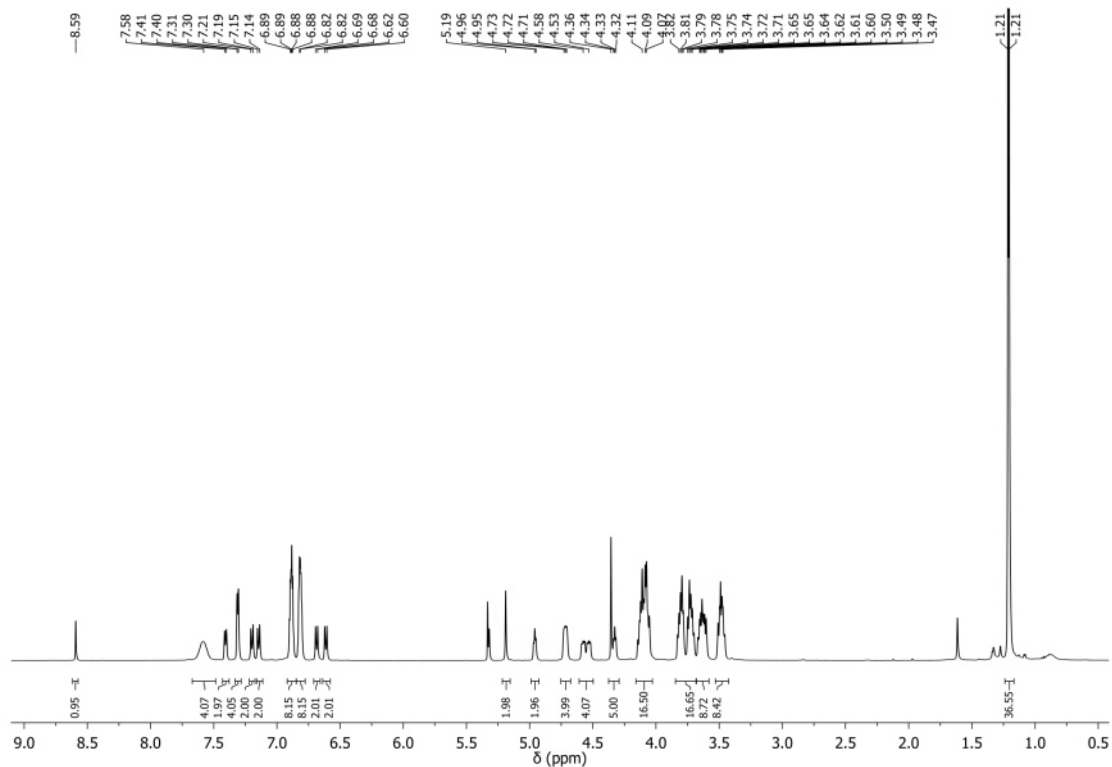


Figure 20.  $^1\text{H}$  NMR spectrum of  $\text{RotH}_2^{3+}$  ( $\text{CD}_2\text{Cl}_2$ , 298 K, 500 MHz).

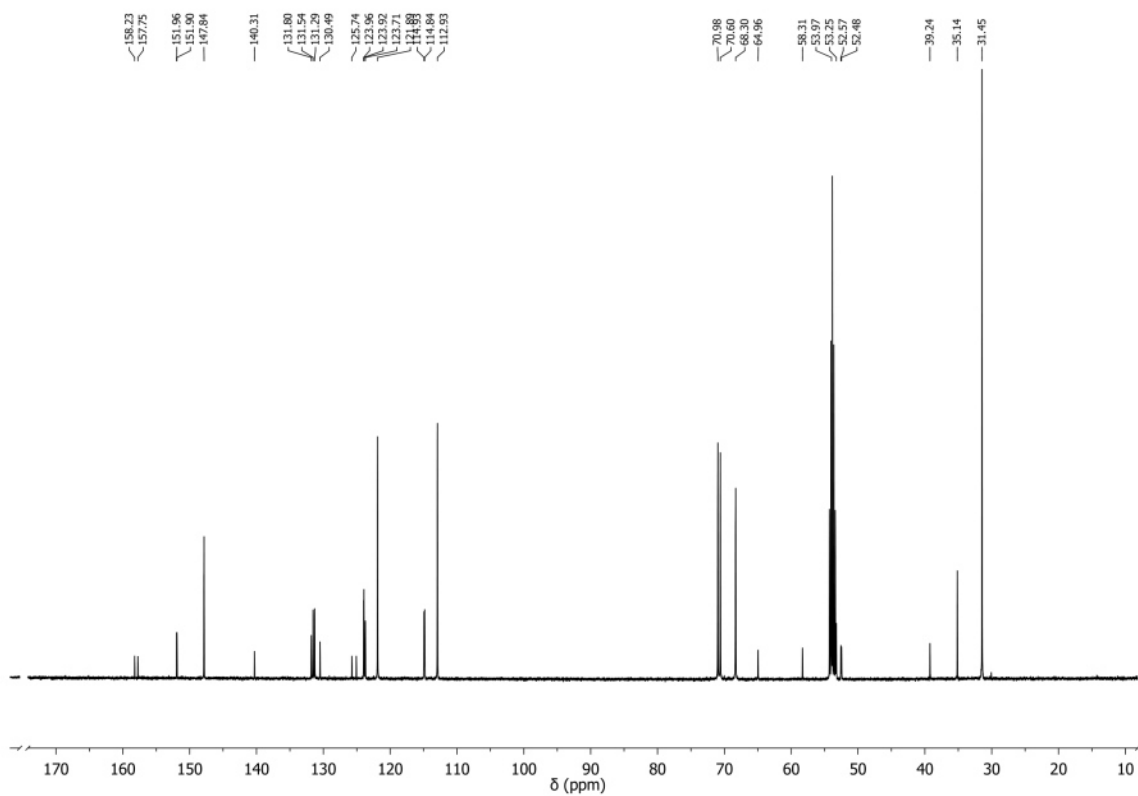


Figure 21.  $^{13}\text{C}$  NMR spectrum of  $\text{RotH}_2^{3+}$  ( $\text{CD}_2\text{Cl}_2$ , 298 K, 126 MHz).

## HSQC and HMBC spectra of $\text{RotH}_2^{3+}$

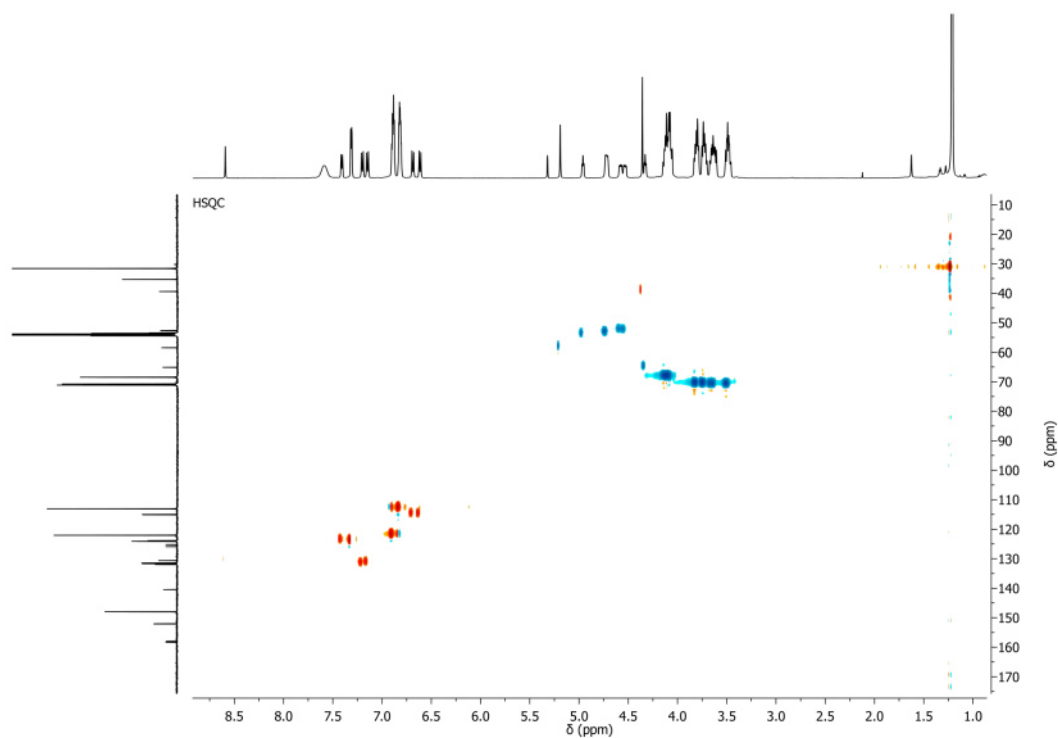


Figure 22. Heteronuclear Single Quantum coherence Spectroscopy (HSQC).  $\text{RotH}_2^{3+}$ , f1:  $^{13}\text{C}$  NMR, f2:  $^1\text{H}$  NMR, ( $\text{CD}_2\text{Cl}_2$ , 298 K, 126 MHz, 500 MHz).

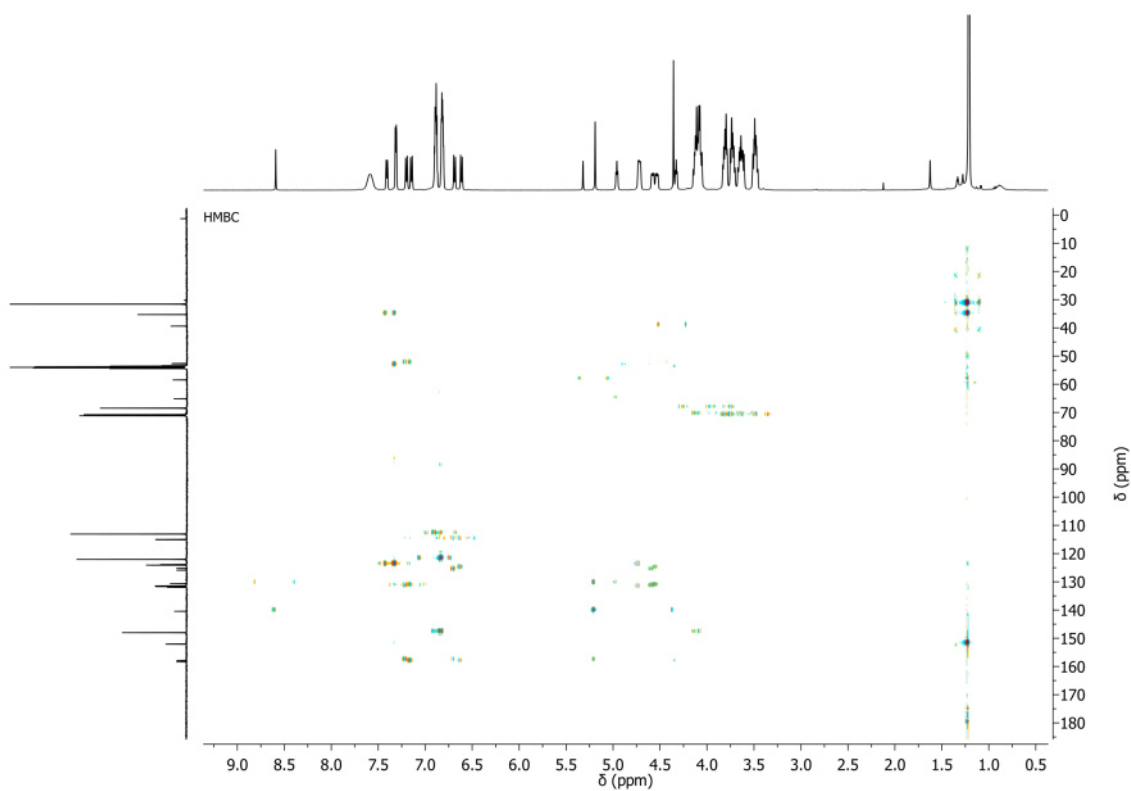


Figure 23. Heteronuclear Multiple Bond Correlation (HMBC).  $\text{RotH}_2^{3+}$ , f1:  $^{13}\text{C}$  NMR, f2:  $^1\text{H}$  NMR, ( $\text{CD}_2\text{Cl}_2$ , 298 K, 126 MHz, 500 MHz).

# $^1\text{H}$ and $^{13}\text{C}$ NMR spectra of **Rot**<sup>+</sup>

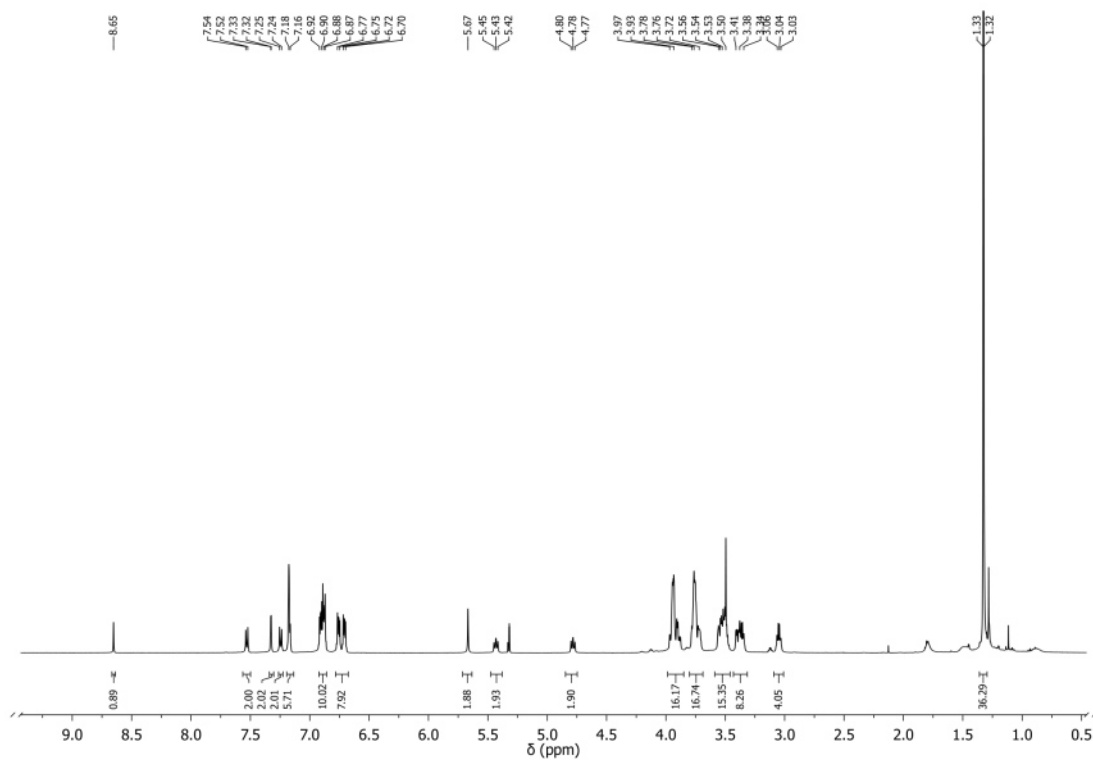


Figure 24.  $^1\text{H}$  NMR spectrum of **Rot**<sup>+</sup> ( $\text{CD}_2\text{Cl}_2$ , 298 K, 500 MHz).

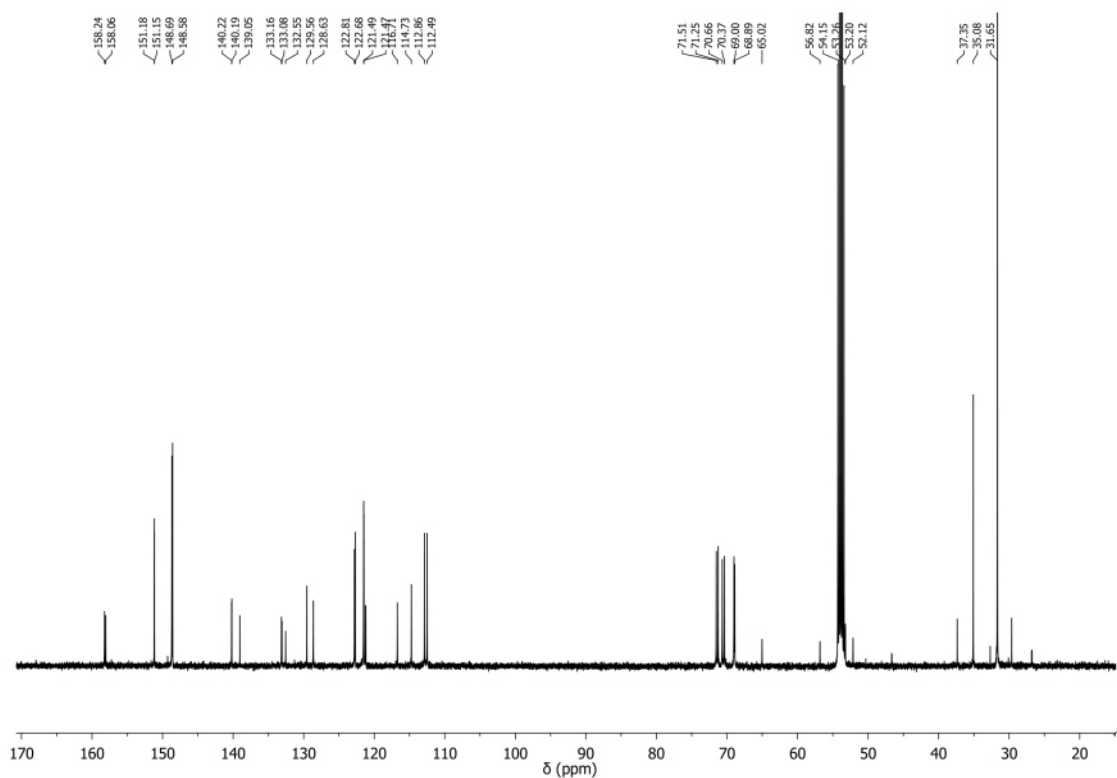


Figure 25.  $^{13}\text{C}$  NMR spectrum of **Rot**<sup>+</sup> ( $\text{CD}_2\text{Cl}_2$ , 298 K, 126 MHz).

## HSQC and HMBC spectra of **Rot**<sup>+</sup>

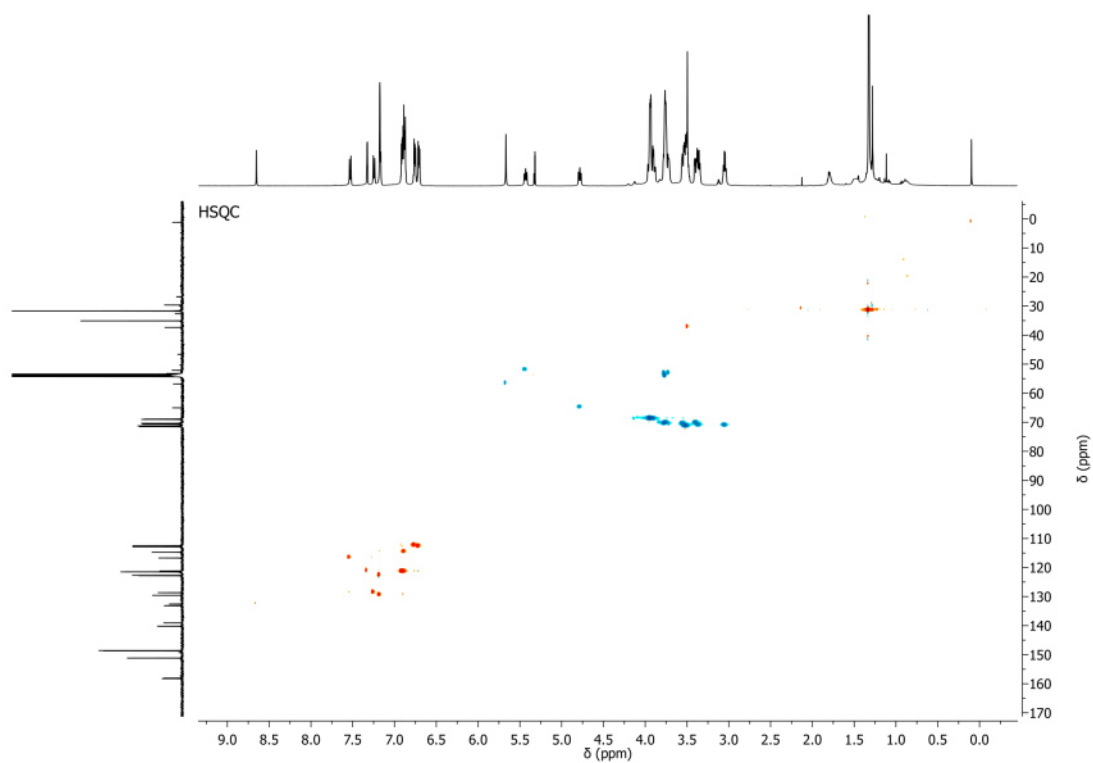


Figure 26. Heteronuclear Single Quantum coherence Spectroscopy (HSQC). **Rot**<sup>+</sup>, *f1*: <sup>13</sup>C NMR, *f2*: <sup>1</sup>H NMR, (CD<sub>2</sub>Cl<sub>2</sub>, 298 K, 126 MHz, 500 MHz).

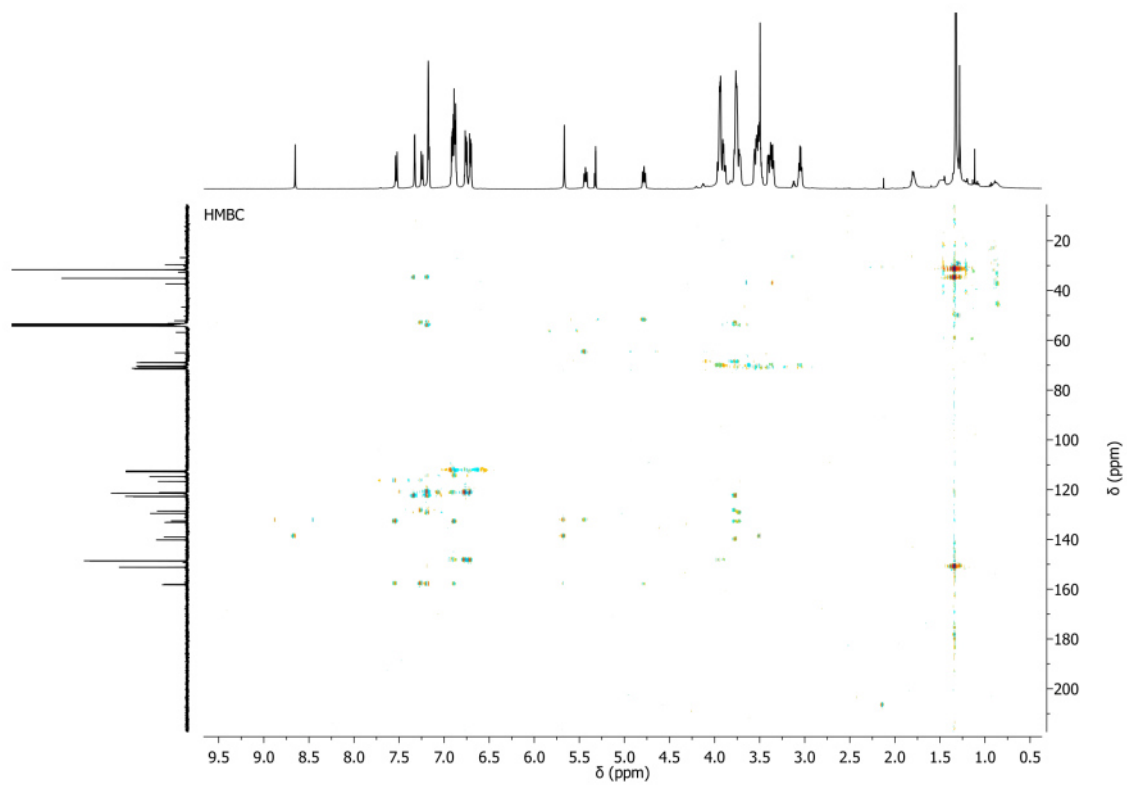


Figure 27. Heteronuclear Multiple Bond Correlation (HMBC). **Rot**<sup>+</sup>, *f1*: <sup>13</sup>C NMR, *f2*: <sup>1</sup>H NMR, (CD<sub>2</sub>Cl<sub>2</sub>, 298 K, 126 MHz, 500 MHz).

### 3.12. References

1. K. Mayumi, K. Ito, K. Kato, *Polyrotaxane and Slide-Ring Materials*; RSC Publishing: Cambridge, U.K., **2015**.
2. T. Oku, Y. Furusho, T. Takata, *Angew. Chem., Int. Ed.*, **2004**, *43*, 966–969.
3. M. Nakahata, S. Mori, Y. Takashima, H. Yamaguchi, A. Harada, *Chem.*, **2016**, *1*, 766–775.
4. K. Iwaso, Y. Takashima, A. Harada, *Nat. Chem.*, **2016**, *8*, 625–632.
5. A. Goujon, T. Lang, G. Mariani, E. Moulin, G. Fuks, J. Raya, E. Buhler, N. Giuseppone, *J. Am. Chem. Soc.*, **2017**, *139*, 14825–14828.
6. M. Dommaschk, J. Echavarren, D. A. Leigh, V. Marcos, T. A. Singleton, *Angew. Chem., Int. Ed.*, **2019**, *58*, 14955–14958.
7. A. W. Heard, S. M. Goldup, *Chem.*, **2020**, *6*, 994–1006.
8. M. W. Ambrogio, C. R. Thomas, Y.-L. Zhao, J. I. Zink, J. F. Stoddart, *Acc. Chem. Res.*, **2011**, *44*, 903–913.
9. J. E. Green, et al., *Nature*, **2007**, *445*, 414–417.
10. H. V. Schroder, C. A. Schalley, *Chem. Sci.*, **2019**, *10*, 9626–9639.
11. G. De Bo, M. A. Y. Gall, S. Kuschel, J. De Winter, P. Gerbaux, D. A. Leigh, *Nat. Nanotechnol.*, **2018**, *13*, 381–385.
12. Q. Zhang, S.-J. Rao, T. Xie, X. Li, T.-Y. Xu, D.-W. Li, D.-H. Qu, T.-T. Long, H.-Tian, *Chem.*, **2018**, *4*, 2670–2684.
13. Y. Qiu, et al, *Science*, **2020**, *368*, 1247–1253.
14. J. P. Sauvage, C. Dietrich-Buchecker, *Molecular Catenanes, Rotaxanes and Knots*; Wiley: New York, **1999**.
15. C. J. Brun, J. F. Stoddart, *The Nature of the Mechanical Bond: From Molecules to Machines*; Wiley: Hoboken, NJ, **2016**.
16. M. Curcio, F. Nicoli, E. Paltrinieri, E. Fois, G. Tabacchi, L. Cavallo, S. Silvi, M. Baroncini & A. Credi, *J. Am. Chem. Soc.*, **2021**, *143*(21), 8046-8055.
17. K. Nakazono, T. Takata, *Chem. - Eur. J.*, **2010**, *16*, 13783–13794.
18. Y. Matsuoka, Y. Mutoh, I. Azumaya, S. Kikkawa, T. Kasama, S. Saito, *J. Org. Chem.*, **2016**, *81*, 3479–3487.
19. B. Riss-Yaw, C. Clavel, P. Laurent, P. Waeleès, F. Coutrot, *Chem. - Eur. J.*, **2018**, *24*, 13659–13666.

20. J. Echavarren, M. A. Y. Gall, A. Haertsch, D. A. Leigh, V. Marcos, D. J. Tetlow, *Chem. Sci.*, **2019**, *10*, 7269–7273.
21. Y. Segawa, M. Kuwayama, Y. Hijikata, M. Fushimi, T. Nishihara, J. Pirillo, J. Shirasaki, N. Kubota, K. Itami, *Science*, **2019**, *365*, 272–276.
22. Y. Sakata, T. Ogura, S. Akine, *Chem. Commun.* **2020**, *56*, 8735–8738.
23. N. Kihara, Y. Tachibana, H. Kawasaki, T. Takata, *Chem. Lett.*, **2000**, *29*, 506–507.
24. G. Ragazzon, A. Credi, B. Colasson, *Chem. - Eur. J.*, **2017**, *23*, 2149–2156.
25. G. Ragazzon, C. Schaefer, P. Franchi, S. Silvi, B. Colasson, M. Lucarini, A. Credi, *PNAS*, **2018**, *115*, 9385–9390.
26. K. Zhu, V. N. Vukotic, S. J. Loeb, *Chem. - Asian J.*, **2016**, *11*, 3258–3266.
27. K. Zhu, G. Baggi, S. J. Loeb, *Nat. Chem.*, **2018**, *10*, 625–630.
28. H.-Y. Zhou, Q.-S. Zong, Y. Han, C.-F. Chen, *Chem. Comm.*, **2020**, *56*, 9916–9936.
29. M. Baroncini, S. Silvi, M. Venturi & A. Credi, *Chem. Eur. J.*, **2010**, *16*, 11580–11587.
30. P. Waeleš, K. Fournel-Marotte, F. Coutrot, *Chem. - Eur. J.*, **2017**, *23*, 640–11529–11539.
31. Y.-X. Ma, Z. Meng, C.-F. Chen, *Org. Lett.*, **2014**, *16*, 1860–1863.
32. C. Romuald, E. Busseron, F. Coutrot, *J. Org. Chem.*, **2010**, *75*, 6516–6531.
33. V. Blanco, D. A. Leigh, V. Marcos, J. A. Morales-Serna, A. L. A. Nussbaumer, *J. Am. Chem. Soc.*, **2014**, *136*, 4905–4908.
34. M. Gauthier, F. Coutrot, F. Coutrot, *Eur. J. Org. Chem.*, **2019**, *21*, 3391–3395.
35. P. R. Ashton, R. Ballardini, V. Balzani, M. Gomez-Lopez, S. E. Lawrence, M. V. Martinez-Diaz, M. Montalti, A. Piersanti, L. Prodi, J. F. Stoddart, D. J. Williams, *J. Am. Chem. Soc.*, **1997**, *119*, 10641–10651.
36. A. Laio, M. Parrinello, *PNAS*, **2002**, *99*, 12562–12566.
37. M. Iannuzzi, A. Laio, M. Parrinello, *Phys. Rev. Lett.*, **2003**, *90*, 238302.
38. A. Barducci, M. Bonomi, M. Parrinello, *Metadynamics*. Wiley Interdiscip. Rev.: Comput. Mol. Sci. **2011**, *1*, 826–843.
39. P. Raiteri, G. Bussi, C. S. Cucinotta, A. Credi, J. F. Stoddart, M. Parrinello, *Angew. Chem., Int. Ed.*, **2008**, *47*, 3536–3539.
40. R IBM Corp. CPMD code. <http://www.cpmc.org> (accessed 2021- 04-23).
41. J. Groppi, L. Casimiro, M. Canton, S. Corra, M. Jafari-Nasab, G. Tabacchi, L. Cavallo, M. Baroncini, S. Silvi, E. Fois, A. Credi, *Angew. Chem., Int. Ed.*, **2020**, *59*, 14825–14834.

42. T. H. Dunning, *J. Chem. Phys.*, **1989**, *90*, 1007-1023.
43. J.-D. Chai, M. Head-Gordon, *Phys. Chem. Chem. Phys.*, **2008**, *10*, 6615.
44. J. Gauss, *J. Chem. Phys.*, **1993**, *99*, 3629-3643.
45. D. E. Woon, T. H. Dunning, *J. Chem. Phys.*, **1993**, *98*, 1358-1371.
46. R. Jain, T. Bally, P. R. Rablen, *J. Org. Chem.*, **2009**, *74*, 4017-4023.
47. M. J. Frisch, G. W. Trucks, H. B. Schlegel, G. E. Scuseria, M. A. Robb, J. R. Cheeseman, G. Scalmani, V. Barone, B. Mennucci, G. A. Petersson, H. Nakatsuji, M. Caricato, X. Li, H. P. Hratchian, A. F. Izmaylov, J. Bloino, G. Zheng, D. J. Sonnenb, Gaussian 09, Revision E.01., Gaussian, Inc.: Wallingford CT 2009.
48. J. Tomasi, B. Mennucci, R. Cammi, *Chem. Rev.*, **2005**, *105*, 2999-3094.
49. R. Car, M. Parrinello, *Phys. Rev. Lett.*, **1985**, *55*, 2471-2474.
50. A. Laio, M. Parrinello, *PNAS*, **2002**, *99*, 12562-12566.
51. M. Iannuzzi, A. Laio, M. Parrinello, *Phys. Rev. Lett.*, **2003**, *90*, 4.
52. J. P. Perdew, K. Burke, M. Ernzerhof, *Phys. Rev. Lett.*, **1996**, *77*, 3865-3868.
53. S. Grimme, *J. Comput. Chem.*, **2006**, *27*, 1787-1799.
54. D. Vanderbilt, *Phys. Rev. B*, **1990**, *41*, 7892-7895.
55. S. Nosé, *J. Chem. Phys.*, **1984**, *81*, 511-519.
56. W. G. Hoover, *Phys. Rev. A*, **1985**, *31*, 1695-1697.
57. D. Marx, J. Hutter, *Ab Initio Molecular Dynamics*; Cambridge University Press: Cambridge, **2009**.
58. IBM Corp. 1990–2017; MPI für Festkörperforschung Stuttgart 1997–2001. *CPMD: Car Parrinello Molecular Dynamics*. **2017**.

# Conclusion

---

This thesis started with an introductory chapter concerning the main structural and functional aspects of artificial molecular machines. Mechanically interlocked molecules, i.e., MIMs, have a central role in this area of Chemistry; the reason for their importance is that mechanomolecules possess unique stereochemical properties derived from the presence of the mechanical bond. Some examples were reported to prove the potential of interlocked compounds in the realization of mechanical movements resembling those exhibited by macroscopic machines. However, the differences between the chemical and physical aspects that govern the macro- and nano- machines operation were delineated to avoid some common and risky misinterpretations.

After this part, the heart of the thesis was disclosed, and three experimental projects were reported. In the first project, a linear motor prototype was described; this molecule, whose synthesis was accurately detailed, presents a peculiar behavior upon irradiation with UV light. In the dark, the linear motor self-assembles with macrocycles resulting in the formation of a pseudorotaxane, the subsequent irradiation of the system induces a release of the macrocycles into the solution. This is particularly interesting since light seems to sustain an out of equilibrium state that is realized through a complex scheme of photochemical and complexation reactions. Furthermore, this study presents a rather novel approach to investigate a challenging network of reactions by combining  $^1\text{H}$  and  $^{19}\text{F}$  NMR experiments.

The thesis continued with a second project in which light was again the protagonist. In this case, a photoresponsive [2]rotaxane was investigated, the synthesis is noteworthy since the stoppering reaction coincides with the formation of a novel and unreported photochromic station. The system, endowed with a pH sensitive recognition site, was thoroughly characterized by NMR and UV-visible spectroscopy. The experimental data obtained from accurately designed experiments suggest that a photoinduced proton transfer can be achieved between the isomeric forms (*E*, *Z*) of this rotaxane. In the interpretation proposed, the acid-base reaction occurs together with a co-conformational rearrangement of the rotaxane components that coincides with the ring shuttling between the two stations; this mechanism represents a new strategy to achieve a light-induced shuttling process in a rotaxane and is interesting in the research domain of the synthesis and operation of autonomous molecular machines.

The protagonist of the last project is a [3]rotaxane characterized by two lateral pH sensitive stations and one central non-deactivable recognition site for two DB24C8. Upon external control is possible to generate a family of different [3]rotaxanes that differ for the relative ratio between rings and recognition sites; these species are again connected by a scheme of acid-base reactions. Combining UV-vis and NMR experiments, it was possible to prove that the mechanical bond has consequences on the thermodynamic properties of the pH sensitive station; particularly, the acidity of a complexed recognition site resulted decreased if the shuttling toward the central non-deactivable station was hindered by the occupancy of the latter by a macrocycle. Another interesting aspect of this work was the characterization of the dynamic properties of the [3]rotaxane in which two macrocycles were held around the central station by weak forces; an arrangement that is rarely reported. To study this system, variable temperature NMR experiments and computational techniques were employed, the results proved the existence of different stable co-conformations whose population distribution depends on the temperature. This work highlighted the unusual properties of interlocked systems, which present a mismatch between the number of rings and stations; moreover, in spite of their huge potential [3]rotaxanes are still scarcely investigated.

In conclusion, it should be obvious to a careful reader that many of the reaction schemes depicting the operation of the described systems actually represent complex networks of reactions encompassing mutually interconverting interlocked species. The throughout comprehension of these type of reaction networks represent a novel and very active area of research, which promises to open a new and interesting perspective for the exploitation of the unique properties of the interlocked compounds. Indeed, the rational design of complex reaction networks encompassing MIMs species could enable to create artificial analogues of the emerging properties realized by the natural biochemical networks present within living cells.



# Acknowledgement

---

Quando ho iniziato questo percorso di dottorato non avevo la minima idea di quanto sarebbero stati intensi questi tre anni. A rendere questa esperienza così ricca è stata la cura che tu Alberto hai riservato per tutti noi componenti di questo gruppo di ricerca, ti devo tantissimo perché mi hai sempre incoraggiato a dare la possibilità di crescere scientificamente (e non solo); in te ho trovato un riferimento che porterò sempre con me.

Gli scambi con te Massimo sono sempre stati fonte di spunti di riflessione che mi hanno agevolato il lavoro, ti sono molto grato per questo e per la tua costante disponibilità. Serena, nelle occasioni di confronto che abbiamo avuto sei sempre stata generosa spendendo il tuo tempo per analizzare criticamente i risultati sperimentali per questo ti ringrazio.

Mi reputo fortunato perché in questi tre anni ho avuto delle “guide” fantastiche a cui devo tanto; voglio ringraziare Jessica, da te ho imparato moltissima della Chimica che è riportata in questa tesi ma soprattutto ho imparato un approccio alla sintesi logico e rigoroso. Max, lavorare insieme è stata una esperienza bellissima, hai sempre una soluzione a qualsiasi problema e non ti stanchi mai di parlare di Scienza, la cosa di cui ti sono più grato è di avermi insegnato come portare avanti le proprie idee, in te ho trovato un vero amico. *Another person that I want to thank is Marina, you were the “light” of my research, and not only because we worked on photoactive molecules! The thing that I admired more about you is your ability to face complex data, I will remember this attitude in my future challenges.* Ultimo, ma non per importanza, Stefano sei sempre stato prontissimo a spiegarmi e a fornirmi riferimenti dei concetti più importanti del nostro ambito di ricerca, questo mi ha permesso di accelerare molto, ti ringrazio davvero per questo.

Erica abbiamo iniziato questa avventura insieme e ho condiviso tante gioie e dolori. Sei stata un’ottima compagna di viaggio e sono felice di aver trovato una amica in te, è bello guardare indietro e pensare di essere cambiati alla fine di questo percorso.

Ci sono poi delle persone che pur non avendo condiviso con me il laboratorio hanno reso possibile tutto questo, la mia famiglia. A loro sono infinitamente grato per aver sostenuto tutto il mio percorso fin dal primo laboratorio casalingo.

Linda Amore mio, non so se mai riuscirò a ripagare l'incredibile pazienza che hai dimostrato nel sopportarmi durante la stesura di questa tesi! Da te risale la forza con cui affronto tutte le mie sfide, sarei poco senza di te.